National Technical University of Athens
School of Mechanical Engineering
Thermal Energy Sector
Laboratory of Steam Boilers and Thermal Plants

PhD Thesis:

THERMODYNAMIC ANALYSIS AND EXPERIMENTAL INVESTIGATION OF SOLAR DRIVEN SMALL SCALE SYSTEMS FOR HEATING, COOLING AND POWER PRODUCTION

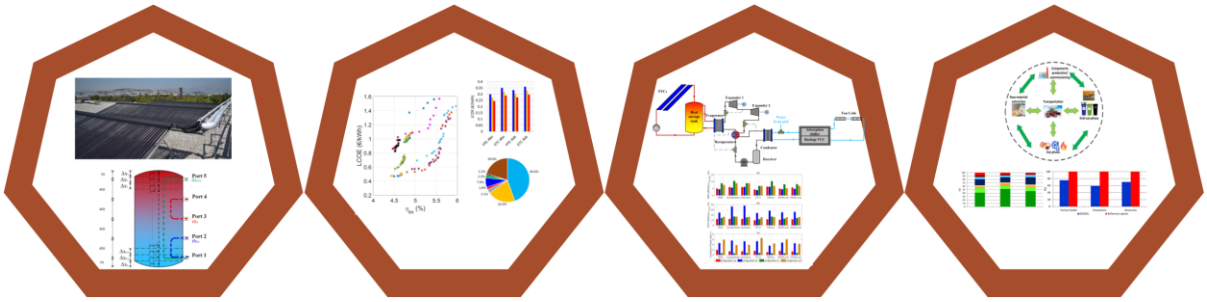

Tryfon Roumpedakis
MSc. Mechanical Engineer

Supervisor: Prof. Sotirios Karellas

Athens, October 2021

Επιβλέπων Καθηγητής

Δρ. Σ. Καρέλλας

Καθηγητής ΕΜΠ

Τριμελής Συμβουλευτική Επιτροπή

Δρ. Ε. Κακαράς

Καθηγητής ΕΜΠ

Δρ. Σ. Καρέλλας

Καθηγητής ΕΜΠ

Δρ. Ειρήνη Κορωνάκη

Αναπληρώτρια Καθηγήτρια ΕΜΠ

Επταμελής Εξεταστική Επιτροπή

Δρ. Σωτήριος Καρέλλας	Καθηγητής ΕΜΠ
Δρ. Εμμανουήλ Κακαράς	Καθηγητής ΕΜΠ
Δρ. Εμμανουήλ Ρογδάκης	Καθηγητής ΕΜΠ
Δρ. Άγις Παπαδόπουλος	Καθηγητής ΑΠΘ
Δρ. Σωτήρης Καλογήρου	Καθηγητής Τεχνολογικό Πανεπιστήμιο Κύπρου
Δρ. Andrea Lazzaretto	Καθηγητής University of Padova
Δρ. Ειρήνη Κορωνάκη	Αναπληρώτρια Καθηγήτρια ΕΜΠ

Acknowledgements

I would like to deeply thank Professor S. Karellas for the opportunity to be involved in such a challenging and interesting dissertation topic, as well as for the overall guidance and cooperation throughout all the years of my presence in the laboratory. Moreover, I would like to express my gratitude to a number of colleagues, without the help of whom the completion of this dissertation would be almost impossible. Namely, Dr. P. Pallis, Dr. A. Nikoglou, Dr. A. Leontaritis, Dr. K. Braimakis, Dipl-Ing. Stratis Varvagiannis, Dipl-Ing. Antonios Charalampidis, Dipl-Ing. Despina Magiri-Skouloudi, Dipl-Ing. Evropi Monokrousou. and Eythimios Dimitriadis. Last but not least, I would like to thank Dipl-Ing. George Kallis, who assisted tirelessly and with great patience towards the realization of many presented in this dissertation studies.

Finally, I would like to thank my family, my fiancé and my friends for their patience and support over these years.
This work is dedicated to the memory of my father.

Special Acknowledgement

I would also like to express my sincere gratitude to Onassis Foundation for the overall support during my doctoral studies. Its assistance was crucial for the smooth completion of my studies throughout these three and half years.

Summary

Climate change is more and more evident lately, pressing humanity for quick measures towards the energy transition to a more sustainable basis. Within this context, a number of measures and policies have been introduced across the world, to promote the use of clean, zero carbon footprint technologies. On EU basis, the Energy Efficiency Directive 2018/2002 established a detailed policy for the promotion of renewables within the EU, setting a target of at least 32.5% renewable energy contribution in the total energy share by 2030. Moreover, each member state of the EU has set specific targets and has introduced a number of financial and other indirect incentives to further promote the penetration of renewables. In this perspective, the present work focused in the evaluation of small scale solar driven systems for heating, cooling and/or power production. The study included the detailed modelling and, whenever possible, the experimental validation of the developed models, the techno-economic optimization of solar driven power generation and solar heating and cooling setups, the assessment of solar driven trigeneration systems and the environmental assessment of the aforementioned systems.

Chapter 1 provides a brief review of key set targets and directives on EU and national, for Greece, bases. In order to have a clearer view of the energy status quo, an up-to-date analysis of the Greek and EU27 energy mix is presented, which allows to quantify the potential for the renewables' penetration. As many of the considered technologies have drawn attention over the last two decades, a discussion on the respective market is also provided. Despite the growth of the solar market, solar driven systems require a number of financial incentives to turn them competitive against more conventional technologies and therefore a list of the available tools in Greece and, for the needs of comparison, in Italy is discussed. Finally, the scope and the outline of dissertation are presented.

In order to assess both techno-economically and environmentally the performance of solar driven systems, it is necessary to develop a number of accurate simulation models, based on the needs of each dedicated study. Within this context, Chapter 2 provides a detailed description of the developed models and the corresponding experimental procedure to validate their accuracy. In addition to the validation experiments, a number of tests were conducted with novel components to assess their potential and evaluate their field performance.

Owing to the variety of the evaluated technologies in the dissertation, there was a number of components/subsystems without any available experimental test rig for validation. In Chapter 3, are discussed all those simulation models that were developed based on data validation from literature or previous works.

Once all components' models are developed and presented, they are combined to formulate the various solar driven systems for evaluation and optimization. In Chapter 4, a techno-economic optimization of the available solar cooling/heating systems is presented. The systems are evaluated for use in a residential application for the case of an existing building, while the economics are calculated under the assumption that the proposed systems will replace the existing conventional heating and cooling systems of the building. A dedicated genetic algorithm is applied for the needs of the techno-economic optimization, identifying the optimal design aspects of each system to maximize its competitiveness. Similarly to the solar cooling/heating study, a techno-economic optimization procedure is also discussed for the case of a solar driven Organic Rankine Cycle (ORC) system. This procedure is divided in

two subroutines, one for a low-grade heat source and one for a medium-grade heat source, with the use of concentrating solar collectors.

The techno-economic optimization of the separate systems and its promising results are followed by the evaluation of the solar driven combined cooling, heating and power (CCHP) system, presented in Chapter 5. A system allocation study was conducted to define the optimal configuration towards the maximization of the first and second law performance. In fact, the results revealed a satisfactory performance, reaching exergetic efficiencies up to 40%.

Given the growing environmental concerns, it is worth assessing the sustainability of the investigated systems from an environmental viewpoint and over their entire life cycle, as the use phase impact is only a margin of the total system's emissions. Therefore, Chapter 6 presents the conducted life cycle analyses on the solar cooling/heating systems in comparison to the conventional alternatives, to identify the optimal environmentally system. Moreover, a similar life cycle study is presented for a small-scale ORC, with two alternative designs, one solar driven and one for waste heat recovery. In all life cycle analyses, a number of case studies is also analyzed to evaluate key influencing factors on the environmental performance of the evaluated systems.

In final Chapter 7, the key conclusions and the general highlights of the dissertation are discussed, followed by some potential recommendation for future work.

Περίληψη

Η κλιματική αλλαγή είναι ολοένα και πιο εμφανής τα τελευταία χρόνια, πιέζοντας την ανθρωπότητα για άμεσα μέτρα προς την κατεύθυνση της ενεργειακής μετάβασης σε πιο βιώμισες μορφές ενέργειας. Προς αυτή την κατεύθυνση, μια σειρά μέτρων και πολιτικών έχουν εφαρμοστεί παγκοσμίως, για την προώθηση της χρήσης καθαρών τεχνολογιών μηδενικού αποτυπώματος. Σε επίπεδο ΕΕ, η οδηγία για την ενεργειακή απόδοση 2018/2002 καθιέρωσε ένα αναλυτικό πολιτικό πλαίσιο για την προώθηση των ανανεώσιμων πηγών ενέργειας (ΑΠΕ) εντός της ΕΕ, θέτοντας στόχο τουλάχιστον 32,5% συνεισφοράς των ανανεώσιμων πηγών ενέργειας στο συνολικό ενεργειακό μερίδιο έως το 2030. Επιπλέον, κάθε κράτος μέλος της ΕΕ έχει θέσει συγκεκριμένους στόχους και έχει εισαγάγει μια σειρά οικονομικών και άλλων έμμεσων κινήτρων για την περαιτέρω προώθηση της διείσδυσης των ΑΠΕ. Με βάση και τα παραπάνω, η παρούσα διδακτορική διατριβή επικεντρώθηκε στην αξιολόγηση των ηλιακών συστημάτων μικρής κλίμακας για θέρμανση, ψύξη και/ή παραγωγή ενέργειας. Η μελέτη περιελάμβανε τη λεπτομερή μοντελοποίηση και, όπου ήταν δυνατόν, την πειραματική διακρίβωση των αναπτυγμένων μοντέλων, την τεχνο-οικονομική βελτιστοποίηση της ηλιακής παραγωγής ενέργειας και των ηλιακών εγκαταστάσεων θέρμανσης και ψύξης, την αξιολόγηση των συστημάτων τροφοδοσίας με ηλιακή ενέργεια και την περιβαλλοντική εκτίμηση των προαναφερθέντων συστημάτων.

Το Κεφάλαιο 1 παρουσιάζει μια σύντομη ανασκόπηση των βασικών προκαθορισμένων στόχων και οδηγιών σε κοινοτικό και εθνικό, για την Ελλάδα, επίπεδο. Προκειμένου να υπάρξει μια πιο σαφής εικόνα της τρέχουσας ενεργειακής κατάστασης, παρουσιάζεται μια επικαιροποιημένη ανάλυση του ενεργειακού μείγματος Ελλάδας και ΕΕ27, η οποία επιτρέπει τον ποσοτικό προσδιορισμό των δυνατοτήτων διείσδυσης των ανανεώσιμων πηγών ενέργειας. Καθώς πολλές από τις εξεταζόμενες τεχνολογίες δραστηριοποιούνται κυρίως τις τελευταίες δύο δεκαετίες, παρέχεται επίσης μία σχετική συζήτηση για την αντίστοιχη αγορά. Παρά την ανάπτυξη της αγοράς ηλιακής ενέργειας, τα ηλιακά συστήματα απαιτούν μια σειρά οικονομικών κινήτρων για να καταστούν ανταγωνιστικά έναντι πιο συμβατικών τεχνολογιών και συνεπώς συζητείται μια λίστα με τα διαθέσιμα οικονομικά κίνητρα στην Ελλάδα και, για τις ανάγκες σύγκρισης, στην Ιταλία. Τέλος, παρουσιάζονται οι κύριοι στόχοι και το συνολικό πλάνο της διατριβής.

Προκειμένου να εκτιμηθεί τόσο τεχνο-οικονομικά όσο και περιβαλλοντικά η απόδοση των ηλιακών συστημάτων, είναι απαραίτητο να αναπτυχθούν μια σειρά μοντέλων προσομοίωσης ακριβείας, με βάση τις ανάγκες κάθε στοχευμένης μελέτης. Σε αυτό το πλαίσιο, το Κεφάλαιο 2 παρέχει μια λεπτομερή περιγραφή των αναπτυχθέντων μοντέλων και την αντίστοιχη πειραματική διαδικασία για την διακρίβωσή τους. Εκτός από τα πειράματα διακρίβωσης, πραγματοποιήθηκε μια σειρά δοκιμών με καινοτόμες εγκαταστάσεις για την αξιολόγηση των δυνατοτήτων τους και την αξιολόγηση των επιδόσεων τους σε πραγματικές συνθήκες λειτουργίας.

Λόγω του εύρους των αξιολογούμενων τεχνολογιών στη διατριβή, υπήρχε μια σειρά εξαρτημάτων/υποσυστημάτων χωρίς καμία διαθέσιμη πειραματική δοκιμαστική πλατφόρμα για επικύρωση. Στο Κεφάλαιο 3, συζητούνται όλα εκείνα τα μοντέλα προσομοίωσης που αναπτύχθηκαν με βάση την διακρίβωση δεδομένων από βιβλιογραφία ή προηγούμενες διατριβές.

Μόλις αναπτυχθούν και παρουσιαστούν όλα τα επιμέρους μοντέλα, αυτά συνδυάζονται για να διαμορφώσουν τα διάφορα ηλιακά συστήματα προς αξιολόγηση και βελτιστοποίηση. Στο

Κεφάλαιο 4, παρουσιάζεται μια τεχνοοικονομική βελτιστοποίηση των διαθέσιμων ηλιακών συστημάτων ψύξης/θέρμανσης. Τα συστήματα αξιολογούνται για χρήση σε οικιακή εφαρμογή για την περίπτωση υπάρχοντος κτηρίου, ενώ τα οικονομικά υπολογίζονται με την παραδοχή ότι τα προτεινόμενα συστήματα θα αντικαταστήσουν τα υπάρχοντα συμβατικά συστήματα θέρμανσης και ψύξης του κτηρίου. Ένας ειδικός γενετικός αλγόριθμος εφαρμόζεται για τις ανάγκες της τεχνοοικονομικής βελτιστοποίησης, προσδιορίζοντας τις βέλτιστες πτυχές σχεδιασμού κάθε συστήματος για τη μεγιστοποίηση της ανταγωνιστικότητάς του. Ομοίως με τη μελέτη ηλιακής ψύξης/θέρμανσης, συζητείται επίσης μια διαδικασία τεχνοοικονομικής βελτιστοποίησης για την περίπτωση ενός ηλιακού συστήματος Οργανικού Κύκλου Rankine (ORC). Αυτή η διαδικασία χωρίζεται σε δύο υπο-ρουτίνες, μία για πηγή θερμότητας χαμηλής θερμοκρασίας και μία για πηγή θερμότητας μέσης θερμοκρασίας, με τη χρήση συγκεντρωτικών ηλιακών συλλεκτών.

Η τεχνοοικονομική βελτιστοποίηση των ξεχωριστών συστημάτων και τα πολύ υποσχόμενα αποτελέσματά της, ακολουθούνται από την αξιολόγηση ενός συστήματος ηλιακής ενέργειας συνδυασμένης ψύξης, θέρμανσης και ισχύος (CCHP), που παρουσιάζεται στο Κεφάλαιο 5. Διεξήχθη μελέτη στο σημείο λειτουργίας για τον καθορισμό της βέλτιστης διαμόρφωσης προς τη μεγιστοποίηση της απόδοσης του πρώτου και του δεύτερου θερμοδυναμικού νόμου. Τα αποτελέσματα αποκάλυψαν μια ικανοποιητική απόδοση, φτάνοντας σε εξεργειακούς βαθμούς απόδοσης έως και 40%.

Λαμβάνοντας υπόψη τις αυξανόμενες περιβαλλοντικές ανησυχίες, αξίζει να αξιολογηθεί η βιωσιμότητα των υπό διερεύνηση συστημάτων από περιβαλλοντική σκοπιά και σε βάθος ολόκληρου του κύκλου ζωής τους, καθώς το περιβαλλοντικό αποτύπωμα της φάσης χρήσης είναι μόνο ένα τμήμα των συνολικών εκπομπών του συστήματος. Ως εκ τούτου, το Κεφάλαιο 6 παρουσιάζει τις αναλύσεις του κύκλου ζωής στα ηλιακά συστήματα ψύξης/θέρμανσης σε σύγκριση με τις συμβατικές εναλλακτικές, για τον προσδιορισμό του βέλτιστου περιβαλλοντικού συστήματος. Επιπλέον, μια παρόμοια μελέτη κύκλου ζωής παρουσιάζεται για ένα ORC μικρής κλίμακας, με δύο εναλλακτικά σχέδια, ένα ηλιακό και ένα για ανάκτηση θερμότητας. Σε όλες τις αναλύσεις του κύκλου ζωής, αναλύονται επίσης μια σειρά από μελέτες περιπτώσεων για την αξιολόγηση βασικών παραγόντων που επηρεάζουν την περιβαλλοντική απόδοση των αξιολογούμενων συστημάτων.

Στο τελευταίο κεφάλαιο 7, συζητούνται τα βασικά συμπεράσματα και τα γενικά σημεία ενδιαφέροντος της διατριβής, ακολουθούμενα από κάποιες πιθανές προτάσεις για μελλοντική εργασία.

Table of Contents

List of Figures

List of Tables

Nomenclature

A	Surface,	[m²]
A_c	Conduction surface,	[m²]
A_o	Outer surface,	[m²]
Bo	Boiling number,	[-]
C	Cost,	[€]
c_{el}	Electricity price,	[€/kWh]
c_{gas}	Natural gas price,	[€/kWh]
C_{main}	Maintenance cost,	[€]
c_p	Specific heat capacity,	[J/(kg K)]
cf	Correction factor,	[-]
COP	Coefficient of performance,	[-]
COP_{Carnot}	Carnot's cycle coefficient of performance,	[-]
CRF	Capital recovery factor,	[-]
D	Diameter,	[m]
E_a	Activation energy,	[J/kg]
EER	Energy efficiency ratio,	[-]
$\dot{E}x$	Rate of exergy change,	[KJ/s]
f	Friction factor,	[-]
f_{fan}	Fan frequency ratio,	[-]
ff	Filling factor,	[-]
h	Enthalpy	[J/kg]
h_{fg}	Heat of vaporization,	[J/kg]
h_j	Enthalpy of water in zone j,	[J/kg]
I_{sol}	Solar irradiance,	[W/m²]
$LCOE$	Levelized cost of electricity/energy,	[€/kWh]
L_p	Vertical plate length,	[m]
M_j	Total mass in zone j,	[kg]
$\dot{m}$	Mass flowrate,	[kg/s]
$\dot{m}_B$	Mass flowrate of the gas boiler stream,	[kg/s]
$\dot{m}_{DHW}$	Mass flowrate of the DHW stream,	[kg/s]
$\dot{m}_{SH}$	Mass flowrate of the space heating stream,	[kg/s]
N_{exp}	Expander's rotational speed,	[rpm]
N_p	Pump's rotational speed,	[rpm]
N_{pl}	Number of plates,	[-]
n	Zone number / number of element,	[-]
NPV	Net present value,	[€]
Nu	Nusselt number,	[-]
p	Pressure,	[bar]
p_s	Saturation pressure,	[bar]
p_w	Partial vapor pressure,	[bar]
PbP	Payback period,	[years]
Pr	Prandtl number,	[-]
p_{red}	Reduced pressure,	[-]

$\dot{Q}$	Heat,	[W]
Q_{st}	Isosteric heat of adsorption,	[J/kg]
R	Gas constant,	[J/(kg K)]
r	Discount rate,	[-]
r_f	Annual increase in the fuel price,	[-]
r_{om}	Annual increase in operational and maintenance costs,	[-]
R_p	Average pore radius	[m]
Re	Reynolds number,	[-]
s	Entropy,	[J/(kg K)]
T	Temperature,	[K]
t	Time,	[s]
U_j	Internal energy in zone j,	[J/kg]
U_l	Heat transfer losses coefficient,	[W/(m² K)]
$\dot{W}_{el}$	Electric power,	[W]
$\dot{W}_{mech}$	Mechanical power,	[W]
V	Volumetric capacity,	[m³]
$\dot{V}$	Volumetric flowrate,	[m³/s]
V_{sw}	Swept volume,	[cc/rev]
v	Velocity,	[m/s]
x	Adsorbate uptake,	[kg/kg]
x_o	Limiting adsorbate uptake,	[kg/kg]
x^*	Equilibrium adsorbate uptake,	[kg/kg]
Δp	Pressure drop,	[bar]
Δt	Time step,	[s]
ΔT_{lm}	Logarithmic mean temperature difference,	[K]
Δx_j	Height of zone j,	[m]

Greek letters

θ	Temperature,	[°C]
λ	Thermal conductivity,	[W/(m K)]
η	Efficiency,	[-]
π	Pressure ratio,	[-]
ρ	Density,	[kg/m³]
φ	Chevron angle,	[deg]

Subscripts/Superscripts

ab	Absorber
abs	Absorption
abs-HP	Absorption reversible heat pump
ads	Adsorption / Adsorber
ahex	Air cooled heat exchanger
amb	Ambient
an	Annual
av	Average

ch,w	Chilled water
col	Collectors
cold	Heat exchanger’s cold stream
com	Compressor
cond	Condenser
cool	Cooling
cpump	Circulators/pumps
crit	Critical
cu	Copper
cw	Cooling water
d	Daily average
dc	Dry Cooler
el	Electrical
eq	Equivalent
evap	Evaporator
ex	Exergy
exp	Expander
Fancoil	Referring to fan coils
fg	Flue gas
fl	Working fluid
gen	Generator
hardw	Hardware
heat	Heating
hex	Heat exchanger
hot	Heat exchanger’s hot stream
HP	Heat pump
HT	High temperature circuit
hyd	Hydraulic
i	Inlet
inst	Installation
inv	Inverter
iorc	Intermediate ORC circuit
is	Isentropic
L	Liquid
LT	Low temperature circuit
motor	Pump’s motor
MT	Medium temperature circuit
o	Outlet
orc	Related to ORC system
p	Pump
phex	Plate heat exchanger
rec	Recuperator
ref	Reference
refr	Refrigerant
rt	Receiver tank

screw	Screw expander
scroll	Scroll expander
st	Storage
st*	Storage tank with coils
sthex	Shell & tube heat exchanger
su	Expander's suction
th	Thermal
tot	Total
w	Water
ze	Zeolite

Abbreviations

CCHP	Combined cooling, heat and power
CCP	Combined cooling and power
CHP	Combined heat and power
CSP	Concentrated solar power
DHW	Domestic hot water
DHWP	Domestic hot water pump
EER	Energy efficiency ratio
EPBR	Energy Performance of Buildings Regulation
ETC	Evacuated tube collector
FPC	Flat plate collector
GHG	Greenhouse gas
HTF	Heat transfer fluid
HWBP	Hot water from boiler pump
LFR	Linear Fresnel reflector
NECP	National Energy and Climate Plan
NG	Natural Gas
nZEB	Nearly-zero energy building
ORC	Organic Rankine cycle
PCM	Phase change material
PDC	Parabolic dish collector
PTC	Parabolic trough collector
PV	Photovoltaic
R&D	Research and Development
RES	Renewable energy sources
RMSE	Root Mean Square Error
SES	Seasonal energy storage
SHP	Space heating pump
STC	Solar thermal collector
STES	Seasonal thermal energy storage

Chapter 1. Introduction

1.1 The energy transition and the EU targets for 2030

One of the most crucial challenges humanity is currently facing is climate change. The increasing energy demand and the use of conventional energy sources has caused an increase in CO_2 and other greenhouse gas (GHG) emissions. As a consequence, the greenhouse effect is more and more visible in the climate, globally. In addition to the above, the reduction of fossil fuel reserves requires quick measures to meet the global energy demands on a new sustainable basis.

A number of measures and policies have been introduced across the world, to promote the use of clean, zero carbon footprint technologies and expand their market, making them economically viable in long term. On EU basis, the Renewable Energy Directive 2009/28/EC [1] established the first detailed policy for the promotion of renewables within the EU, setting a target of at least 32% renewable energy contribution in the total energy share by 2030, with an intermediate goal of 20% by 2020. Based on the aforementioned Directive, each member state is able to set specific national targets, provided that they are more ambitious than the limits set by the Directive. In 2018, a revision was brought into force with Renewable Energy Directive 2018/2001 [2], which introduced a common framework for the increase in the use of renewables, towards the climate neutrality by 2050, and set a binding target for the overall share of energy from renewable sources in the EU's gross final energy consumption in 2030. Moreover, the Energy Efficiency Directive 2018/2002 [3] set a new target of at least 32.5% renewable energy contribution. A number of sub-targets was also agreed, with a 14% renewable share in transportation section by 2030 an EU level, while each member should achieve at least 0.8% annual savings on final energy consumption for the period between 2021 and 2030.

In order to conform with the aforementioned Directives, Greece developed the revised National Energy and Climate Plan (NECP) [4], which set a number of more ambitious targets for the decarbonization of the Greek energy sector. Main aspect of this plan is the phase out of all lignite-fired power plants by 2028 [5]. An overview of the key quantitative goals set on the NECP are summarized in Fig. 1.1.

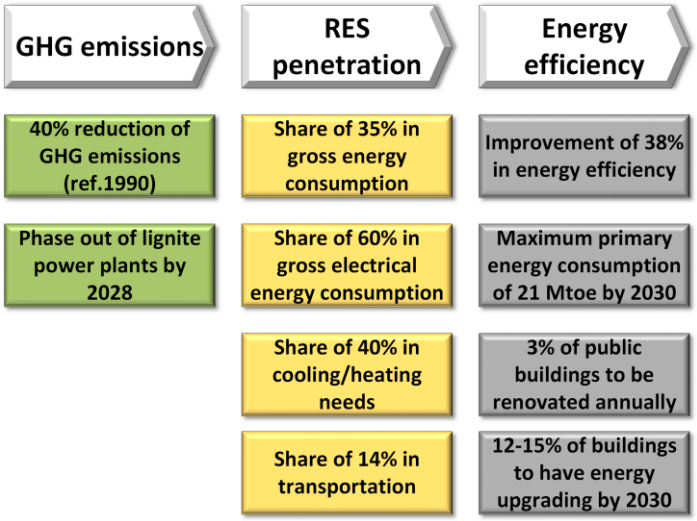

Fig. 1.1. Overview of NECP main goals. Based on data from [4]

As seen in Fig. 1.1., the goal for the phase out of the lignite-fired power plants along with the different targets for the increase in the share of renewable energy systems (RES) in both electricity and heating/cooling production highlights the growing attention towards efficient renewable driven systems at both larger and medium scales. On the other hand, the targets for the energy renovation of buildings creates similar opportunities for smaller (residential) scale systems.

A closer view on the intermediate goals defined by NECP is presented in Fig. 1.2. Specific milestones have been set until 2030 in order to create a certain roadmap for the increased penetration of RES systems. Already by 2022, a target has been set to reach a 38.6% of RES share in the electricity consumption and a corresponding 33.8% in cooling/heating consumption, as shown in Fig. 1.2 (a). These targets make quite clear the high potential of RES in the Greek market so as to comply with both the NECP and the EU Directives' targets.

In particular, as seen in Fig. 1.2 (b), a breakdown for the space heating loads has been defined with certain increase in the use of particular RES, with the solar energy having to contribute annually with 303 ktoes by 2022 and a total of 411 ktoes by 2030. In fact, despite the abundance of solar irradiance in Greece, solar energy is not prioritized in the NECP, due to reasons which will be further addressed within this dissertation.

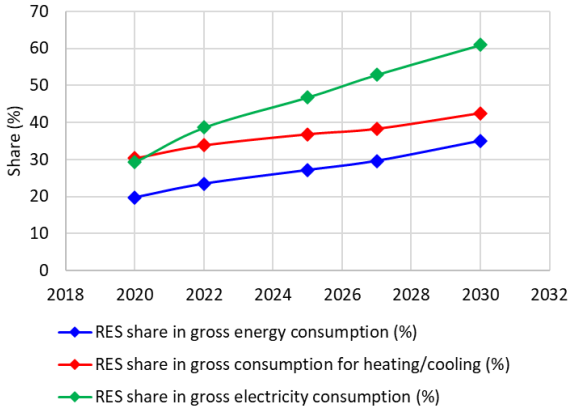

(a)

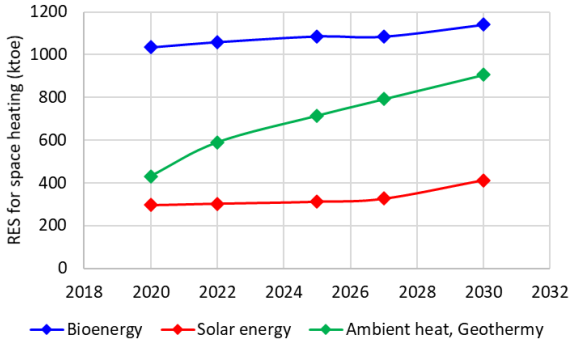

(b)

Fig. 1.2. Intermediate goals of the NECP for the penetration of RES (a) in different sectors and (b) for different types of RES in space heating. Based on data from: [4]

Among the various renewable sources, solar energy offers a lot of advantages including its large availability, the maturity of solar harvesting technologies and its smaller environmental footprint. On the other hand, the intermittence of the sun poses as the main challenge to solar

driven technologies for higher contribution to the energy mix and highlights the necessity of storage options for minimizing the dependency on backup conventional systems [6].

Solar powered systems can be mainly divided in photovoltaic (PV) driven systems and solar thermal systems. Thanks to the dedicated incentives in the past decades, PV market is quite large and such systems are characterized by high competitiveness with respect to conventional systems both economically and energetically. As a result, the focus of this dissertation will be in the solar thermally driven systems, aiming to reduce the gap towards the expansion of their market and their larger contribution to the decarbonization schemes both on national as well as on European level.

1.2 Energy mix in EU27 and Greece

Prior to a presentation of the solar market and the respective solar coupled systems, it is important to provide a brief overview of the energy status on EU and national level. Fig. 1.3 (a) presents the evolution of the gross inland consumption on the EU27 level for the period between 1990 and 2018, which was the most recent period with detailed energy statistics, as derived by Eurostat's database [7]. Furthermore, Fig. 1.3 (b) depicts an overview of the respective values of the various renewable and biofuel-powered systems. As can be seen, the total gross inland consumption peaked in the period of 2004-2008. In the last decade, the total consumption has reduced by 9% compared to maximum reported total of 1.61 Gtoes in 2006. The reason behind this decrease is twofold. First of all, the economic crisis of the European South has resulted in a certain decrease in the consumption of the respective countries. However, a significant amount of the gross consumption reduction is attributed to the enhancement of the energy transformation efficiency and the energy upgrading of various end user sectors, which resulted in smaller loads.

With respect to the renewable and biofuel-powered systems of Fig. 1.3(b), the gross inland consumption is constantly growing over the years, with an absolute increase of 150 Mtoes between 1990 and 2018, corresponding to a 211% increase. The largest share in 2018, among the various sources, belongs to primary solid biofuels with a 41.6% within the RES and biofuels and a 6.2% out of the total annual gross inland consumption.

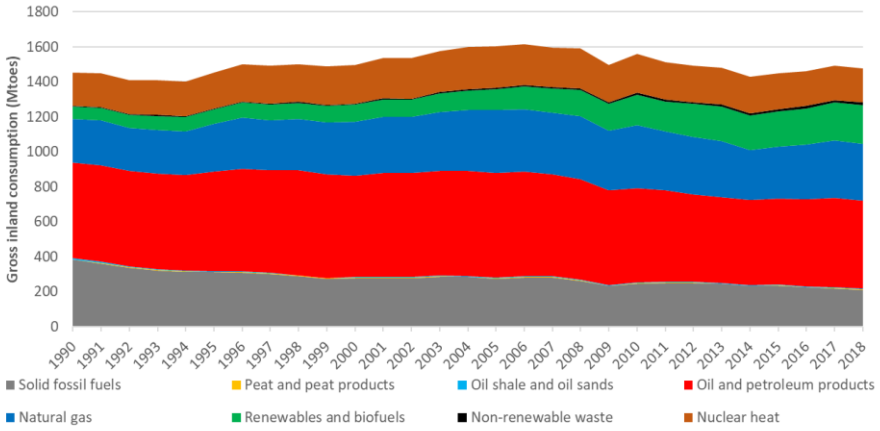

(a)

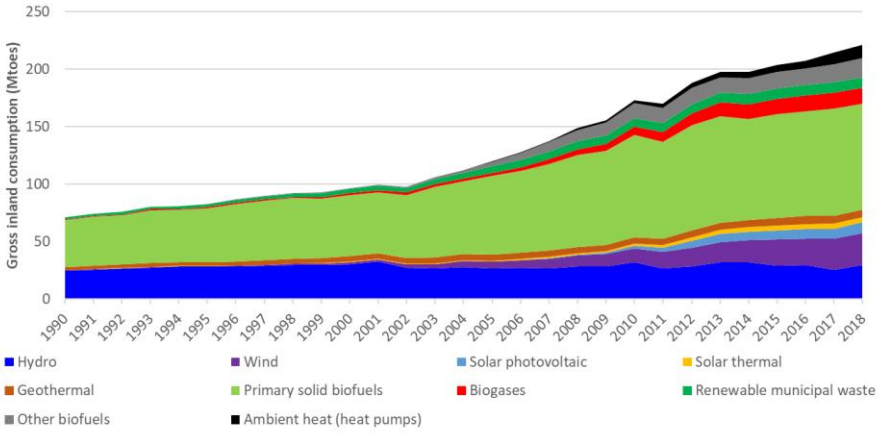

(b)

Fig. 1.3. Contribution of different types of energy sources in gross inland energy consumption for 2018 for the EU27 (a) simplified data with single listing for RES and (b) RES breakdown. Based on data from: [7].

As seen in Fig. 1.3(b), solar energy accounts only for a small fraction of the RES and biofuels sources, with only a combined 6.23% for the PVs and the solar thermally driven systems (out of which 4.28% PVs and 1.95% solar thermal systems). However, it has to be noted that the EU27 data is influenced heavily by countries of the central and northern Europe, which are characterized by lower solar potential and therefore no global conclusions can be derived. Therefore, a better overview of the solar energy utilization and prospect can be seen by observing the respective gross inland consumption of Greece, a high solar availability country, which is shown in Fig. 1.4.

Fig. 1.4 (a) has a similar profile with Fig. 1.3(a) by means of recording a peak in the period 2004-2008 and a larger decrease in the last decade, since Greece was impacted by a larger economic depression, affecting also the gross inland consumption. In fact, compared to the maximum reported annual gross inland consumption of 30.9 Mtoes, there was a 24.7% decrease in 2018, corresponding to an absolute difference of 7.6 Mtoes. With respect to the RES and biofuels, Greece reported a 13.5% share in 2018, with the corresponding value for the EU27 to be 15.0%. In terms of the RES and biofuels breakdown of Fig. 1.4 (b), the profile is a deviating from the respective for the EU27. Primary solid biofuels are again the prevailing source with a 27.0%. However, in the last years of the survey there is a high versatility of sources, with hydro and wind accounting for 16.0% and 17.5%, respectively. Solar energy has a significant contribution as well in the Greek gross inland consumption with a total 19.5% share among the RES and biofuels, corresponding to a 2.6% of the total gross inland consumption of the country in 2018. Out of the 19.5% share of the solar energy, solar thermal systems account for 9.0%, with the rest coming from PVs. This data shows the acceptance and the extensive application of solar thermal systems in the country. In this perspective, the use of hybrid solar thermally driven systems either for cooling/heating and/or electricity has great potential in Greece, which is further strengthened by the high solar availability throughout the year.

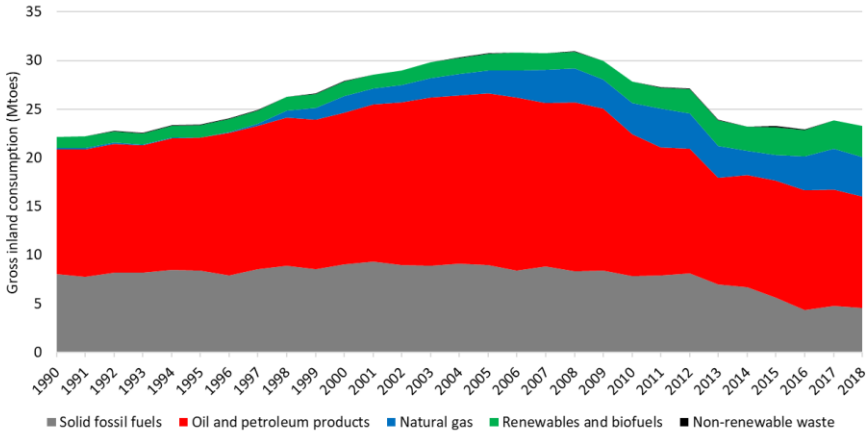

(a)

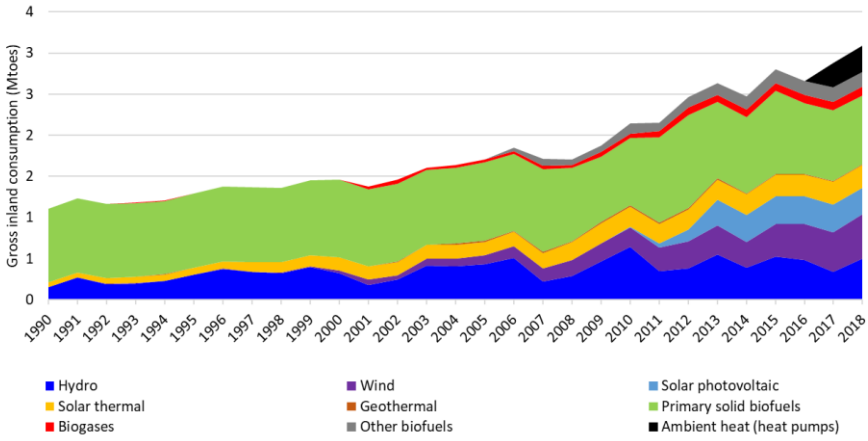

(b)

Fig. 1.4. Contribution of different types of energy sources in gross inland energy consumption for 2018 for Greece (a) simplified data with single listing for RES and (b) RES breakdown. Based on data from: [7].

A closer look in the evolution of the energy mix is provided in Fig. 1.5 and Fig. 1.6, with the comparison of the primary energy production in Greece for the years 1990 and 2018. At this point, it has to be clarified, that the difference of the primary energy production profile with the gross inland consumption is attributed mainly to the imports/exports. As in previous cases, Fig. 1.5 provides a simplified approach with a single listing for the RES and biofuels. Between 1990 and 2018, as seen in Fig. 1.5, the share of fossil fuels in the primary energy production has been reduced from 87.99% down to 59.96% Given the reduction in the primary energy production of 1.6 Mtoes between 1990 and 2018, the reduction in the primary energy derived from fossils was equal to -3605 ktoes. The corresponding increase in the primary energy produced from RES and biofuels was equal to 1912 ktoes. A breakdown of the increased penetration of the different types of RES and biofuels is presented in Fig. 1.6. Back in 1990, the main primary energy production was from primary solid biofuels with 893 ktoes, hydropower recorded a share of 152 ktoes, with the solar thermal systems accounting only for 56 ktoes. On the contrary, in 2018 the energy mix is a lot more versatile, as shown in Fig. 1.6 (b). The primary energy produced from biofuels increased by 153 ktoes, while significant contribution in the total primary energy produced by RES and biofuels came from wind and hydropower, with 542 ktoes and 494 ktoes, respectively. Solar energy was responsible for the

production of 603 ktoes, with 326 ktoes (share of 10.8%) coming from PVs and 277 ktoes (share of 9.19%) from solar thermal systems.

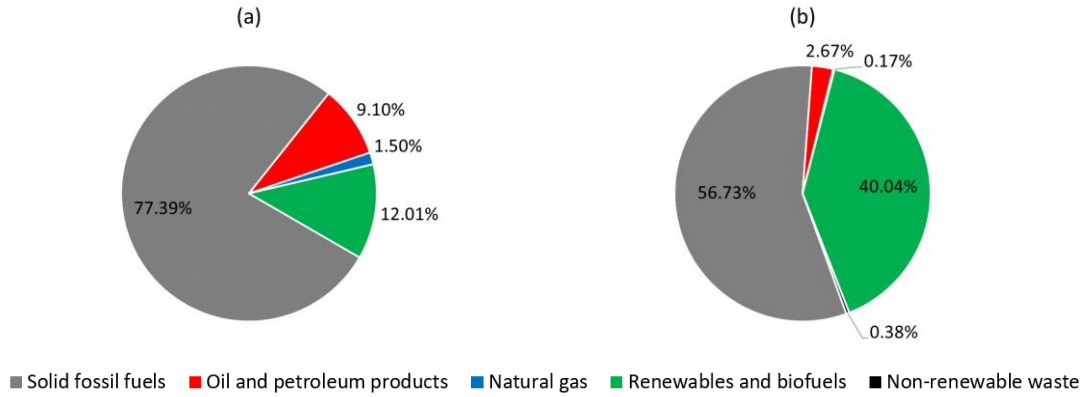

Fig. 1.5. Comparison of the different primary energy production in Greece: concentrated data with single listing for RES and biofuels (a) for 1990 and (b) for 2018. Based on data from: [7].

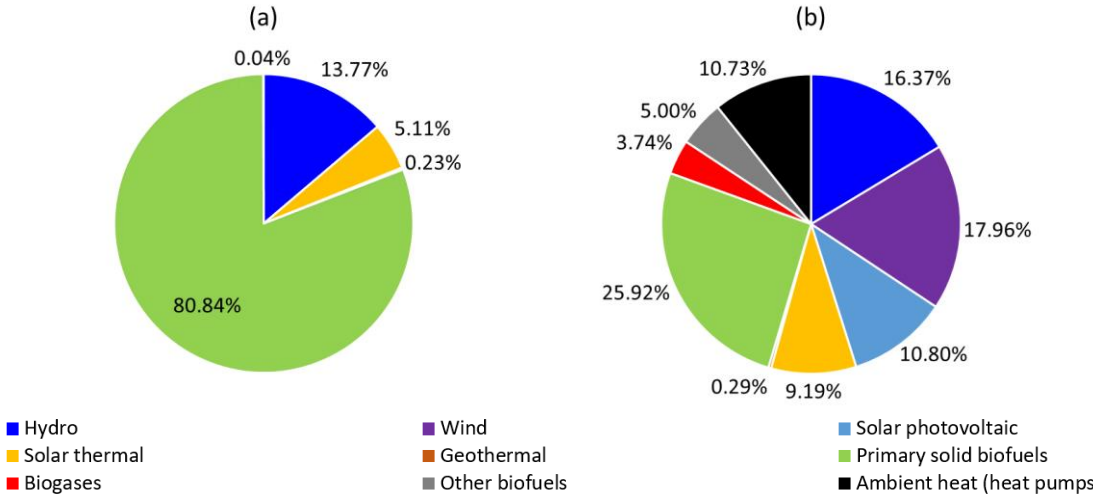

Fig. 1.6. Comparison of the different primary energy production in Greece: breakdown of Fig. 1.5 RES and biofuels (a) for 1990 and (b) for 2018. Based on data from: [7].

1.2.1 Household sector

As already discussed, the EU directives and the national guidelines in Greece, set a promising path for the increased penetration of renewables and solar energy, in specific. However, apart from the larger scale approach, it is crucial to identify the energy intensive sectors, which offer potential for exploitation of decentralized RES applications. Towards this direction, Fig. 1.7 presents the sector share on the final energy contribution for Greece, EU27 and Italy. As Italy has, similarly to Greece, high solar availability is another high potential country for solar energy applications and will be analyzed in specific case studies evaluated within this dissertation. As shown in all three pie charts of Fig. 1.7, there are similar profiles allowing for more generalized remarks. In all three cases, transport has the largest share in the final energy consumption, with a 38.92% share in the EU27, with Italy and Greece having relatively smaller shares with 31.10% and 30.52%, respectively. On the contrary, in Greece and Italy industry has an increased share, with shares of 25.77% and 21.24%, respectively, compared to the 18.09% EU27. These rather high shares of the industry highlight the potential for application of decentralized RES power, combined heat and power (CHP) or combined cooling, heat and

power (CCHP) and in particular of solar driven systems for the countries of the "solar abundant" European south.

One sector that requires particular attention is the households. In all three cases of Fig. 1.7, is the second more consuming sector with shares in the range 25.82%-28.02%. Furthermore, if one considers that a considerable part of the commercial and public services sector is also referring to buildings' consumption, it is made clear that the energy upgrading of buildings and the introduction of RES small to medium scale systems is of key importance towards the targets for 2030 set by the EU. Moreover, the higher prices of conventional energy for the residential sector compared to utility customers, enhances the economic competitiveness of residential RES applications [8, 9]. Therefore, a large part of the dissertation is analyzing alternatives on building scale.

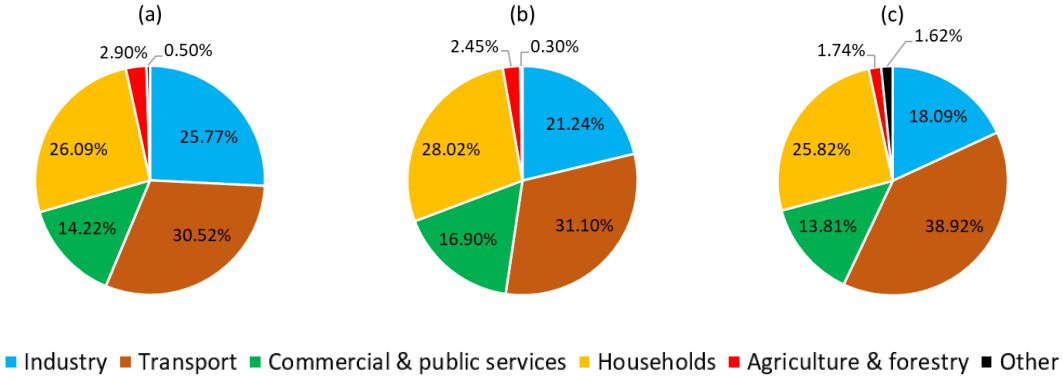

Fig. 1.7. Final energy consumption by sector for 2018 (a) in Greece, (b) in Italy and (c) in EU27. Based on data from: [7].

At this point has to be stated that, as the available data for households from Eurostat [10] does not include EU27 listings and in order to provide a comparison to the Greek status, Italian data is presented in the rest of this section.

As it is clear, there is a number of end-uses within the household sector responsible for the total contribution in Fig. 1.7. The contribution of the various end uses in the total energy consumption in households for 2018 for Greece and Italy is shown in Fig. 1.8. As seen in Fig. 1.8, there is a small deviation in the energy distribution in Greece and Italy. In Greece, space heating was responsible for the largest part of the total energy consumption with 54.5%, followed by lighting & appliances and water heating with 20.5% and 15.2 %, respectively. On the contrary, in Italy space heating accounts for 66.6% of the total energy consumption, followed by lighting and appliances with a 12.5% and water heating with a 12.4%. In both countries, cooling has a small share with 3.6% for Greece and only 0.7% for Italy, respectively. Based on these results, it is evident that both countries have significant amounts of heating/cooling loads, which is expected to favor RES based cooling/heating applications.

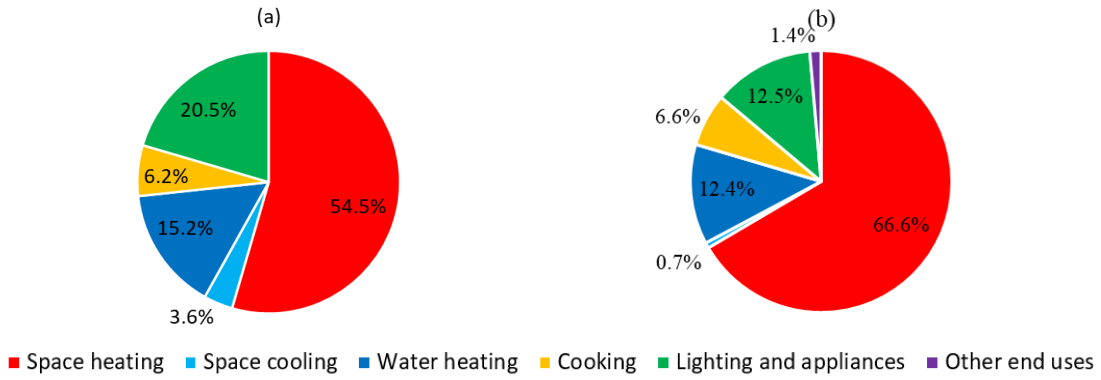

Fig. 1.8. Contribution of each type of end use in the total energy consumption in households for 2018 (a) in Greece and (b) in Italy. Based on data from: [10].

As seen in Fig. 1.9, the majority of electricity in residential sector is consumed for lighting and appliances for both Greece and Italy, based on data for 2018 [10], with a share of 55.3% and 71.5%, respectively. Considerable, electricity consumption is also reported on both countries for water heating, as usually electrical resistances are used for domestic hot water (DHW). From the scope of this study, the energy upgrading of lighting and appliances will not be investigated; however, the energy consumption for DHW shows the potential for covering those loads as well with a RES based hybrid system.

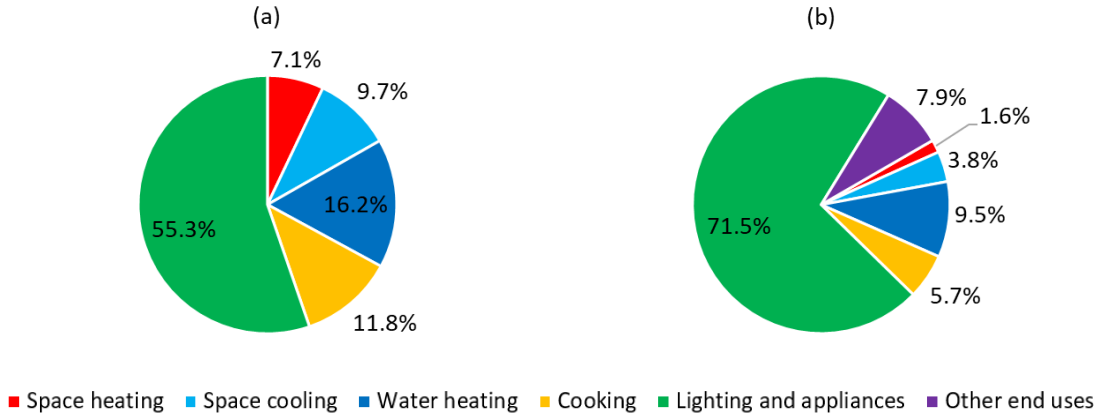

Fig. 1.9. Share of each type of end use in the total electricity consumption in households for 2018 (a) in Greece and (b) in Italy. Based on data from: [10].

In Fig. 1.10 is presented a breakdown of the various sources contributing to the space heating loads of Greece, Fig. 1.10 (a), and Italy, Fig. 1.10 (b). Both countries are heavily dependent on fossil fuels to cover the space heating loads, with Greece covering 58.2% of its heating loads with natural gas, oil petroleum products. The corresponding percentage for Italy is even higher with 68.25%. Solid biofuels have also a significant share with 31.06% in Greece, and 26.11% in Italy, respectively. Apart from solid biofuels, other RES & biofuels' systems have minimal contribution with shares of less than 2.5% in Greece, and less than 5.2% in Italy. On both cases, RES systems for heating are mainly coming from ground source heat pumps (derived heat listing in Fig. 1.10), while solar energy systems are practically negligible in both cases. Towards the climate neutrality target set by 2050 by EU, the aforementioned large shares of fossil fuel derived energy could be substituted by a number of RES alternatives, including solar cooling/heating systems, which is one of the main aspects of this study.

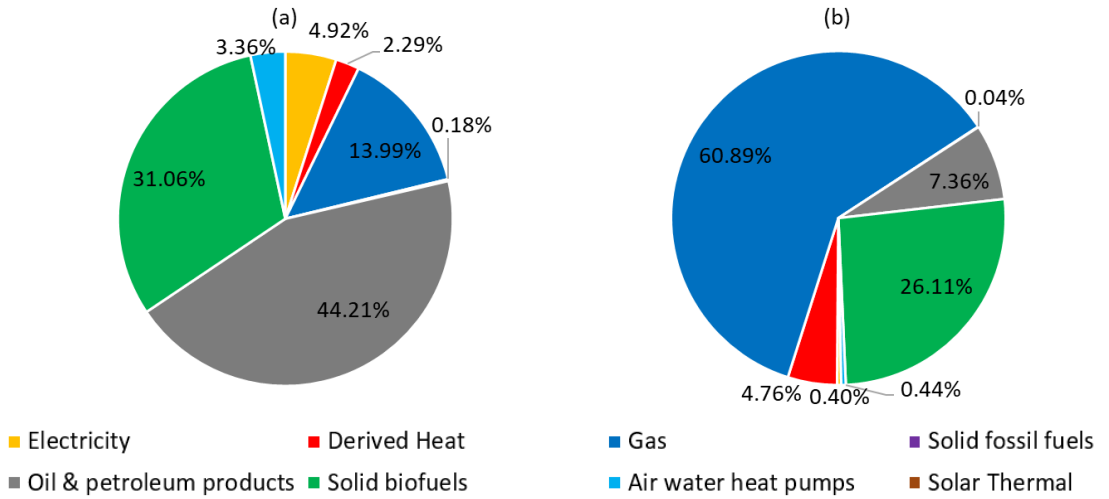

Fig. 1.10. Share of each energy source in the total energy consumption for space heating in households for 2018 (a) in Greece and (b) in Italy. Based on data from: [10].

With respect to the residential space cooling, both Italy and Greece were solely using electrical driven systems. Fig. 1.11 presents the evolution of the annual space cooling consumption between 2015-2018, for the two countries, based on data from Eurostat [10]. Despite, the decrease of almost 0.5 TWh in Greece, from 2017 to 2018, the energy consumption is still at comparable levels with Italy. Taking into account the inhabitants of Greece and Italy over the same period [11], it is shown that the Greek annual consumption for space cooling per capita is significantly higher than the respective Italian values, showing the large room for improvement in the residential cooling sector.

Finally, Fig. 1.12 provides the contribution of the various energy sources in the water heating loads of the residential sector for Greece and Italy in 2018. As seen, in Greece the use of solar thermal systems is quite extensive with a share of 44.8%, followed by electricity with a share of 39.4%. On the contrary, Italy is heavily based, still, on conventional energy with natural gas having a share of 67.3% and electricity accounting for 12.5%, while the solar thermal systems are limited to a 3.6% share. The large shares of conventional sources of energy for DHW indicates that there is significant room for energy upgrading, in particular for Italy, by increasing the solar energy applications, taking into consideration also the high solar availability in a large part of the country. With respect to Greece, the large share of solar thermal systems indicates the maturity of such systems for DHW applications and allow for an easier expansion of the market by providing hybridized solutions that could cover both DHW, heating and cooling loads.

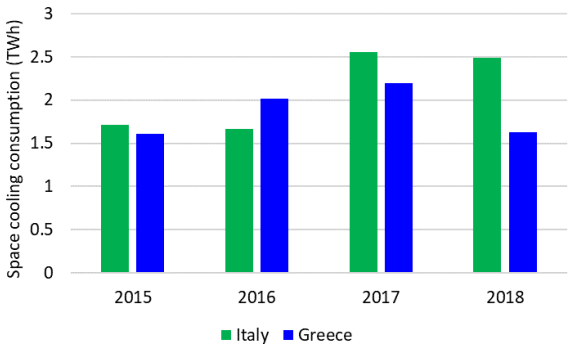

(a)

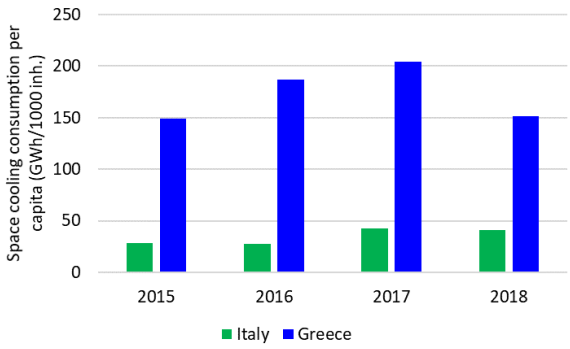

(b)

Fig. 1.11. Annual space cooling consumption for Italy in Greece between 2015-2018 (a) in absolute numbers and (b) per 1000 inhabitants. Based on data from: [10].

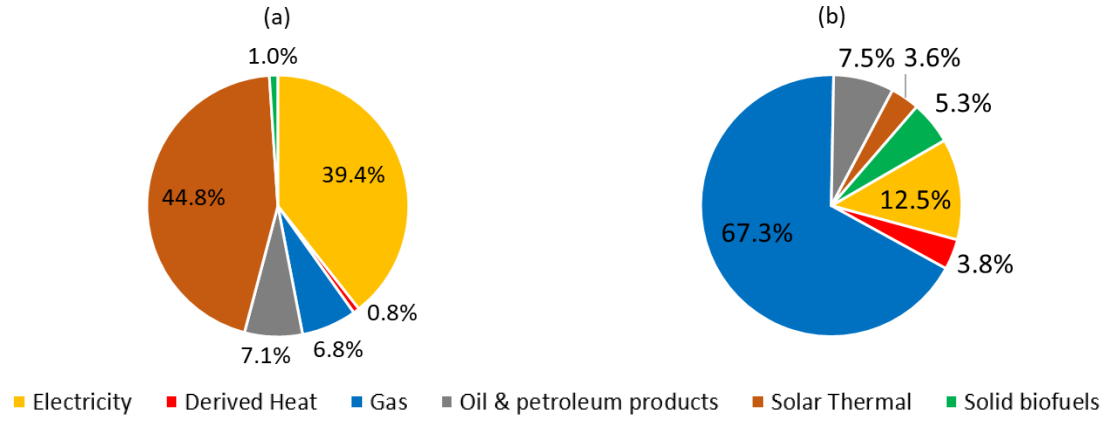

Fig. 1.12. Share of each energy source in the total energy consumption for DHW in households for 2018 (a) in Greece and (b) in Italy. Based on data from: [10].

1.3 Market status of solar applications

As discussed in previous section, the relatively high electrical and thermal loads create significant potential for the implementation of solar driven systems. However, the competitiveness of the solar systems is heavily related to the size of the respective market. The share of new solar thermal installations in 2018 across Europe is presented in Fig. 1.13 (a). As shown, Germany had the largest share of new installations with a 22.4% followed by Greece with a 15.9%, while Italy is ranked sixth with a 6.7%. Similarly, Germany is had the highest value of installed collector's area with almost 20 km^2. Italy and Greece are ranked third and fourth, respectively, with approximately 5 km^2 of installed solar collectors, as shown in Fig. 1.13 (b). One important aspect, however, to objectively assess the expansion of the solar market is the ratio of the installed solar capacity and the total population of the country. The estimation of this metric is shown in Fig. 1.13 (c). As can be seen, Cyprus and Greece are the two leading countries in the EU in terms of installed solar capacity per 1000 inhabitants. This fact, highlights the acceptance and large operational experience on solar driven systems in the two countries which may be used as a springboard for the introduction of solar hybrid systems, as the ones discussed in latter Chapters.

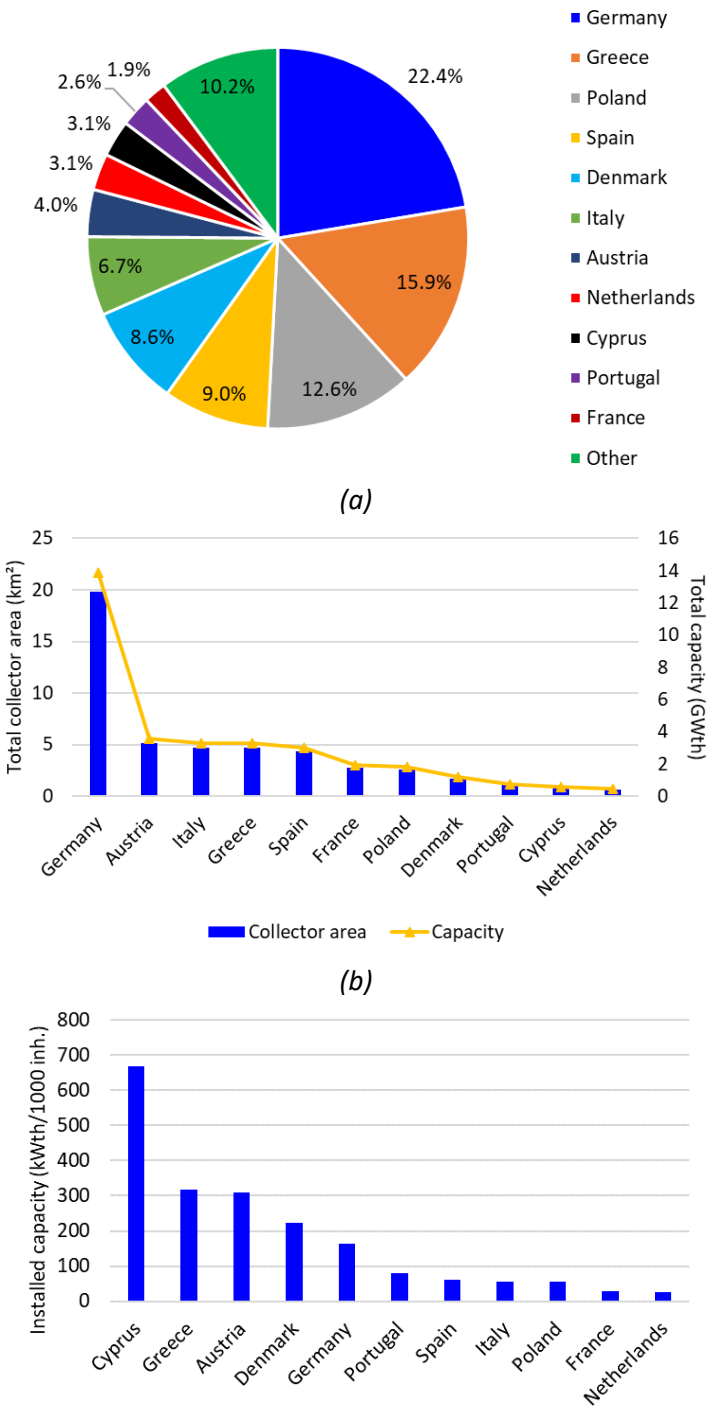

Fig. 1.13. (a) Share of new solar installations in 2018 in Europe, based on data from [12], (b) total installed thermal collectors' area for the same year in the top countries of Europe ,based on data from: [13] and (c) installed solar thermal capacity per 1000 inhabitants

A more detailed view of the solar market status both globally and in Europe can be shown in Fig. 1.14. As shown, both on global basis and in Europe, the majority of the solar thermal applications are occupied by single-family systems used to cover the DHW needs of the house. On global basis, DHW for multi-family and utility buildings is also quite common with a share of 37%, while the corresponding value in Europe was a lot lower with a 12%. On the contrary, in Europe can be found a lot more solar combi systems, which cover parts of both heating and

DHW loads, recording a share of 17% of the total European solar thermal installations. As shown in Fig. 1.14., solar cooling applications are quite limited with approximately 3% in Europe and a 2% worldwide. The aforementioned statistics reveal that, despite its potential, solar cooling market is still limited and requires specific policies and incentives towards its expansion.

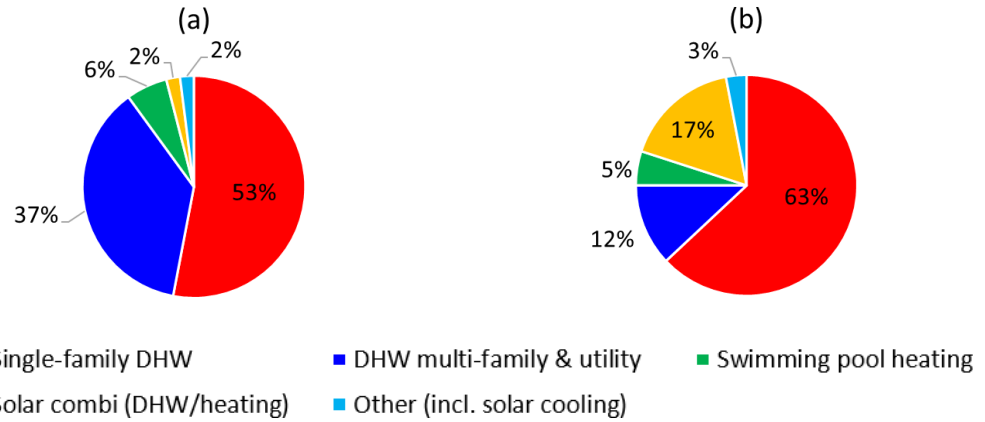

Fig. 1.14. Breakdown of solar thermal systems' applications in 2018 (a) worldwide and (b) in Europe. Based on data from: [13]

By the time of this dissertation, most publicly available statistic reports include data up to mid 2019. Therefore, Fig. 1.15 presents a gross estimation of the capacity additions in solar thermal installations within 2019, for the top 20 countries in the world. As shown, China is by far the largest market in solar thermal applications with more than 350 GWth installed capacity (including the estimated additions of 2019), based on the report of IEA Solar Heating & Cooling Programme [13]. Based on the same findings, Greece was ranked tenth with a similar capacity with Italy, which was ranked eleventh based on this study. One important finding of the aforementioned study was that 60% of the 2019 installations worldwide comprised of solar DHW and solar combi systems. In fact, the small complexity of solar combi systems, the relative low costs of purchase and the extensive operational experience on such systems, make them an attractive solution to reduce the energy consumption in a household as well as in utility buildings. In particular, for households, if one considers the share of energy consumption for space heating needs, the implementation of solar thermal systems seems one of the most promising solution towards a nearly-zero energy building (nZEB).

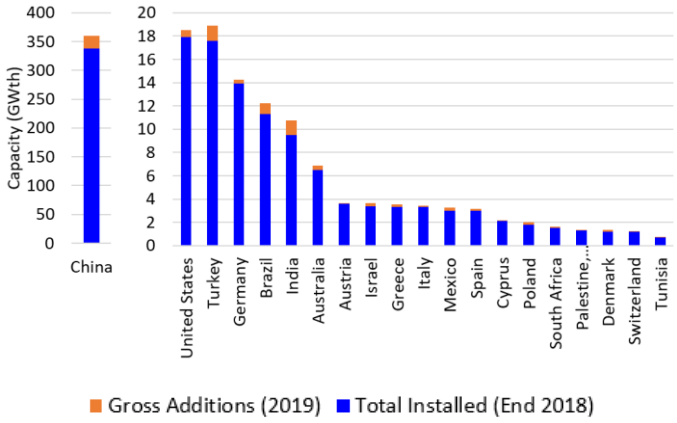

Fig. 1.15. Overview of the top 20 countries worldwide in installed capacity by 2018 and gross additions of 2019. Based on data from: [13]

1.3.1 Solar cooling/heating

According to International Energy Agency (IEA) projections, energy consumption for space cooling is expected to record a sharp rise in the future, reaching a value as high as 6200 TWh by 2050, which corresponds to three times the electricity consumption for space cooling in 2016 (2020 TWh) [14]. Moreover, based on the same study [14], the share of the residential sector in the space cooling energy consumption is expected to range between 45%-65%. An overview of the simulated predictions on the space cooling consumption until 2050 is presented in Fig. 1.16, as derived from the same study [14].

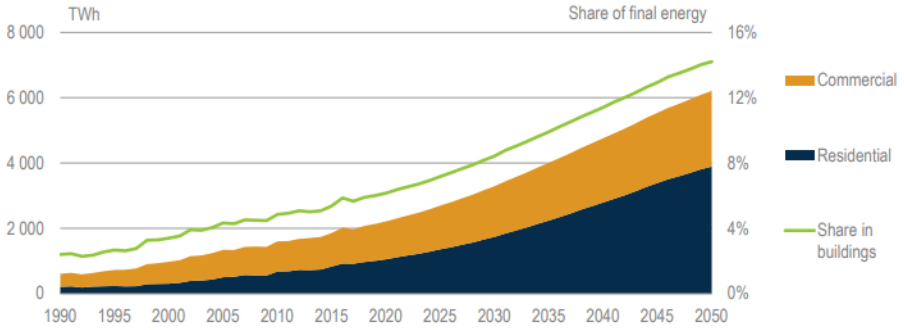

Fig. 1.16. Projects of worldwide space cooling consumption. Source: [14] IEA (2018) The Future of Cooling, https://www.iea.org/reports/the-future-of-cooling. All rights reserved.

Taking into consideration these concerning predictions, it is made clear that cooling and heating installations will have a dominant role in the final energy consumption both in residential sector as well as in industry. Therefore, the development of sustainable solutions to minimize the energy consumption of space cooling and heating is expected to become a scientific field of particular importance in the short future.

Above all considered, solar cooling/heating is a field of growing interest, owing to the maturity of the separate technologies. Coupling solar collectors with heat pumps/chillers has a lot of benefits, including the cover of all thermal and domestic hot water loads by a single system, with significantly reduced environmental impact and minimum dependence on conventional energy sources. Solar thermal collectors can be used to provide the required heat to drive sorption (adsorption/ absorption) reversible heat pumps to cover all the aforementioned loads, achieving solar fractions as high as 70% at reasonable investment payback periods. However, the high capital costs of solar driven sorption heat pumps and the system complexity tackles the expansion of solar cooling/heating market. In this perspective, a key step towards the expansion of the solar cooling market is the increase in policies and incentives both on European and national levels, a topic which will be discussed more in section 1.4.

Based on the above limitations, solar cooling market is rather small, with estimations of approximately 2000 systems by 2019, worldwide [15]. However, as shown in Fig. 1.17, the total number of systems has increased considerably the last years, with a 344% increase using as reference 2009 and a corresponding 66.7% increase between 2014-2019. According to [15], 70% of the aforementioned systems are located in Europe, highlighting the growing interest of European countries in solar cooling.

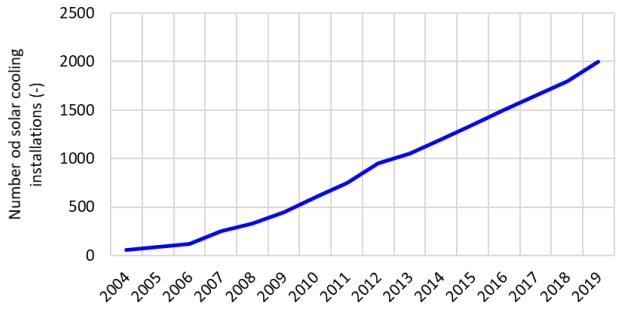

Fig. 1.17. Approximate evolution of the number of solar cooling installations worldwide between 2004-2019, based on data from [15]

1.3.2 Solar thermally driven power production

The extensive use of fossil fuels in the electricity mix of Greece, as discussed in Section 1.1, as well as the significant electricity consumption in different sectors, including households, highlights the necessity for alternative renewable based systems. In particular for low and medium temperature sources (<250 °C), which includes solar thermal systems, Organic Rankine cycle (ORC) is the most promising technology, with several prototype and commercial systems worldwide [16, 17].

The ORC offers a number of advantages which can be summarized in the following points [18]:

- Potential low temperature heat recovery due to the lower boiling point of organic fluids
- Efficient part-load operation
- Simple in terms of control start-up and stop procedures
- Reduction of the need for superheating by using dry organic fluids
- Reduced risk of damaging the expander due to absence of droplet formation
- Operation of expander under less sever conditions and thus longer lifetime
- Smaller gap losses in the turbine/expander as a result of higher mass flows
- Reduced operational and maintenance costs
- Overall components' size reduction and thus reduced capital costs
- Simple construction and operation

ORC applications range from few kW up to several MWs, while research projects focus also on the development of micro ORCs, with capacities of less than 1 kWe [19]. In terms, of the solar driven ORCs, they are mainly focused on larger capacities, which is highly dependable on the type of collectors and the site of installation per case. However, in most commercial applications the nominal power output is larger than 500 kWe and the driving temperatures are exceeding 300 °C. Table 1.1 provides a non-exhaustive review on the currently running solar ORC installations across the world (excluding ORC systems powered by solar power tower systems).

Table 1.1. Non-exhaustive list of commercial solar driven ORC applications [18, 20]

Name (country)	Type of collectors	Solar field area (m^2)	$T_{sol,max}$ (°C)	Heat transfer fluid	Capacity (MW)	Start of operation
Saguaro Power Plant (USA)	PTC	10340	300	Xceltherm-600	1	2006
Lafayette Plant (USA)	PTC	1051	121	Water	0.05	2012
eCare Solar Thermal Project (Morocco)	LFR	10000	280	Water	1	2014

Airlight Energy Ait-Baha (Morocco)	PTC	6159	570	Air	3	2014
Rende-CSP Plant (Italy)	LFR	9780	280	Diathermic Oil	1	2014
Tampa Plant (USA)	PTC	1021	116	Glycol	0.05	2014
IRESEN 1 MW CSP_ORC pilot project (Morocco)	LFR	11400	300	Mineral Oil	1	2014
Archimede (Italy)	PTC	8000	305	Thermal oil	1	2015
Stillwater Geo-Solar Plant (USA)	PTC	24778	n/a	Water	2	2015
Aalborg CSP (Denmark) [21]	PTC	26929	330	n/a	16.6 (thermal)	2016
Ottana solar facility (Italy)	LFR	8592	275	Thermal oil	0.6	2017

LFR: linear Fresnel reflector, PTC: Parabolic trough collector, u/c: under construction

As observed by Table 1.1, the number of operating or/under development solar ORC systems is rather limited. However, the large potential in solar irradiance abundant countries, like the countries of the Mediterranean region, is expected to shift the number of operating systems in the years to come, a fact that can be also affected by the commercialization of several ORC systems. In fact, there is a relatively high variety of alternatives, as shown in Table 1.2, considered the size of the ORC market, despite its constant growth.

Table 1.2. Non-exhaustive list of commercial ORC systems [19, 22, 23]

Manufacturer (Country)	**Driving temperature (°C)**	**Working fluid**	**Capacity (kW)**
Calnetix/Ingeco (USA) [24]	From 82	R245fa	<125
Climeon (Sweden) [25]	80-120	n/a	150
ElectraTherm (USA) [26]	70-150	R245fa	<150
Enerbasque (Spain)	from 85	n/a	5-100
Enertime (France) [27]	90-200	n/a	100-3000
Enogia (France)	70-120	R1233zd	10-180
Entropea Labs (UK) [28]	90-250	n/a	25-100
E-rational (Belgium) [29]	85-175	n/a	55-355
Exergy (Italy) [30]	n/a	n/a	100-25000
General Electric (USA) [31]	155	R245fa	50-140
Kaishan (USA) [32]	>80	n/a	50- 3358
ORCAN (Germany) [33]	>80	n/a	500-2000 (thermal input)
ORMAT (USA)	n/a	n/a	n/a
Rank (Spain) [34]	90-210	n/a	2.5-25
TAS (USA) [35]	90-200	n/a	n/a
Triogen (Netherlands) [36]	>350 (flue gas)	Toluene	50-170
Turboden (Italy) [37]	n/a	n/a	<20000
ZE (UK) [38]	220-280	n/a	95-130
Zuccato Energia (Italy) [39]	>95	n/a	30-50

The wide range of commercial products, shown in Table 1.2, reveal a rather growing market with high flexibility on the heat sources. However, according to a market study conducted by Tartière and Astolfi [19] the largest share of the installed power capacity of ORCs was in geothermal applications, followed by biomass and waste heat recovery applications, as shown in Fig. 1.18. Solar ORCs represented only a very small fraction, revealing the limited field of so-far applications. The expansion of the solar ORCs is mainly limited by the high costs of the system and the solar intermittence, which worsen the economic competitiveness of the solar ORCs. Therefore, the introduction of certain incentives is crucial to enhance the economic performance of solar ORCs towards the expansion of their market and the creation of a economically viable decentralized alternative for sustainable power production. Apart from the dependence of the ORC market in the funding schemes, Fig. 1.19 reveals a strong connection with the crude oil price. Taking into consideration, the depletion in the fossil fuel reserves and its effect on the fuel prices, the ORC market is expected to gain further interest in the future.

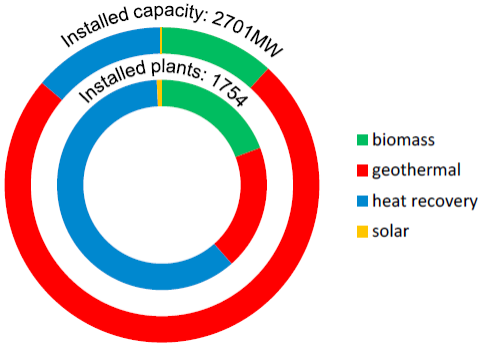

Fig. 1.18. Share of installed ORC capacity by application. Source: Tartière and Astolfi [19]

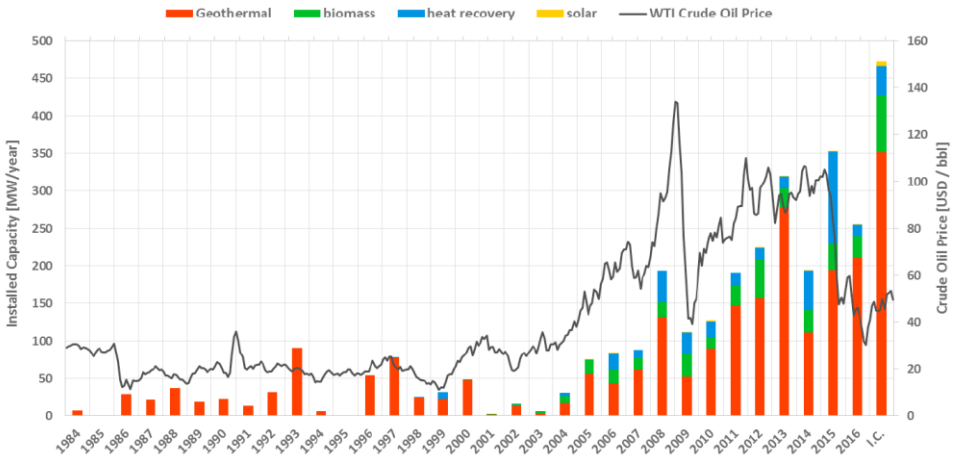

Fig. 1.19. Evolution of the annual installed capacity of ORCs in comparison to the crude oil price Source: Tartière and Astolfi [19]

1.4 Financial instruments

As already discussed, one of the key barriers for the broader expansion of the solar applications market is the initial cost of the respective systems. In particular, solar powered poly-generation systems, which are the main topic of this doctoral study, are limited by their high purchase costs and are therefore outperformed by alternative options. However, the

energy transition already partially adapted with certain measures in Europe, as discussed in a previous section, highlights the necessity for a number of financial instruments to expand the market. Each country has a dedicated number of policies, targeting at investments in R&D, subsidies in the purchase and the manufacturing of such systems, tax credits and feed-in-tariffs [40]. In fact, a study conducted in Australia by Simpson and Clifton [41] revealed the 70% of the survey participants prioritized financial incentives for decision making of adapting solar energy.

Although, solar thermal collectors' market is quite large over the last decade, with countries such as Greece, Cyprus and Italy being in top 20 countries in terms of installed capacity, as shown in section 1.3, most new installations are focused in DHW and solar combi (DHW and heating) systems. Both solar cooling/heating and small-scale solar ORC are rather niche markets. This is mainly owed to the high initial investment costs which harm the economic competitiveness of such systems. Given also the projections for significant increase in the cooling needs (Fig. 1.16) as well as the necessity for the introduction of environmentally friendlier power generation technologies, it is crucial to introduce certain measures and policies in order to promote the expansion of these markets. Over the last years, many countries have adopted a more intensive strategy with respect to the promotion of RES, in particular within Europe with respect also to the agreed targets of the EU for 2030 and 2050, as discussed in section 1.1. In the following section is provided a non-exhaustive review of the key available financial incentives in two countries of interest, namely Greece and Italy.

1.4.1 Financial and other indirect incentives in Greece

Over the last years, Greece has adopted a number of regulations and introduced several financial and indirect incentives towards the increase in the penetration of RES systems both in medium and large scale as well in small/residential scale. Below are listed the key measures that are in effect at the time of this dissertation in Greece in line with the Renewable Energy Directive 2018/2001 [2], the Energy Efficiency Directive 2018/2002 [3] and the revised National Energy and Climate Plan (NECP) [4]:

- Development law 4399/2016 [42]: Support provided to large, medium, small and very small enterprises. This law provides options to partially fund investments in equipment or provide equal amount of tax avoidance over the net profits over a 15-year period. The rates can be as high as 55% of the total investment cost, based on the geographical location of the investment plan.
- "Quality modernization" [43]: An act co-funded by Greek and European funds aiming to enhance the competitiveness of medium-sized enterprises. Similarly to the development law 4399/2016, this act includes investments in electricity, heating and cooling equipment with a rate of up to 50% and up to a total investment cost of 400 k€.
- Competitiveness Toolkit for Small and Very Small Businesses [44]: Act aiming to strengthen the small and micro businesses, including investments in equipment. This act covers investments in the range of 30-120 k€ and subsidizes up to 75% of the total investment. Although, the period for enrollment at this act closed at January 2021, as the procedures are still ongoing, it was listed in this section.
- Energy saving-autonomize [45]: European and Greek co-funded act for energy related refurbishment of multi- and single-family residential buildings. This act is ideal for the installation of solar driven systems, as the financing rates are increasing with the

improvement of the building's energy class, reaching rates up to 85% of the total investment cost.

- Law 4646/2019 [46]: This law applies a tax regulation over a four-year period to the natural persons that invested in the energy upgrading of a building. The amount of the tax reduction is equal to 40% of the total expenses for the services of the energy upgrading up to a maximum discount of 6.4 k€.
- Law 1045/2020 of reference prices on the compensation of small RES systems [47]: Fixed tariff for a number of RES options to be connected to the grid from 1st May 2021 and onwards. Data on the solar driven systems that are included in the fixed tariff law based on their type and capacity is listed in Table 1.3.

Table 1.3. List of reference prices for different solar driven power systems based on law 1045/2020 [47]

System	Reference value (€/MWh)
Photovoltaic systems connected to residential users (<6 kW)	87
Photovoltaic systems <500 kW	63
Photovoltaic systems, as part of an energy community<1 MW	65
Photovoltaic systems, belonging to farmers <500 kW	65
Solar thermal power plants without storage	248
Solar thermal power plants with at least 2h storage	268

- Law 759/2019 [48]: Policy to allow individual users and energy communities to apply net metering and virtual net metering policies, on the power produced by photovoltaic systems. The net metering and virtual net metering are applied on the competitive part of the charges. For instance, for a conventional residential user the competitive part of the charges corresponds on average to 110.6 €/MWh out of a 177.2 €/MWh (for the case of "Γ1" residential tariff and less than 2 MWh consumption [49]).
- (Indirect) Law 4759/2020 [50]: Policies and measures to increase the NZEB's proportion. If a building during its energy design is classified in the best category of A+, the building ratio is increased by 5%. For residential buildings that have annual energy consumption of less than 16% of the reference building of the Energy Performance of Buildings Regulation (EPBR-KENAK 2017 [51]).
- (Indirect) EPBR-KENAK 2017 [51] & Law 4122/2013 [52]: In all new and renovated buildings, it is obligatory to cover 60% of the DHW demands using solar thermal or other types of RES. If the coverage of the DHW demands at the specified rate is impossible by the energy efficiency study of the building, 15% of the reference building DHW energy savings by the use of solar thermal collectors should be counter-balanced in the investigated building via equal energy savings by solar thermal or other RES systems in another type of energy use (e.g., space heating/cooling).

From the aforementioned list of financial tools and RES promoting policies, it is clear that there is an adequate number of tools for the increased penetration of RES in a wide range of capacities. However, in terms of solar thermal systems in specific, the largest concern lies in the fact that all relevant measures allow also the use of PV systems which, thanks to their

commercial maturity and the large market, are currently a lot more competent. Of key importance towards the inversion of the situation are the new reference prices introduced by law 1045/2020. As stated in Table 1.3, the tariffs for PV systems are three times lower than the respective for solar thermal power plants and approximately half the tariff of the net metering policy (in which any excess of produced energy is not returning any profits). Hence, these tools can be used as a starting point towards the competitiveness improvement of the solar thermal systems compared to PVs and the expansion of their market. Although, the aforementioned measures directly affect the solar thermal power production systems, the consequent expansion of the solar thermal market is expected to also influence the solar cooling/heating as the solar thermal subsystem covers a significant share of the total investment costs.

1.4.2 Financial and other indirect incentives in Italy

The selection of Italy as a second case study in the financial and other indirect incentives section was dictated by the expansion of the solar market in this country in comparable levels with Greece and the high solar availability as already discussed in previous sections. Italy has a strong deviation from Greece in the dependence on the natural gas and the increased penetration of RES. Moreover, the conventional energy prices are higher in Italy compared to Greece, with the cost of electricity for residential users to be 31.2% more expensive in Italy and the cost of natural gas to be 73.5% higher, according to data from Eurostat [9, 53]. As a result the total costs for the annual energy consumption from conventional systems are considerably higher, turning economic viability of a potential replacement with RES systems quite attractive. In this direction and in accordance to the EU directives, Italy has adopted a number of policies and incentives towards the faster transition to environmentally friendlier technologies. Hereby are listed a number of key corresponding measures/incentives issued by the Italian government:

- Conto Termico 2.0 [54]: Program providing support to energy efficiency upgrade and thermal energy production from RES. Target audience includes both private owners and public administrations. Two types of project categories can be eligible for funding: (i) upgrading of building envelopes and replacement of existing systems for space heating and DHW with condensing boiler and (ii) small-scale projects related to thermal energy production from RES, among which solar cooling installations, biomass boilers and heat pumps. Between 40% and 65% of the total expenditure is returned to the beneficiaries within two months from the signing of the agreement, with a maximum limit of 5 k€ in a single installment for private owners.
- EcoBonus [55]: Scheme to provide support via tax reduction for energy efficiency measures in existing building stock in residential, healthcare, commercial and other types of buildings. Tax deduction rates are up to 65% with a maximum deduction of 60 k€ per building, distributed in ten annual payments of equal amount.
- Superbonus 110 % [55]: Another tax relief scheme, introduced by the Relaunch Decree DL 34/2020 which integrates the existing tax benefits, increasing the deduction rate up to 110%. Solar thermal and PVs, up to 48 k€, are eligible to the incentive if made together with one of the three following driving interventions: (i) thermal insulation, (ii) replacement of air conditioning systems and/or (iii) interventions for anti-seismic safety.

- Bonus Ristrutturazione [55]: This restructuring bonus provides support for restoration, conservative rehabilitation and renovation of residential buildings in the form of tax deduction. The scheme is eligible for investments in heating and cooling equipment and involves tax deduction of 50% up to a maximum of 96 k€ in renovation costs per building, with the option of tax credit transfer. The aforementioned deduction is applied over a period of 10 years, divided into 10 equal instalments.
- FER1 Decree [56]: This scheme enacted in 2019 provides RES systems with a nominal capacity exceeding 20 KW are admitted to the new incentive mechanism. Priority is given to integrated photovoltaic systems built on schools, hospitals and other public buildings or on rural building with the removal of asbestos; those plants will be entitled to an additional premium of 12 €/MWh. For the rest projects there is a different reference price based on the capacity of the plant. In Table 1.4 are listed the different reference prices set by FER1 Decree. Within this scheme, there is no defined price for solar thermal power systems, which, unlike the case of Greece, creates important obstacles in the development of the solar thermal power production market.

Table 1.4. List of reference prices for different solar PV systems based on FER1 Decree

System	Reference value (€/MWh)
Photovoltaic systems (20 kW < P < 100 kW)	105
Photovoltaic systems (100 kW < P < 1000 kW)	90
Photovoltaic systems >1000 kW	70

It is worth mentioning that the decree has also a certain clause for a potential increase in the market price beyond the applicable tariff for each renewable technology. In that case, the selected installations not only would no longer receive a premium but they would instead have to give back to the Italian authorities the additional revenue.

- Scambio sul Posto (net-metering scheme) [57]: is a form of auto-consumption that allows producers to offset the generated electricity which is supplied to the network at a certain moment with the energy taken from the grid. Therefore, the electricity system is used as a tool for the virtual storage of electricity produced but not self-consumed in the moment in which it is produced. The “scambio sul posto” can be combined with tax deductions. Furthermore, in case the electricity, fed in the grid, is on surplus in the metering balance, plant operators are entitled to have an economic compensation, based on prices, defined by the energy source.
- (indirect) Legislative Decree DL 28/11 [58]: similarly to the Greek legislation, this law sets a minium share of RES systems in new and renovated buildings. More specifically, all new buildings and buildings being renovated must cover 50% of the DHW demands from RES systems. At the same time, all aforementioned buildings have to meet certain shares of the sum of DHW, space heating and space cooling loads from RES systems. The shares depended on the period of interest as shown below:
    - 20% share, since the law came into force until 31/12 2013
    - 35% share, between 01/01/2014 and 31/12/2017
    - 50% share, after 01/01/2018

- (indirect) Growth Decree-Law 34/19 [59]: this law granted funding to municipalities to be invested in public works relevant (among others) to increasing energy efficiency in public buildings and the development of decentralized RES powered energy production plants.

As already discussed, the schemes related to power generation do not consider the option of solar thermal systems, which makes them a less attractive alternative in Italy. On the contrary, as can be observed there is a number of dedicated measures for thermal systems, in which solar thermal systems (e.g., solar cooling/heating) can have a dominant role. This can be partially validated by the share of solar thermal systems granted either tax deduction, Fig. 1.20(a), or received funding within the Conto Termico scheme, Fig. 1.20(b), based on data from the Integrated National Energy and climate plan of Italy [60]. In fact, solar thermal systems account for more than 68 M€ of annual investment within the tax deduction schemes and more than 70 M€ within the Conto Termico program, which corresponded to a 27.9% and 28.0% of the total annual investment per scheme. Above all considered, it is worth investigating the prospect of solar thermal installations in household sector in Italy in order to assess the steps needed for the further enlargement of the solar thermal market in the country.

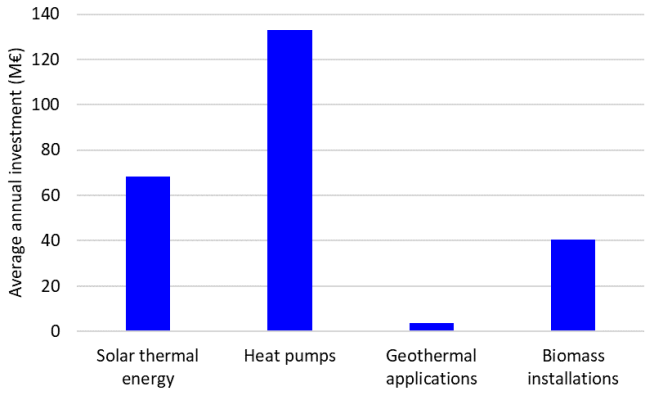

(a)

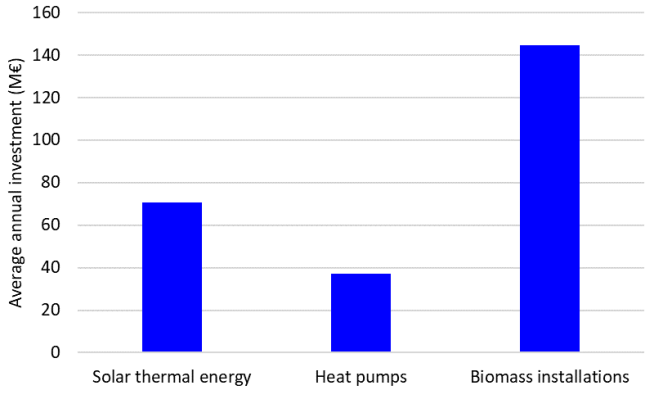

(b)

Fig. 1.20. (a) Share per type of system acquired in the tax deduction schemes in Italy and (b) share per type of system acquired in Conto Termico. Data acquired from: [60]

1.5 Scope of dissertation

As shown both by the financial and other indirect incentives (Section 1.4), the current status of energy use in households (Section 1.2.1) and the respective targets set by EU and NECP (Section 1.1), it is clear that there is a great potential for the RES driven polygeneration systems in residential (small) scale. Fig. 1.21 presents a number of alternative combinations for power and/or heating/cooling production either by RES or other types of energy sources (e.g., waste heat). However, as mentioned already, this dissertation focuses in the solar thermal energy. Energy storage, mainly in the form of heat storage, is an indispensable addition in solar thermal energy systems, not only to store excess of energy and prolong the exploitation of solar harvested energy in periods of the day with inadequacy of solar irradiance, but also to insert a thermal inertia in the system and allow downdraft thermally driven sub-systems operate at more stable conditions.

The analysis is mainly focusing on commercial collectors for small scale applications, which are in most cases non-concentrating collectors, resulting in working temperatures not exceeding 150-200 ^{o}C [61]. The main candidates to exploit such heat sources for power production are the Kalina cycle and the ORC. As Kalina cycle is an alternative which is not commercially mature, the dissertation is focusing on ORC, while comparing with conventional power production systems. With respect to cooling/heating systems, the two main alternatives to conventional systems are the reversible heat pumps based on the vapor compression cycle (VCC) and the sorption reversible heat pumps (absorption/adsorption). As also implied in Fig. 1.21, the aforementioned systems will be examined within the dissertation in separate cases (sole power production via a solar ORC, solar cooling/heating) as well as in a hybrid polygeneration system. As solar energy is the selected prime mover, in the relevant studies, PV systems will also be assessed, as a second reference case, however without particular focus on their optimization nor in their detailed modeling, due the abundance of relevant data in literature.

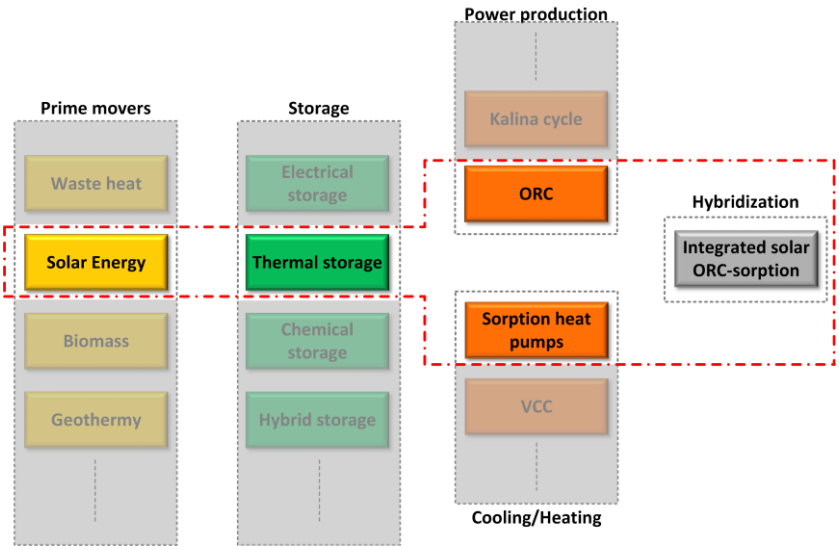

Fig. 1.21. Non exhaustive overview of available technologies for a small-scale power and/or heating/cooling system

As base and starting point of this study is the detailed modelling and the experimental validation, whenever possible, of the considered component/subsystem. The developed models are quasi-steady state, as the main scope of the analysis is the assessment of the

techno-economic competitiveness of the investigated system. Once the performance models are finalized, the scenarios to be assessed are presented and the optimization problem is defined, identifying the optimization variables and the objective functions. Two separate studies are analyzed for the small scale solar thermal power production with an ORC and the potential of the solar cooling/heating systems based on the status quo of the respective market. In the third level of the study, there is the analysis for the system integration of the solar ORC and the solar cooling/heating system into a hybrid polygeneration system. The study on the hybrid system focuses on the optimal allocation of the ORC and the sorption cycle with respect to the solar prime mover, in order to enhance the total system's efficiency. At the last stage of the study, the environmental footprint of the aforementioned systems is quantified over their entire life cycle via separate life cycle analyses (LCA). An overview of the different stages of the dissertation, as discussed above, is presented visually in Fig. 1.22.

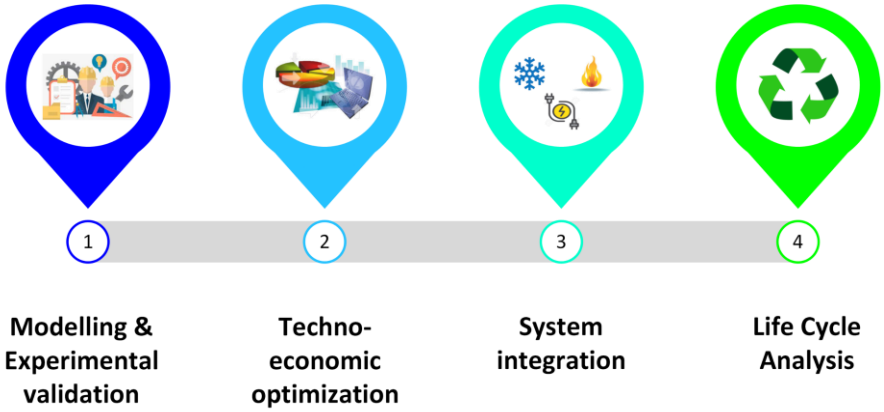

Fig. 1.22. Stages of the dissertation

Chapter 2. Modelling, experimental validation and components experimental characterization

The second chapter of the dissertation is dedicated to the formulation of the theoretical models for the sizing and the simulation of the on- and off-design performance of the separate components comprising the solar driven cooling/heating, solar ORC and eventually the polygeneration systems, which are evaluated and optimized in the next sections of the study. Following, a sequential order from the prime mover towards the end use (similarly to Fig. 1.21), this Chapter will present the proposed models for the simulation of different solar collectors, sensible heat storage, heat exchangers, expander, pumps and other secondary ORC components along with both electric and ab/adsorption heat pumps and whenever this was made possible from respective test rigs, assess the accuracy of the used models prior to the start of the optimization procedures for each component. Parts of the following modelling procedure, as will be also clearly cited in-text, are published in the journal articles "Exergetic and economic analysis of a solar driven small scale ORC" [62], "Life cycle analysis of ZEOSOL solar cooling and heating system" [63] and "Techno-Economic Optimization of Medium Temperature Solar-Driven Subcritical Organic Rankine Cycle" [64].

2.1 Solar thermal collectors

Solar thermal collectors are practically the key component in every solar thermally driven system, as they are responsible for harvesting the solar energy and drive the downdraft systems. Solar thermal collectors are mainly distinguished in non-concentrating and concentrating collectors. Non-concentrating collectors have a single surface for direct absorption of the solar irradiance, while concentrating collectors have reflector which focus solar irradiance to a receiver area [65]. *Fig.* 2.1 presents an overview of the main types of developed solar thermal collectors.

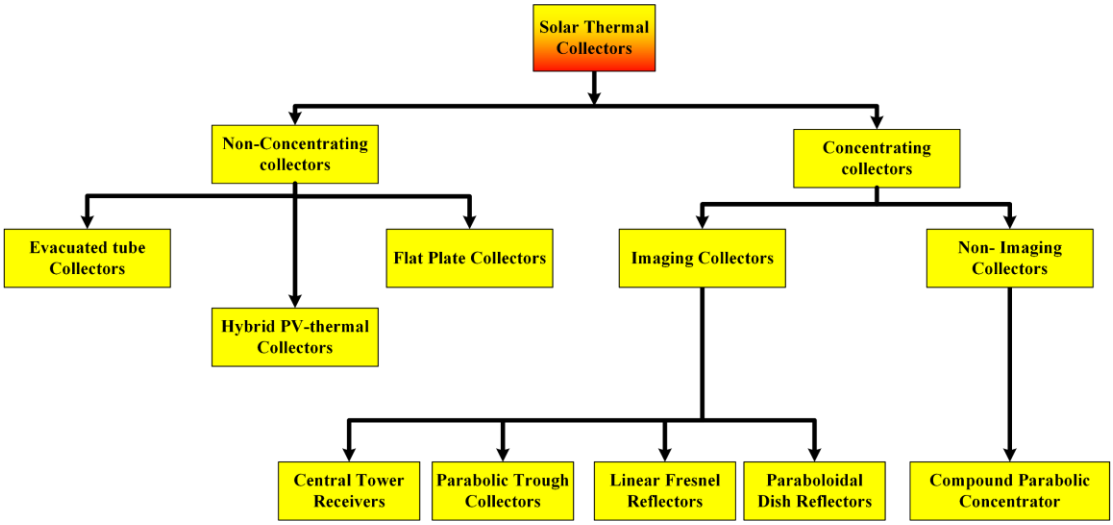

Fig. 2.1. Diagram of main solar thermal collector types [66]

2.1.1 Solar collectors modelling

For the modelling of the solar collectors, a model was used based on an empirical polynomial which estimates the solar collectors' efficiency [67]. This polynomial is widely used in solar

collectors' modelling approaches, as solar collectors' certification solar Keymark [68] provides experimental estimations on the polynomial's constants with accurate lab testing procedures.

$$\eta_{col} = c_0 - c_1\left(\frac{\bar{T}_{col} - T_{amb}}{I_{sol}}\right) - c_2\, I_{sol}\left(\frac{\bar{T}_{col} - T_{amb}}{I_{sol}}\right)^2 \quad (2.1)$$

In equation (2.1), the term $\bar{T}_{col}$ stands for the average fluid temperature in the collector, T_{amb} is the ambient temperature, c_0, c_1 and c_2 are empirical coefficients, and, finally, I_{sol} refers to global irradiance for the case of non-concentrating collectors, namely flat plate collectors (FPCs) and evacuated tube collectors (ETCs). On the other hand, I_{sol} refers to direct irradiance for concentrating collectors, which include parabolic trough collectors (PTCs) and parabolic dish collectors (PDCs). In Table 2.1 are presented the coefficients of different types of collectors, which will be used in the simulation studies in the next Chapters.

Table 2.1. Eq. (2.1) coefficients for the different types of solar collectors [62-64].

Type of collectors	FPC [69]	ETC [70]	PTC-1 [67]	PTC-2 [71]	PDC [72]
c_0	0.868	0.774	0.76	0.673	0.7053
c_1	3.188	1.936	0.22	0.2243	1.2503
c_2	0.018	0.006	-	-	-

As already discussed, equation (2.1) requires as input the ambient conditions, by means of the temperature and the solar irradiance, as well as the average fluid temperature in the collector, which in return is a function of the collectors' efficiency, therefore an iterative loop has to be realized to estimate both the collector's efficiency and the average fluid temperature. The collectors' efficiency is defined as the ratio of the absorbed heat divided by the total solar irradiance on the tilted surface of the collector:

$$\eta_{col} = \frac{\dot{Q}_{col}}{A_{col} \cdot I_{sol}} \Rightarrow \dot{Q}_{col} = \eta_{col} \cdot A_{col} \cdot I_{sol} \quad (2.2)$$

With A_{col} to be the aperture area of the collector. Eventually, applying an energy balance in the collector, the outlet, and thus the average fluid temperature can be estimated:

$$h_{col,o} = h_{col,i} + \frac{\dot{Q}_{col}}{\dot{m}_{col}} \quad (2.3)$$

$$T_{col,o} = \mathrm{f}(h_{col,o}, p_{col}) \quad (2.4)$$

$$\bar{T}_{col} = \frac{T_{col,o} + T_{col,\mathrm{i}}}{2} \quad (2.5)$$

The iteration stop criterion was defined the minimization of the average temperature's relative error, below a 0.025%, which corresponded to an absolute error of 0.1 K.

2.1.2 Solar collectors test rig

The set of equations, listed above, is a well-approved approach for the design/sizing procedure of a solar driven system, however, it is worthy assessing the accuracy of the same

model for implementation in a more generalized quasi steady state model. Towards this direction, experimental tests were conducted in an experimental solar field, installed and operating in the National Technical University of Athens.

The 40 m^2 evacuated tube collectors' solar field was installed at the Laboratory of Steam Boilers and Thermal Plants of the National Technical University of Athens, Greece, in spring 2019 as a part of the Zeosol EU Horizon 2020 funded project, aiming to drive a hybrid sorption chiller. In the experiments discussed in this section, the solar field was isolated and therefore, more details on the other components of the test rig will be provided in a dedicated section with the solar adsorption experiments. A schematic of the solar subcircuit along with an image of the installed solar field is presented in Fig. 2.2. The working fluid of the setup was a mixture of propylene glycol, which after being heated in the solar collectors, was directed to a 1 m^3 storage tank, charging via helical coils the desalinated water of the storage tank. As shown in Fig. 2.2 (a), a number of measuring devices was installed in the system to allow for proper monitoring and evaluating of the solar collectors' performance.

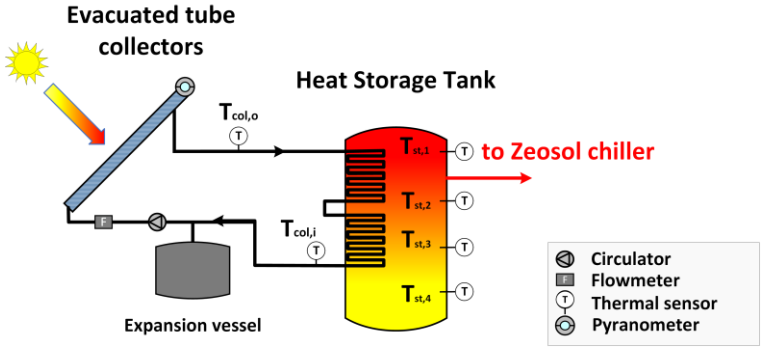

(a)

(b)

Fig. 2.2. (a) Schematic and (b) images of the developed test rig at the Laboratory of Steam Boilers and Thermal Plants, National Technical University of Athens

For the realization of the experimental procedure, a number of measuring instruments were installed, as shown in Fig. 2.2 (a). The key technical specifications of the involved equipment are listed below, as it is crucial for the error analysis in the calculations.

I. Pyranometer

The pyranometer LSI DPA863 is installed at the roof of the NTUA building in order to allow for more accurate measurements on the ambient conditions of the measurements.

Table 2.2. Technical specifications of the pyranometer used in the solar collectors' test rig

Model	**LSI DPA863**
Measurement range	0-1500 W/m²
ISO 9060 Class	Second Class
Ambient temperature (min/max)	-40/80 °C
Temperature response	<7% (-10/40 °C) / +0.14%/°C (>40 °C)
Output	4-20 mA
Power supply	10-30 Vdc

II. Air temperature sensor

The weather station is also equipped with an air temperature sensor, Pt100, to accurately measure the ambient conditions at the time of the experiments and in particular the performance of the dry cooler which is highly dependent on the ambient temperature.

Table 2.3. Technical specifications of the air temperature sensors used in the solar collectors' test rig

Model	**LSI DMA033**
Type	Pt100
DIN EN 60751 Class	AA
Output	4-20 mA
Ambient temperature (min/max)	-50 / 70 °C
Accuracy	0.1 °C
Resolution	0.01 °C

III. Flow meter

As shown in Fig. 2.2 (a), two main sub-circuits can be identified in the test rig. In order to construct the energy balances and estimate the performance of the subsystems, flow meters are required to provide measurements for the flow rate per circuit.

Table 2.4. Technical specifications of the flow meters used in the installation

Model	**TA FTS5-85DL**
Maximum flow rate	85 l/min
Pressure drop at maximum flow rate (FS)	20 kPa at max flowrate
Output	0.5-10 V
Maximum pressure range	18 bar (at 40 ^{o}C)
Medium temperature (min/max)	-40 / 125 °C
Measuring accuracy flow	±2% of FS
Min. flow measurement	1% of FS
Ambient temperature	0-50 °C

IV. Resistance thermometers Pt1000

Temperature along with the mass flow rate are the most important measurements to be taken for an accurate evaluation of the system's performance. For this reason, Pt1000 sensors have been installed in several locations within the system, allowing for a complete monitoring of the system's operation and at the same time ensuring an accurate estimation of the system's performance.

Table 2.5. Technical specifications of the Pt1000 temperature sensors used in the installation

Model	**TA 01/KEKTY**
Measuring insert	Stainless steel 14751 ø6mm
DIN EN 60751 Class	A
Output	4-20 mA
Medium temperature (min/max)	0 / 160 °C
Accuracy	0.1 °C

V. Pressure sensors

Pressure sensors and pressure gauges are crucial for the monitoring system, especially to identify potential leakage and system over-pressure errors due to faulty operation of some electrical vanes. Furthermore, for the accurate calculation of the streams' energy content, data for the pressure is required along with the temperature. As the two collectors' subcircuits are mixed on a common head, a single pressure sensor is sufficient to estimate the overall system's pressure.

Table 2.6. Technical specifications of the pressure sensors used in the installation

Model	**TA 01/PRS0-6DL**
Measuring range	0-6 bar
Output	4-20 mA
Overpressure range	12 bar
Accuracy pressure	±0.5% @ 25°C
Total errors	±2.0% @-40°C / ±2.0% @ 105°C:
Medium temperature (min/max)	-2 / 90 °C

2.1.3 Experimental validation

Taking into account the accuracy of the involved measuring equipment, discussed above, it is crucial to estimate the error propagation, towards a more objective presentation of the evaluated model's accuracy with respect to the experimental results. In this perspective, the used equations for the estimation of the error propagation are listed below:

$$d\mathrm{h} = \sqrt{dT^2 \cdot \left.\frac{\partial^2 h}{\partial T^2}\right|_p + dp^2 \cdot \left.\frac{\partial^2 h}{\partial P^2}\right|_T} \quad (2.6)$$

$$d(\Delta\mathrm{h}) = \sqrt{dh_{col,i}^2 + dh_{col,o}^2} \quad (2.7)$$

$$d\rho = \sqrt{dT^2 \cdot \left.\frac{\partial^2 \rho}{\partial T^2}\right|_p + dp^2 \cdot \left.\frac{\partial^2 \rho}{\partial P^2}\right|_T} \quad (2.8)$$

$$d\dot{m}_{\mathrm{col}} = \sqrt{d\dot{V}_{col}^2 \cdot \left.\frac{\partial^2 \dot{m}_{\mathrm{col}}}{\partial(\rho)^2}\right|_{\dot{V}_{col}} + d(\rho)^2 \cdot \left.\frac{\partial^2 \dot{m}_{\mathrm{col}}}{\partial(\dot{V}_{col})^2}\right|_{\rho}} \quad (2.9)$$

$$d\dot{\mathrm{Q}}_{\mathrm{col}} = \sqrt{d\dot{m}_{col}^2 \cdot \left.\frac{\partial^2 \dot{\mathrm{Q}}_{\mathrm{col}}}{\partial(\Delta h)^2}\right|_{\dot{m}_{col}} + d(\Delta h)^2 \cdot \left.\frac{\partial^2 \dot{\mathrm{Q}}_{\mathrm{col}}}{\partial(\dot{m}_{col})^2}\right|_{\Delta h}} \quad (2.10)$$

$$\mathrm{d}\eta_{col} = \sqrt{d\dot{\mathrm{Q}}_{\mathrm{col}}^2 \cdot \left.\frac{\partial^2 \eta}{\partial(I_{sol})^2}\right|_{\dot{\mathrm{Q}}_{\mathrm{col}}} + dI_{sol}^2 \cdot \left.\frac{\partial^2 \eta}{\partial(\dot{\mathrm{Q}}_{\mathrm{col}})^2}\right|_{I_{sol}}} \quad (2.11)$$

For the needs of the model evaluation on quasi-steady state conditions, two daily tests are presented below. The first set of experiments was conducted in 03 December 2020 under winter conditions, to test the collector's model under more rapidly varying conditions with lower values of ambient temperature and solar irradiance, as shown in Fig. 2.3.

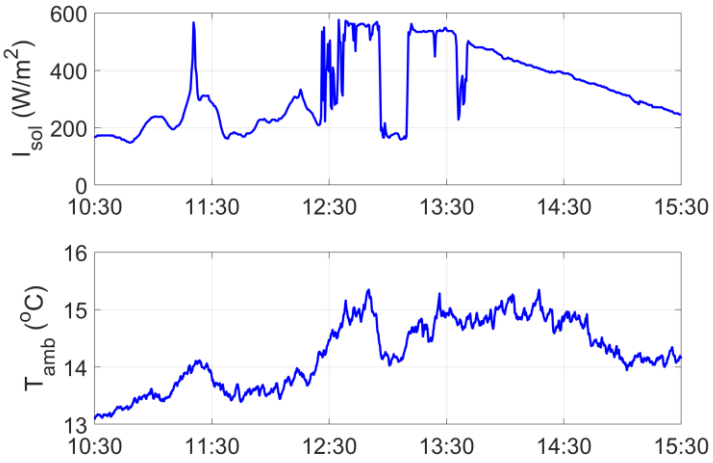

Fig. 2.3. Ambient conditions measured during the tests of 03 December 2020

The analysis of the experimental data, summarized in the plots of Fig. 2.4, reveals an adequate accuracy between the simulated results and the experimental ones. At this point, it is crucial to mention that the sampling rate by the data acquisition system is set to be 30 seconds by default. In order to further minimize fluctuations, the comparison between simulations and experiments was conducted in the basis of ten-minute steps, applying an averaging in the experimental data within every respective timestep. In fact, given that the meteorological data on most databases is on hourly steps, at best, the ten-minute step evaluation is selected to show that such an approach is accurate also in faster time steps, than the ones that will be evaluated in the following Chapters of the study.

By using as input in the simulation model the ambient conditions measured during the day of the experiments, the resulting temperature profile at the outlet of the collector has a very good accuracy with respect to the measured temperatures values, considering the 0.1 K accuracy of the used Pt resistances, as shown in Fig. 2.4 (a). A similar behavior is observed in Fig. 2.4 (b), with the collector's efficiency. The combination of the errors in the enthalpy calculations, eq. (2.6), and the uncertainty of the pyranometer, result in higher uncertainties in the measured solar collector's efficiency. However, on most cases the estimated by the simulation's values are within the error range. In order, to assess the effect of the deviations in the solar collector's efficiency between experiments and simulations in the solar collectors' performance, it is worthy analyzing the respective deviations in the instantaneous (within the considered time interval) harvested energy and the accumulative harvested energy from the start of the day's experiments, as shown in Fig. 2.4(c) and Fig. 2.4(d), respectively. In a similar manner to the collector's efficiency, there can be observed deviations in the harvested energy, with cases of under- and over-predictions by the simulations' model. However, as indicated by Fig. 2.4(d), the accumulative harvested energy error is constantly decreasing leading to a final relative error of -2.29% at the end of the day's experiments, which corresponds to an absolute error of 402 W, which for the case

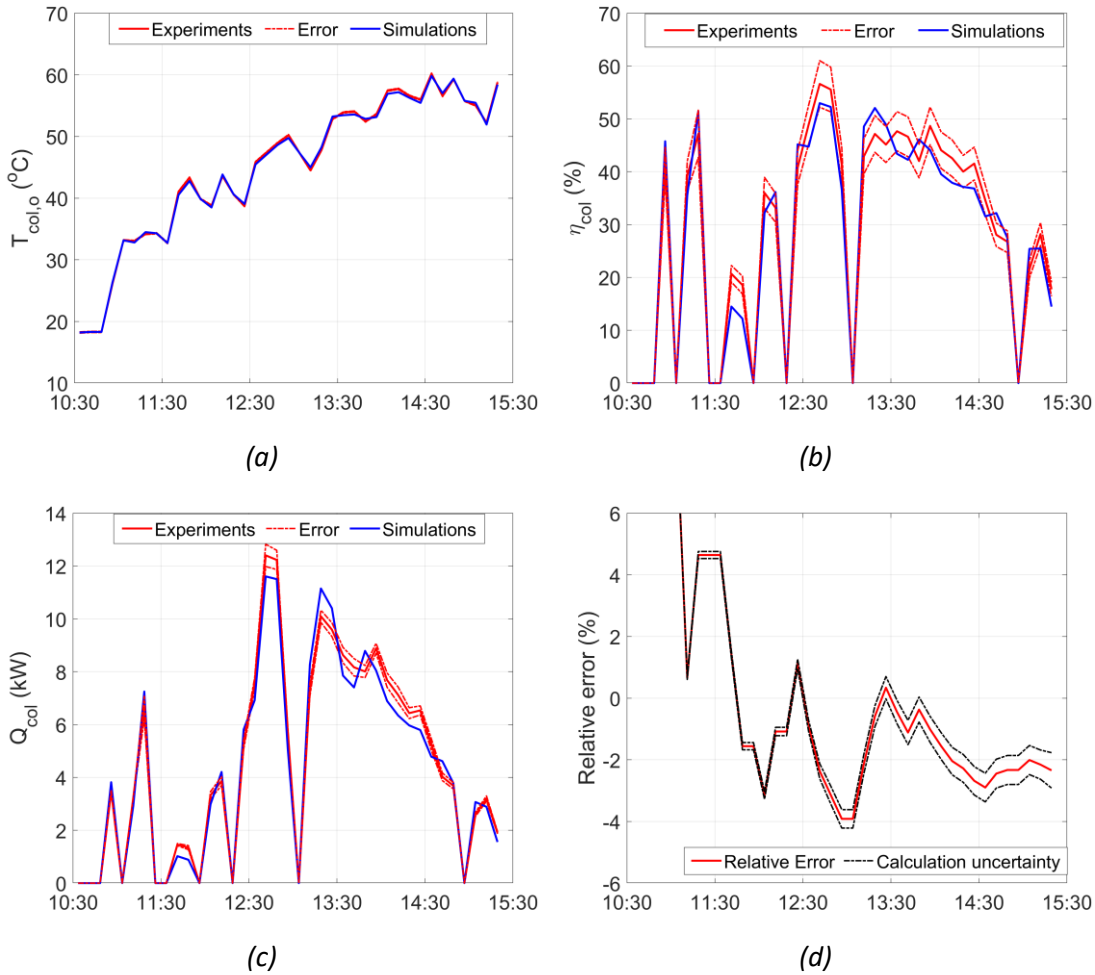

Fig. 2.4. Comparison of experimental and simulation results of the tests of 03 December 2020 (a) with respect to the outlet temperature of the collectors, (b) the instantaneous collector's efficiency, (c) the harvested energy and (d) the error in the accumulative solar harvested energy

As mentioned, a second set of experiments was conducted in 25th May 2021 in order to assess the accuracy of the model also in full load conditions. In fact, as shown in Fig. 2.5, the tested day was characterized by both high temperatures of up to 33 °C and high solar irradiance values up to 1050 W/m^2. The higher values of solar irradiance tend to result in small over-predictions of the collectors' performance, ending in a relative error of 1.9% on the total harvested energy over the entire tested day, according to Fig. 2.6 (d). This effect leads to the conclusion that possibly the coefficients, provided in Table 2.1 for the ETC and correspond to the tested collectors, need a fine-tuning to take into account the recorded further losses in performance. Moreover, as can be observed Fig. 2.6 (b)-(c), simulations tend to predict a smoother operation, which is less sensitive to the variations of the ambient conditions, pointing out that a dedicated tuning would be required in the coefficients of the first and second order terms of eq. (2.1) in order to further minimize the total error in the collector's performance. However, as a daily error in terms of the total harvested energy is of less than 2.5%, it is considered as sufficient for the needs of on-/off-design simulations, which will be presented in the next Chapter.

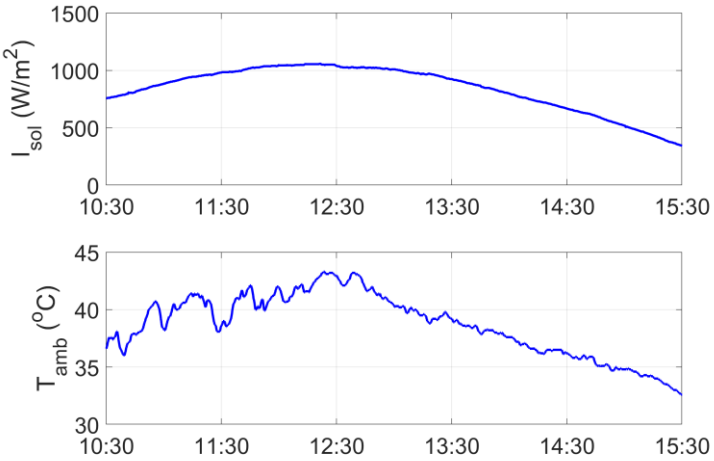

Fig. 2.5. Ambient conditions measured during the tests of 25 May 2021

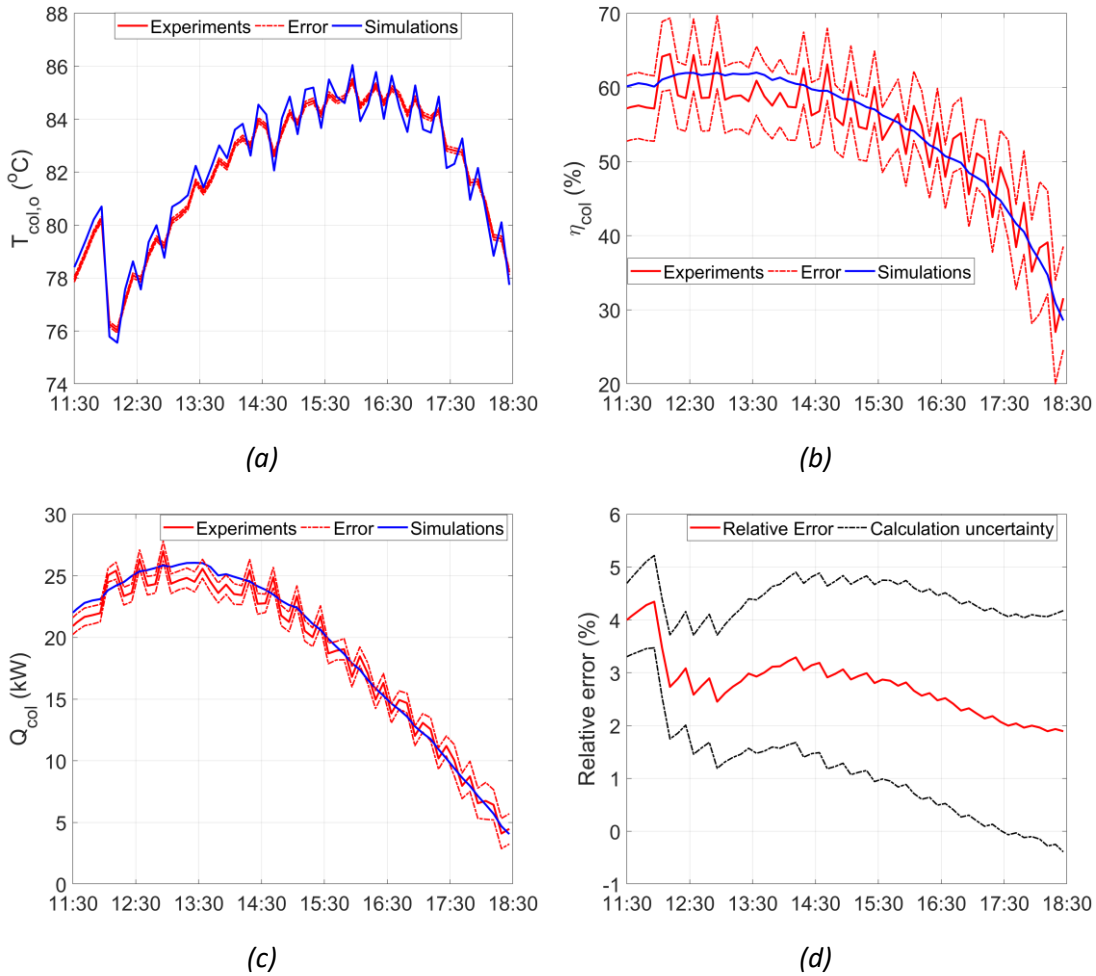

Fig. 2.6. Comparison of experimental and simulation results of the tests of 25 May 2021 (a) with respect to the outlet temperature of the collectors, (b) the instantaneous collector's efficiency, (c) the harvested energy and (d) the error in the accumulative solar harvested energy

2.1.4 Experiments on novel direct flow evacuated tube collectors

Both literature as well as companies focus lately in the development of evacuated tube collectors of direct flow type, in which no intermediate working medium is used and therefore

heat transfer losses are minimized, further enhancing the collector's efficiency [73, 74]. Towards this direction, a comparative experimental analysis was conducted between the commercial heat pipe evacuated tube collectors, which were analyzed in the previous sections, and novel direct flow evacuated tube collectors.

The test rig was developed as a part of the SWS-heating EU Horizon 2020 funded project, in order to test the novel direct flow evacuated tube collectors in direct comparison with commercial heat pipe type ETCs, both manufactured by company AKOTEC Produktionsgessellschaft mbH. A schematic of the installed test rig along with an image of the tested types of collectors in parallel series allocations is presented in Fig. 2.7. The parallel allocation ensures a common inlet fluid temperature and therefore evaluation on identical conditions on all times, a crucial design aspect, given the fact that experiments repeatability is nearly impossible in experiments that are heavily dependent on the weather conditions. In a similar manner, the outlet streams from both collectors are mixed in a common head and driven to the heat storage tank, in which heat is transferred to the heat sink medium. The working fluid was selected water with a colouring agent to ensure enhanced absorptivity, as will be further discussed in a following section. With respect to the measuring equipment, as shown in Fig. 2.7 (a), the system is equipped with all the required instruments to construct the energy balances in the two collectors and estimate the respective efficiency. As similar equipment was used in this test rig and the one discussed in section 2.1.2, the key technical specifications of the involved equipment can be found in Table 2.2-Table 2.6. Lastly, it has to be mentioned that given the fact that the investigated collectors are not yet commercial, the efficiency curves will be presented parametrically, due to confidentiality implications.

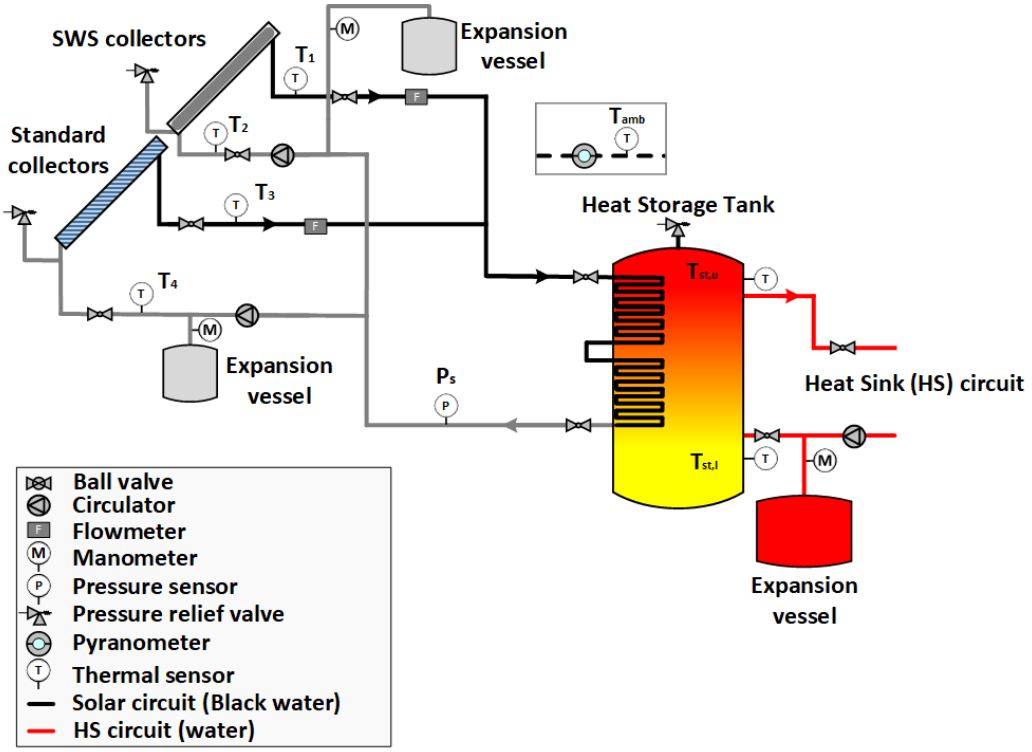

(a)

(b)

Fig. 2.7. (a) Schematic and (b) image of the developed test rig at the Laboratory of Steam Boilers and Thermal Plants, National Technical University of Athens

I. Real-time performance comparison

Similarly to the calibration calculations of the previous section, two weekly sets of experiments will be presented, one in winter conditions and one in summer operation, with respect to the performance evaluations of the two types of collectors. The main considered performance indicator will be the daily average efficiency along with the outlet temperature from the collectors, calculated as shown below:

$$\eta_{col,d} = \frac{\int_{day} \dot{Q}_{col}}{A_{col} \cdot \int_{day} I_{sol}} \qquad (2.12)$$

As the working medium in this test rig is desalinated water with a colouring agent, the thermodynamic properties required for the estimation of $\dot{Q}_{col}$, based on equations (2.2)-(2.5), were derived from Refprop from the respective water properties.

The first test week was in February 2021 (06/02-12/02), characterized by rather high maxima in the temperatures. However, the rapidly variable ambient conditions, as shown in Fig. 2.8(a), allowed the comparison of the two collectors in rather unsteady conditions.

The main conclusion by both the temperature profiles of Fig. 2.8(b) and the daily average efficiencies of Fig. 2.8(c), is that the direct flow collectors tend to perform efficiently and at a comparable level to the commercial heat pipes ones, especially in days with less fluctuations in the solar irradiance (e.g., 09/02, in which the highest daily average efficiency was reported with a value of more than 68%). On the other hand, days -as the 11/02- with high fluctuations and on average lower values in the solar irradiance (cloudy days) the commercial heat pipe collectors tend to perform better.

In order to have a clearer view on the performance comparison of the two types of collectors, the experiments were also conducted during summer period, when the solar irradiance values are at their maximum levels. Fig. 2.9 presents an overview of the measured data for the week 29/06-05/07/2021. This week was selected to be presented as the solar irradiance reached a maximum value of approximately 1250 W/m², while the temperatures were kept relatively low (for the period in Greece), which both allowed for close to maximum performance of both the collectors. In fact, the performance of the two types of collectors was comparable on all

days of the weekly measurements, with the direct flow collectors to be more efficient on the days that the solar irradiance was more stable and sky was clear without any clouds, similarly to the observed results from the winter week. However, it must be noted that the high uncertainty of the measurements, with respect to the calculation of the solar collectors' efficiency, hinders the extraction of definite conclusions. On the other hand, it must be noted that the efficiency results, shown in Fig. 2.9(c), were calculated with respect to the aperture area. Hence, if the results were calculated with respect to the gross area, the direct flow collectors would out-perform the heat pipe collectors, owing to the higher aperture to gross area ratio, which is equal to 0.902 compared to the 0.625 for the heat piper collectors, respectively.

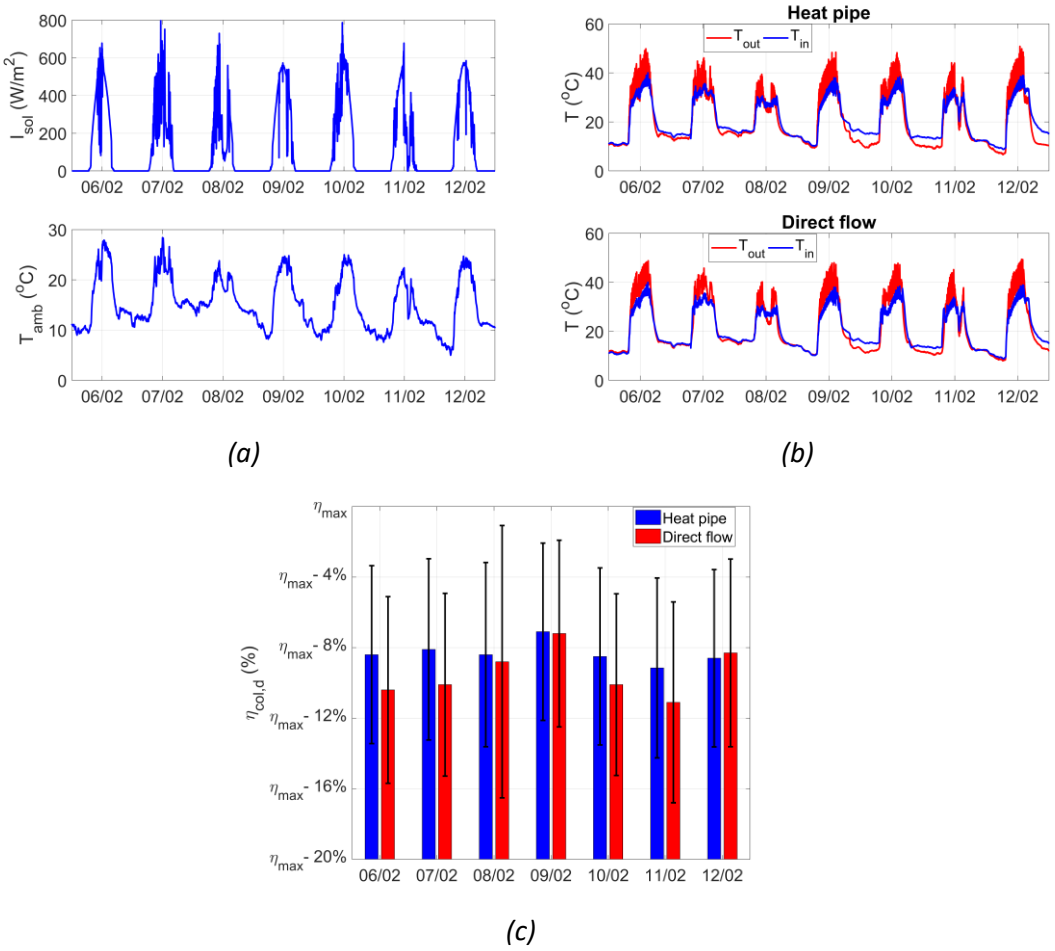

Fig. 2.8. (a) Ambient conditions, (b) measured inlet/outlet temperatures and (c) daily average solar efficiency for the heat pipe and the direct flow evacuated tube collectors over a week in February 2021

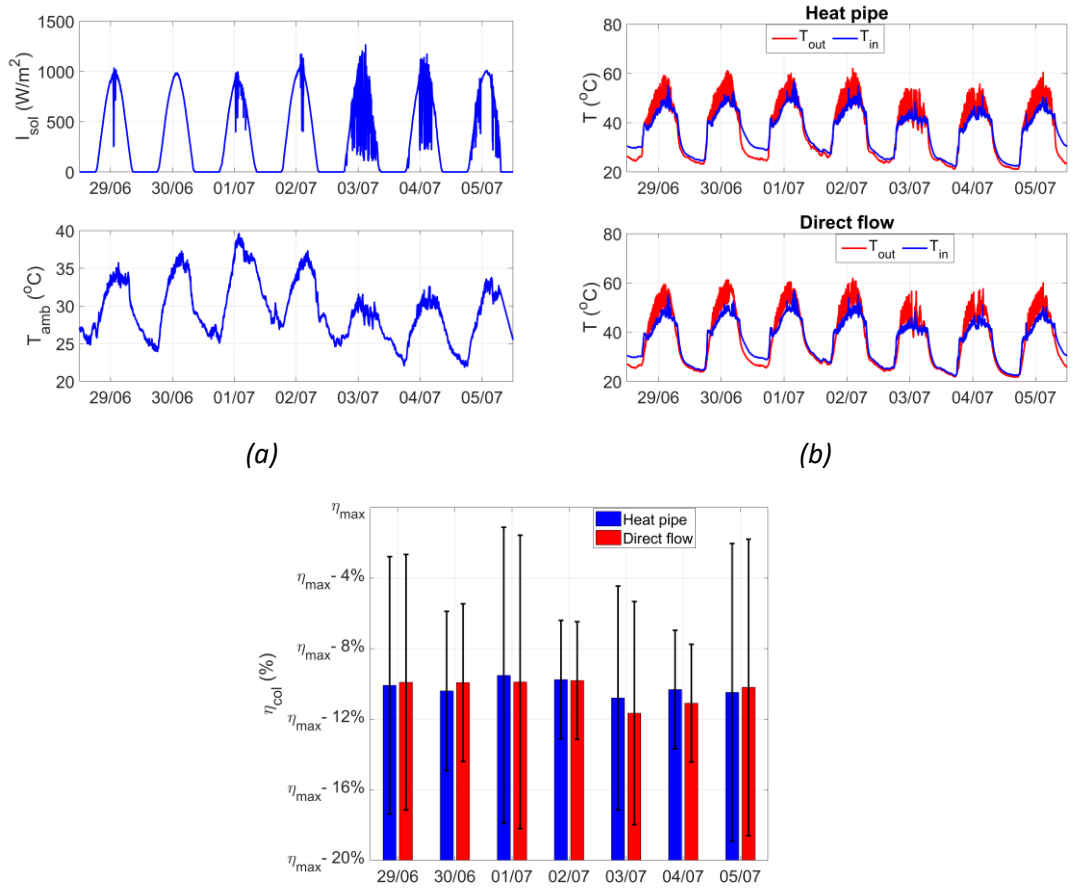

Fig. 2.9. (a) Ambient conditions, (b) measured inlet/outlet temperatures and (c) daily average solar efficiency for the heat pipe and the direct flow evacuated tube collectors over a week in July 2021

II. Effect of colouring agent

As already mentioned, the working medium in the test rig was desalinated water with a colouring agent, in order to have a black colour and maximize the absorptance of solar irradiance in the direct flow collectors. Within this context, three sets of experiments were conducted. Each presented set was evaluated for at least a week (between February and April), given also the timeline of the overall experimental procedure. The concentration in each set is presented in Table 2.7.

The high variability of the solar irradiance (mainly) posed several barriers in the direct comparison of the different concentrations' performances. Therefore, apart from the graph showing the performance for different solar irradiance values, the performance was also shown in the right plot of Fig. 2.10 with respect to the ratio $\frac{(\bar{T}_{col}-T_{amb})^2}{\cdot I_{sol}}$ which is the second term of eq. (2.1) in order to partially rationalize the results and allow a more proper comparison between the different testing periods. In fact, there is identified a small enhancement in the performance of the direct flow solar collectors with increasing concentration, within, however, the range of uncertainty of the measurements. In order to have more conclusive results, it is suggested to evaluate on a second stage using artificial light which is more accurately measured and therefore can allow for a lot higher precision result.

Table 2.7. Overview of coloring agent concentrations in the three sets of experiments

	Coloring agent added volume (ml)	Concentration (ml/l)
1st addition	60	1.538
2nd addition	120	3.077
3rd addition	180	4.615

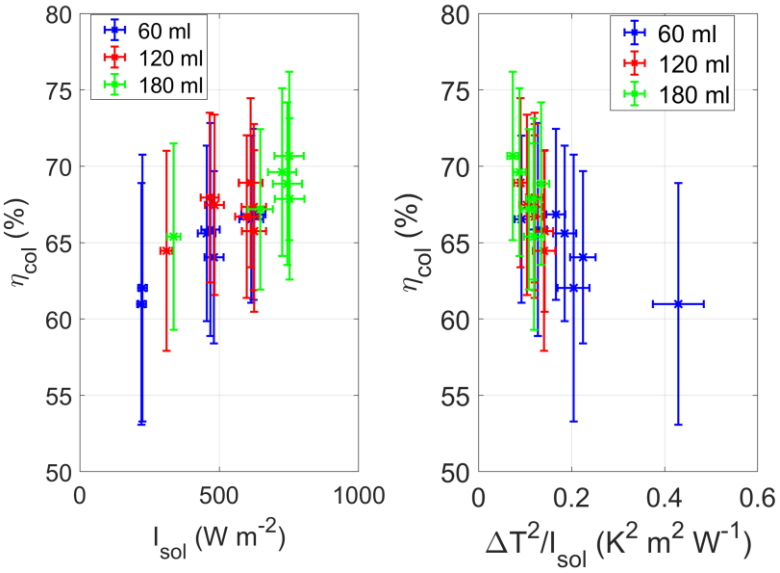

Fig. 2.10. Measured daily average solar efficiencies for different concentrations of colouring agent

III. Conclusions from conducted experiments

Direct flow type ETCs, despite being in pre-commercial stage, have a comparable performance to standard heat pipe ETCs, as shown from the performance tests above and the respective measurements in the daily average solar efficiencies. As the experiments on the test rig are ongoing at the time of this dissertation, particular focus is given in the estimation of the incidence angle modifier's effect in the overall performance of the direct flow collectors. In fact, on the theoretical level of the estimated coefficients for the solar efficiency polynomial curve of eq. (2.1), for small incidence angles of the direct solar irradiance (less than 20^o) or cases with higher values of diffusion to direct solar irradiance, the performance of the direct flow collectors result in higher efficiencies. This fact is also partially proved in the winter tests shown in Fig. 2.8, during which the efficiencies of the direct flow were comparable to the commercial heat pipe collectors (maximum performance deviation in favor of the heat pipe collectors of 2.5%). Moreover, from an economic point of view, the current estimation on the specific costs for the purchase of the direct flow collectors per unit of surface are only 5-10% more expensive than the respective value for the heat pipe collectors sold by AKOTEC GmbH.

2.2 Thermal storage tank

In order to minimize the thermal spikes and also tackle the time variability of solar energy, thermal energy storage is extensively applied in coupling to solar harvesting systems [75].

There can be distinguished three types of thermal energy storage: sensible heat storage, latent heat storage and thermo-chemical heat storage [76]. In sensible heat storage, a storage

medium is at such working conditions that its charging will cause only a shift in temperature and no phase change. In most simple version, sensible heat storage is realized by a single tank, filled with a heat transfer fluid. The storage tank is either an open circuit with respect to the heat source circuit (i.e., solar collectors circuit) or is supplied with a helical coil within which the hot stream flows and charges the storage tank, causing the increase in the temperature of the storage medium [77]. Other types of sensible heat storage include underground heat storage, rock beds and storage using concrete modules [18, 78]. In latent heat storage, the storage medium is a phase change material (PCM), which during charging and discharging phases are solidified and melted, respectively [79]. The large phase change enthalpies enhance the energy density of latent heat storage systems in comparison to sensible storage and hence lead to more compact systems [80]. Finally, thermo-chemical energy storage is based on a chemical reaction that can be reversed [81]. The most important advantage of thermo-chemical energy storage is the high storge capacity, with studies revealing a storage capacity of several times higher than conventional sensible storage systems [82, 83].

In most solar driven residential applications, sensible heat storage is used thanks to its simplicity, high market availability and low costs [84]. Several studies discuss performance characteristics, modeling aspects and system integration concepts [85-87]. Raccanello et al. [77] evaluated different order models for several types of single tank storage systems, to identify the reliability of simplified modelling procedures for inclusion of storage tank models in complex systems, without severely affecting the computational cost. Tian and Zhao [88] conducted a detailed review on different types of solar thermal collectors and high temperature thermal energy storage systems.

Ismaeel and Yumrutas [89] simulated the performance of a solar assisted heat pump connected with an underground thermal energy storage for wheat drying. For a solar field area of 70 m^2 and a storage tank volume of 200 m^3, the estimated coefficient of performance (COP) of the heat pump was equal to 4.4. Syed et al. [90] evaluated experimentally a solar absorption cooling system coupled with a 2 m^3 stratified storage tank in the city of Madrid, Spain. The 35 kW nominal capacity absorption chiller, driven by a solar field of 50 m^2 flat plate collectors (FPC), managed to reach a daily average COP of 0.42. Karim et al. [91] evaluated the performance of stratified storage tanks for heating/cooling applications and concluded that tanks with higher height to diameter ratios tend to reduce mixing and thus reduce heat losses. In the same direction, Pintaldi et al. [92] evaluated the energetic performance of sensible and latent heat storage scenarios for solar cooling setups. The analysis found that, for the evaluated scenarios, a minimum specific collector area of 2 m^2 per kW of cooling capacity is required for target solar fractions higher than 50%. Jung et al. [93] assessed control strategies for the optimal operation of a heating system consisting of a heat pump and a thermal storage tank for use in Seoul, South Korea.

Based on the above, it is realized that the performance of the thermal storage tank in coupling with the distribution system is crucial for the overall system efficiency. Within this context, a simulation model was developed and an experimental test-rig was installed and used to both calibrate the simulation model and experimentally evaluate the performance of the tested combi-storage tank. The test rig was developed as a part of the SWS-heating EU Horizon 2020 funded project, in order to assess the performance of a thermal energy storage configuration driven by direct flow evacuated tube collectors, similar to the ones tested in section 2.1.4. The distribution of the available solar heat and the heat stored in the seasonal thermal energy

storage (STES) is realized via a residential heating and DHW distribution system based on a thermally stratified water tank. The tank is working as a diurnal thermal energy storage device, coupled with a natural gas boiler. The solar heat is used to charge the combi-storage tank and/or the STES. A floor heating system is considered in the connected user, while DHW is supplied via a dedicated heat exchanger. STES is used either as a backup or to cover peak loads at days with inadequate solar irradiance. A condensing gas boiler operates as a back-up thermal energy source to ensure thermal comfort at any time of year. A schematic of the test rig can be shown in Fig. 2.11.

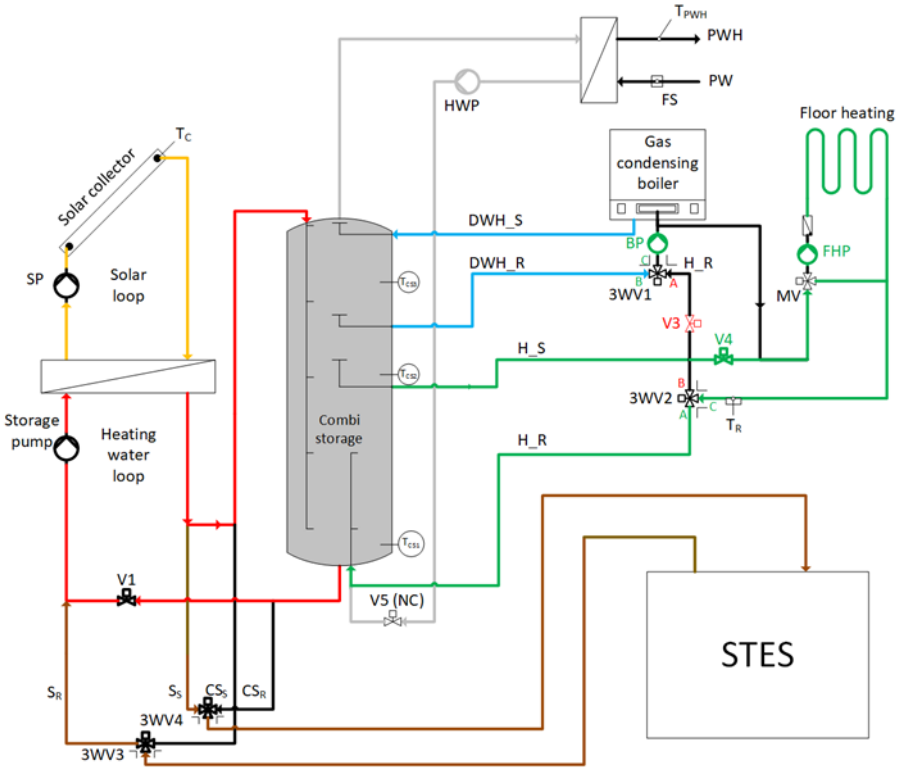

Fig. 2.11. Schematic of the considered system. Different colors denote the various loops of the system at different temperature levels: Solar loop (orange), STES charging (Brown), Solar charging of Combi-storage tank (Red), Space Heating (Green), DHW (Grey) and Boiler charging the CST for DHW (Light Blue)

2.2.1 Test rig description

In order to simulate the energy demand of a residential nearly zero energy building (nZEB) building, a dedicated test rig was developed at the Laboratory of Steam Boilers and Thermal power Plants, National Technical University of Athens, Greece. The DHW and Floor heating loads are simulated using two heat exchangers connected to a heat sink (Fig. 2.12). A gas condensing boiler is used to provide the necessary charging of the combi-storage tank simulating the solar collectors and the STES. Depending on the available water temperature, space heating hot water can be supplied solely from the tank, using the tank stored heat and a possible recharging via the boiler or solely from the boiler, bypassing the tank, to achieve the necessary temperature for thermal comfort. More specifically, in case of heating demand and no stored energy in the space heating section of the tank (Fig. 2.12), if the boiler is not used for charging the DHW section, the heating demand is met using the natural gas boiler for

reheating (brown line in Fig. 2.12) or directly as the main heat source (blue line in Fig. 2.12). For this reason, a modulating boiler was selected for this system.

The switching between the different heating operational modes is achieved using 3-way valves, while the temperature of the delivered water for space heating is ensured using a mixing valve controlled with a PID control. In addition, in each of three loops of Fig. 2.12, namely DHW, heating and charging loop, a different circulation pump is used, according to the energy demand. DHW and heating demand profiles are used according to EU standards and residential nZEB simulations. As shown, the solar collectors were not coupled with the test rig to avoid the time variability of solar heat for the needs of the conducted experiments.

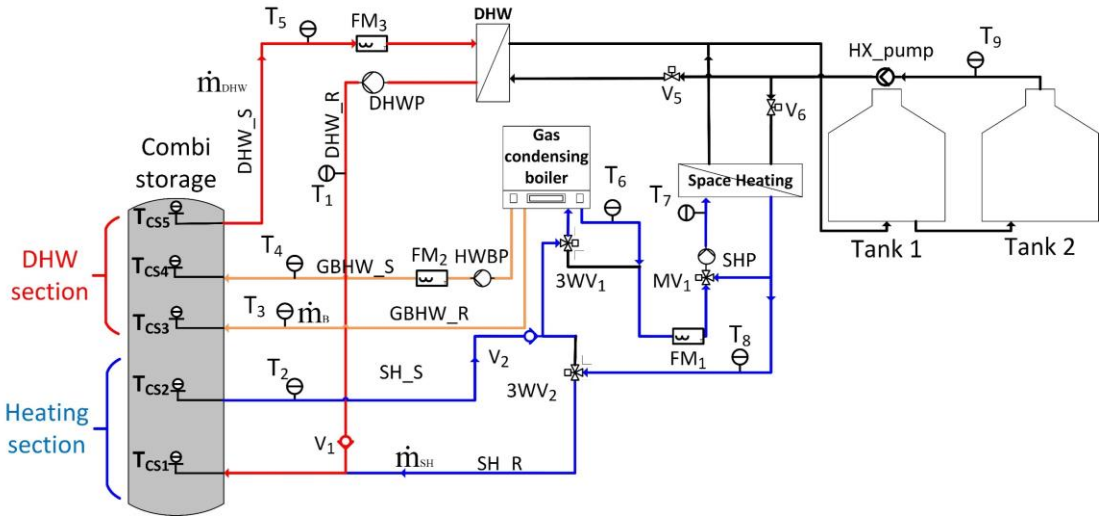

Fig. 2.12. Schematic of the experimental test-rig. Different colors denote the various loops of the system at different temperature levels: a) Domestic Hot Water loop (orange) b) Space heating loop (Blue) c) Charging of the tank's upper part (Brown)

An overview of the actual test-rig layout is depicted below in Fig. 2.13, along with some additional information on the key specifications of the involved components.

I. Combi-storage tank

The combi-storage water tank is thermally stratified and works as a temporary thermal energy storage in the form of hot water. The combi-storage tank capacity is equal to 535 lt. For the thermal stratification to be preserved and at the same time minimize the heat losses, the tank needs to be highly insulated. This is achieved by a vacuum wall insulated tank. This way the thermal losses via conduction and convection are minimized, due to the absence of air, and the radiant losses are predominant. Table 2.8 presents additional technical specifications on the tank, required for the modelling procedure, which will be described in the following section.

There are 5 available ports in the combi-storage tank, numbered as shown in the schematic of Fig. 2.12, all entering vertically from the bottom of the tank to different heights of its interior, with the corresponding dimensions of Fig. 2.14. At the same height with each port, there is a Pt1000 thermal resistance sensor, to ensure accurate measurement of the temperature in each subcircuit of the system.

Fig. 2.13. Experimental test-rig configuration

Table 2.8. Technical specifications of the Combi-storage tank

Property	Value
Maximum operating pressure (bar)	3
Maximum operating temperature (°C)	95
Total height (mm)	2555
External tank diameter (mm)	1000
Inner tank volume (lt)	535
Inner tank diameter (mm)	650
Insulation thermal conductivity (W/m K)	0.008

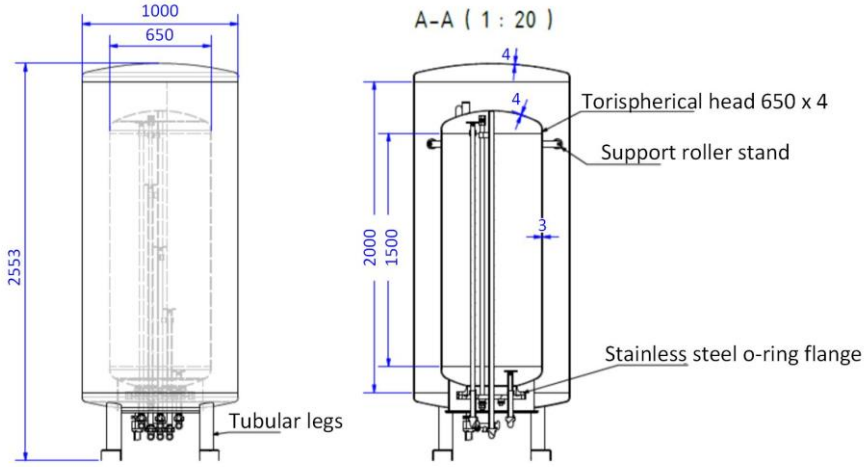

(a)

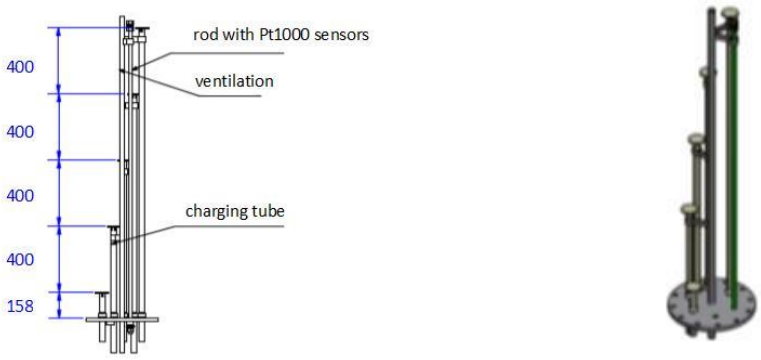

(b) *(c)*

Fig. 2.14. (a) Schematic of combi-storage tank, (b) piping drawing and (c)3-D sketch of the piping geometry of Combi-storage tank

II. Condensing gas boiler

A modulating boiler was required to operate on two different temperature setpoints. The sizing of the boiler was dictated by the need to cover at maximum capacity 18.8 kW for DHW production and 10 kW for space heating. To achieve higher efficiencies, the gas boiler was selected to be a condensing one. A condensing boiler recovers the latent heat of evaporation from the water vapor in the exhaust gas, which would otherwise have been wasted [94]. The relatively small temperature differences that were required for the considered application, indicated the need of a combi boiler with a lower limit of its power capacity being as small as permitted by the commercially available products.

Following a market search, the boiler chosen was the natural gas condensing boiler "Riello Residence Condens 25KIS e" [95]. The boiler can achieve reduced thermal power for DHW production of 3.3 kW and reduced thermal power for heating mode equal to 3.8 kW for a temperature rise from 30°C to 50°C. The nominal thermal power for DHW and space heating are 26.3 kW (average nominal thermal power for different DHW modes) and 21.2 kW (50°-30°), respectively.

III. Heat exchangers and auxiliary equipment

The heat exchangers were sized based on the inlet and outlet temperatures for both the hot and cold sides, and thus the respective heat duty of each one. In the case of the DHW heat exchanger, the DHW demand profile was estimated based on the cycle no2 as described in the European Standard [96]. This cycle corresponds to 100.2 equivalent hot water liters at 60°C, which is considered adequate for a small family household. In the aforementioned standard [96] are also defined the required flowrates for each demand type. All above considered, the heat duty of the DHW heat exchanger was estimated to be 18.8 kW.

In the case of the space heating heat exchanger, the tank side inlet temperature is set at 38°C and the outlet at 28°C with a maximum rated power of 10 kW based on typical nZEB buildings simulations [97, 98]. Due to the small size of this power demand, and the high flow rates in the heat exchanger, larger inlet/outlet ports were preferred to avoid large pressure drops. The heat exchanger duty was estimated at 10 kW with a temperature difference of 10°C at a nominal flow rate of 0.24 l/s on the hot (tank-heat exchanger) side.

The three circulator pumps used in the circuits connected to the combi storage tank (see Fig. 2.11), namely the domestic hot water pump (DHWP), the hot water from boiler pump (HWBP)

and the space heating pump (SHP), all were the same commercial model, Grundfos UPS2 32-80 180, working at different design point.
Five Pt-100 thermal sensors were embodied by the tank manufacturer at the same heights with the respective ports in order to monitor the temperature of the combi-storage tank. Additionally, in the pipelines connected to the heat exchangers and the gas boiler, a total of seven additional Pt-100 thermal sensors were implemented with a transmitter of 4-20 mA output. The uncertainty of each sensor at the nominal operating temperatures is equal to ±(0.15+0.2%*MV)°C, where MV is the measured value plus ±0.2°C due to transmitter error. With respect to water flow measurements, three identical ultrasonic flow meters were used with a maximum allowable flowrate of 0.78 lt/s, model Bellimo FM020R-SZ, and an uncertainty of 1.2% of the measured value.

2.2.2 Storage tank modeling

The scope of the experimental test rig was dual. Firstly, it was developed to assess the potential of the combi-storage tank for efficiently storing heat at different temperature levels and covering the heating and DHW loads of a building. On second level, the sets of experiments and their results were used to evaluate the accuracy of a numerical model towards its implementation in more complicated systems.
In this perspective, the combi-storage tank was modelled by fractionating it in a number of mixing zones, with uniform temperature within each zone. By applying the energy balances for every mixing zone, a set of differential equations is created and solved numerically via an implicit Euler discretization. The selection of the implicit scheme was dictated to enhance the stability of the solution [99].
Based on the geometry of the combi-storage tank, shown in Fig. 2.14, it was selected to adapt the height of the mixing zones in such a way, that the first and the last mixing zones do not include the top and bottom ports, respectively, and therefore only heat transfer by conduction and heat transfer losses take place in these zones. This choice was made in order to ensure that all the ports of the combi storage tank are in the middle of a mixing zone, independently of the selected number of zones, as shown in Fig. 2.15. This will allow a fairer evaluation of the optimal number of mixing zones in comparison to the experiments.
Based on the splitting of the storage tank in n mixing zones, the energy balance within a single mixing zone j for a time interval Δt can be expressed by the following equations [77, 100]:

$$M_j \frac{U_{t,j} - U_{t-1,j}}{\Delta t} = \frac{\lambda_j + \Delta\lambda_j}{\Delta x_j} A_c \left(T_{t,j-1} - T_{t,j}\right) + \frac{\lambda_j + \Delta\lambda_j}{\Delta x_j} A_c (T_{t,j+1} - T_{t,j}) - \dot{m}_{DHW}\left(h_{t,j} - h_{t,j+1}\right) + \dot{m}_B\left(h_{t,j-1} - h_{t,j}\right) - \dot{m}_{SH}\left(h_{t,j} - h_{t,j+1}\right) - U_l A_{o,j} \cdot \left(T_{t,j} - T_{t,amb}\right) \quad (2.13)$$

In equation (2.13), M_j is the total mass of water in zone j, U is the internal energy, h_j is the enthalpy of water at zone j, λ_j is the thermal conductivity, A_c refers to the conduction surface between two consequent zones, $\dot{m}_{DHW}$, $\dot{m}_B$, $\dot{m}_{SH}$ are the mass flowrates of the DHW, gas boiler and space heating respectively, as shown in Fig. 2.15. The term U_l refers to the heat transfer losses coefficient to the surroundings from the outer surface, $A_{o,j}$, of each zone, while T_{amb} is the ambient temperature at time t. Finally, Δx_j is the height of zone j, which is variable to allow all ports of the tank be located at the center of a zone, independently of the number of mixing zones selected:

$$\Delta x_j = \begin{cases} 0.05 - \dfrac{0.8}{n-3} & , \quad for\ j = 1\ or\ j = n \\ \dfrac{1.7 - 2 * \Delta x_1}{n-2} & , \quad for\ j = 2{:}(n-1) \end{cases} \tag{2.14}$$

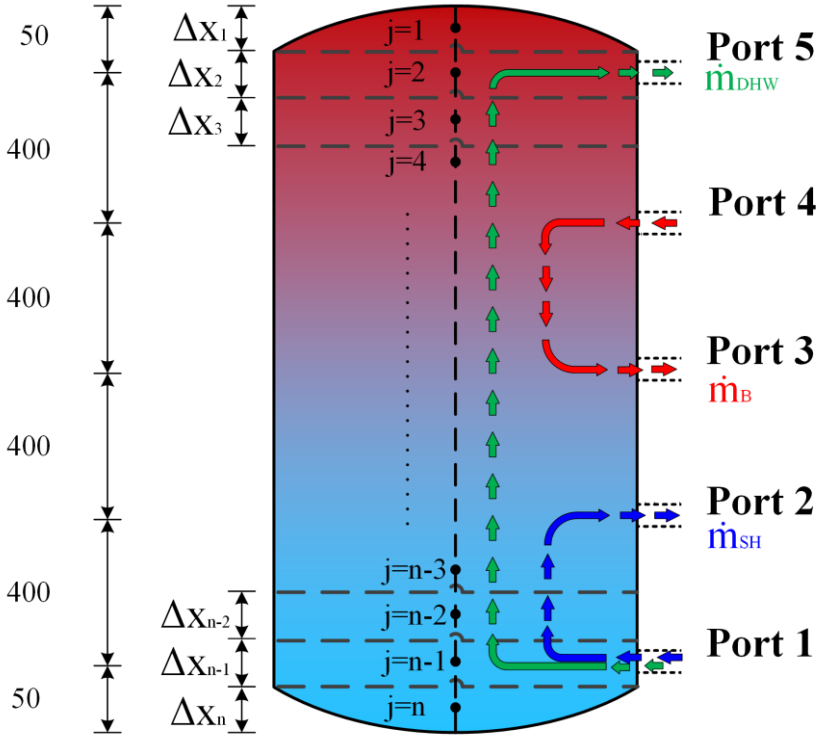

Fig. 2.15. Schematic of combi storage tank discretization along with the key dimensions (in mm) and streams' conditions

To allow for a more direct solution of the system of equations for all the mixing zones, the enthalpies in equation (2.13), are modified to temperatures based on the approximation of $h \cong c_p\theta$, with c_p to be the specific heat capacity and θ the temperature in degrees Celsius, which has a relative error of less than 0.4% for the subcooled water at the pressure of the tests, as calculated in RefProp. However, as in all cases in equation (2.13), there are enthalpy differences to be calculated, the temperature difference in degrees Celsius can be substituted by the absolute temperature difference, $\Delta\theta = \Delta T$, hence the equation (2.13) can be transformed into:

$$M_j \frac{U_{t,j} - U_{t-1,j}}{\Delta t} = \frac{\lambda_j + \Delta\lambda_j}{\Delta x_j} A_c (T_{t,j-1} - T_{t,j}) + \frac{\lambda_j + \Delta\lambda_j}{\Delta x_j} A_c (T_{t,j+1} - T_{t,j}) - \dot{m}_{DHW} c_p (T_{t,j} - T_{t,j+1}) + \dot{m}_B c_p (T_{t,j-1} - T_{t,j}) - \dot{m}_{SH} c_p (T_{t,j} - T_{t,j+1}) - U_l A_{o,j} \cdot (T_{t,j} - T_{t,amb}) \tag{2.15}$$

Obviously, based in Fig. 2.15, the mass flowrates considered in equation (2.15) are equal to zero in some zones. Therefore, based also on the location of the ports (see also in Fig. 2.15) the generic equation (2.15) has the inputs listed in Table 2.9, based on the corresponding zone that is applied.

Table 2.9. Input conditions for equation (2.15) based on evaluated mixing zone for a total of n mixing zones

Number of zone	Input conditions
$\boldsymbol{j = 1}$	$\dot{m}_{DHW} = \dot{m}_B = \dot{m}_{SH} = 0$
$\boldsymbol{j = 2\ (port\ 5)} \quad \div \quad \boldsymbol{j = 1 + \frac{0.4}{\Delta x_2}\ (before\ port\ 4)}$	$\dot{m}_B = \dot{m}_{SH} = 0$
$\boldsymbol{i = 2 + \frac{0.4}{\Delta x_2}\ (port\ 4)} \quad \div \quad \boldsymbol{j = 2 + \frac{0.8}{\Delta x_2}\ (port\ 3)}$	$\dot{m}_{SH} = 0$
$\boldsymbol{j = 3 + \frac{0.8}{\Delta x_2}\ (after\ port\ 3)} \quad \div \quad \boldsymbol{j = 1 + \frac{1.2}{\Delta x_2}\ (before\ port\ 2)}$	$\dot{m}_B = \dot{m}_{SH} = 0$
$\boldsymbol{j = 2 + \frac{1.2}{\Delta x_2}\ (port\ 2)} \quad \div \quad \boldsymbol{j = 2 + \frac{1.6}{\Delta x_2}\ (port\ 1)}$	$\dot{m}_B = 0$
$\boldsymbol{j = n}$	$\dot{m}_{DHW} = \dot{m}_B = \dot{m}_{SH} = 0$

The determination of all thermal properties of the tank's water content in the developed model were conducted via RefProp database [101].

2.2.3 Storage tank experimental validation

I. Nodes' number

First step in the experimental evaluation of the developed model, concerned the selection of the number of nodes to be used in the model. For this reason, three relevant charging experiments were conducted and parametrically simulated in order to evaluate the model's reliability for various number of nodes. The operating conditions of the conducted tests are summarized in Table 2.10.

Table 2.10. Operating conditions for the charging experiments

	Test 1	Test 2	Test 3
Initial temperature (°C)	25	45	25
Charging flow rate (l/min)	2	3.3	3.3
Charging temperature (°C)	65	65	45
Inlet port (Fig. 2.15)	Port 5	Port 5	Port 3
Outlet port (Fig. 2.15)	Port 1	Port 1	Port 1

Eight different simulation cases with number of nodes equal to 10, 20, 30, 60, 90, 120, 150 and 180 nodes, respectively, were compared to three different charging experiments. The Root Mean Square Error (RMSE) between the time each temperature measured by the 5 different ports reaches the test's completion setpoint, is compared for each case with the experimental results for all three experiments, and presented in Fig. 2.16. As can be observed, for number of nodes higher than 60, the improvement is relatively small. In fact, this comes in agreement with the study by Wischhusen [100], which mentions that for relatively low number of nodes (n<20), the buoyancy effects harm the accuracy of the model. Similarly, Nash et al. [102] calculated almost negligible improvements in a dynamic model of a sensible heat storage tank for a number of nodes higher than 30 nodes, with an RMSE in the range of 0.05. Hence, to minimize, as possible, the calculation time, the number of nodes used in the following tests was set to be equal to 60.

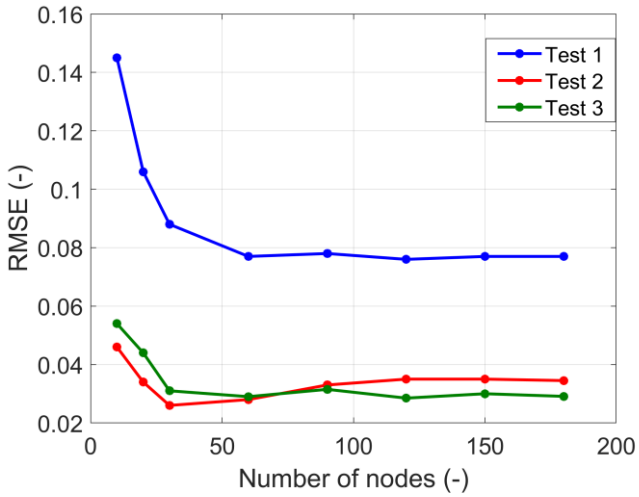

Fig. 2.16. Overview of the statistical comparison of tank model with experimental data for the various numbers of nodes

Within the context of the combi-storage tank use for DHW and space heating, four additional experiments were conducted and will be presented in the following three subsections. The reason for these experiments is twofold: the further validation of the simulation model and the experimental assessment of the proposed combi-storage tank for use in a residential space heating and DHW application.

II. Charging case of entire tank

The first experiment involved the charging of both sections of the tank in two consequent steps. In the first step, the upper part of the tank was charged via port 4 (Fig. 2.15). The flowrate of the HWBP was set at 0.14 l/s, while the gas boiler setpoint was equal to 60 °C. The initial conditions in the combi-tank included a uniform temperature of approximately 36 °C and the target values were 58 °C for the temperatures T_{CS4} and T_{CS5}. In the second step of the test, after the upper part was charged, the lower part of the tank, dedicated to cover the space heating loads was also heated via port 1 with a flow rate of 0.25 l/s. The respective boiler setpoint was set at a water temperature of 50°C.

As shown in Fig. 2.17, in the first step of the charging process, there is a good agreement between the experimental and the simulation results after approximately 1800 seconds. As the heat is introduced in the tank via port 4, temperatures T_{CS4} and T_{CS5} rise from the start in a close range, while T_{CS3} has a delayed increase in the temperature. Finally, T_{CS1} and T_{CS2} are practically not influenced throughout this step, revealing a good stratification behavior of the tank. Once the second step is initiated, and heat is fed via the tank's lower port (port 1), T_{CS1} and T_{CS2} show a sharp rise; on the other hand, T_{CS3} is also influenced, tending to mix with the lower parts of the tank and therefore reducing its temperature. The stepwise change in the flowrates results in a deviation between the model and the experiments, in particular for T_{CS3}, which re-converges after approximately 1000 seconds. Finally, T_{CS4} and T_{CS5} tend to be unaffected by the space heating charging, a behavior which comes in agreement on both experimental and simulation results.

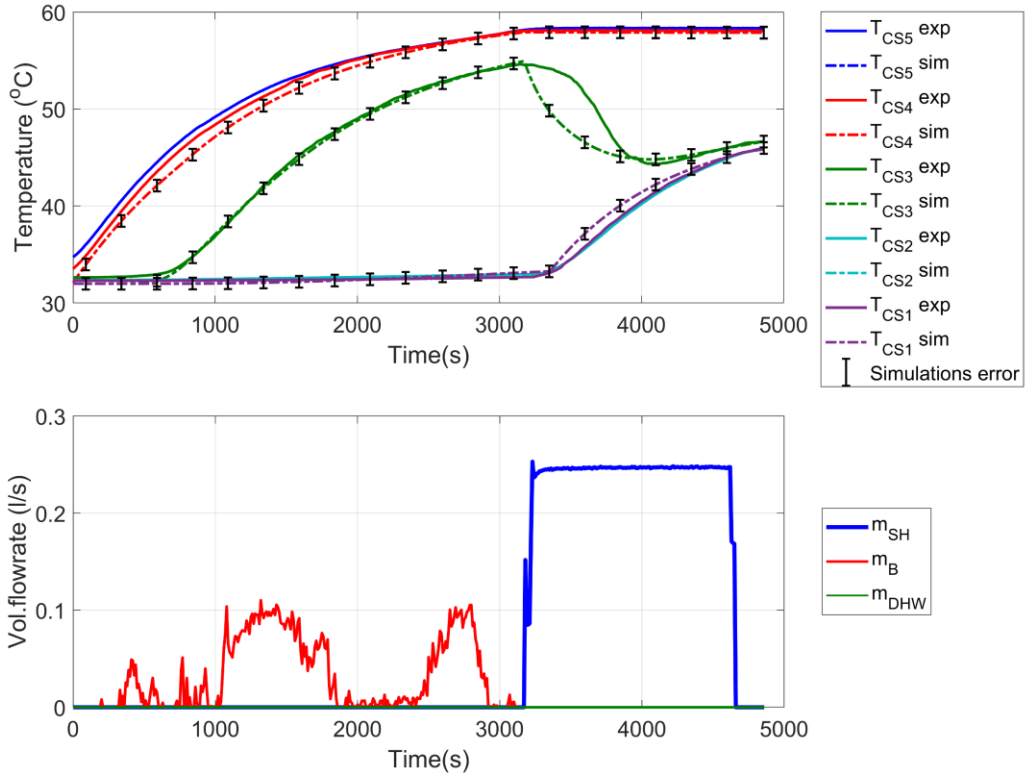

Fig. 2.17. Full charging case study of the combi-storage tank

III. Heating test

The next set of experiments aimed at testing the space heating performance of the experimental system and the simulation model, respectively. The supply flow rate for this experiment was equal to 0.14 l/s, corresponding to a temperature difference equal to 10 K (considering a supply temperature from the tank of 43 °C and a return temperature of 33 °C). The total thermal power corresponded approximately to 6 kW. This power supply to the heating system was estimated to be the maximum thermal power needed, based on typical nZEB buildings simulations [97, 103]. When space heating is supplied exclusively from the combi-storage tank, the space heating supply temperature to the heat exchanger (Fig. 2.12) is regulated by a mixing valve, so that the inlet to the hypothetical floor heating system is kept at 38°C. As can be observed by the results of Fig. 2.18, although, the model predicts accurately the final temperature profiles of the tank, there are some deviations occurring due to the lack of detailed inertia modeling of both the tank and the rest of the system components. This is especially evident as far as T_{CS3} is concerned, which is influenced the most by inertia phenomena as was also observed in the experimental data. In this scenario, T_{CS3} shows a stronger trend to mix with the lower section of the tank compared to the simulation. Thus, the simulation model presents a slightly better stratification behavior than the experimental procedure actually revealed.

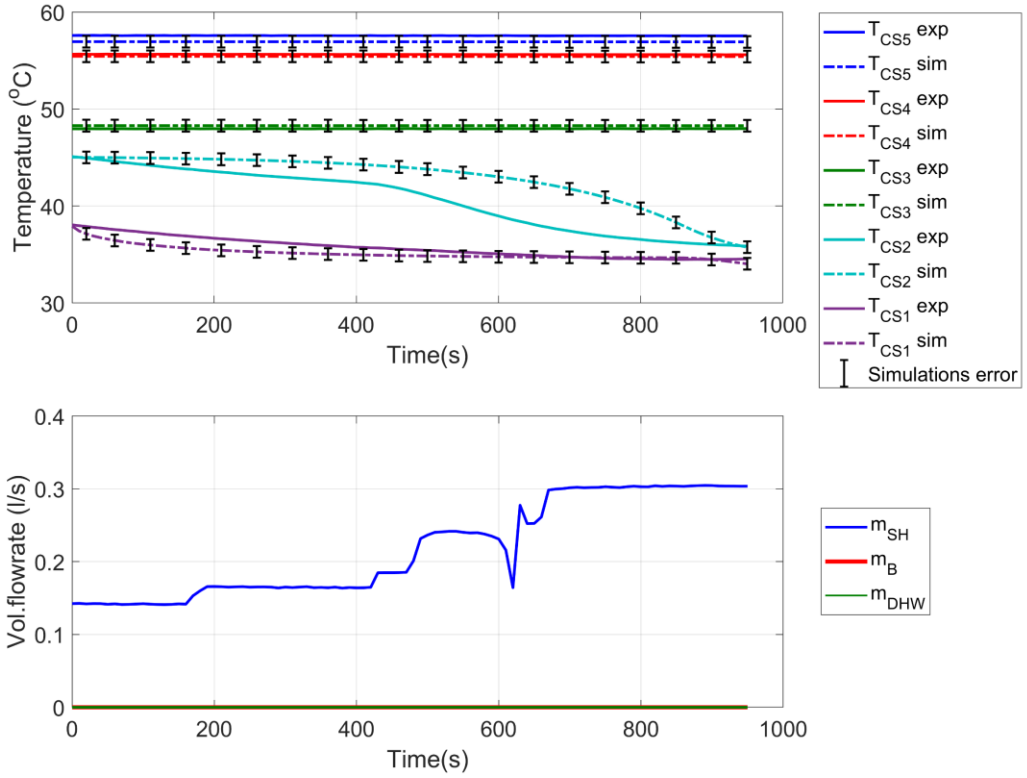

Fig. 2.18. Heating case study of the combi-storage tank

IV. DHW tests

In order the DHW tests to be conducted, the combi-storage tank is priorly fully charged. The first test conducted with respect to DHW, investigated the maximum power (worst case) scenario, which corresponded to the largest power consumption of the used water profile (as mentioned in section 2.2.1, load profiles for cycle no2 of the European Standard [96] were used). Hence, a 18.81 kW load was considered, for a total duration of 18.65 minutes which corresponds to the total consumed energy of 5.85 kWh. The boiler was turned on when T_{CS4}<55.5 °C, with a nominal DHW flowrate of 0.3 l/s and with a ΔT equal to 15 K. The above selection in the ΔT and the corresponding flowrate was partially dictated by the available cold-water supply in Athens, Greece, during the time of experiments (July 2020) and was equal to approximately 27 °C. The nominal supply and return temperatures were set equal to 58 °C and 33 °C, respectively.

As seen in Fig. 2.19, the used working conditions maintained the temperatures T_{CS1} and T_{CS2} above 42 °C, during the experiment, despite the low temperature return of the DHW consumption. However, in the upper part of the tank, temperatures decreased rapidly, resulting in the need to turn on the boiler after 490 seconds. With respect to the simulation model results, as shown in Fig. 2.19, the rapid temperature changes, in particular T_{CS4} and T_{CS5}, were not accurately predicted by the model, which required approximately 1000 seconds and close to steady state conditions in order to converge at an acceptable level. These results highlight that such 1D storage tank models can be used for steady state (on-/off-design) simulations, which in particular for solar driven systems commonly have hourly or

larger steps, but should be avoided for dynamic and semi-dynamic simulations as they tend to deviate considerably.

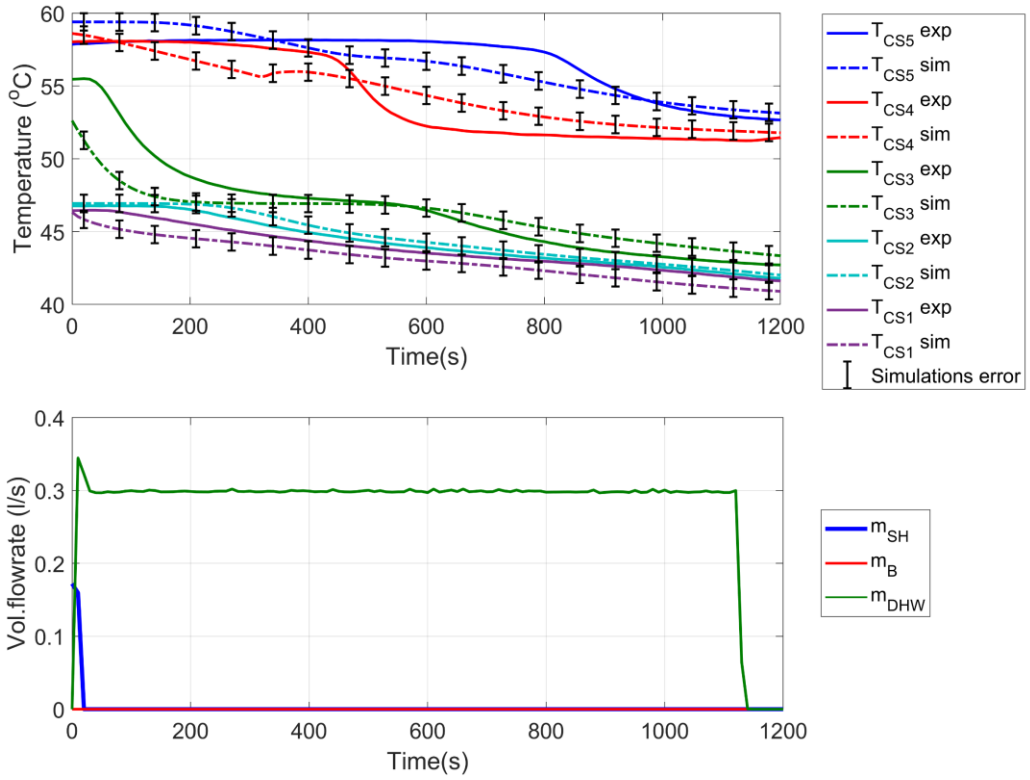

Fig. 2.19. DHW single consumption equal to a daily energy demand

In order to find a suitable criterion for the use of the boiler, the combi-storage tank's behavior was therefore further investigated by conducting a second DHW test. In this case, a combination of both T_{CS4} and T_{CS5} ($\frac{T_{CS4}+T_{CS5}}{2}$ <53 °C) was introduced in the control criteria in order to be able to deal with the temperature drop due to DHW consumption and provide hot water at acceptable temperature levels. Moreover, two alternative criteria were set for the boiler to be turned on in order to deal with the temperature drop due to heat losses and internal mixing (T_{CS4} <50 °C or T_{CS5} <56 °C). Eventually, the boiler was turned on in case any of the aforementioned three criteria was not satisfied. The boiler was then turned off again, when T_{CS5} was heated above 58 °C.

For the needs of this experiment, an equivalent profile was created by grouping the original DHW profile of the European standard's consumptions into 8 different groups, as presented in Table 2.11. Two complete cycles were executed in the experiment, to ensure that the performance of the tank was adequate even in the case it was partially discharged at the beginning of the cycle.

The results of this experiment are presented in Fig. 2.20 along with the respective simulation model results. The used criteria are considered to be adequate, as T_{CS5} remains well above 50 °C in all cases, which is an acceptable scenario for DHW use. However, as can be observed, the boiler is needed to operate with relatively high temperature input and for small ΔT (minimum T_{CS4} was 47.1 °C and minimum T_{CS3} was 45.9 °C), not allowing the condensation to take place and thus dramatically decreasing the boiler's efficiency. With respect to the

simulation model, similarly to the previous cases, the transient states are not adequately predicted by the model, with the temperatures of the upper levels of the tank to be over-predicted constantly and the lower levels' temperatures to be under-predicted. This larger duration experiment and with more fluctuations, highlights again the incompatibility of the model for transient simulations. However, it has to be noted that in cases the transient phenomena are not of concern and the time-step of the simulations is larger, the 1D model can adequately predict the storage's behavior, since also in Fig. 2.20, eventually the temperature profiles converge to the temperatures measured during the experiments.

Table 2.11. Equivalent daily demand profile for DHW

No. of consumption	Starting time (hh:mm)	Duration of consumption for 18.81 kW (s)	No. of equivalent consumption	Duration of equivalent consumption (s)
1	07:00	20.09		
2	07:17	267.94		
3	07:30	20.09	1	308.13
4	08:00	20.09		
5	08:15	20.09		
6	08:30	20.09		
7	08:45	20.09		
8	09:00	20.09		
9	09:30	20.09	2	120.57
10	10:30	20.09		
11	11:30	20.09		
12	11:45	20.09	3	60.29
13	12:45	60.28	4	60.28
14	14:30	20.09		
15	15:30	20.09		
16	16:30	20.09	5	60.29
17	18:00	20.09		
18	18:15	20.09		
19	18:30	20.09		
20	19:00	20.09	6	80.38
21	20:30	140.67		
22	21:15	20.09	7	140.67
23	21:30	267.94	8	288.04

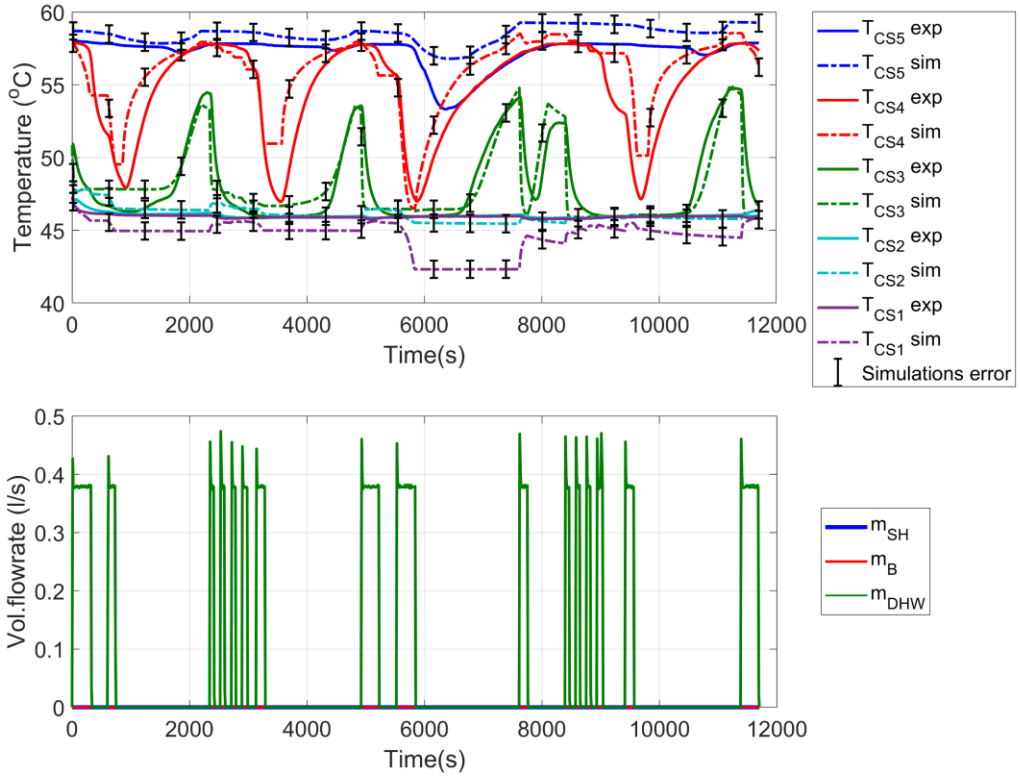

Fig. 2.20. Equivalent DHW profile testing over a 2-day period demand

2.2.4 Storage tank conclusions

Within section 2.2, the experiments conducted in a combi-storage tank test rig used to cover the space heating and DHW needs of a nZEB building were analyzed. A dedicated 1D simulation model was developed and tested in comparison to the experimental data. The main conclusions of the analysis can be summarized below:

Based on the case study and the specifications of the storage tank there is a number of nodes for the simulation model discretization, beyond which the benefits in the model's accuracy are negligible. In this study, this threshold was found to be the 30 nodes.

In the charging test of the upper part of the tank, there was a good stratification profile in the tank, which was also predicted sufficiently by the model. However, once the charging of the lower parts of the tank started, the deviation of the model to the experiments increased and required a sufficient time to re-converge, revealing an inadequacy of the model to predict transient phenomena.

A similar behavior was obtained during the heating tests, as the lack of detailed inertia modeling of both the tank and the rest of the system components resulted in deviations during transient condition, despite predicting accurately the final temperature profiles of the tank. Moreover, the aforementioned deviations resulted in the simulation model to present a slightly better stratification behavior than the actually measured during the experiments.

With respect to DHW tests, a multi-criteria approach was introduced to successfully control the operation of the gas boiler and ensure an acceptable performance of the combi-storage tank under the considered DHW loads. In fact, the upper temperature of the tank was kept in

all cases above 50 °C, with time margins that the boiler was needed to heat up the lower parts of the tank. On the other hand, the simulation model failed to predict the transient states of the tank, while the final levels of the temperature are well predicted in all five points of measurement in the tank.
Eventually, the 1D simulation model developed and tested in this study is adequate for use in on- and off-design models where the transient phenomena are not of importance, while for dynamic and semi-dynamic simulations more detailed models should be preferred.

2.3 Solar adsorption cooling – The Zeosol project

After the finalization of the experimental investigations and the validation of the simulation models for the solar collectors and the thermal storage tank, the following section will present the conducted experiments and the development of the corresponding simulation models for a solar driven hybrid cooling and heating setup based on adsorption cycle, which is one of the main alternatives in the design studies, presented in a following Chapter. The following sections were published in the study "Performance results of a solar adsorption cooling and heating unit" [104].

2.3.1 The Zeosol test rig

As mentioned already in section 2.1.2, for the Zeosol EU Horizon 2020 funded project consisted in the development of a solar driven hybrid adsorption cooling and heating setup, installed and tested at the Laboratory of Steam Boilers and Thermal Plants of the National Technical University of Athens, Greece. The prototype system was designed to fully cover the thermal loads of a residential building of 12.5 kW peak cooling load.
The proposed system focused in the coupling of a zeolite-water adsorption chiller with novel solar thermal collectors. The cooling capacity of the developed sorption chiller was exceeding 10 kW with a maximum reported thermal COP of 0.65. To reduce the chiller's capacity and thus the required solar field area, enhancing simultaneously the efficiency on part-load operation, a backup electrically driven heat pump was coupled with the adsorption chiller. The backup heat pump was originally designed to have a nominal cooling capacity of 10 kW and was used mainly to cover peak loads. The solar field consisted of three rows of advanced evacuated tube collectors with a total surface of 40 m², as shown in Fig. 2.22(a).
To enhance solar collector's performance and allow risk-free operation on low ambient temperatures, a propylene glycol solution was used as the working medium for the solar subsystem. Moreover, all secondary circuits of the adsorption chiller were using pure water. The 1 m³ heat storage tank -Fig. 2.22(c)- was equipped with heat coils, via which heat was transferred from the glycol solution towards the hot water, which in turn drove the adsorption chiller. A "V shaped" dry cooler -Fig. 2.22(b)- was implemented as the heat rejection unit for both the adsorption chiller and the backup heat pump, retrofitted for the specific application. Finally, the cooling/heating output, during the tests that will be presented in the following sections, was supplied to three fan coil units in a test room located in the laboratory, Fig. 2.22(d). An overview of the prototype, including the installed measuring devices is shown in Fig. 2.21.

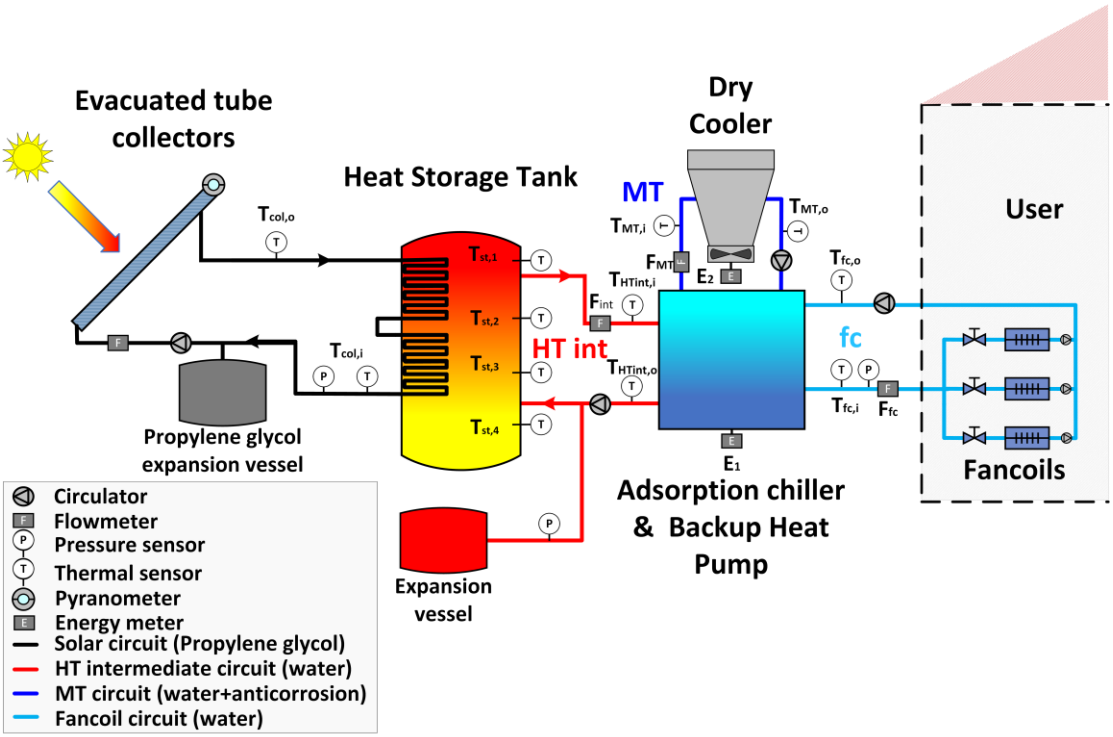

(a)

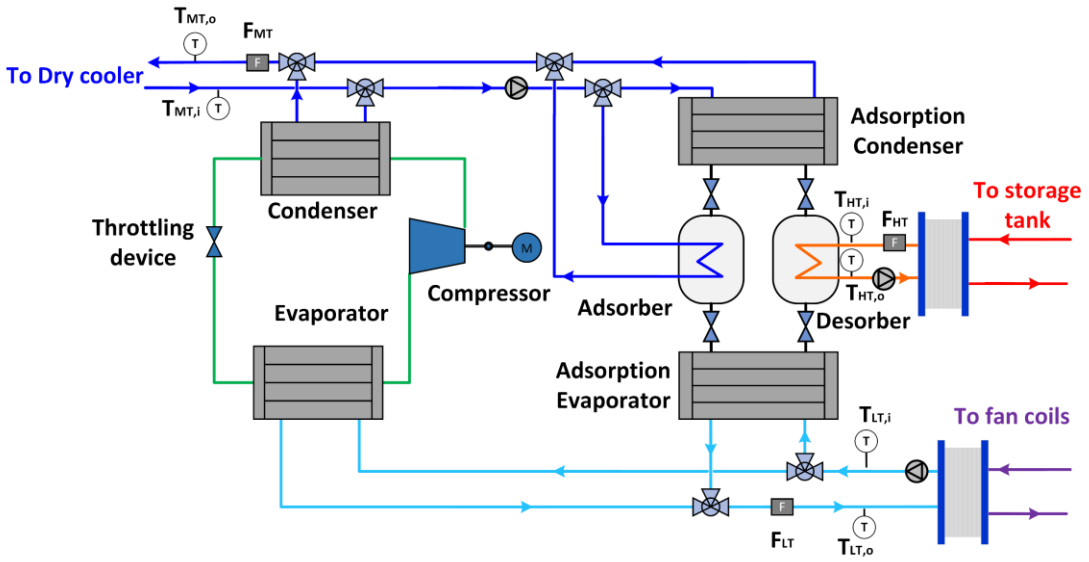

(b)

Fig. 2.21. (a) Schematic of Zeosol system prototype with all the involved measuring devices and (b) detailed schematic of the hybrid adsorption chiller/backup heat pump

Additionally to the measuring devices, presented in Tables 2.2-2.6 of section 2.1.2, there was a number of measuring devices installed in the test rig in order to monitor and assess the system's behavior. In total, downdraft the storage tank, the system was equipped with ten Pt100 thermal sensors, five flow meters, three pressure sensors and two energy meters. Below are listed some details on each sensor.

(a)

(b)

(c)

(d)

Fig. 2.22. Overview of the experimental setup components: (a) the ETCs solar field, (b) the hybrid chiller-dry cooler setup, (c) the solar station and the storage tank and (d) the hydronic ducted fan coil unit

I. Resistance thermometers Pt100

In Zeosol setup, Pt100 sensors were installed in several locations within the system, for a complete monitoring of the system's operation and at the same time ensuring an accurate estimation of the system's performance.

Table 2.12. Technical specifications of the Pt100 temperature sensors used in the installation

Model	**Uteco SUR/09**
Measuring insert	Stainless steel 14751 ø6mm
DIN EN 60751 Class	A
Output	4-20 mA
Medium temperature (min/max)	0 / 120 °C
Accuracy	0.1 °C

II. Flow meter

As shown in Fig. 2.21(a), system separation was realized in both high and low temperature circuits of the hybrid chiller. Hence, in order to properly construct the energy balances, additional flow meters were required for each respective circuit.

Table 2.13. Technical specifications of the flow meters used in the installation

Model	**BELIMO FM040R-SZ**
Maximum flow rate	3.0 l/s
Pressure drop at maximum flow rate (FS)	7 kPa at max flowrate
Output	0.5-10 V
Medium temperature (min/max)	-20 / 120 °C
Measuring accuracy flow	±1.2% of FS (0...20% FS) ±6% of measured value (20...100% FS)
Min. flow measurement	1% of FS
Ambient temperature	0-50 °C

III. Pressure sensors

In a similar manner to all additional sensors, the existence of several subcircuits dictated the installation of one pressure sensor per case for the monitoring of the operation and the construction of the energy balances.

Table 2.14. Technical specifications of the pressure sensors used in the installation

Model	**Belimo 22WP-135**
Measuring range	0-6 bar
Output	4-20 mA
Overpressure range	20 bar
Accuracy pressure	±0.5% @ 25°C
Total errors	±2.0% @-40°C / ±2.0% @ 105°C:
Medium temperature (min/max)	-40 / 105 °C

IV. Energy meters

Two energy meters were installed in the setup to accurately measure the electrical consumptions of the dry cooler, the adsorption chiller circulators, the backup heat pump and the miscellaneous electrical consumptions in the installation. This measurement, allows for an accurate estimation of the backup heat pump's coefficient of performance (COP) and the energy efficiency ratio (EER) of the overall system.

Table 2.15. Technical specifications of the energy meters used in the installation

Model	**DUCA LCD96 485-IO**
Measuring accuracy voltage/current	±0.5%
Measuring accuracy active power	±1.0%
Output	4-20 A

2.3.2 Experimental measuring and modeling of separate components

The preliminary measuring of the proposed system was divided in three parts: (a) the experimental assessment of the solar collectors and the storage tank, (b) the performance testing of the hybrid adsorption chiller and (c) the dry cooler along with all the involved auxiliary equipment (e.g. circulations pumps).

The solar collectors used in the system, as already discussed in section 2.1.2, were heat pipe evacuated tube collectors, manufactured by AKOTEC specifically for ZEOSOL system and being able to operate efficiently between 65-95 °C. The collectors were tested by a certified institute according to ISO 9806. The collector efficiency, shown in Fig. 2.23, is calculated based on equation (2.1), while the corresponding coefficients are listed in Table 2.1 for the case of ETCs. The reason for selecting these collectors as the representative type of evacuated tube type collectors was based on the fact that analytical and up-to-date data was provided for the costs and the life-cycle inventory, thus in combination with the experimental performance data available, it would allow for accurate calculations on ETC driven systems.

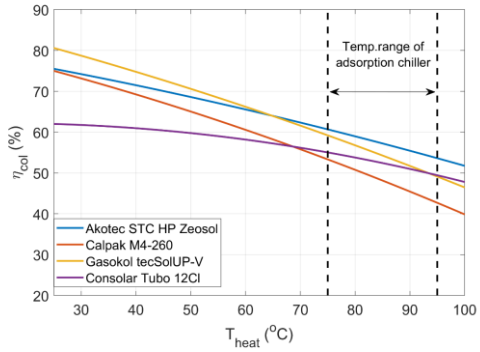

Fig. 2.23. Performance curve of the developed solar collectors for ZEOSOL system (blue line) in comparison to other commercial solar collectors

The total electric power consumption of the system is a crucial metric for the system's overall performance. For its determination, apart from the electrical consumption of the dry cooler, $\dot{W}_{el,dc}$, are contributing also (i) the power consumption of the heat pump's compressor, $\dot{W}_{el,com}$, and (ii) the electrical consumption for the six pumps/circulators of the system, $\sum \dot{W}_{el,pumps}$. The total electrical power consumption is calculated as follows:

$$\dot{W}_{el,tot} = \dot{W}_{el,com} + \dot{W}_{el,dc} + \sum \dot{W}_{el,pumps} \qquad (2.16)$$

The polynomial fittings for the power consumption of the HT, MT and LT pumps were based on the experimental data found at [105]. Moreover, the fan coils pump (fc pump) is identical to the LT pump, thus the same power consumption profile was realized. The solar collector's circuit pump, installed at the solar station of the setup, is a Grundfos pump, model UPM3 Solar

25-145. On the other hand, the storage -intermediate hot circuit- pump (HT int pump) is a pump from the same manufacturer, model UPS2 15-50. The electric power consumption curves of all aforementioned pumps are shown in Fig. 2.24.

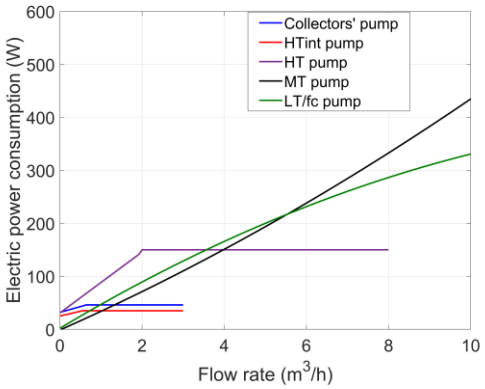

Fig. 2.24. Electric consumption of the different used pumps/circulators

As the dry cooler was directly connected with an energy meter and the frequencies of the fans were controlled and measured by the hybrid chiller's control and data acquisition module, relevant data was collected during the different tests of the Zeosol test rig and a dedicated 4th degree polynomial fitting (R^2=0.995) was developed for the estimation of the electric power consumption for various fan frequencies, as shown in Fig. 2.25(a).

$$\dot{W}_{el,dc} = -4.5687 \cdot 10^{-5} f_{fan}^4 + 8.4198 \cdot 10^{-3} f_{fan}^3 - 0.37218 f_{fan}^2 + 6.868 f_{fan} - 0.10516 \quad (2.17)$$

With respect to the heat transfer performance of the dry cooler, as practically an air heat exchanger, the heat rejection capacity is mainly a function of the fans' frequency and the temperature difference between the inlet stream of the medium temperature (MT) circuit at the dry cooler and the ambient temperature. Fig. 2.25(b) presents two case studies, with 8 K and 5 K temperature difference. The rejected heat in every data point, $\dot{Q}_{MT}$, was estimated based on heat balance of the MT circuit, while the corresponding error was estimated by applying the equations (2.6)-(2.10):

$$\dot{Q}_{MT} = \bar{\rho}_{MT}\, \dot{V}_{MT} (h_{MT,i} - h_{MT,o}) \quad (2.18)$$

As expected, the performance of the dry cooler is proportional to the temperature difference for a given fan frequency, which highlights the strong dependence in the dry cooler's performance and as a result the entire solar sorption setup in the ambient conditions, a point which will be experimentally evaluated in the following section with the experimental results of the entire Zeosol system.

With respect to the developed simulation model, polynomial fittings were constructed based on the experimental data per given temperature difference, in order to estimate the required fan frequency to achieve the desired heat rejection. In all cases, second order polynomials were used as they achieved sufficient values for the coefficient of determination. For instance, for the cases shown in Fig. 2.25(b), for a temperature difference of 5 K the R^2 was equal to 0.9942, while for ΔT=8 K the R^2 was equal to 0.9961. W

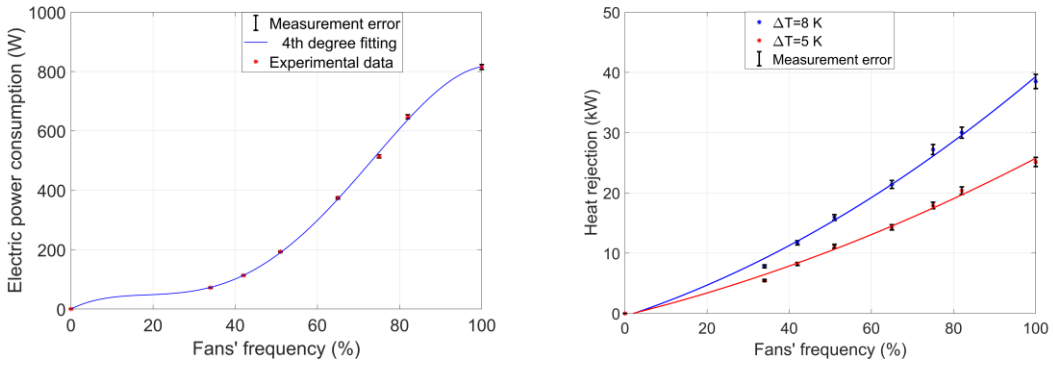

(a) *(b)*

Fig. 2.25. (a) Measured electric consumption and data fitting of the dry cooler for different loads

The electric reversible heat pump of the Zeosol system was designed and manufactured as a part of the collaboration of Fahrenheit GmbH and CNR ITAE. As the reversible heat pump is a conventional component, implemented in the system for the peak loads and the cases with insufficient solar irradiance, its characterization was conducted in separate experiments, in which the adsorption chiller was turned off, and under various ambient conditions to allow for broader working range of the performance map. Each measurement was conducted after the heat pump reached steady state conditions, based on the predefined by the user setpoint for the cooling and heating experiments, respectively. The main performance indicator, used for these experiments, was the COP for cooling and heating, which were defined as shown below, per case:

$$\mathrm{COP}_{\mathrm{cool}} = \frac{\dot{Q}_{cool}}{\dot{W}_{el}} = \frac{\dot{Q}_{evap}}{\dot{W}_{el}} \tag{2.19}$$

$$\mathrm{COP}_{heat} = \frac{\dot{Q}_{heat}}{\dot{W}_{el}} = \frac{\dot{Q}_{cond}}{\dot{W}_{el}} \tag{2.20}$$

As the adsorption chiller was turned off, the energy meter, connected to the hybrid chiller, was solely measuring the power consumption of the heat pump. On the other hand, the cooling/ heating outputs, per case, were measured by applying a heat balance of the fan coils circuit, based on equation (2.18), which in the case of cooling was connected to the evaporator of the reversible heat pump and on heating mode was connected to the condenser. In order to estimate, the exergy efficiency of the reversible heat pump, the COP of the corresponding Carnot cycle for the used temperatures of each measurement point has also to be estimated, as shown below for the cases of cooling and heating operation, respectively:

$$\mathrm{COP}_{\mathrm{Carnot,cool}} = \frac{T_{av,C}}{T_{av,H} - T_{av,C}} \tag{2.21}$$

$$\eta_{ex,\mathrm{cool}} = \frac{\mathrm{COP}_{\mathrm{cool}}}{\mathrm{COP}_{\mathrm{Carnot,cool}}} \tag{2.22}$$

$$\mathrm{COP}_{\mathrm{Carnot},heat} = \frac{T_{av,H}}{T_{av,H} - T_{av,C}} \tag{2.23}$$

$$\eta_{ex,heat} = \frac{\mathrm{COP}_{heat}}{\mathrm{COP}_{\mathrm{Carnot},heat}} \tag{2.24}$$

Finally, the error for the calculated performance indicators, in a similar manner to equations (2.6)-(2.11), was calculated with the use of the following expressions:

$$dCOP_{cool} = \sqrt{d\dot{Q}_{cool}^2 \cdot \frac{\partial^2 COP}{\partial(\dot{W}_{el})^2}\bigg|_{\dot{Q}_{cool}} + d(\dot{W}_{el})^2 \cdot \frac{\partial^2 \mathrm{COP}}{\partial(\dot{Q}_{cool})^2}\bigg|_{\dot{W}_{el}}} \quad (2.25)$$

$$d\mathrm{COP}_{\mathrm{Carnot}} = \sqrt{dT_{av,c}^2 \cdot \frac{\partial^2 \mathrm{COP}_{\mathrm{Carnot}}}{\partial(T_{av,H})^2}\bigg|_{T_{av,C}} + d(T_{av,H})^2 \cdot \frac{\partial^2 \mathrm{COP}_{\mathrm{Carnot}}}{\partial(T_{av,C})^2}\bigg|_{T_{av,H}}} \quad (2.26)$$

$$d\eta_{ex} = \sqrt{dCOP^2 \cdot \frac{\partial^2 \eta_{ex}}{\partial(\mathrm{COP}_{\mathrm{Carnot}})^2}\bigg|_{COP} + d(\mathrm{COP}_{\mathrm{Carnot}})^2 \cdot \frac{\partial^2 \eta_{ex}}{\partial(COP)^2}\bigg|_{\mathrm{COP}_{\mathrm{Carnot}}}} \quad (2.27)$$

The model of the heat pump, which was used in the relevant studies presented in following Chapters of this dissertation, was a spline interpolation based on the experimental data collected for the cooling/heating output of the heat pump and the corresponding COP as a function of the temperature lift, difference between average temperatures of the secondary streams of the condenser and evaporator. Based on the estimated COP, and by applying equations (2.21)-(2.24), the exergy efficiency was also estimated. In Fig. 2.26, are shown the experimental results and the corresponding data fitting curves on cooling mode. As expected, there is a decreasing trend with the increase of the temperature lift, as a result of the severe conditions under which the heat pump is operating. On the other hand, for a temperature lift of less than 10 K, the cooling capacity was above 30 kW (± 1.01 kW) and the corresponding COP was exceeding 7, while the exergy efficiency was approximately 32%. With respect to the developed model, as it is based on spline interpolation, the simulations using this model had certain control loops to ensure that the function is not called outside the measurements' region.

Fig. 2.27 presents the respective performance results of the heating mode. As shown, the heating capacity was as high as 39.0±1.2 kW for a temperature lift of 7.2 K and the corresponding COP was equal to 8.95. Similarly to cooling mode, by increasing the temperature lift there is a decrease in the heat pump's performance.

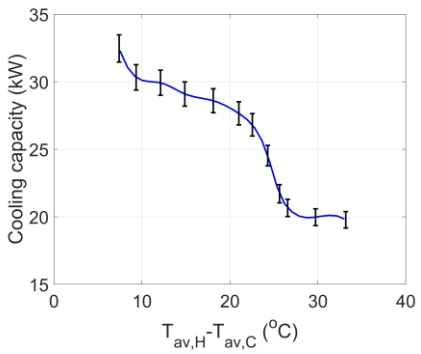

(a)

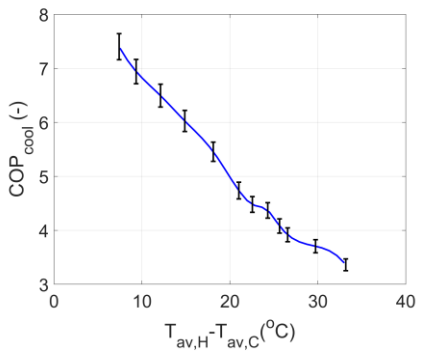

(b)

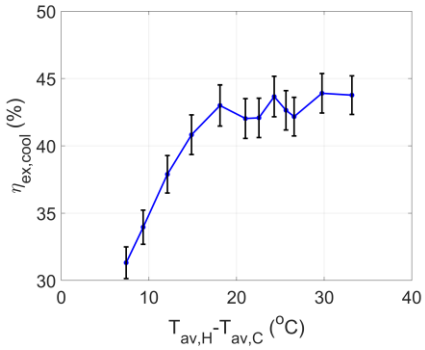

(c)

Fig. 2.26. Performance maps of the tested reversible heat pump on cooling mode with varying temperature lift

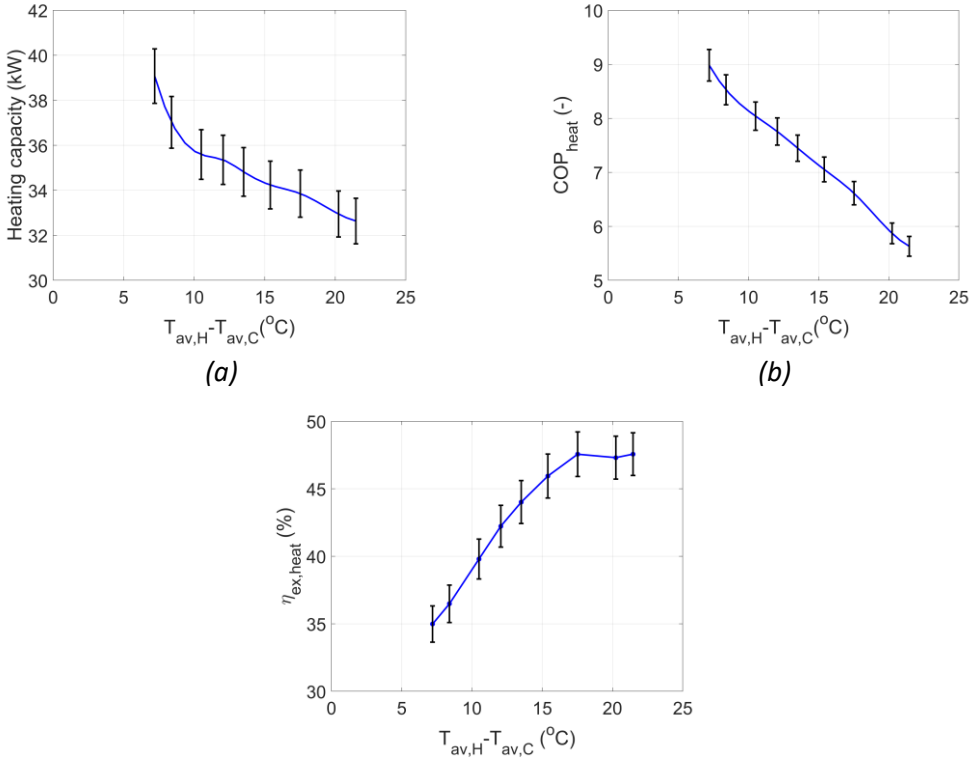

(a) *(b)*

(c)

Fig. 2.27. Performance maps of the tested reversible heat pump on heating mode with varying temperature lift

Finally, the adsorption chiller was developed by Fahrenheit GmbH and was sent at NTUA after being coupled and tested along with the reversible heat pump. Similar wise to the reversible heat pump characterization, the adsorption chiller was tested for a number of different sets of HT, MT and LT temperatures and the corresponding performance maps were developed. Each point of measurement was collected, once the chiller reached steady state conditions, which corresponded to a same profile for at least three consecutive adsorption cycles). The results of the cooling output and the power consumption for the case of LT setpoint of 15 °C on cooling mode are presented in Fig. 2.28. A cubic spline interpolation was applied for the performance model of the adsorption chiller, with the corresponding fitting curves for the presented case to be also shown in Fig. 2.28. As expected, the increase in the MT circuit inlet

temperature reduces the performance of the adsorption chiller, which comes in agreement with relevant literature [105, 106], while a similar effect is observed with the decrease in the HT circuit inlet temperature. On the other hand, for the minimum measured MT circuit inlet temperature (approximately 25.8 °C), the cooling capacity is maximized for heat source temperatures of 80-90 °C, with a maximum reported value of 14.41±0.58 kW.

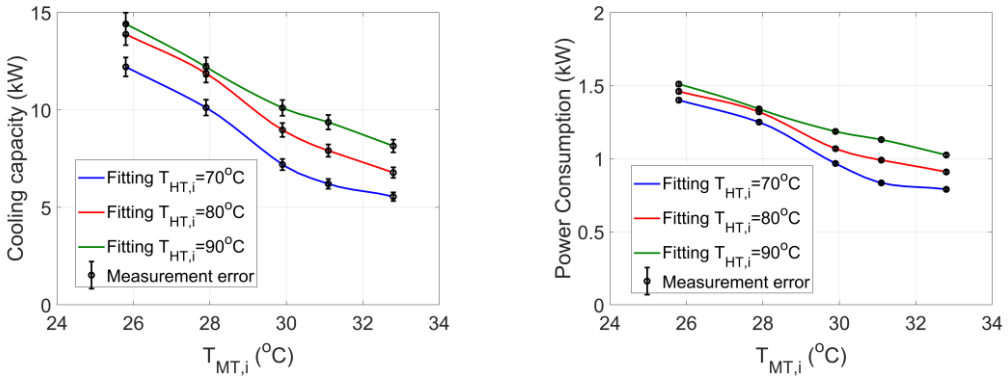

(a) *(b)*

Fig. 2.28. Cooling capacity and power consumption of the adsorption chiller module for a number of different HT and MT temperatures ($T_{LT,o}$=15 °C)

The main performance indicators for the sorption chiller and the overall system are the coefficient of performance (COP) and the energy efficiency ratio (EER). The COP for the adsorption chiller is defined by the following equation:

$$COP_{ads,cool} = \frac{\dot{Q}_{LT}}{\dot{Q}_{HT}} \tag{2.28}$$

With HT referring to the driving heat supplied to adsorption chiller and LT to the low temperature stream which provides the cooling effect. On the other hand, the EER is defined as the ratio between the cooling capacity $\dot{Q}_{LT}$ and the total electric power consumption of the adsorption module, $\dot{W}_{el,ads}$:

$$EER_{cool} = \frac{\dot{Q}_{LT}}{\dot{W}_{el,ads}} \tag{2.29}$$

At this point, is crucial to mention that current evaluation of EER, refers entirely to the adsorption chiller module and, therefore, the consumption of the dry cooler was excluded.
On the other hand, to estimate the exergy efficiency for the adsorption cycle, at first the Carnot COP has to be estimated. Based on [107-109], the Carnot coefficient of performance for an adsorption cycle is calculated by the following expression:

$$\mathrm{COP}_{\mathrm{ads,Carnot,cool}} = \frac{\theta_{evap}(\theta_{des} - \theta_{cond})}{\theta_{des}(\theta_{cond} - \theta_{evap})} \tag{2.30}$$

$$\eta_{ex,\mathrm{cool}} = \frac{\mathrm{COP}_{\mathrm{ads,cool}}}{\mathrm{COP}_{\mathrm{ads,Carnot,cool}}} \tag{2.31}$$

The term θ in equation (2.30) refers to the corresponding average temperatures in degrees Celsius. Eventually, in order to present the aforementioned performance indicators based on

the adsorption chiller characterization tests, the error propagation in the COP was estimated by equation (2.32).

$$dCOP_{ads,cool} = \sqrt{d\dot{Q}_{LT}^2 \cdot \left.\frac{\partial^2 COP}{\partial(\dot{Q}_{HT})^2}\right|_{\dot{Q}_{LT}} + d(\dot{Q}_{HT})^2 \cdot \left.\frac{\partial^2 \mathrm{COP}}{\partial(\dot{Q}_{LT})^2}\right|_{\dot{Q}_{HT}}} \quad (2.32)$$

$$dEER_{cool} = \sqrt{d\dot{Q}_{LT}^2 \cdot \left.\frac{\partial^2 EER}{\partial(\dot{W}_{el,ads})^2}\right|_{\dot{Q}_{LT}} + d(\dot{W}_{el})^2 \cdot \left.\frac{\partial^2 EER}{\partial(\dot{Q}_{LT})^2}\right|_{\dot{W}_{el,ads}}} \quad (2.33)$$

On the other hand, the exergy efficiency's error was estimated by equation (2.27). The results for the three performance indicators are shown in Fig. 2.29, for the case of a LT setpoint of 15 °C. In fact, the results reveal a satisfactory performance of the adsorption chiller, given the reported COPs for zeolite-based adsorption cooling [110-112]. The maximum reported COP, shown in Fig. 2.29(a), was approximately 0.53 (±0.03). On the ither hand, EER reveals one of the main advantages of adsorption technology, with values exceeding 9. In both COP and EER, the profiles follow the trend of the cooling capacity, with a performance deterioration with increasing MT circuit inlet temperature. On the contrary, the exergy efficiency, shown in Fig. 2.29(c), has a reverse behavior, with an improved efficiency with the increase in the MT circuit temperature. This is justified by the sharp decrease in Carnot's COP for higher levels of MT circuit temperatures, showing that the adsorption module tends to achieve as high exergy efficiencies as more than 80%.

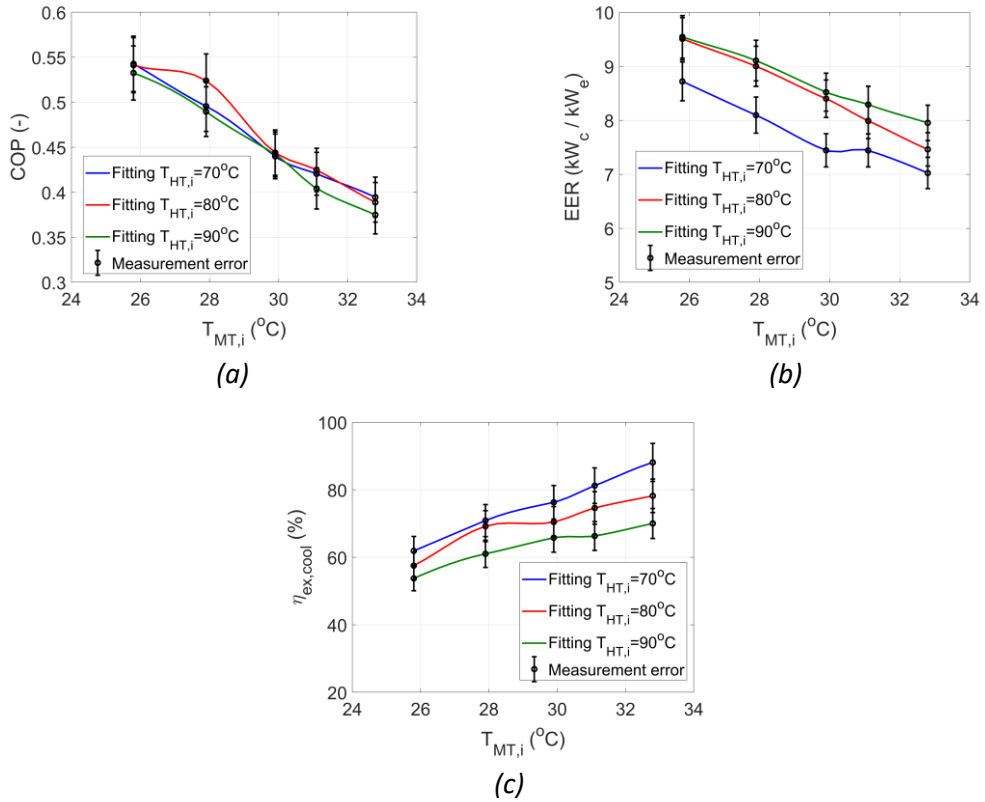

Fig. 2.29. Performance indicators of the adsorption chiller module (a) COP, (b) EER and (c) exergy efficiency for a number of different HT and MT temperatures ($T_{LT,o}$=15 °C)

The aforementioned analysis, presented the adsorption module results only in cooling mode, as the setup tested at the Laboratory of Steam Boilers and Thermal Plants was still under developmental stage and the adsorption heating mode was not realized. Nonetheless, as heating mode is practically realized by the utilization of the MT heat rejection, its performance can be easily estimated, by applying the adsorption simulation model for the estimation of the cooling capacity, the COP and the power consumption, since the rejected heat is approximately equal to the sum of the driving heat of the HT circuit and the cooling production at the LT circuit:

$$\dot{Q}_{MT} \approx \dot{Q}_{LT} + \dot{Q}_{HT} \tag{2.34}$$

$$\mathrm{COP}_{ads,heat} = \frac{\dot{Q}_{heat}}{\dot{Q}_{cons}} = \frac{\dot{Q}_{MT}}{\dot{Q}_{HT}} \tag{2.35}$$

$$\mathrm{COP}_{\mathrm{ads,Carnot,heat}} = 1 + \mathrm{COP}_{\mathrm{ads,Carnot,cool}} \tag{2.36}$$

$$\eta_{ex,\mathrm{heat}} = \frac{\mathrm{COP}_{\mathrm{ads,heat}}}{\mathrm{COP}_{\mathrm{ads,Carnot,heat}}} \tag{2.37}$$

2.3.3 Experimental characterization of Zeosol hybrid system

The following section discussed the experimental results of the developed setup operating solely with the adsorption chiller. The analysis has also been published in [104], however, for the needs of this dissertation some of the figures were modified in accordance to the previous presentations of results. The presented experiments were conducted in the summer-autumn of 2019.

Fig. 2.30 shows the ambient conditions and the temperature trends in a typical summer week. In particular Fig. 2.30(a) presents an overview of the ambient conditions, with respect to the temperature and the solar irradiance for the week of the measurements. As shown in Fig. 2.30(a), the solar irradiance in the evaluated week –second week of August 2019- is at rather lower than the average peak values for the summer of the typical year in Athens, without exceeding 1000 W/m². On the other hand, the simultaneous higher ambient temperatures that occurred in the investigated days resulted in operating all the components at higher temperature levels, which decreased their efficiency, as already discussed in the standalone experiments of the main components. Fig. 2.30(b) and (c) present the temperature profiles for the solar collectors-storage tank module and for the adsorption chiller secondary streams, respectively. The adsorption chiller was set to start its operation at 65 °C for the HT in stream, resulting -in combination with the available solar irradiance- in operating only a few hours per day close to the solar noon. Despite the less optimal conditions, the system is able to cool down the water to the target 15 °C, which is the setpoint for the low temperature circuit, even though the driving temperature was less than 80 °C on all cases; however, at the expense of lower overall performance. The profiles of Fig. 2.30 (c) outline the necessity for a modification of the control strategy for the involved circulating pumps so that higher driving temperatures are obtained ensuring maximum efficiency of the chiller. At this point, it has to be highlighted that Fig. 2.30 refers to adsorption only mode, thus at the absence of driving solar heat the system is off, which results in no operation at night.

Fig. 2.31 presents the performance results for the entire ZEOSOL system, on adsorption-only cooling mode, based on the definitions of eq. (2.28)-(2.29) in a typical summer day. Fig. 2.31(a) shows the cooling power production of the chiller during the investigated week and the total electrical power consumption, as defined by eq.(2.16). As shown in Fig. 2.31 (a) the maximum

obtained cooling power output is around 7 ±0.3 kW, which is approximately 45% of the nominal chiller's cooling capacity and is mainly attributed to the lower driving temperatures during the period of the measurements. On the other hand, the electrical power consumption is significantly low, with a maximum of approximately 1 kW, mainly due to the operation of the dry cooler, which accounts for more than 60% of the total power consumption of the system, on adsorption-only mode. The corresponding performance indicators are presented in Fig. 2.31(b). The maximum obtained thermal COP is approximately 0.535 (±0.030), for a maximum reported driving temperature of 79 °C, while the corresponding maximum EER was as high as 7.4 (±0.8), with an average operation at approximately 5.8 (±0.6). Similarly to Fig. 2.30, both the cooling production as well as the EER of the system, highlight the necessity for further optimization of the system's control and operational strategy to both maximize cooling output at a reduced specific power consumption.

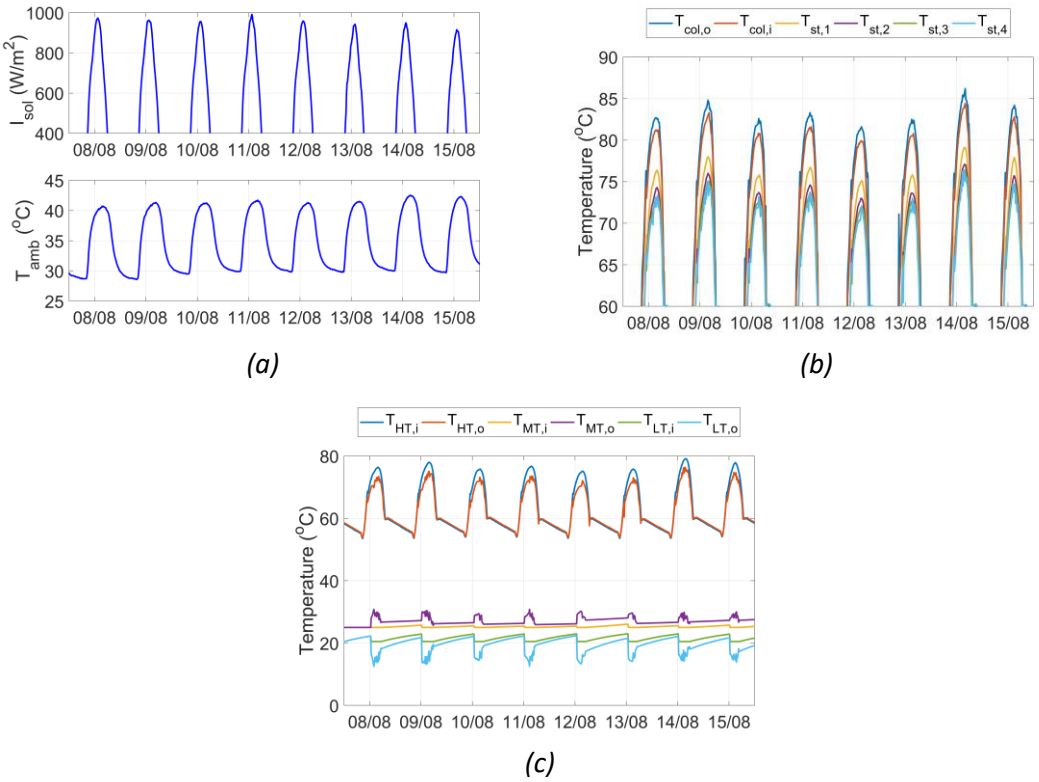

Fig. 2.30. (a) Ambient conditions at the period of the experiments (b) experimental results with respect to the solar sub-circuit temperatures and (c) with respect to the chiller's secondary streams' temperatures

Fig. 2.32-Fig. 2.36 present, instead, the comparison of the performance results for the ZEOSOL system, in hot summer days and in cloudy days (end of September).

As shown in Fig. 2.33(a) the solar field is capable to provide hot water at good thermal level when the solar radiation ranges between 800 and 1000 W/m² while the pump of the solar loop continuously switches off and on to preserve water stratification in the storage tank in cloudy days or when the solar radiation drops below 800 W/m² (Fig. 2.33(b)).

As shown in Fig. 2.34, the adsorption chiller can produce cold water at 15 °C and release the process heat at 25-30 °C both in a hot day and in cloudy day; however, cold production is not continuous with a lower solar radiation thus demonstrating the need of the operation of the electrical back-up unit not only to cover the remaining loads but also allow for sufficient re-

charging of the storage tank for more efficient operation of the adsorption module upon resume of its operation.

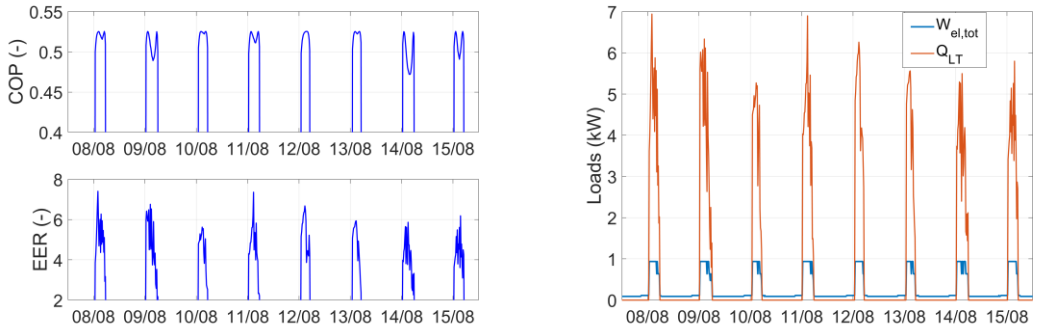

(a) *(b)*

Fig. 2.31. Performance results of proposed system prototype with respect to (a) the produced cooling output and the respective electrical consumption and (b) the corresponding COP and EER values.

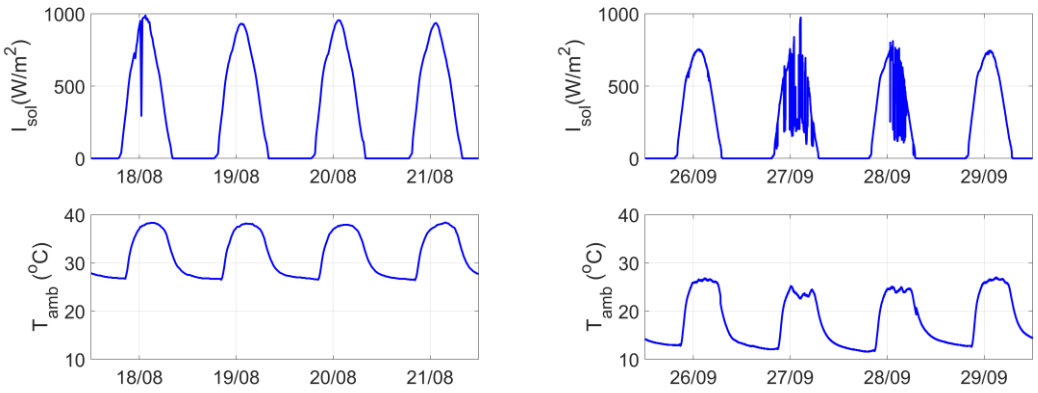

(a) *(b)*

Fig. 2.32. Ambient conditions (a) at the tested hot summer days and (b) at the tested cloudy days

Finally, as depicted in Fig. 2.35 the maximum obtained cooling power output is around 6 kW in hot day while it ranges between 2 and 7 kW when it is cloudy, due to the lower driving temperatures. During the same measurements, the electrical power consumption is significantly low, ranging between 50 (electronic consumption) and 1000 W (operation of the fans the dry cooler). Hence, the maximum obtained thermal COP, as shown in Fig. 2.36, is approximately 0.53 (±0.03) for driving temperature of 80 °C, while the corresponding average EER is approximately 5-6 (±0.6). In cloudy days, there can be observed some spikes of maximum values for the cooling production and, thus, the EER, however, these are most related to the start-up of the chiller and on average the performance tends to be lower due to the lower driving temperatures by the insufficiently charged solar field. In both cases is also shown that the driving temperatures were ranging, on most times, between 70-75 °C, which pointed out the need for additional solar heat to allow for operation at higher, and more efficient for the adsorption chiller, temperatures.

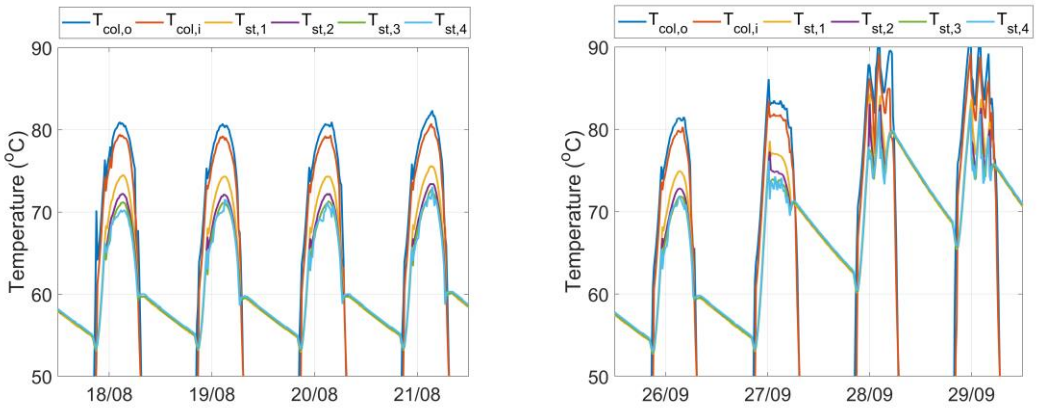

(a) *(b)*

Fig. 2.33. Experimental results with respect to the solar sub-circuit temperatures (a) at the tested hot summer days and (b) at the tested cloudy days

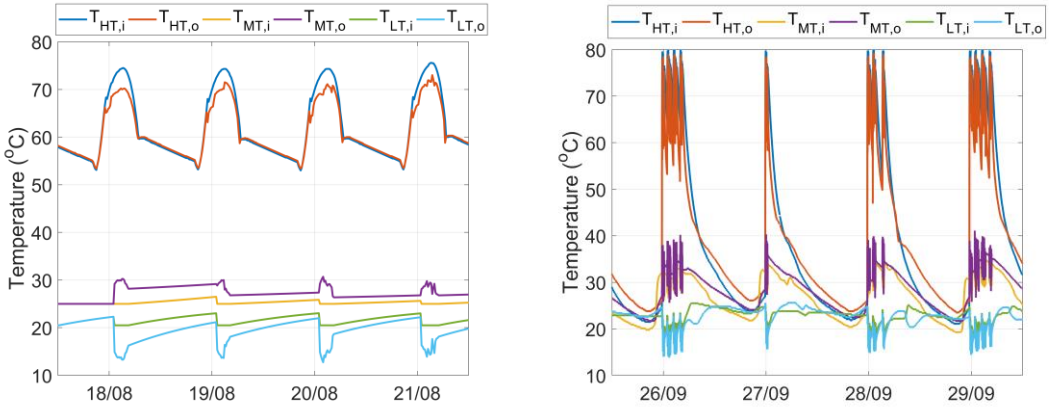

(a) *(b)*

Fig. 2.34. Experimental results with respect to the temperatures of secondary chiller's streams (a) at the tested hot summer days and (b) at the tested cloudy days

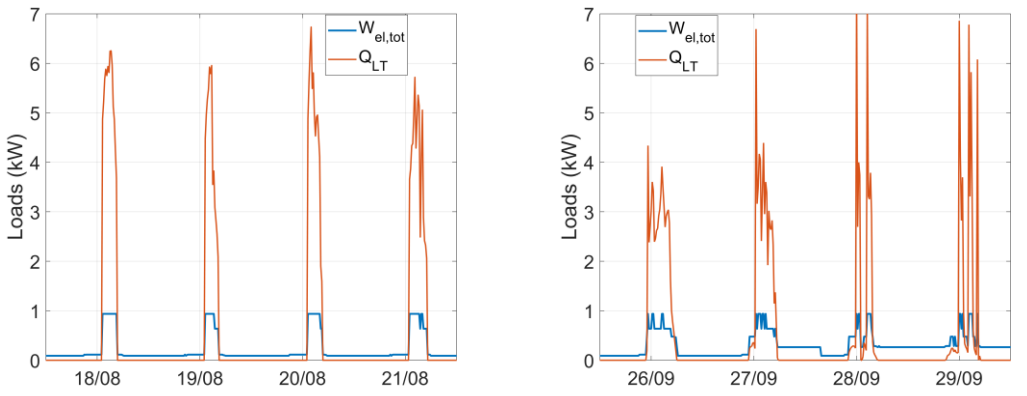

(a) *(b)*

Fig. 2.35. The produced cooling output and the respective electrical consumption a) in hot summer days; b) in cloudy days.

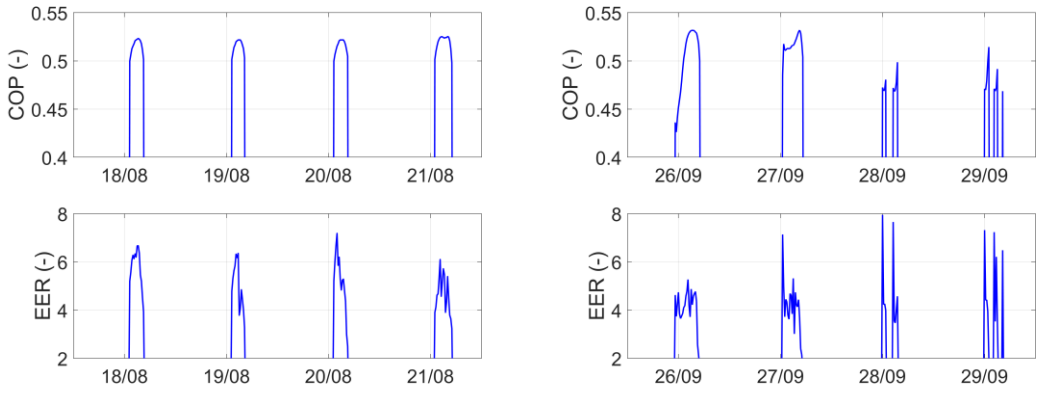

(a) *(b)*

Fig. 2.36. COP and EER results a) in hot summer days; b) in cloudy days.

2.3.4 Conclusions on Zeosol system experiments and modelling procedure

In section 2.3 were discussed the modelling of solar driven adsorption cooling/heating components and the models' validation based on the experimental results of Zeosol test rig, along with an experimental characterization of the Zeosol system itself.

With respect to the modelling, the dry cooler and the system's circulators, which are the main contributors in the total power consumption of the system -when the electric heat pump is off-, can be accurately modelled with polynomial fittings of their respective power consumption as a function of a design variable per case. On the other hand, for an accurate model of the off-design (steady state) performance of the electric heat pump and the adsorption chiller, were required spline interpolation models as a function of the working/target temperatures of each cycle in order to achieve values for the R^2 higher than 0.98.

As mentioned in section 2.3.1, the adsorption module was designed only for cooling mode in the evaluated test rig and therefore the Zeosol experiments were focused on the solar driven adsorption only cooling. The experimental analysis of the Zeosol chiller revealed that the system despite non optimal conditions (smaller solar irradiance, high ambient temperatures) operated at a satisfactory level, with a maximum COP of 0.535. The developed system was proven to decrease significantly the electrical power consumption, achieving a maximum EER of 7.4 (±0.8), with more than 60% of the total consumption coming from the system's dry cooler. In this perspective, and given the performance/design limitations of the considered adsorption working pairs, the main aspects for improvement were identified to be the consumption of the adsorption module's circulators and the system's control. On the contrary, on design level the performance of the adsorption module revealed that additional solar heat is required to ensure higher temperature operation, which as consequence can lead to higher overall performance. This can be achieved in two ways, either increase the solar field by approximately 10% (4 m^2) or decrease the storage tank's capacity, since much of the harvested solar energy is used to heat the lower levels of the 1 m^3 and any storage benefit is eventually lost by the induced lower COPs of the adsorption chiller, due to the lower driving temperatures of the storage feed to the chiller.

2.4 Solar adsorption cooling – The Wassermod2 project

2.4.1 Test rig description

The Wassermod2 project is a project closely related to the previously described Zeosol project, which finished in February 2020. On the contrary, the main experiments of Wassermod2 project started in summer 2020. Focus of Wassermod2 project was the development of a new sorption chiller based on novel zeolite-based sorbent materials. The developed chiller, manufactured also by Fahrenheit GmbH, was based on SAPO-34 zeolite-water working pair and had similar cooling capacity to the Zeosol adsorption chiller. The design philosophy of the chiller was similar to Zeosol's module with a number of modifications on the control and the selection of some components (adaptations in the adsorption chambers and introduction of lower consumption circulators), based on the operational experience gained from Zeosol. As the project was chiller-focused, the new chiller was installed in parallel to the Zeosol hybrid chiller and was driven by the same solar field. As a main challenge faced in Zeosol experiments was the insufficient driving heat in spring, as well as in very hot summer days, on which the chiller worked by definition on lower COPs, a gas boiler was installed in line with the storage tank to provide also some tests solely on the chiller's performance.

Moreover, to allow for a proper evaluation of the chiller's adequacy on real-time conditions, a number of fan coils was installed in first floor offices of the laboratory's building. Therefore, during early spring or late-autumn, when no actual cooling production is needed at the offices, the cooling output from the chiller was switched to the test room used for Zeosol's tests, while during the actual cooling period, all the cooling production from the Wassermod2 chiller was delivered to the offices based on the needs of each office. Each office was equipped with a room-temperature controller, so that each user is able to adapt the needs of the room, accordingly. Moreover, for freezing protection on cold days, both for the dry cooler and chiller itself, a residential electric boiler was installed in the system, which ensured that the respective circuits would always be above 10 °C. An overview of the solar cooling/heating system, with the integrated Wassermod2 chiller and the aforementioned additions, is presented in Fig. 2.37.

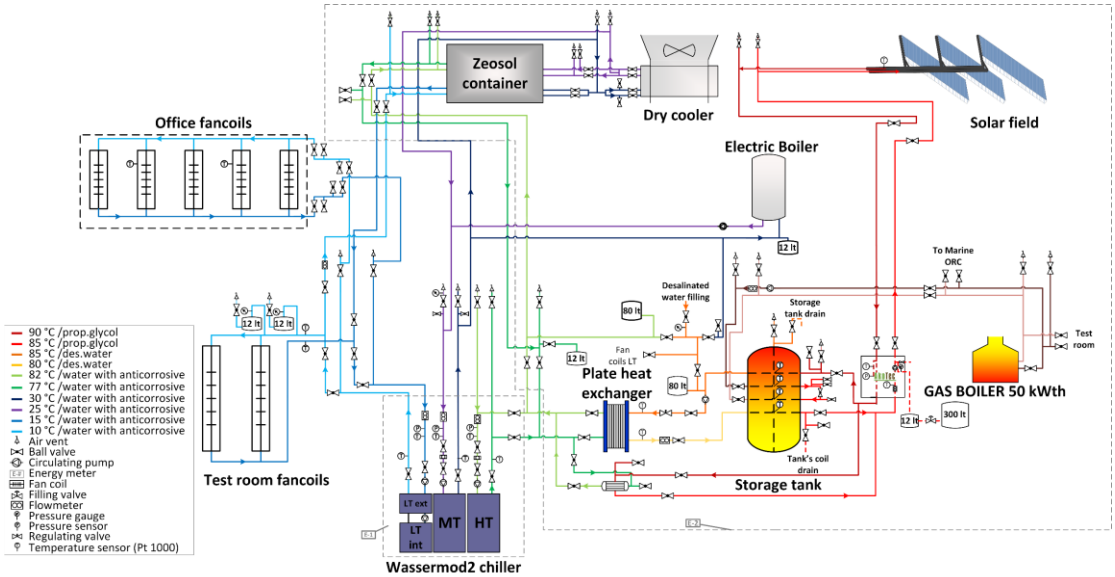

Fig. 2.37. Schematic of the complete solar cooling/heating setup of the system.

Similarly to the main solar components, a number of the already presented instrumentation was used for the experimental procedure of Wassermod2. Additional thermal resistances, pressure sensors and flow meters were installed at pipelines close to the connections of the chiller. Eventually, the total used measuring devices, apart from the weather station for the ambient conditions, consisted of the sixteen Pt1000 thermal sensors (see data on Table 2.5), six flow meters (see data on Table 2.13), five pressure sensors (see data on Table 2.14) and two energy meters (see data on Table 2.15).

2.4.2 Off-design modelling and experimental validation of plate heat exchanger

Within the context of the Wassermod2 experiments and by taking advantage of the additional measuring equipment installed in the test rig, an experimental was conducted to evaluate the off-design model of a, dedicated for single-phase heat transfer, plate heat exchanger. An overview of the test rig, is shown in Fig. 2.38.

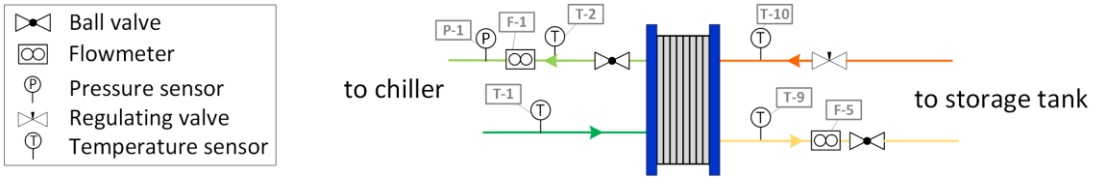

Fig. 2.38. Schematic of the measuring devices during the plate heat exchanger experiments

The off-design heat exchanger model, also presented in [62], was based on a quasi-steady state model developed on the basis of moving boundaries method [113].

The estimation of the outlet temperatures on the two streams was realized via an iterative method, until the system of equations (2.38)-(2.43) is satisfied, using as inputs the mass flowrates and the inlet temperatures of the two streams.

$$\dot{Q}_{hex} = \dot{Q}_{hex,cold} = \dot{Q}_{hex,hot} = UA\ \Delta T_{lm} \tag{2.38}$$

$$\dot{Q}_{hex,cold} = \dot{m}_{cold}(h_{cold,o} - h_{cold,i}) \tag{2.39}$$

$$\dot{Q}_{hex,hot} = \dot{m}_{hot}(h_{hot,i} - h_{hot,o}) \tag{2.40}$$

With the logarithmic mean temperature difference to be defined as [114]:

$$\Delta T_{lm} = \frac{(T_{hot,i} - T_{cold,i}) - (T_{hot,o} - T_{cold,o})}{\ln\left(\frac{T_{hot,i} - T_{cold,i}}{T_{hot,o} - T_{cold,o}}\right)} \tag{2.41}$$

On the other hand, for the estimation of the overall heat transfer coefficient, U, is used the single phase Nusselt number by the correlation proposed by Donowski and Kandlikar [115], while the friction factor is estimated from the correlation of Focke et al. [116]:

$$Nu = 0.2875\ Pr^{1/3}\ Re^{0.78} \tag{2.42}$$

$$f = 5.03 + 755/Re, \qquad 90 < Re < 400\ \ (\varphi = 60°)$$
$$f = 26.8Re^{-0.209}, \qquad 400 < Re < 16{,}000 \tag{2.43}$$

The results from the off-design model were compared against experimental data over a period of 4000 s, using a timestep of 1 s, which was the sampling rate during the experiment. An

overview of the comparison between the experimentally measured outlet temperatures and the simulation predictions is shown in Fig. 2.39(a)-(b). Fig. 2.39(c) presents also the input mass flowrates, which were used as input in the off-design model. As shown, the off-design model has an acceptable accuracy, with the relative error, presented in Fig. 2.39(d), having spikes during step-wise changes in the mass flowrate of the cold (chiller) stream, while re-converging after approximately 100-200 s. As a result, the absolute relative error was less than 5% on most cases, with even lower values during steady conditions in the mass flowrates, which leads to the conclusion that the model can be trustworthy on larger time-steps.

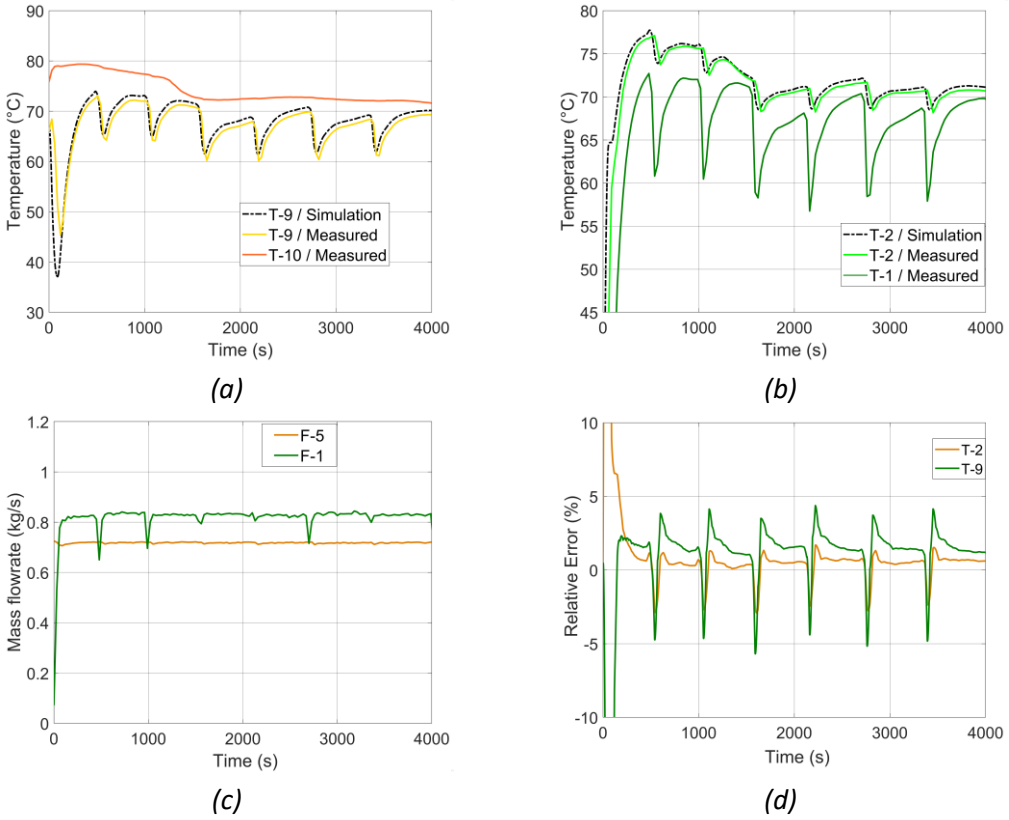

Fig. 2.39. Off-design model comparison against experimental data: (a) hot stream temperatures comparison, (b) cold stream temperatures comparison, (c) mass flowrates of the two streams, used as input in the model and (d) relative error of the model

2.4.3 Experimental characterization of Wassermod2 chiller

The experiments of the Wassermod2 chiller involved mainly the cooling periods of years 2020 and 2021. Hereby are compared the system performances for one hot summer day (24th June 2021) and one autumn day (9th September 2020) with cooling loads but also lower solar irradiances and lower ambient temperature, as shown in Fig. 2.40 (a)-(b). As already shown from Fig. 2.40 (c)-(f), in both cases is observed a decreasing profile in the temperatures, which highlights the issue of insufficient driving force, also discussed in previous section with Zeosol's experiments. In both presented days of experiments, the system is kept on for a reasonable period of time, which is obviously reduced in the autumn period, yet the insufficient solar heat results in a constant temperature decrease in the HT circuit of the chiller, with the corresponding drop in the performance, which is presented in Fig. 2.41. This effect is more visible in the summer period, owing to the high ambient temperature which causes the dry cooler, and hence the MT circuit, operate at higher temperature levels and, by definition, decrease the COP of the adsorption cycle.

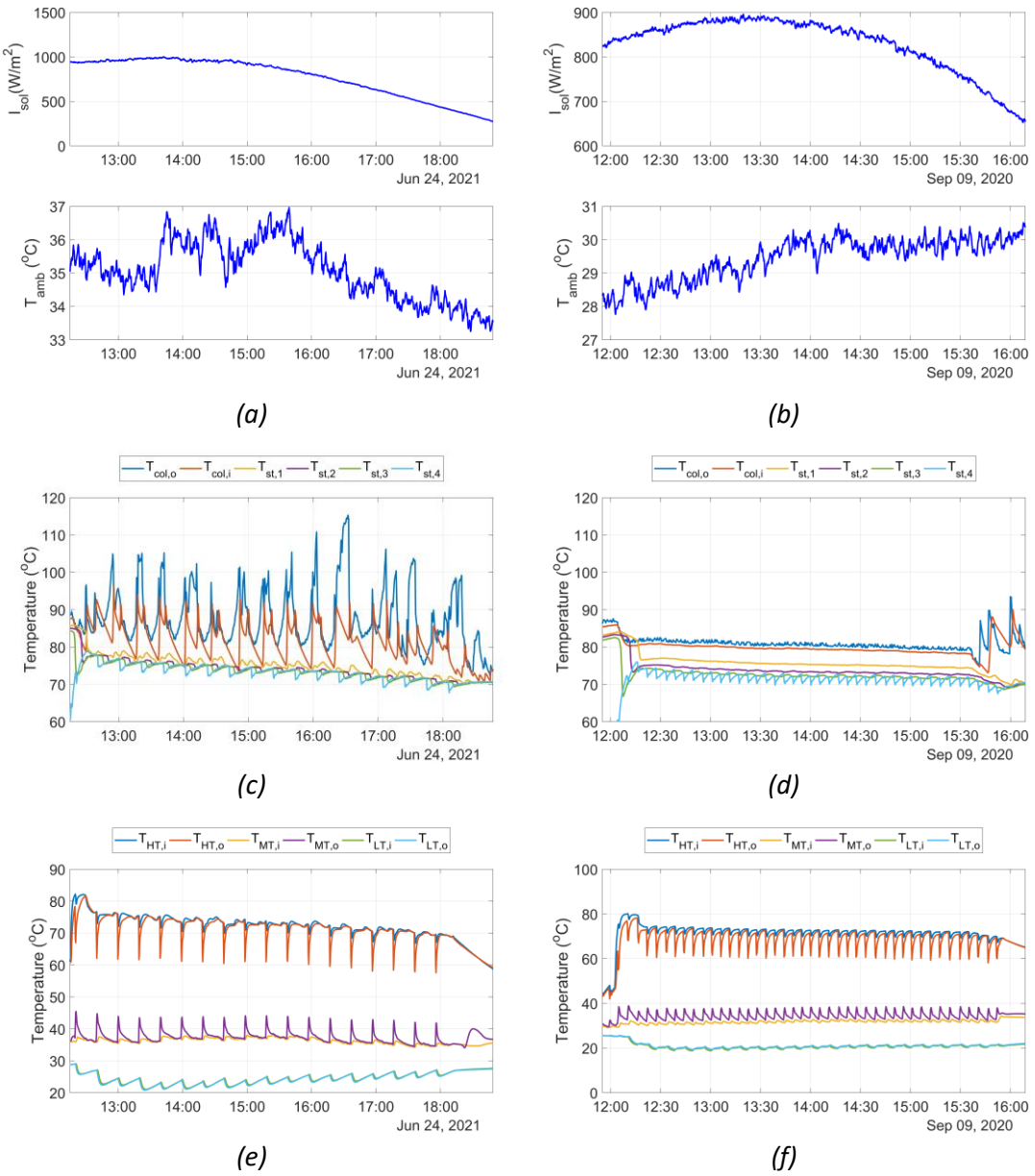

Fig. 2.40. Ambient conditions for (a) a hot summer day and (b) a day in autumn; Corresponding solar subsystem temperatures for (c) a hot summer day and (d) a day in autumn and secondary chiller circuits' temperatures for (e) a hot summer day and (f) a day in autumn

In fact, the deterioration of the HT circuit temperature profiles of Fig. 2.40 (e)-(f), results in a drop on the performance which is clearer in the cooling effect of the two measured offices. In particular for the summer day, Fig. 2.41(e), after the first minutes of operation, which caused a significant temperature drop, in both rooms' temperature tends to increase, highlighting the inadequacy of the chiller's operation to provide thermal comfort. Thermal comfort conditions are better approached in the presented autumn day, Fig. 2.41(f), as one of the offices increased the temperature setpoint, decreasing the total requested load by the chiller and therefore achieving more stable conditions on both rooms. On the other hand, as shown from the performance indicators of the Fig. 2.41(d), the lower irradiance and the relatively high ambient temperature for the period, resulted in relatively low performance with the average

EER to be less than 4, while the corresponding value for the tested summer day, reached instantaneous EER values as high as 11, as shown in Fig. 2.41(c).

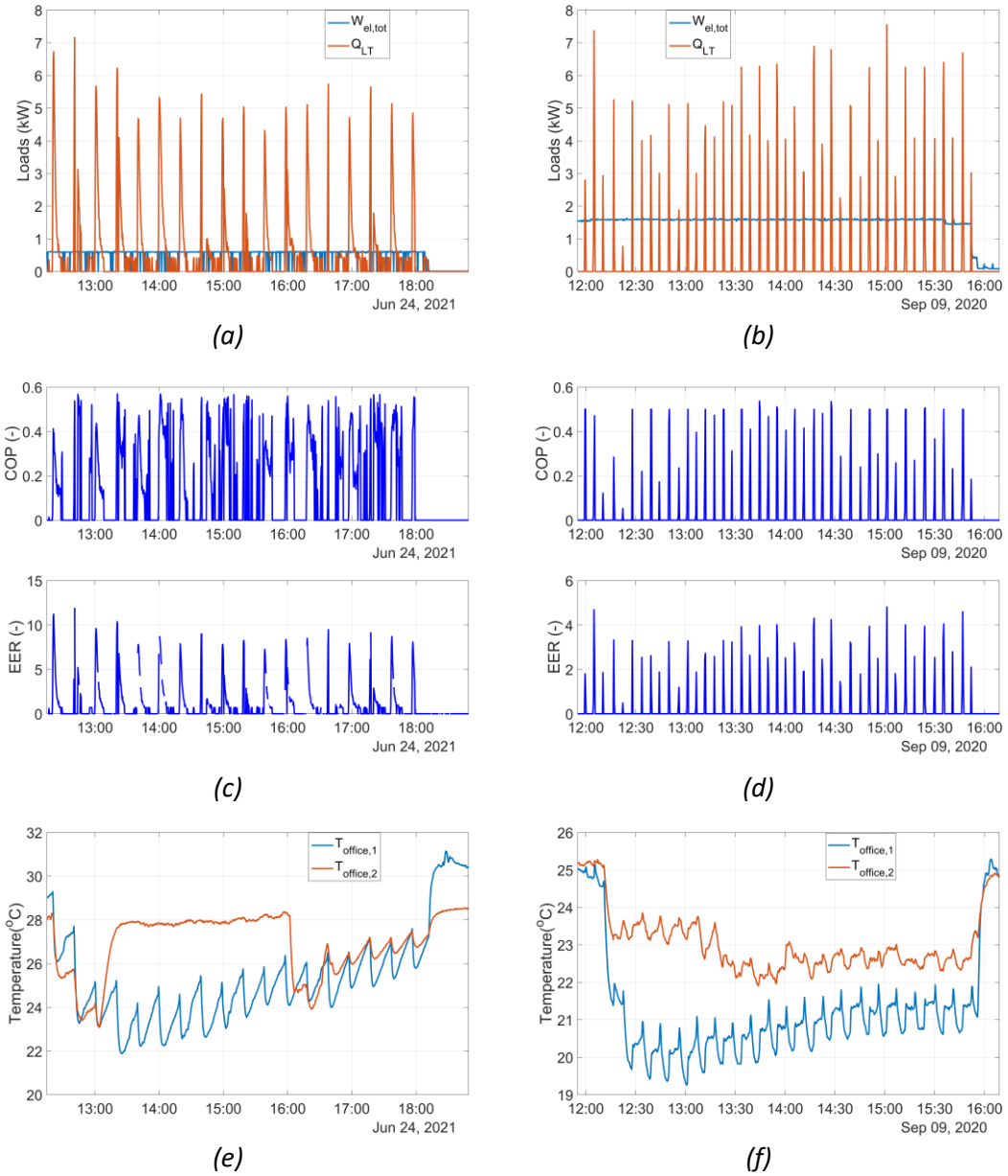

Fig. 2.41. Measured loads for (a) a hot summer day and (b) a day in autumn; Corresponding performance indicators for (c) a hot summer day and (d) a day in autumn and measured office temperatures for (e) a hot summer day and (f) a day in autumn

2.4.4 Experiment with backup heat source

Owing to the main conclusion of the previous experiments for the insufficiency of the solar heat mainly during hot days, it was decided to conduct an experiment bypassing the solar collectors circuit and directly heating the storage tank via the backup gas boiler. Given the higher capacity of the gas boiler, these experiments would be able to showcase whether the sorption chiller can cover properly the thermal needs of the measured offices. The experiment took place in the afternoon of July 26th 2021, at an ambient temperature of approximately 30-32 °C, as shown in Fig. 2.42(a). For the needs of the experiment, the setpoint of the boiler was

at 86 °C, so that the HT inlet temperature at the chiller is stabilized close to 80 °C, as shown in Fig. 2.42(b).

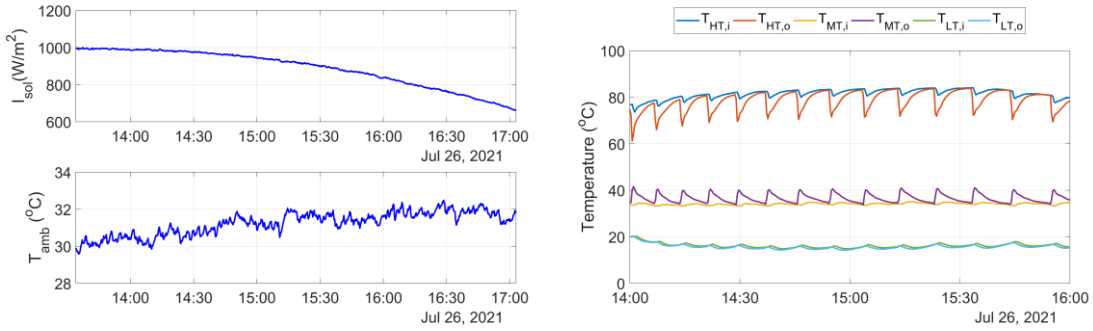

(a) *(b)*

Fig. 2.42. Experimental results during charging with the backup gas boiler (a) ambient conditions during the experiments and (b) secondary chiller circuits' temperatures

As expected, the cooling output was enhanced by the operation of the boiler, as shown in Fig. 2.43(a), reaching values close to nominal. The corresponding instantaneous COP was most of the time above 0.5, which is also close to the maximum for the used sorption working pair, while the EER was in the range 6-8. The enhanced performance of the chiller was mostly visible from the achieved room temperatures on both offices, as shown in Fig. 2.43(c). In fact, both offices were able to maintain their temperatures at the thermal comfort levels, with the different levels to be related to the setpoints of each respective user.

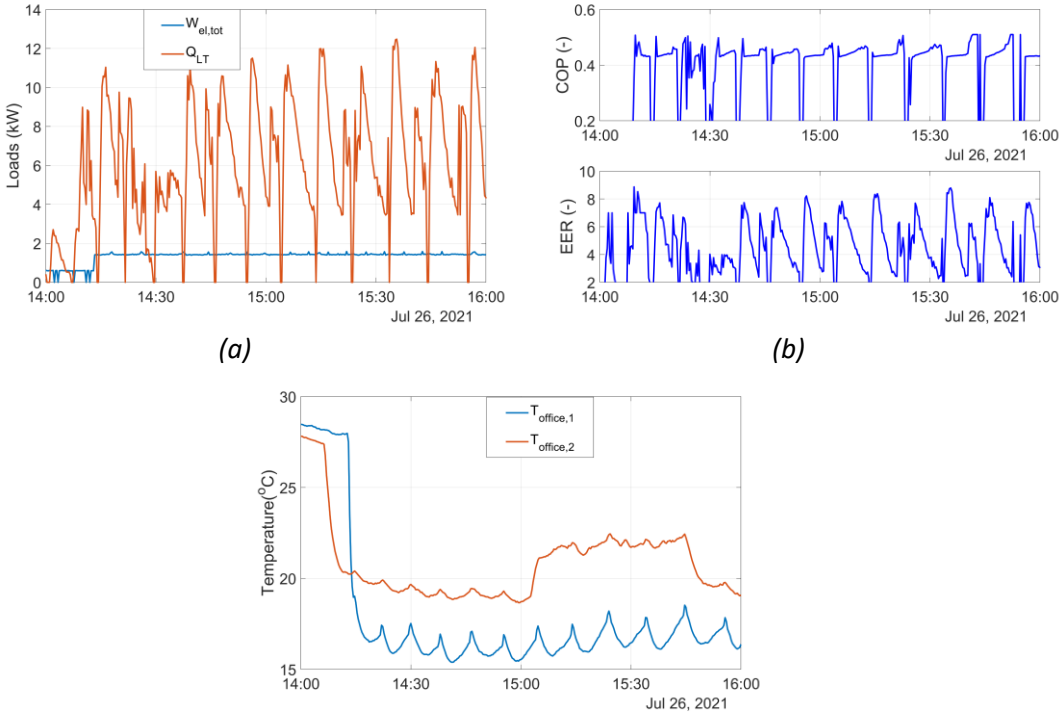

(a) *(b)*

(c)

Fig. 2.43. Experimental results during charging with the backup gas boiler: (a) measured loads (b) performance indicators (COP, EER) and (c) measured office temperatures.

2.4.5 Conclusions on Wassermod2 chiller experiments

Given the fact that Wassermod2 chiller is a modified version of the one used in Zeosol experiments of section 2.3, similar conclusions were derived. The office temperature

monitoring revealed the mismatch of the solar system sizing and the chiller required heat to operate efficiently at the relatively high temperatures of Athens. Hence, it is suggested that the ratio of solar collectors' field to storage tank's capacity should increase in order to ensure that the feed stream in the chiller can reach and maintain temperatures at the level of 80-90 °C, depending on the ambient conditions. One other alternative could also be the use of a wet cooling tower to replace the dry cooler, which would ensure that the MT circuit operates at lower temperatures and hence also the HT circuit could work efficiently at lower driving temperatures. However, the latter solution would further increase the costs of the system.
In any case, it is also suggested that a control strategy optimization is conducted towards the maximization of the stored heat in the tank and its efficient utilization by the chiller.

Chapter 3. Simulations models based on other studies

This chapter includes the presentation of all, included in the simulations, components which were modelled based on data from other studies or experiments that were not conducted within the author's doctorate studies.

3.1 Absorption reversible heat pump

In order to have an objective comparison of the different available solutions on solar cooling technologies, apart from the solar adsorption system, a respective absorption one needs to be modelled. In fact, solar absorption cooling is considered the most competitive option in solar thermally driven cooling/heating technology [67].

The absorption simulations were conducted with a previously developed model by the author [117] for a single-effect LiBr-H_2O absorption chiller (Fig. 3.1), based on the study of Kim and Infante-Ferreira [118].

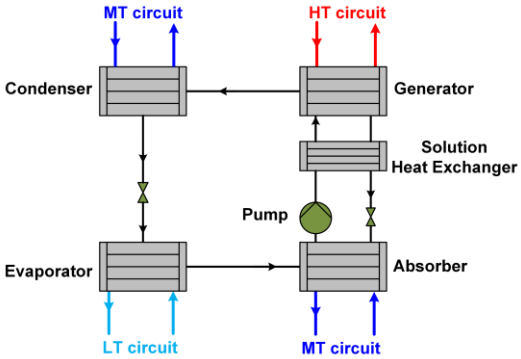

Fig. 3.1. Schematic of the modelled single-effect absorption chiller configuration

Specific details on the simulation model can be found in [66]. Prior to presenting its results, it is important to define the main performance indicators for absorption, which are the COP and the exergy efficiency.

$$COP_{abs,cool} = \frac{\dot{Q}_{evap}}{\dot{Q}_{gen}} \tag{3.1}$$

With $\dot{Q}_{evap}$, referring to the cooling power production at the chiller's evaporator and $\dot{Q}_{gen}$ to be the driving heat supplied to chiller's generator.

On the other hand, to estimate the exergy efficiency for the absorption cycle, at first the Carnot COP has to be estimated. Based on Gordon and Ng [119], the Carnot coefficient of performance for an absorption cycle is calculated by the following expression:

$$\mathrm{COP}_{\mathrm{abs,Carnot,cool}} = \frac{T_{evap}(T_{gen} - T_{ab})}{T_{gen}(T_{ab} - T_{evap})} \tag{3.2}$$

$$\eta_{ex,\mathrm{abs,cool}} = \frac{\mathrm{COP}_{\mathrm{abs,cool}}}{\mathrm{COP}_{\mathrm{abs,Carnot,cool}}} \tag{3.3}$$

Similarly to adsorption, for heating mode, the corresponding definitions are modified, as shown below:

$$COP_{abs,heat} = \frac{\dot{Q}_{ab} + \dot{Q}_{cond}}{\dot{Q}_{gen}} \quad (3.4)$$

$$\mathrm{COP}_{\mathrm{abs,Carnot,heat}} = 1 + \mathrm{COP}_{\mathrm{abs,Carnot,cool}} \quad (3.5)$$

$$\eta_{ex,\mathrm{abs,heat}} = \frac{\mathrm{COP}_{\mathrm{abs,heat}}}{\mathrm{COP}_{\mathrm{abs,Carnot,heat}}} \quad (3.6)$$

The developed model receives as inputs the secondary streams inlet temperatures and is able to calculate the off-design performance of the absorption chiller. The capacity of the chiller can be modified accordingly, by varying the nominal mass flowrate of the weak solution, which in the initial chiller's capacity was set equal to 0.0556 kg/s. An overview of the predicted by the model chiller's performance can be shown in Figs. 3.2-3.3. As expected, the medium temperature (secondary streams of condenser and absorber) has significant impact, with lower values to favor the chiller's performance. On the other hand, on heating mode, since higher temperatures are required in the MT circuit, a combination of higher driving (generator's) and evaporation temperatures are needed for more efficient operation. As shown by both Figs. 3.2-3.3, the default cooling capacity of the model is at 16 kW, with a maximum COP of 0.83, which is in close agreement with the relevant values of literature [120-122].

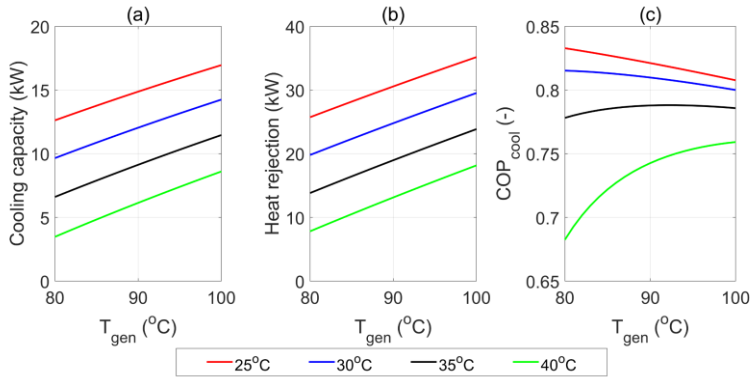

Fig. 3.2. Performance results for the absorption reversible heat pump model with varying generator's secondary stream temperature ($\theta_{evap} = 15$ °C): (a)Cooling load, (b) COP in chiller mode and (c) exergy efficiency.

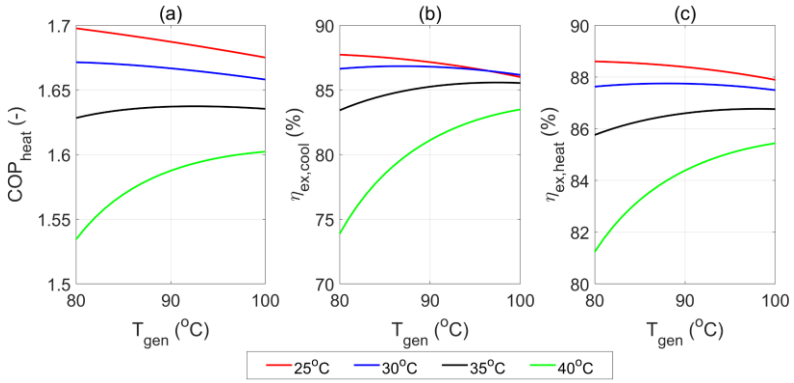

Fig. 3.3. Performance results for the absorption reversible heat pump model with varying generator's secondary stream temperature ($\theta_{evap} = 15$ °C) on heating mode: (a) Heat rejection, (b) COP and (c) exergy efficiency.

3.2 Reference reversible electric heat pump

In order to evaluate the solar cooling/heating technologies in a reference building, it is worth assessing the economics of the potential investment, not only in comparison to the conventional systems for cooling and heating, but also with the scenario of installing an electric reversible heat pump. On the contrary, as the purpose behind the use of a heat pump model is for comparison, it was selected to use real data from a commercially available heat pump model. Nominal and off-design performance of the reversible heat pump was incorporated in the developed model, with respect to the ambient and the water temperature (secondary circuits of condenser and evaporator). The data was fitted using cubic interpolations, using the aforementioned two temperatures as inputs and delivering as outputs the heating/cooling production, depending on the mode of operation, the corresponding COP and exergy efficiency. Given the residential scale of the considered applications, a small scale series of heat pump was considered, namely 30AW, manufactured by Carrier, with a cooling capacity range of 3-15 kW. The incorporation of data for several products in the aforementioned product series served the purpose to evaluate the heat pump's operation in the different climatic zones of Greece, which tend to have considerable deviations in terms of the thermal loads, as will be discussed in section 3.3. Both heat pump series operate interact with the environment via an air-cooled heat exchanger, while the secondary stream's working fluid in the HEX 1 (based on Fig. 3.4) is water.

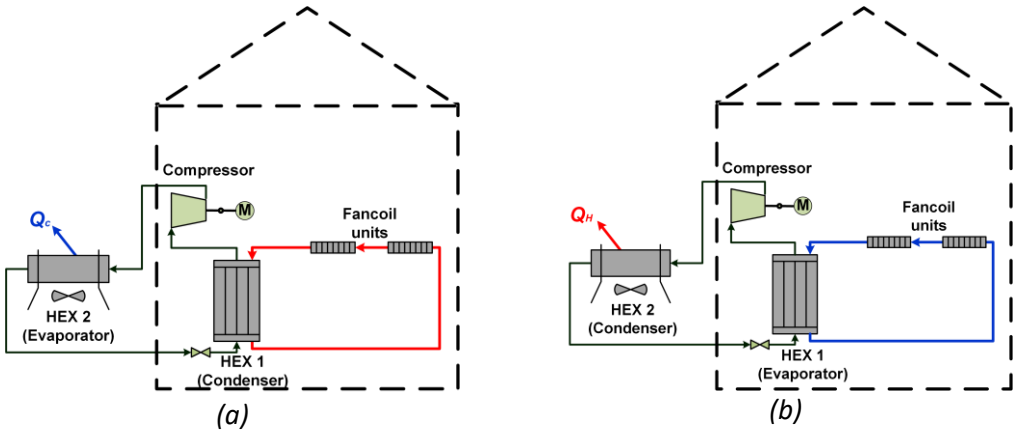

Fig. 3.4. Simplified schematic of the two modes of operation for the reversible heat pump (a) heating mode and (b) cooling mode

Figs. 3.5-3.6 present the performance results of the modelled heat pump on both cooling (Fig. 3.5) and heating mode (Fig. 3.6). As can be seen, the performance is slightly lower than the experimental heat pump, tested in section 2.3.2. In terms of the COP, as expected, both for heating and cooling, the maximum performance is when the ambient temperature is closer to 20 °C and deteriorates with the more extreme temperatures. With respect to exergy efficiencies, the results are in the same range with the experimental heat pump, with the main difference to be spotted in Fig. 3.6(c), with the optimum values per different heating setpoint to be attributed to the significant increase in the COP with increasing ambient temperature, especially for the cases of 35 and 40 °C.

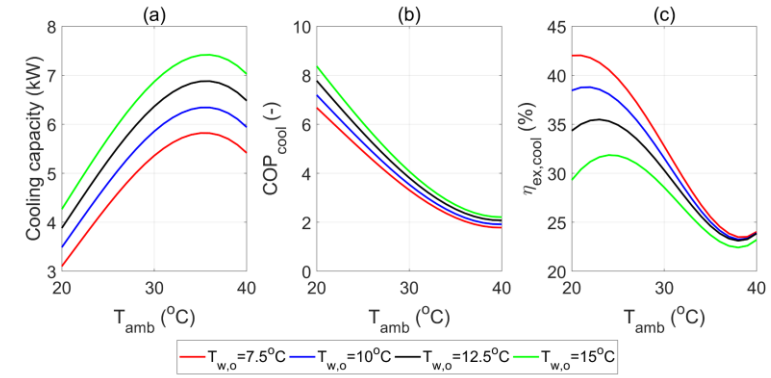

Fig. 3.5. Overview of reversible heat pump's performance (model 30AW-006) in cooling mode: (a) cooling capacity, (b) COP and (c) exergy efficiency for varying ambient and outlet water temperatures.

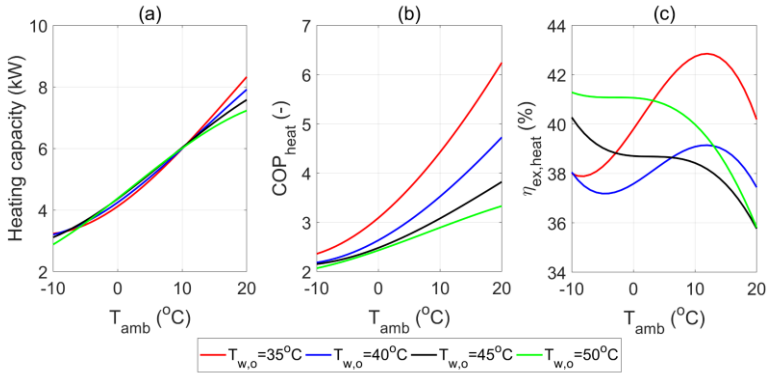

Fig. 3.6. Overview of reversible heat pump's performance (model 30AW-006) in heating mode: (a) heating capacity, (b) COP and (c) exergy efficiency for varying ambient and outlet water temperatures.

3.3 Reference building and thermal loads

As already discussed, for the solar cooling/heating system studies the loads of a reference building were required. In order to perform a uniform analysis, both techno-economically, as well as environmentally, the same building was used in all cases. The estimation of the thermal loads was realized via TRNSYS software. A single-family building was imported in the software with a total floor area of 115 m^2. As the effect of the different climatic zones of Greece was evaluated, four simulations were conducted, one for each zone, with the meteorological data of Chania (zone A), Athens (zone B), Thessaloniki (zone C) and Kozani (zone D) to be used for the analyses. An overview of the different climatic zones of Greece and the considered locations is shown in Fig. 3.7. The aforementioned meteorological data was imported in the TRNSYS simulation model by weather files applied in EnergyPlus software.

The considered single-floor building had south orientation. The key specifications for the reference building are listed in Table 3.1, based on data from Tabula WebTool [123]. The considered period of construction was 2001-2010. The selection of the period was made as a compromise between performance and installation cost since new buildings tend to have significantly lower thermal needs, which in turn results in very high costs for the investment in such technologies and eventually significantly lower return rates. In fact, this was calculated and proved in a study, in which the author of this dissertation took part [124]. According to this study, the life cycle costs for the investment in a Variable Refrigerant Volume (VRV) heat

pump to cover the thermal loads of a newly constructed building in zone B were exceeding 1450 €/m^2, while the corresponding costs for the case of a building in the same zone, constructed in the period 1980-2000, were 4 times lower.

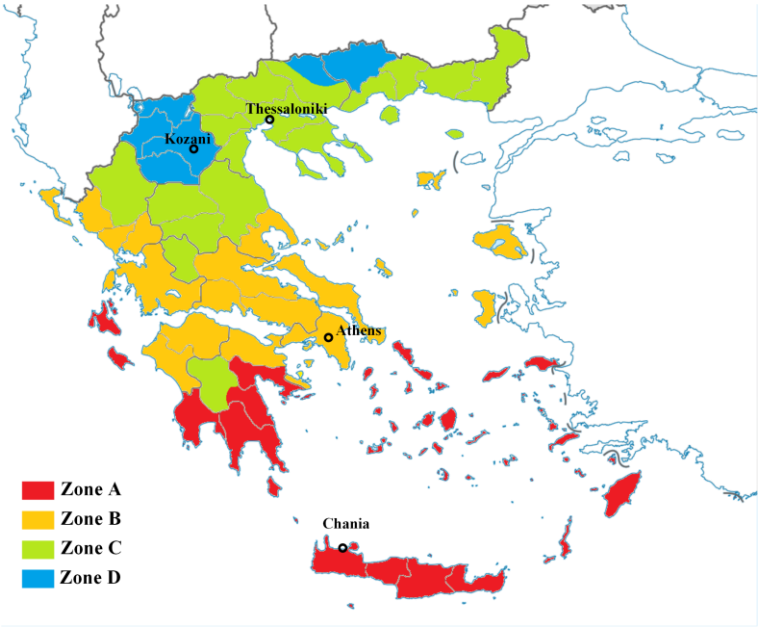

Fig. 3.7. Climatic regions of Greece and considered reference building's locations

Table 3.1. Technical specifications of the reference building [123].

Model	Value
Walls heat transfer coefficient (W m^{-2} K^{-1})	0.70
Roof heat transfer coefficient (W m^{-2} K^{-1})	0.50
Floor heat transfer coefficient (W m^{-2} K^{-1})	1.15
Windows heat transfer coefficient (W m^{-2} K^{-1})	2.80
Windows solar energy transmittance – g (-)	0.64
Door heat transfer coefficient (W m^{-2} K^{-1})	3.50
Total ceilings' area (m^2)	115
Infiltration (h^{-1})	0.13
Glazing coverage (%)	20
Number of residents (-)	3

With respect to the setpoints, the cooling setpoint was set at 26 ^{o}C, while the setback temperature was set at 32 ^{o}C when unoccupied. The respective heating setpoint was at 20 ^{o}C, with a setback temperature of 15 ^{o}C. The reference heating system was realized via a gas condensing boiler with a thermal efficiency of 96.1%, with respect to the higher heating value, and a heating capacity of 10 kW which is the smallest commercially available capacity. The boiler's electric consumption was estimated based on performance data from commercial model, Riello gas condensing boiler model 20 IS-E [125]. The respective cooling loads were considered to be covered by a total of three single-split air-conditioning (a/c) units, with a total capacity of 7.92 kW (3 units of 9000 Btu/h) [126]. The EER of the considered single split units was equal to 10.24 Btu/(W h), which corresponds to a COP of 3. The aforementioned COP may be considered low for new single split units, however, as these systems refer to the reference case of 2001-2010, the performance of an older model was selected, namely DAIKIN FT10JXV1/R09CXV1 unit. Based on all above, the thermal loads for the four respective

locations were calculated and are listed in Fig. 3.8, while Table 3.2 provides the total sums and the maximum values for the respective consumptions on each location.

Table 3.2. Annual loads of the reference building for the considered locations.

Type of load	Chania (Zone A)	Athens (Zone B)	Thessaloniki (Zone C)	Kozani (Zone D)
Annual heating demand (kWh/year)	3944.51	5864.7	8036.18	9481.9
Annual electricity demand for heating (kWh_{el}/year)	39.0	57.9	65.5	77.3
Annual natural gas consumption (Nm^3/year)	383.1	569.5	780.4	920.8
Annual cooling demand (kWh/year)	2084.13	2216.2	1587.18	1181.8
Annual electricity demand for cooling (kWh_{el}/year)	694.71	738.7	529.06	393.93

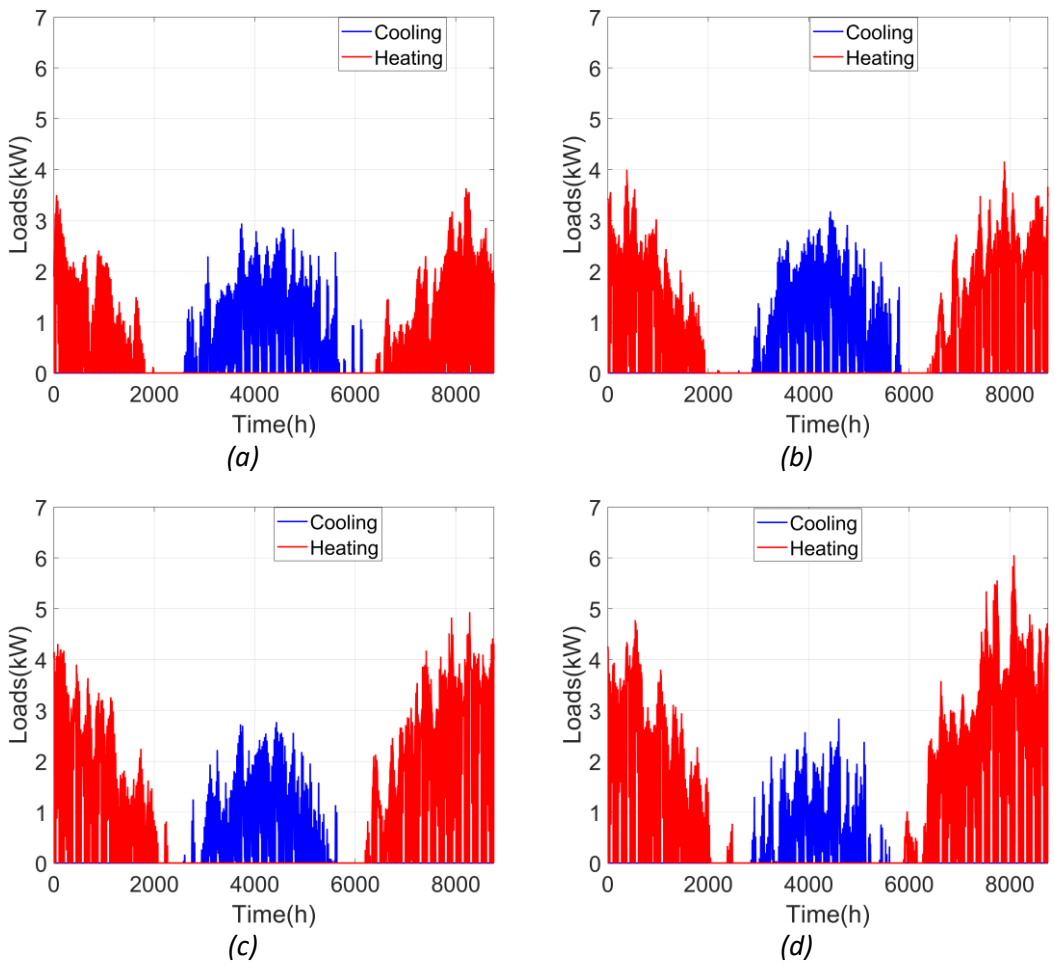

Fig. 3.8. Annual profiles of cooling/heating loads for (a) Chania, (b) Athens, (c) Thessaloniki and (d) Kozani

3.4 Photovoltaic panels & battery

3.4.1 System description

The PV system consists of the photovoltaic modules that generate power, a battery to store the excess of produced power and an inverter/regulator that firstly deals with the conversion of the DC generated power to AC to supply either the loads or the grid and secondly regulates the power flow between the modules, the grid, the battery and the loads.

Concerning the photovoltaic modules, they operate using the Maximum Power Point Tracking (MPPT) control strategy to ensure maximum power generation under different weather conditions, namely solar irradiation and ambient temperature. On the one hand, their nominal capacity, expressed in peak power generation, was selected based on the maximum simulated electrical load, which results from the heating/cooling loads met by the heat pump. In particular, the total rated power of the modules should match the maximum electrical demand, under the standard test conditions (STC) of 25 °C ambient temperature 1000 W/m2 of incident solar irradiation and air mass (AM) of 1.5. This criterion provides a first indication of the number of the modules. On the other hand, their configuration, i.e. the number of modules installed in series forming a string and the number of parallel strings, is restricted by the inverter ratings, with regard to its input voltage range and maximum current. This part of the sizing was performed assuming extreme cell temperatures (-20 and 70 °C) since the generated voltage and current depend on cell temperatures. It is noted that the model TP660P of 275 Wp of the TALESUN company was used as building unit [127].

For the needs of the PV module, technical data from commercial model TP660P [127] was implemented into TRNSYS. Table 3.3 provides a number of key technical specifications of the used commercial PV model.

As far as the inverter is concerned, its nominal capacity was determined by the maximum demand and in conjunction with the abovementioned constraints of the PVs. Commercial inverters were taken into account, namely the series Galvo of the Fronius company [128]. Regarding the battery, a lead-acid battery of 12 V was selected, formed by parallel strings of six 2 V lead-acid cells. The nominal capacity of each cell was varied from 30 to 50 Ah and the number of parallel strings was determined to ensure the desired total capacity expressed in Wh, which was varied from 25 to 100% of the nominal maximum power of the PV array, in steps of 25%.

3.4.2 System modelling

The PV system was modeled using the TRNSYS18 software. In particular, Type 190d was used for the PV panels implementing the five-parameter model of De Soto et al.[129]. Battery was simulated via Type 47a which expresses the state of charge (SOC) of the battery in terms of energy and performs an energy balance according to the input power from and the PVs and the output power to the load. Eventually, Type 48b was used for the regulator/inverter. The model parameters for the main components are listed in Tables 3.3-3.5. It is stressed that the majority of the parameters was retrieved from manufacturers specification and the rest was taken from the study of Varvagiannis et al. [130]. In addition, some parameters such as the number of strings in Table 3.3, appear as ranges including all the simulated cases. Concluding, the TRNSYS model is depicted in Fig. 3.9.

Table 3.3. PV array model parameters [127]

Description	Value
Module reference short-circuit current (A)	9.17
Module reference open-circuit voltage (V)	38.7
Module reference current at MPP (A)	8.69
Module reference voltage at MPP (V)	31.7
Reference short-circuit current temperature coefficient (A/K)	0.0055
Reference open-circuit voltage temperature coefficient (V/K)	0.1200
Module cells (-)	60
Number of strings (-)	1
Modules per string (-)	5-8
Transmittance-absorptance product for normal incidence (-)	0.9
Semiconductor bandgap (eV)	1.12
Cover extinction coefficient (m^{-1})	4
Cover thickness (mm)	3.2
Module slope (deg)	30
Module absorption area (m^2)	1.46

Table 3.4. Battery model parameters

Description	Value
Cell voltage (V)	2
Cell capacity (Wh)	60-100
Number of cells' strings (-)	1-6
Cells per string (-)	6
Battery voltage (V)	12
Battery capacity (Wh)	360-2160
Charging efficiency (-)	0.9
Maximum SOC (-)	1.00
Minimum SOC (-)	0.15
SOC turning point from charging to discharging (-)	0.75

Table 3.5. Inverter/regulator specifications model parameters

Description	Value
Regulator rated efficiency (-)	0.90
Inverter rated efficiency (-)	0.96
Maximum input power (Wp)	3000-5000
Maximum output power (W)	1500-2500
Rated input voltage (V)	140-185
Minimum input voltage for MPPT operation (V)	120-165
Maximum input voltage for MPPT operation (V)	420-440
Maximum input current (A)	13.3-17.8
Night consumption (W)	0.4

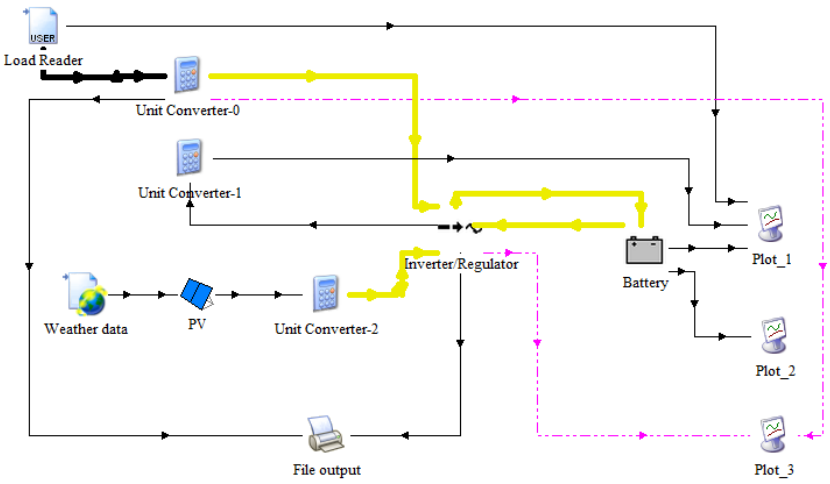

Fig. 3.9. Overview of the TRNSYS simulation model

3.5 Organic Rankine Cycle components

As mentioned in section 1.5, the power production in the considered scenarios, mainly due to the range of the driving temperatures from the investigated solar thermal collectors, was realized via Organic Rankine Cycle (ORC) systems. The modelling of each respective component will be presented in the following subsections. At this point is important to mention that the pump's modelling despite being experimentally validated by a test rig of the Laboratory of Steam Boilers and Thermal Plants, as this has been already discussed in the doctoral dissertation of Pallis [131], it was preferred to be included in Chapter 3, along with the other ORC components. The reason behind the absence of respective validation for the other ORC components lies in the fact that different types of components were modelled as being the more commonly used in the respective scale. For instance, the scroll expander model was preferred to be a hermetic one, which is a more common type of expander used in such applications, while the laboratory's test rig included two open drive scroll expanders. Subsections 3.5.1-3.5.2 and 3.5.4-3.5.5 were published in the article "Exergetic and economic analysis of a solar driven small scale ORC" [62]. Subsection 3.5.3 was published in the article "Techno-economic optimization of medium temperature solar driven subcritical Organic Rankine Cycle" [64].

3.5.1 Diaphragm pump

A multi-diaphragm pump is considered, the technical specifications of which are presented in Table 3.6. The modelling of the pump was based on performance correlations provided by the manufacturer [132]:

$$\dot{V}_p = \frac{N_p - 22{,}681}{46{,}705} \tag{3.7}$$

$$\dot{W}_{mech,p} = 15\frac{N_p}{84{,}428} + \frac{\dot{V}_p \cdot \Delta p}{511} \tag{3.8}$$

$$\eta_p = \frac{\dot{W}_{hyd}}{\dot{W}_{mech,p}} = \frac{\dot{V}_p.\Delta p}{\dot{W}_{mech,p}} \quad (3.9)$$

The rotational speed of the pump in equations (3.7) and (3.8) is expressed in rpm and the volumetric flowrate in lpm.

Table 3.6. Technical specifications of the multi-diaphragm pump. [132]

Model	Maximum rpm	Maximum inlet pressure (bar)	Maximum discharge pressure (bar)	Maximum flow (l/min)
Hydra Cell D10-X	1450	17	69	30.6

As mentioned above, the pump's model was validated based on experimental data from an existing test rig in the laboratory of Steam Boilers and Thermal Plants, namely the marine ORC prototype. The following description of the system was published in the study "Experimental Investigation and CFD Analysis of Heat Transfer in Single Phase Subcooler of a Small Scale Waste Heat Recovery ORC" [133].

The Marine ORC is using R134a as the working fluid and it is designed to be powered by the waste heat from the jacket water of marine diesel auxiliary ICEs. The unit produces 3.7 kWel net electrical power at a cycle pressure of 25 bar and a high temperature of 82 °C. Regarding the system configuration, which is also presented in Fig. 3.10, a conventional subcritical ORC cycle is implemented. The waste heat source is simulated by a natural gas boiler of a nominal thermal output of 90 kW_{th}. The evaporator is a plate type heat exchanger, while both the subcooler and the condenser are shell & tube heat exchangers. Two scroll expanders have been installed in parallel allocation so that part load operation can be realized by operating a single expander at higher speed rather an inefficient simultaneous low speed operation of both expanders. The low pressure of the cycle is equal to approximately 9.5 bar, while via the diaphragm pump a high pressure of 25 bar is achieved. More specifically, the feed pump is a positive displacement multi-diaphragm pump, which serves both the pressure increase in the working fluid stream and as a circulator. At a nominal speed of 3000 rpm, a flow rate of 0.4 kg/s is achieved. The rotational speed of the pump is controlled by a frequency drive. The frequency of the pump is thus adjusted according to the mode of the operation, as it is defined by the unit's automation. To connect the generators to the 50Hz/400V electrical grid, regenerative inverters have been implemented, enhancing the grid stability and the rotational control of the generators.

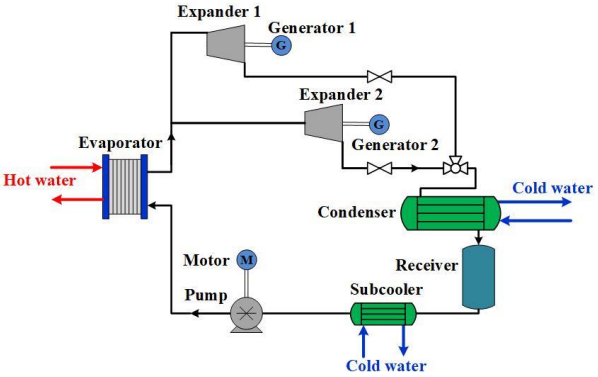

Fig. 3.10. Simplified schematic of the marine ORC

With respect to the measuring devices for the needs of the pump's experiments, the main used instruments, included a Coriolis flowmeter, two pressure sensors, two temperature resistances Pt100, an energy meter (see Table 2.15) and a tachometer. Data for the aforementioned measuring instruments can be found in Table 3.7-Table 3.10 below.

Table 3.7. Technical specifications of the temperature sensors in the pump's experiments.

Type/ Model	**Pt100 3W WIKA T19**
Output	4-20 mA
Medium temperature (min/max)	0 / 100 °C
Accuracy	0.5 %

Table 3.8. Technical specifications of the pressure sensors in the pump's experiments.

Type/ Model	**WIKA S-10**
Measuring range	0-25 bar
Output	4-20 mA
Accuracy pressure	±0.5% @ 25°C
Medium temperature (min/max)	-30 / 100 °C

Table 3.9. Technical specifications of the Coriolis flowmeter in the pump's experiments.

Type/ Model	**KROHNE OPTIMASS MFS 1000 S25**
Measuring range	0-3.89 m/s
Output	4-20 mA
Accuracy	±0.2%
Ambient temperature (min/max)	-40 / 65 °C

Table 3.10. Technical specifications of the tachometer in the pump's experiments.

Type/ Model	**9210.001 / 9210.004**
Frequency range	0.034-60,000 Hz
Output	4-20 mA
Accuracy	±0.005%

Within the context of the marine ORC tests, a performance evaluation of the pump was conducted, using steady state measurements of the rotational speed at the shaft of the pump and volumetric flowrate, via the Coriolis flowmeter. The results, shown in Fig. 3.11, revealed a small deviation from the manufacturer's data, which is increasing with the rotational speed. In fact, the measured volumetric flowrate at 1080 rpm and at a discharge pressure of 23 bar, was lower by 5.8% than the corresponding value provided by the manufacturer for a discharge pressure of 14 bar.

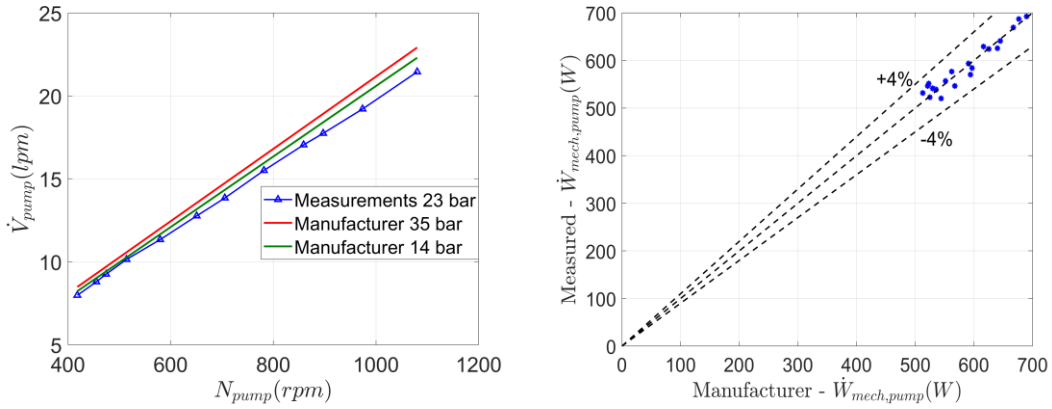

(a) *(b)*

Fig. 3.11. Overview of manufacturer's curve comparison against experimental data [131]: (a) with respect to the volumetric flowrate and (b) with respect to the mechanical power of the pump

3.5.2 Scroll expander

For the considered small-scale low temperature application, the single stage conventional OR was considered to be operating with a scroll expander. The selection of the specific type of expanders was defined by the general specifications of the considered small scale system (<5 kWel), for which scroll expanders are the most common and efficient type (Fig. 3.12), while custom-made expanders or high rotational speed turbomachinery were considered to increase significantly the cost of the system to be further evaluated.

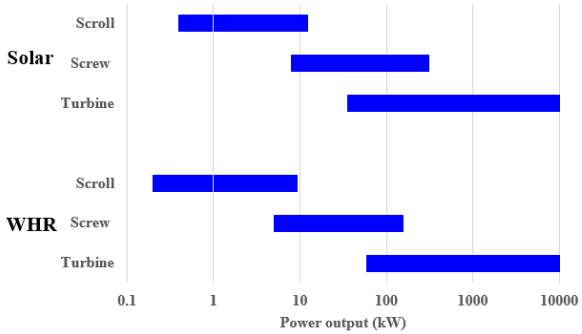

Fig. 3.12. Overview of expander types and their power ranges [134]

The modeling of the expander was based on cubic interpolation of experimental data from Dumont et al. [135], in which was developed a graphic correlation of the expander isentropic efficiency, rotational speed, N_{exp}, and expansion pressure ratio, π:

$$\eta_{is,exp} = f(\pi, N_{exp}) \tag{3.10}$$

An overview of the fitting along with the used experimental data from Dumont et al. [135] are presented in Fig. 3.13.

The rotational speed was calculated based on the operating conditions of the expander taking into account the definition of the filling factor:

$$ff = \frac{\dot{m}_{exp} 60}{\dot{V}_{exp} \cdot N_{exp} \cdot \rho_{su}} \Rightarrow N_{exp} = \frac{\dot{m}_{exp} 60}{\dot{V}_{exp} \cdot ff \cdot \rho_{su}} \tag{3.11}$$

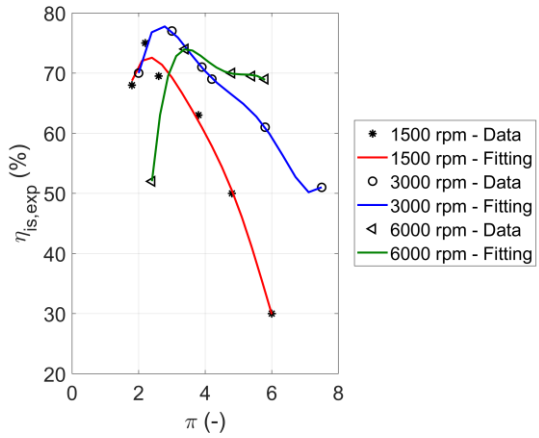

Fig. 3.13. Overview of fitted data for the isentropic efficiency of a scroll expander with varying rotational speed and expansion pressure ratio

The filling factor is calculated based on the model described by Declaye et al. [136]:

$$ff = 0.7514 + 0.337 \ln\left(\frac{N_{exp}}{3000}\right) + 0.0239 r_p^* + 0.0366 p^* \qquad (3.12)$$

with

$$p^*(bar) = \frac{p_{i,exp}(bar) - 10}{10} \qquad (3.13)$$

$$r_p^* = \frac{\pi - 4}{4} \qquad (3.14)$$

Finally, by considering 5% heat losses [137], as well as taking into account the efficiencies of the inverter and the generator as polynomial functions of the expander's rotational speed and the power generated at the expander [138], the power output to the grid is equal to:

$$\dot{W}_{el} = 0.95\, \eta_{is,exp}\, \dot{W}_{is,exp}\, \eta_{el,inv}\, \eta_{el,gen} \qquad (3.15)$$

3.5.3 Screw expander

For the medium or higher temperature heat sources (>150 °C) study, a screw expander was preferred owing to their larger working range, mainly for the technically feasible volume ratios [139]. A correlation between the isentropic efficiency and the pressure ratio of the screw machine was derived based on the experimental data of the study by Hsu et al. [140], in which the performance of a screw expander coupled with an ORC system for various working conditions was investigated. Due to the limitations of the pressure ratio of screw machines, it was considered that the system may contain a maximum of two expanders functioning with pressure ratio varying between 2.4 and 6.1 [134, 140]. The correlation between the isentropic efficiency of a screw expander and its pressure ratio (π) is the following:

$$\eta_{is,exp} = 0.001082\pi^5 - 0.027767\pi^4 + 0.2871\pi^3 - 1.51052\pi^2 + 4.06965\pi - 3.78 \qquad (3.16)$$

Thus, when the high and low pressures of the ORC are known, the isentropic efficiency of the expander can be calculated from equation (3.16), considering that both expanders work at the same pressure ratios, equal to the square root of the ORC's high pressure to low pressure ratio. In order to estimate the power production in the expanders, the involved in the expansion process losses have to be taken into account. Apart from the isentropic efficiency, the inverter's and the generator's efficiencies, there has to be a term for the heat losses in the expander. In literature, there is a large deviation on the estimated heat losses of the expanders. For example, Wang et al. [141] reported heat losses of up to 0.65 kW for a screw expander of approximately 7 kWe (9.2%). Lemort et al. [142] measured the heat losses for a scroll expander to be almost 4%, while the study from Giuffrida [143] estimated losses to the ambient of more than 6%. Due to these deviations, this study considered an average value for the heat losses, in the range of 5%, in a homogeneous approach with the low temperature ORC study, hence, the net produced power in the expander can be calculated by the equation (3.15).
The displacement volume of the expander, required for the cost estimation of the ex-pander, is calculated, by modification of equation (3.11):

$$\dot{V}_{exp} = \frac{\dot{m}_{exp} 60}{N_{exp} \cdot ff \cdot \rho_{su}} \tag{3.17}$$

Eventually, The value of the filling factor is derived by applying a polynomial expression based on the experimental data presented by Dumont et al. [135], as shown in Fig. 3.14.

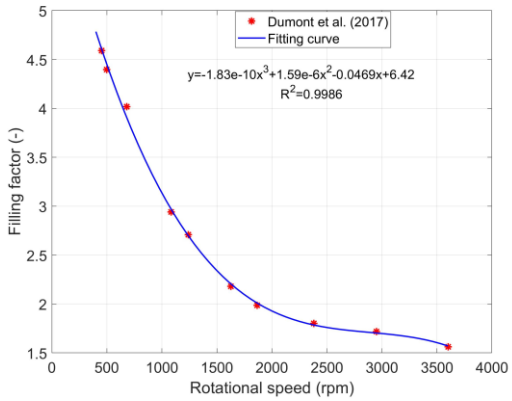

Fig. 3.14. Filling factor estimation based on data from Dumont et al. [135]

3.5.4 Generator -Inverter

The efficiency of the inverter and the generator were modeled as a function of the rotational speed and the power generated at the expander. The used correlations were based on data from Ziviani et al. [138].

$$\eta_{el,inv} = a_o + a_1 \cdot lnv^* + a_2 \cdot (lnv^*)^2 + a_3 \cdot (lnv^*)^3 + a_4 \cdot lnw^* + \\ + a_5 \cdot (lnw^*)^2 + a_6 \cdot (lnw^*)^3 \tag{3.18}$$

$$\eta_{el,gen} = b_o + b_1 \cdot lnv^* + b_2 \cdot (lnv^*)^2 + b_3 \cdot (lnv^*)^3 + b_4 \cdot \ln\left(\frac{w^*}{v^*}\right) + b_5 \cdot \left[ln\left(\frac{w^*}{v^*}\right)\right]^2 + b_6 \cdot \left[ln\left(\frac{w^*}{v^*}\right)\right]^3 + b_7 \cdot ln\left(\frac{w^*}{v^*}\right) \cdot lnv^* + b_8 \cdot \left[ln\left(\frac{w^*}{v^*}\right)\right]^2 \cdot lnv^* + b_9 \cdot ln\left(\frac{w^*}{v^*}\right) \cdot (lnv^*)^2 + b_{10} \cdot \left[ln\left(\frac{w^*}{v^*}\right)\right]^2 \cdot (lnv^*)^2 \quad (3.19)$$

With,

$$v^* = \frac{N_{exp}}{N_{exp,nom}} \quad (3.20)$$

$$w^* = \frac{\dot{W}_{mech,exp}}{\dot{W}_{mech,exp,nom}} \quad (3.21)$$

The coefficients appearing in the above equations are presented at the aforementioned reference [138].

Table 3.11. Coefficients for equations (3.18)-(3.19)

	Value (-)		Value (-)
a_0	$9.55726922 \cdot 10^{-1}$	**b_0**	$8.93747915 \cdot 10^{-1}$
a_1	$2.60983262 \cdot 10^{-2}$	**b_1**	$3.23048796 \cdot 10^{-2}$
a_2	$2.42349302 \cdot 10^{-2}$	**b_2**	$-1.91761519 \cdot 10^{-2}$
a_3	$1.21191602 \cdot 10^{-2}$	**b_3**	$1.52204756 \cdot 10^{-2}$
a_4	$4.94828374 \cdot 10^{-2}$	**b_4**	$7.32867448 \cdot 10^{-3}$
a_5	$3.3143316 \cdot 10^{-2}$	**b_5**	$-3.17061820 \cdot 10^{-2}$
a_6	$2.27446360 \cdot 10^{-2}$	**b_6**	$2.16415080 \cdot 10^{-2}$
		b_7	$1.63125253 \cdot 10^{-2}$
		b_8	$4.37556935 \cdot 10^{-3}$

3.5.5 Heat exchangers

With respect to the heat exchangers, models for plate heat exchangers were developed for the involved heat exchangers, namely the evaporator, condenser, subcooler and, if required, recuperator. The selection of plate heat exchangers was dictated by their high compactness which is crucial for overall system's size in small scale applications [144]. Moreover, for the required heat duties, plate heat exchangers are the most economical solution and other type of heat exchangers are only selected/used in case of pressure limitations, since the maximum working pressure of conventional plate heat exchangers is around 40 bar [145].

As already presented in section 3.5.1, the marine ORC test rig, included only one plate heat exchanger, namely the ORC's evaporator. The reason behind not conducting any experimental validation based on the data from the test rig is based on the fact that within the aforementioned heat exchanger there were taking place three consequent heat transfer processes, namely pre-heating, evaporation and superheating of the refrigerant. However, given the absence of internal measuring points in the heat exchanger, the knowledge of solely the outlet and inlet conditions in the heat exchanger and thus the estimation of the global heat transfer does not allow for secure calculations in the respective heat transfer zones. In

fact, a relevant study by Dickes et al. [146] showcased this issue, presenting three examples of different sets of convective heat transfer coefficients in the three respective zones of an evaporator. As can be seen from Fig. 3.15, the high deviations in the estimated heat transfer coefficients of each zone, practically, conclude that a possible over-prediction by a correlation in one zone is "fine-tuned" by a malfunctioning under-prediction of another's zone correlation, without the user being able to identify this, unless detailed internal measurements exist. Hence, the modelling both on- and off-design of the ORC heat exchangers was based on theoretical models.

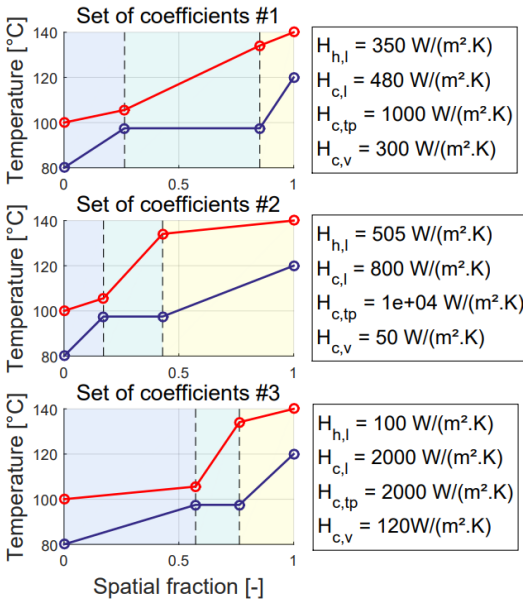

Fig. 3.15. Test of different sets of convective heat transfer coefficients for an identical global heat transfer in an evaporator from Dickes et al. [146]

The design of the heat exchangers was based on the LMTD method [147] for commercial models of plate heat exchangers. The off-design performance of the heat exchangers, was based on a quasi-steady state model developed on the basis of moving boundaries method [113].

The Nusselt number of the evaporation process was estimated based on the correlation of Yan and Lin [148]:

$$Nu = 19.26 {Re_L}^{0.5} {Bo_{eq}}^{0.3} {Pr_L}^{1/3} \qquad (3.22)$$

The pressure drop during evaporation/condensation was calculated by the following equation:

$$\Delta p_{evap} = \frac{f L_p}{D_{hyd}} \cdot \frac{\rho_{evap} {v_{evap}}^2}{2} \qquad (3.23)$$

With L_p the plate length and D_h to be the hydraulic diameter of the plate.

The friction factor, f, for the evaporation process was calculated as follows [148]:

$$f = 6.947 \cdot 10^5 {Re_L}^{-0.5} {Re_{eq}}^{-1.109}, \qquad Re_{eq} < 6{,}000 \qquad (3.24)$$

$$f = 31.21{Re_L}^{-0.5}{Re_{eq}}^{0.04557}, \qquad Re_{eq} \geq 6{,}000$$

The respective correlations for the condensation process (Nusselt number and friction factor) were that of Yan et al. [149]:

$$Nu = 4.118{Re_{eq}}^{0.4}{Pr_L}^{1/3} \tag{3.25}$$

$$f = 94.75Re_{eq}^{-0.0467}Re^{-0.4}Bo^{0.5}p_{red}^{0.8}, \quad \begin{matrix} 500 < Re < 1{,}000 \\ 60 \leq G \leq 120 \end{matrix} \tag{3.26}$$

The single phase Nusselt number was estimated by the correlation proposed by Donowski and Kandlikar [115] and the friction factor from the correlation of Focke et al. [116]:

$$Nu = 0.2875Pr^{1/3}Re^{0.78} \tag{3.27}$$

$$\begin{matrix} f = 5.03 + 755/Re, & 90 < Re < 400 \ \ (\varphi = 60°) \\ f = 26.8Re^{-0.209}, & 400 < Re < 16{,}000 \end{matrix} \tag{3.28}$$

Chapter 4. Design studies

Having defined all the models to be used in the off-design studies for both solar cooling/heating and solar thermal power generation systems in the previous Chapters, this Chapter presents their combination into standalone system's operation models and their evaluation in specific case studies. In all studies, included in this Chapter, dedicated multi-objective genetic algorithms (GA) were developed and executed. The complex nature of the involved modelling systems and the need for optimization with respect to different aspects of performance (economic and technical) dictated the use of a multi-objective optimization algorithm. The implementation of the multi-objective GA allows the solver itself to return a set of optimal solutions, showing the general trend of the system's decision variables (design aspects of the system) with respect to the objective functions [150]. Specifically for solar driven systems, the economic optimal solution is commonly different than the technical optimum and therefore, the estimation of a Pareto front via the multi-objective GA was considered a suitable approach for such optimization problems. In the analyses of this Chapter, all multi-objective GAs were formulated and executed in MATLAB, in correspondence to all previously reported components' models. The meteorological data and the reference building's loads were implemented also in MATLAB in the form of input matrices from the respective TRNSYS simulations.

4.1 Techno- economic analysis of a low temperature solar driven small-scale ORC

The analysis of this section was presented in the article "Exergetic and economic analysis of a solar driven small scale ORC" [62]. However, given that the cost correlations presented in the Appendix I, were developed at a latter stage, the GAs of this study were re-evaluated under the new cost inputs for a uniform analysis. In a similar manner, the simplified storage tank's model was updated based on the model presented in section 2.2.

In the present study, the energy, exergy and economic performance of a solar driven small-scale ORC (Fig. 4.1) taking into account its annual operation in five European cities of both southern and central Europe, namely Athens (Greece), Berlin (Germany), Brussels (Belgium), Rome (Italy) and Madrid (Spain). The selection of the cities aimed to evaluate different profiles of solar irradiance in combination with the large deviation in the selling price of electricity in these regions. Moreover, the different performance in the climatic zones of Greece was assessed, by applying GAs for the other three climatic zones of Greece, using weather data for the cities of Chania (Zone A), Thessaloniki (Zone C) and Kozani (Zone D). Three collector types operating at different temperatures are considered, including flat plate (FPC), evacuated tube (ETC) and parabolic trough collectors. An exergy-based analysis is carried out in order to allow for a direct comparison of the systems with respect to their varying driving temperatures. In each of the above cases, a genetic algorithm is implemented to optimize the system's performance with respect to the solar field area and the capacity of a heat storage tank, having as objective functions the payback period of the investment and the overall annual exergy efficiency.

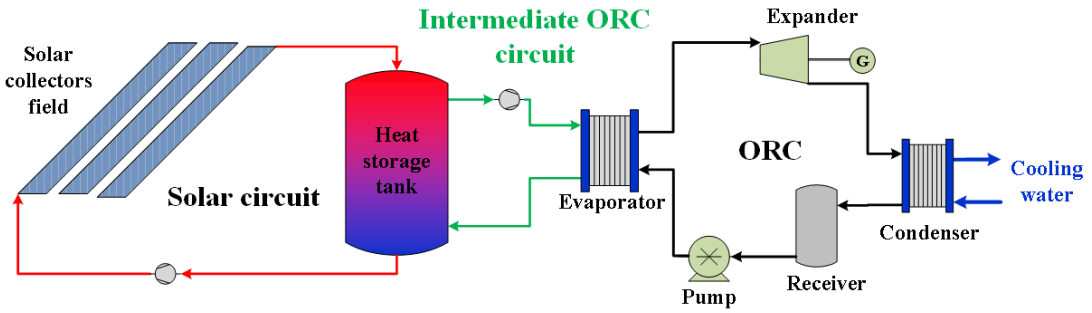

Fig. 4.1. Schematic of the considered solar driven small-scale ORC

4.1.1 ORC system modelling

One important step in the development and optimization of a system which includes an ORC, is the selection of the ORC working fluid, owing to the great influence of the fluid selection in the overall system's performance [151]. The selection of the working fluids to be evaluated was based on their critical temperature, the global warming potential (GWP) and ozone depletion potential (ODP) indexes, the availability of their thermodynamic properties in the used calculation RefProp and their cost/availability for the considered application. The working fluids that were preliminary screened for the investigated application are summarized in Table 4.1, along with their critical properties, ODP, GWP indexes and ASHRAE classification index. In this table, the ultimately selected fluids are marked with green color. At this point it has to be mentioned that RC318 was not considered due to its high cost (>500 €/kg), while R290 and R600a were also rejected due to their high flammability, which would induce additional costs with respect to the safety standards for the use of flammable fluids [152].

Table 4.1. Initial list of potential working fluids for the application [151]

`	T_{crit} (°C)	P_{crit} (bar)	ODP	GWP	ASHRAE classification
R407A	82	45	0	2,107	A1
R1234yf	95	34	0	4	A2L
R290	97	42	0	3.3	A3
R134a	101	41	0	1,430	A1
R227ea	101	29	0	3,220	A1
R1234ze(E)	110	36	0	6	A2l
R152a	112	44	0	124	A2L
RC318	114	28	0	10,300	A1
R600a	135	36	0	3	A3
R236ea	139	34	0	1,370	-
R245fa	153	36	0	1,370	B1

In order to compare all cases on a common basis, some assumptions were considered with respect to the nominal operating conditions of the ORC, as listed in Table 4.2. The nominal driving temperature (i.e. the temperature of the heat transfer fluid at the ORC evaporator inlet) is taken equal to 90°C and 110°C for the FPCs and ETCs/PTCs, respectively. Although higher driving heat temperatures could have been selected for the systems operating with PTCs and, thus, achieve higher electrical ORC efficiencies, this would entail the selection of alternative working fluids with higher critical temperatures, such as natural hydrocarbons,

which have nonetheless increased flammability, and which will be discussed in following paragraph.

Table 4.2. Initial list of potential working fluids for the application

Type of collector	Threshold temperature (°C)	Nominal driving temperature (°C)	$\dot{Q}_{evap}$ (kW_{th})	Superheating degree (°C)	Condenser subcooling (°C)	Cooling water temperature (°C)
FPCs	70	90	20	10	5	25
ETCs/PTCs	90	110	20	10	5	25

Fig. 4.2(a) presents an overview of the operational mode for the entire system for each hour of the year during the annual simulations. At the start of the simulation, all temperatures in the solar circuit and the intermediate ORC circuit are assumed to be equal to the ambient temperature. For the given solar field surface per case, the operation switches ON every hour the solar irradiance, I_{sol}, is positive and the solar collectors start to heat up the storage tank. On the other hand, in absence of solar irradiance, the solar field is disconnected from the storage tank, in order to avoid additional heat losses. When the storage tank top zone reaches a threshold temperature, T_{min}, listed in Table 4.2. for each type of collector, the intermediate ORC system starts to operate heating up the evaporator of the ORC. Based on the heat input from the intermediate ORC circuit and previous state of the ORC, the ORC subsystem is solved based on the flowchart of Fig. 4.2(b) and the assumptions of Table 4.2. For the driving temperatures lower than the nominal value, a ramp scenario was considered to simulate the operation of the ORC as realistically as possible. For each time step, the evaporation and condensation pressures of the ORC are selected by setting a set pinch point in the evaporator and condenser equal to 4.5 and 7.5 K, respectively.

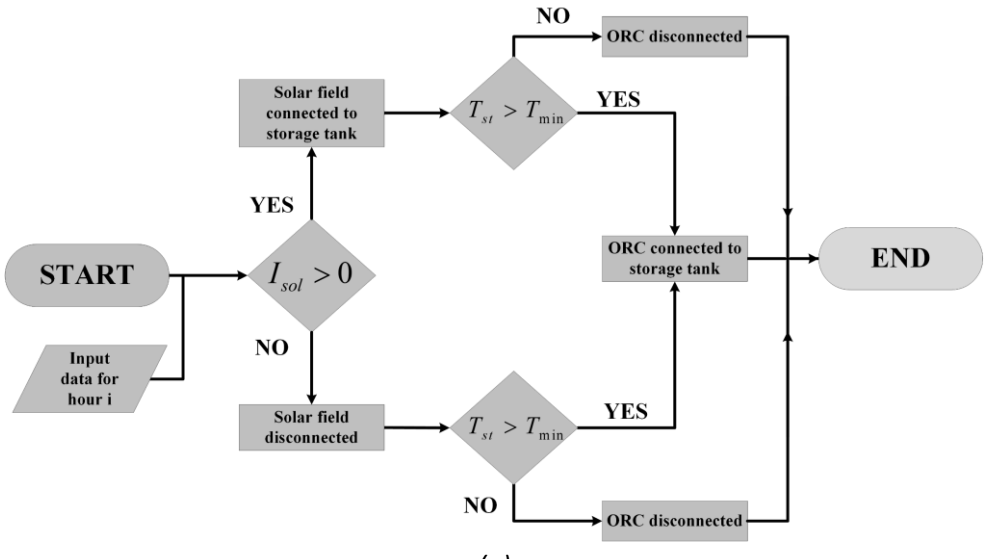

(a)

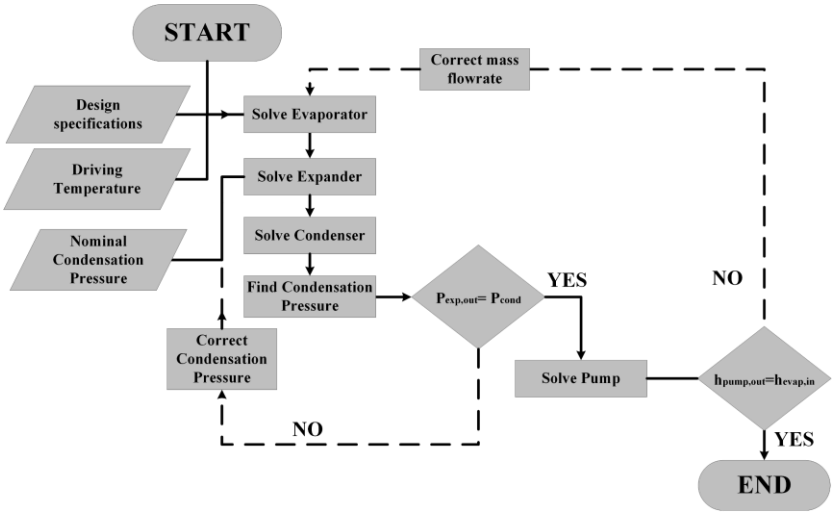

(b)

Fig. 4.2. (a) Operational strategy of solar ORC system and (b) flowchart of ORC subsystem solution

4.1.2 Performance parameters

Prior to application of the genetic algorithm, an evaluation of the design point operation was conducted with respect to the ORC. In particular, the net electric efficiency of the system is calculated for a range of driving heat temperatures. The cycle thermal efficiency is given by the following equation:

$$\eta_{th,orc} = \frac{\dot{W}_{el,gen} - \dot{W}_{el,motor}}{\dot{Q}_{evap}} \qquad (4.1)$$

The results (as shown in Fig. 4.3) indicate that when the heat source temperature is 110°C (ETCs, PTCs), the maximum cycle thermal efficiency is approximately 7% and is achieved by R245fa, followed by R152a, R236a, R1234ze(E), R134a and R227a. On the other hand, at a driving temperature of 90 °C (FPCs), the most efficient working fluid is R245fa, with an efficiency of approximately 5.4%, followed by R236ea, R152a, R1234ze(E), R134a and R227ea.

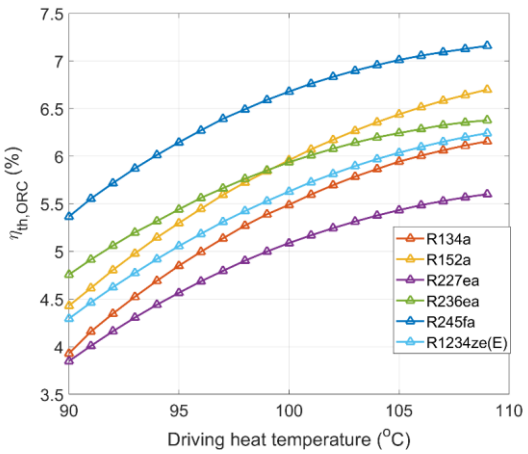

Fig. 4.3. Cycle thermal efficiency of the evaluated working fluids as a function of the driving heat temperature

In order to allow for a direct comparison of the proposed system with alternative options on low-temperature energy conversion technologies, the performance of the overall system is evaluated with respect to its exergy-second law efficiency [153]. The overall annual exergy efficiency of the solar driven ORC is equal to the annual electricity output of the system divided by the total solar exergy input (summing the respective values for each time step i) and can be estimated via the following equation:

$$\eta_{ex} = \frac{\sum \dot{W}_{el,net,i}}{\sum \dot{E}x_{sol,i}} \quad (4.2)$$

The exergy of the solar input to the system is given by the following equation [65]:

$$\dot{E}x_{sol} = \left(1 - \frac{T_{amb}}{T_{ref,sol}}\right) A_{col} \cdot I_{sol} \quad (4.3)$$

The reference solar temperature ($T_{ref,sol}$) and ambient temperature are taken equal to 5771 K and 298 K, respectively. It should be noted that the exergy of solar input based on this equation results in extremely high calculated exergy values, especially compared to the very small exergy input to the heat transfer fluid in the collectors, which has a dramatically lower temperature.

With respect to the economic performance, the system is evaluated by considering the simple payback period, considering that the entire production of the system is supplied to the grid, sold at the current national price per case (Table 4.3). The simple payback period is equal to the ratio of the investment cost divided by the net annual income of the system, according to the equation:

$$PbP = \frac{C_{tot}}{W_{net,an} \cdot c_{el} - C_{main}} \quad (4.4)$$

With the term, $W_{net,an}$, referring to the annual electricity production by the system.

The specific installation costs of FPCs, ETCs and PTCs can be found in Table I.1 of the Appendix I. The maintenance costs for the considered cases were assumed equal to 1% of the capital cost. Apart from the costs of the collectors, a number of cost correlations was implemented to estimate the total costs of the system installation, which were eventually calculated based on the equation below:

$$C_{tot} = C_{col} + C_{st} + C_{cpump} + C_{HTF} + C_{orc} + C_{inst} \quad (4.5)$$

In the above equation, the costs for the storage tank, C_{st}, were calculated from eq.(I.2), the costs of the circulator pumps, C_{cpump}, was estimated by eq.(I.3), the cost of the HTF, C_{HTF}, was estimated by Table I.2, considering a total volume equal to 150% of the storage tank's capacity. Concerning the ORC costs were estimated as the sum of the following sub-costs:

$$C_{orc} = C_{orc,fl} + C_{hex} + C_{scroll} + C_p + C_{motor} + C_{rt} + C_{hardw} \quad (4.6)$$

Concerning the costs of the working fluids, $C_{orc,fl}$, their specific costs are listed in Table I.3 of the Appendix I, based on data from the industry. The costs for the heat exchangers were derived from the equations of section I.6 of the Appendix I, while the costs for the scroll expanders were estimated based on eq. (I.11). The costs for the pump were derived from eq. (I.13), the corresponding costs for the motors were estimated from eq.(I.14) and receiver costs from eq. (I.15). Finally, the hardware costs for the ORC were assumed to be approximately 2,500 €.

Table 4.3. Price of electricity per country of application

Country	Greece	Germany	Belgium	Italy	Spain
c_{el} (€/kWh$_e$) [53]	0.1641	0.3006	0.2702	0.2153	0.2298

For the optimal cases, a further economic analysis was conducted introducing two additional indicators, namely the net present value (NPV) and the levelized cost of electricity (LCOE). For the case of NPV, a lifetime of 25 years was considered for the investment and the NPV was calculated based on the formula:

$$NPV = -C_{tot} + \sum_{t=1}^{25}\left[\frac{W_{net,an}\cdot c_{el}\cdot\left(1+r_f\right)^{t-1} - C_{main}\cdot(1+r_{om})^{t-1}}{(1+r)^t}\right] \qquad (4.7)$$

With the discount rate, r, to be considered equal to 5% [154, 155]. The term r_f refers to the annual increase in the fuel price and was considered equal to 4%, while the term r_{om} refers to the annual increase in the operational and maintenance expenditure and was considered equal to 3% [156].
On the other hand, the levelized cost of electricity can be calculated from the following equation for the same lifetime of the investment:

$$LCOE = \frac{CRF\cdot\left\{C_{tot} + \sum_{t=1}^{25}\left[\frac{C_{main}\cdot(1+r_{om})^{t-1}}{(1+r)^t}\right]\right\}}{W_{net,an}} \qquad (4.8)$$

With the capital recovery factor, CRF, to be calculated by the formula:

$$CRF = \frac{r}{1-(1+r)^{-t}} \qquad (4.9)$$

4.1.3 Results and discussion

The systems were optimized with respect to the two optimization variables which are a) the solar field area and b) the volume of the storage tank. The lower and uppers search bounds of the solar field area were taken equal to 1 and 200 m^2, respectively, considering the envisaged system scale. Accordingly, the corresponding search bounds of the storage tank volume were assumed equal to 0.5 and 5 m^3. The optimization was implemented via the GA optimization toolbox which is integrated into MATLAB. The population size of each generation was set to 50 and the calculation was executed for 10 generations. A brief discussion on the influence of the two optimization variables on the exergy efficiency and the LCOE of the system follows and is subsequently accompanied by the discussion of the results.

The installation of more solar collectors initially enables the absorption of increased solar radiation by the system and the generation of more useful heat that is converted to electricity, since the ORC can operate closer to its design point at its maximum efficiency for longer periods. However, since the maximum thermal capacity of the ORC is fixed, for a given storage tank capacity, increasing the area of the solar field beyond a certain size leads to the generation of excess heat which cannot be utilized and is wasted having a strong negative influence on the LCOE. The above leads to the existence of an optimal solar field area in each case which, for a given storage tank capacity, leads to the minimization of the LCOE. On the other hand, a monotonous, negative correlation between the solar field area and the exergy efficiency is observed. This is due to the fact that, despite leading to an increase in electricity generation, increasing the number of solar collectors leads to higher exergy destruction, due to the significantly high exergy rate of the solar radiation compared to the exergy rate of the heat transfer fluid.

Accordingly, increasing the volume of the storage tank at first enables increasing the operating hours of the system and therefore the generation of more electricity. However, given a specific solar field area, there is no added benefit to increasing the storage capacity of the tank above a certain size, as there is insufficient solar useful heat production. The above is mirrored by a stabilization of the LCOE and also the exergy efficiency of the system for increasing tank capacities.

Due to large number of evaluated scenarios hereby is presented the case of Athens, along with concentrated results for the best working fluid-solar collectors' combinations in all the evaluated cities. The corresponding Pareto fronts for the rest cities are listed in section II.1 of the Appendix II.

The Pareto fronts for the optimization results in Athens for the investigated working fluids and solar collector types are depicted in the diagrams of Fig. 4.4. Firstly, the shape of the Pareto fronts is indicative of the general trade-off between the annual exergy efficiency and the LCOE of the systems. As a matter of fact, increased storage tank capacities are required to maximize the exergy efficiency, which nonetheless encumber the system investment cost.

The influence of the system site, working fluid and collector type on the exergy efficiency and LCOE of the system are subsequently discussed.

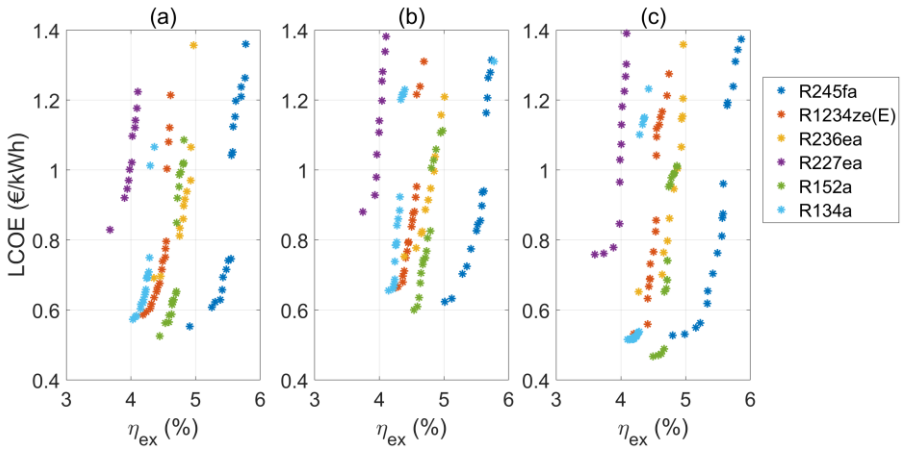

Fig. 4.4. Pareto fronts for the considered working fluids in Zone B (Athens) using (a) FPCs, (b) ETCs and (c) PTCs

I. Exergy efficiency

For more complete picture of the different cities' results, Fig. 4.5(a)-(b), present the pareto fronts of the best performing combinations of working fluid and solar collectors for the considered site of installations, both the ones that record the minimum LCOE and the ones that record the maximum exergy efficiency, respectively. Due to the fact that in all cases the ORC's performance is a heavily limiting factor to the overall system's exergy efficiency, no substantial differences in the exergy efficiency of the systems can be observed.

In all cases, R245fa tends to achieve the highest exergy efficiency, followed by R152a and R236ea, which have a similar performance. In most cases, R1234ze(E) has a slightly inferior performance compared to these aforementioned fluids and is often followed by R134a. Lastly, R227ea is in all cases the working fluid exhibiting the lowest exergy efficiency. Considering the above, a positive correlation between the ORC electrical efficiency and the annual exergy efficiency of the systems can be observed. The overall maximum obtained exergetic efficiency was equal to 5.86% using PTCs, a value that is relatively small but is mainly justified by the high exergy losses imposed by equations (4.2)-(4.3) and the overall low thermal efficiency of the considered low temperature small scale ORC, which results in a corresponding high exergy destruction within the power cycle. Fig. 4.6 presents the contribution of the system's subcomponents in the total exergy destruction. The ORC has the highest contribution with a 66%, mainly due to the exergy losses related to the evaporator and the expander. Similarly, He et al. [157] estimated the evaporator-expander contribution at 73% of the overall exergy destruction in a low temperature ORC.

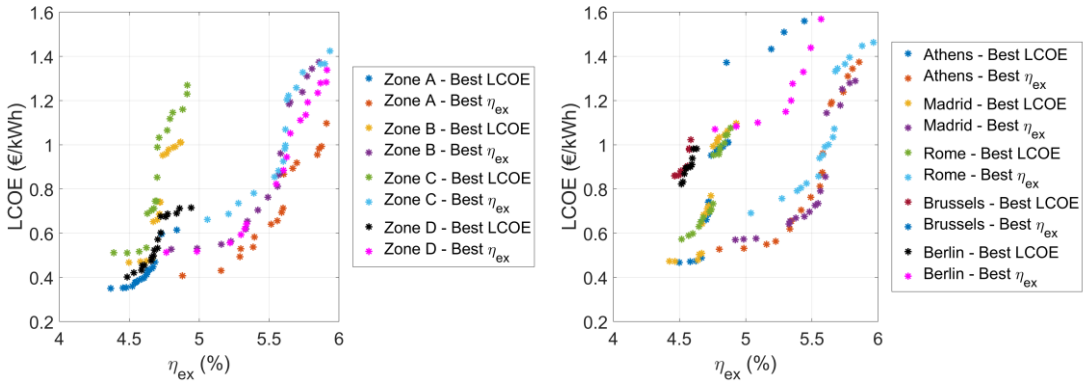

(a) *(b)*

Fig. 4.5. Pareto fronts for the optimal combination of working fluid and solar collector (a) for the climatic zones of Greece and (b) for considered European cities

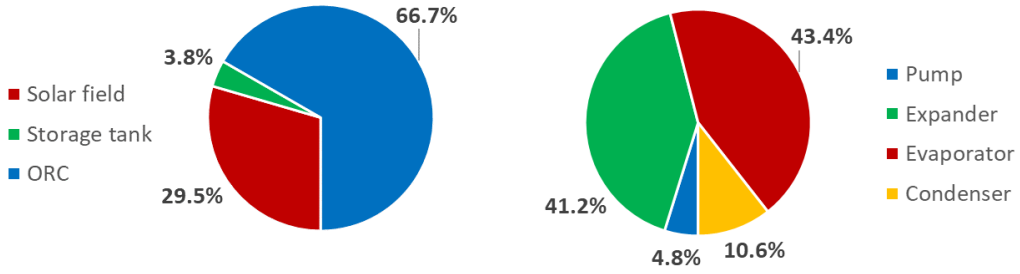

(a) *(b)*

Fig. 4.6. Breakdown of exergy losses in the solar ORC for the case of R245fa driven by PTCs in Athens

Furthermore, it can be observed that there are no significant differences between the exergy efficiency of the different collector types. As a matter of fact, the efficiencies of FPCs and ETCs are similar for the investigated collector temperature range. Meanwhile, although PTCs feature higher efficiency, they utilize a smaller portion of the solar radiation.

II. LCOE

The operation of the system in Athens and Chania, as shown in the Pareto fronts of Fig. 4.4-Fig. 4.5, results in better economic performance, owing to the higher solar irradiance. The excess of solar energy leads to higher useful heat generation and hence enables the operation of the ORC for more hours and at higher efficiencies, eventually leading to increased annual electricity generation. More specifically, the lowest LCOE is observed for all types of collectors in the city of Athens with values of 0.5258 €/kWh for the FPC driven system using R152a, 0.6002 €/kWh for the ETCs scenario with R152a and 0.4677 €/kWh for the PTC driven system using R152a. In fact, the LCOEs calculated are relatively high; however, one should consider that in several countries including Greece, that were investigated in this study, certain financial incentives could be applied -relevant to the penetration of renewables in energy sector and the EU 2030 and 2050 targets [158]- to further enhance system's economics and the overall growth of solar ORC market.

In the majority of the examined cases, R152a shows the lowest LCOE values, followed by R245fa and R1234ze(E), while R227ea as well as R236ea exhibit the worst economic profitability. Based on the above, it can be observed that the main factor guiding the differences in the LCOE among the working fluids is their purchase cost. This is an expected result, considering that the main operating technical and performance specifications of the ORCs operating with the examined fluids are similar, featuring only minor differences in their electrical efficiencies, power outputs, and size of heat exchangers. Regarding the influence of the solar collector type on the LCOE, the superiority of PTCs is clear, as they combine competitive costs with higher efficiencies compared to FPCs and ETCs, which lead to roughly similar LCOEs. An overview of the purchase costs breakdown for a tested scenario with 52.4 m^2 of PTCs and a 0.36 m^3 driving an ORC with R152a is shown in Fig. 4.7.

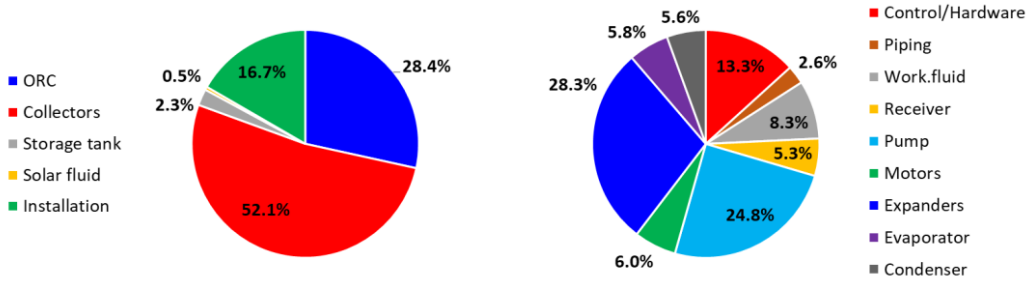

(a) *(b)*

Fig. 4.7. Cost breakdown for a system with 52.4 m^2 of PTCs, a 0.36 m^3 storage tank and an ORC with R152a as working fluid

Fig. 4.8 provides an overview of the optimal solutions determined by the GA for all working fluids in Athens, respectively, considering a PTC-driven ORC. As shown, there is an optimal value of the solar field area for which the LCOE is minimized for both cities, which recorded the lowest values of the LCOE. For higher solar field areas, the increase in the economic competitiveness of the system is negligible. This is due to the fact that the investigated system

includes only one scroll expander and thus the overall power output is constrained by its power capacity limit. As a result, unless the system is designed to higher capacities and thus a second expander is installed or the scroll expander is substituted by a screw device, the system cannot utilize the additional heat supplied by the solar field. Hence, within the range of this study (<5 kWe) the optimal solar field is approximately 75 m². With respect to the storage tank, smaller capacities are favored as it is more beneficial to directly consume all the available heat for the considered scenario.

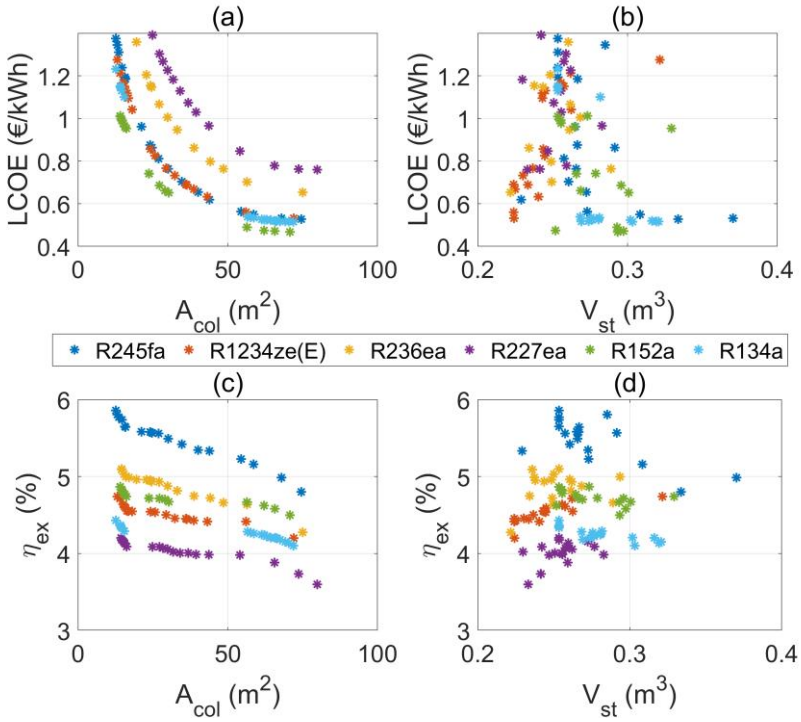

Fig. 4.8. Overview of genetic algorithm results for the case of PTCs in Athens for the considered working fluids

III. NPV and PbP

Following the aforementioned results, an additional analysis was conducted for the economics of the PTCs, which were found to be the most promising -economically- type of solar collectors. Based on equations (4.3)-(4.7), the NPV and the PbP can be calculated for the considered working fluids and the different locations for various solar field areas. Similarly to the LCOE, as shown in Fig. 4.9, the economics of the proposed solutions needs further improvement before being economically viable. The most promising results are identified in the case of Chania, owing to the excess of solar irradiance throughout the year, as shown in Table 4.4-Table 4.5. The maximum NPV reported was equal -8.56 k€ using R152a in Madrid. The corresponding maximum NPV for the case of Athens, which is the second-best performing region, was -14.93 k€. The parabolic shape of almost all lines is justified by the fact that the ORC system is designed with a maximum power output of <5 kW, which makes the use of larger solar fields non-profitable as the additional harvested solar energy cannot be utilized unless the ORC system is oversized and therefore the economics deteriorate for larger solar areas. This behavior is even more clear in Table 4.5, which shows the economic results for the different regions. In fact, as expected the performance of the system deteriorates as the site of installation moves to countries with reduced solar irradiance, such as Germany (Berlin) and Belgium (Brussels). A particular highlight of the optimal results of Table 4.5, is the case of the

optimal economic solution for Madrid, which was the highest reported NPV with -8.13 k€, mainly owed to the higher electricity prices of Spain, in combination with the high solar irradiance values.

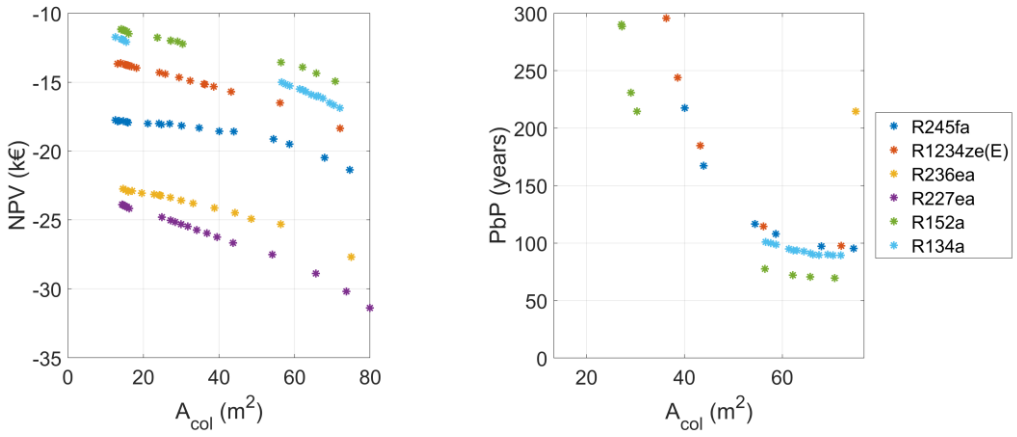

(a) *(b)*

Fig. 4.9. (a) Net present values and (b) Payback periods for different working fluids in Athens using PTCs

Table 4.4. Overview of the optimal combinations of working fluids and solar collector types in the tested cities

City/Objective	Working fluid	Collector type	A_{col} (m²)	V_{st} (m³)
Chania – max η_{ex}	R245fa	PTC	12.66	0.45
Chania – max LCOE	R152a	FPC	52.39	0.36
Athens – max η_{ex}	R245fa	PTC	12.62	0.25
Athens – max LCOE	R152a	PTC	70.72	0.29
Thessaloniki – max η_{ex}	R245fa	ETC	13.12	0.25
Thessaloniki – max LCOE	R152a	PTC	73.84	0.28
Kozani – max η_{ex}	R245fa	PTC	13.74	0.46
Kozani – max LCOE	R152a	FPC	51.20	0.27
Madrid – max η_{ex}	R245fa	FPC	13.21	0.24
Madrid – max LCOE	R152a	PTC	66.91	0.28
Rome – max η_{ex}	R245fa	ETC	13.71	0.20
Rome – max LCOE	R152a	FPC	58.48	0.21
Brussels – max η_{ex}	R245fa	PTC	14.38	0.26
Brussels – max LCOE	R245fa	FPC	85.42	0.22
Berlin – max η_{ex}	R245fa	PTC	13.24	0.22
Berlin – max LCOE	R152a	FPC	64.99	0.23

Table 4.5. Overview of the optimal combinations' results of working fluids and solar collector types in the tested cities

City/Objective	η_{ex} (%)	$LCOE$ (€/kWh)	NPV (k€)	PbP (years)
Chania – max η_{ex}	5.91	1.097	-17.08	n/a
Chania – max LCOE	4.37	0.350	-8.56	38.6
Athens – max η_{ex}	5.86	1.374	-17.76	n/a
Athens – max LCOE	4.50	0.468	-14.93	69.5
Thessaloniki – max η_{ex}	5.93	1.424	-20.12	n/a
Thessaloniki – max LCOE	4.49	0.511	-16.83	87.2

Kozani – max η_{ex}	5.91	1.338	-18.25	n/a
Kozani – max LCOE	4.49	0.402	-10.97	49.9
Madrid – max η_{ex}	5.83	1.289	-16.45	n/a
Madrid – max LCOE	4.47	0.473	-8.13	36.1
Rome – max η_{ex}	5.97	1.463	-19.10	n/a
Rome – max LCOE	4.52	0.573	-13.45	59.4
Brussels – max η_{ex}	5.86	3.684	-19.74	n/a
Brussels – max LCOE	5.10	0.852	-24.97	90.16
Berlin – max η_{ex}	5.87	2.837	-18.31	n/a
Berlin – max LCOE	4.51	0.822	-14.97	63.14

In the aforementioned analysis, has to be noted, that no premiums or subsidies were considered. However, it is worth analyzing the effect that a feed-in tariff would have in the economic competitiveness of the proposed systems. Based on the Greek legislation, there is a 0.248 €/kWh feed-in tariff for solar thermal power generation. Applying this value, in the NPV and PbP calculation of Table 4.5 results, reveals a more promising picture of the low temperature ORCs, which is summarized in Table 4.7. In fact, the case of Chania reported back positive NPV, with a value of 3.14 k€, and a corresponding PbP of 19.3 years.

Table 4.6. Overview of the feed-in tariff effect on the optimal solutions in Greece

City/Objective	η_{ex} **(%)**	$LCOE$ **(€/kWh)**	NPV **(k€)**	PbP **(years)**
Chania – max η_{ex}	5.91	1.097	-14.26	n/a
Chania – max LCOE	4.37	0.350	3.14	19.3
Athens – max η_{ex}	5.86	1.374	-15.55	n/a
Athens – max LCOE	4.50	0.468	-5.41	29.5
Thessaloniki – max η_{ex}	5.93	1.424	-17.77	n/a
Thessaloniki – max LCOE	4.49	0.511	-7.87	34.2
Kozani – max η_{ex}	5.91	1.338	-15.90	n/a
Kozani – max LCOE	4.49	0.402	-0.98	23.4

4.1.4 Sensitivity analysis

As it is evident, the results of the above analysis are sensitive to the respective capital costs of each separate component, the improvements in the component's efficiencies as well as the energy prices in the tested countries. Therefore, a sensitivity analysis was conducted to evaluate the influence of certain variables in the system's performance.

I. Reduction in CAPEX

With the expansion of the ORC market and the component's evolution with the inherent performance improvements, the specific costs for solar ORCs are expected to decrease in the future. As expected, a reduction in the CAPEX would improve system's economic performance. In fact, in all evaluated cities, considering only the optimum LCOE scenarios of Table 4.5, a significant improvement can be observed by assuming a 10% and 20% reduction of the CAPEX, respectively. With respect to the best performing cases, in the scenario of a 20% reduction of the CAPEX, the optimum system in Chania would record a LCOE of 0.280 €/kWh, while the corresponding value for Madrid would be 0.378 €/kWh and the corresponding in

Athens equal to 0.375 €/kWh. An overview of the CAPEX's influence in the system's LCOE for the optimum cases per city can be shown in Fig. 4.10(a).

II. Period of investment

As mentioned above, the base case scenarios were conducted considering a 25 years period of investment, which is a typical value for ORCs. However, studies can be found in literature which consider different lifetimes for ORC systems, ranging mostly between 20 years [159, 160] and 25 years [161-163]. In this analysis, the variation of the LCOE with 20- and 30-years period of investment was considered. The results of the analysis are listed in Fig. 4.10(b). As expected, an increase in the years of investment deteriorates the performance, with the corresponding LCOE for 20 years period of investment and for the optimal case of Chania to be equal to 0.378 €/kWh, while all other reported LCOEs exceed 0.43 €/kWh.

III. Electricity price

An important aspect on the system's economics is the electricity price. Electricity price are expected to increase with the depletion of the fossil fuels and therefore is critical to have a preliminary view of its effect on the economics of systems, such as the tested. Given the fact that the LCOE does not implement the electricity price, according to equation (4.8), Fig. 4.10(c)-(d) present its influence on the PbP and the NPV, respectively. As shown, an increase of 20% in the electricity price (in absolute numbers approximately 3.2 c€ for the case of Greece), resulted in a significant benefit on the solar ORC performance. In fact, the PbP for the optimum case of Chania was reduced to 28.49 years, while the corresponding PbP for Madrid was as low as 26.88 years. The corresponding values for the NPV values of Chania and Madrid were -4.43 k€ and -3.65 k€, respectively.

IV. Solar system and ORC efficiency

In a similar manner to the possible decrease of the CAPEX, the improvements in the involved technologies will lead to direct effects on the system's efficiency and thus improve both the LCOE, Fig. 4.10(e), and the system's exergy efficiency, Fig. 4.10(f). As shown in both figures, the ORC performance enhancement has slightly higher influence on the system's economic and exergetic performance. This is a reasonable outcome, since a possible improvement in the solar harvesting system, without a substantial increase in the ORC's efficiency or a relatively increase in the ORCs capacity, would lead to amounts of solar heat being unused and eventually lost. Hence, for the case of Chania a 10% increase in the ORC's thermal efficiency leads to an LCOE of 0.318 €/kWh and an exergy efficiency of 6.50%, while the corresponding values for a 10% increase in the solar collectors' efficiency are 0.327 €/kWh and 6.32%, respectively.

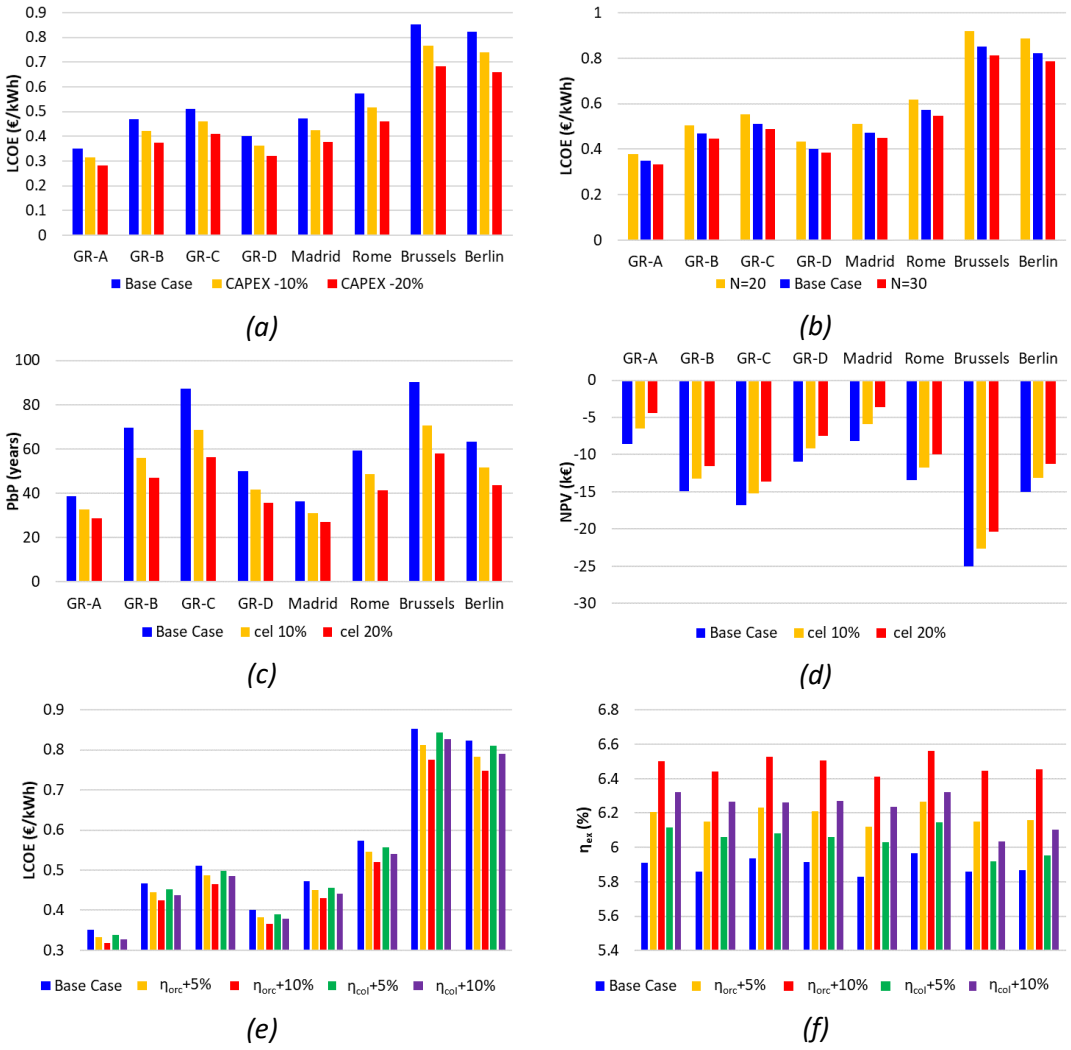

Fig. 4.10. Results of the sensitivity analyses: (a) influence of the reduction in the CAPEX on the LCOE; (b) influence of the period of investment in the LCOE; influence of the electricity prices (c) on the payback period and (d) on the NPV; influence of the solar system and ORC efficiencies (e) on the LCOE and (f) on the exergy efficiency

4.1.5 Conclusions

In this study, a solar-driven small-scale ORC has been optimized using a genetic algorithm with respect to the exergy efficiency and the payback period. The proposed system was evaluated for a number of different solar collector types (FPCs, ETCs and PTCs), working fluids and locations in Europe, namely Athens (Greece), Rome (Italy), Madrid (Spain), Berlin (Germany), Brussels (Belgium). Moreover, the variation of the system's performance in the different climatic zones of Greece was evaluated with the addition of Chania (Zone A), Thessaloniki (Zone C) and Kozani (Zone D). The main conclusions of the study are summarized below:

- Within the examined driving heat temperature range (90-110°C), R245fa had the highest thermal efficiency, which was slightly above 7% at 110°C, followed by R152a and R236ea at higher and lower driving heat temperatures, respectively.
- The exergy efficiencies all collector types are similar for the investigated collector temperature range, since although PTCs have a higher efficiency, they utilize a smaller portion of the solar radiation.

- PTC collectors, despite exploiting only the direct solar irradiance, tend to result in better performance and thus are associated with the lowest LCOE in the range of 0.35 €/kWh, owing to their high efficiency and lower costs.
- The investigated systems have very low exergy efficiencies in the range of 2-6%, mostly due to the poor exergy efficiencies of the solar collectors, considering the extremely high exergy of solar radiation and the low exergy difference of the heat transfer fluid in the collectors.
- Working fluids with the lower prices, such as R152a, R1234ze(E) and R134a are associated with lower LCOEs. Despite not having the lowest cost, R245fa has a very good thermal efficiency and thus represents an attractive trade-off between economic and thermodynamic performance. The working fluid cost can have a significant impact on the economic profitability of such systems and it should not be neglected.
- Lower storage tank capacities are optimal. For each storage tank capacity, increasing the area of the solar field, above a certain threshold, results in excess heat generation and has a monotonous negative influence on the exergy efficiency. Furthermore, although it initially leads at lower payback periods, beyond a certain value it does not improve the economic viability of the system.
- Under a case study considering a PTC-driven ORC with a solar field area of 52.39 m^2 and a 0.36 m^3 storage tank operating with R152a, 52.1% of the investment cost was due to the solar field, while the costs of the ORC and storage tank were equal to 28.4% and 2.3% of the investment cost, respectively. The most significant cost component of the ORC were the expander (28.3%) followed by the pump (24.8%) and the control/hardware (13.3%).
- The optimal economic performance, corresponding to a LCOE of 0.350 €/kWh, was achieved by systems operating with R152a in Chania, due to the high solar irradiance in this site. The economic analysis with respect to NPV, over a lifetime period of 25 years, revealed that no system could achieve positive NPVs.
- The results of the economic analyses highlight the need for certain financial incentives in order the proposed solutions to become competitive with the current status in manufacturing and electricity costs.

4.2 Techno- economic analysis of a medium temperature solar driven small-scale ORC

The analysis of this section was presented in the article “Techno-economic optimization of medium temperature solar driven subcritical Organic Rankine Cycle” [64]. In a similar manner to the study of section 4.1, for a uniform analysis, all GAs of this analysis were re-run under the new cost inputs.

The present work aims at the systematic techno-economic optimization of high-temperature solar ORCs driven by PTCs and parabolic dish collectors (PDCs), considering their off-design, annual performance in five European cities, namely Athens, Madrid, Rome, Brussels and Berlin. The selection of these cities was based on their climate classification according to the Köppen-Geiger climate specification [164]. The abovementioned cities are located southern and central Europe and were chosen in order to ensure adequate annual direct solar irradiation. Regarding the southern ones, all of them are characterized by Mediterranean climate, however with different characteristics in terms of aridity; Rome’s climate is classified

as pure Mediterranean whereas Athens' and Madrid's climates tend to be characterized as hot and cold semi-arid climates, respectively. This temperature variation provides useful insight and was therefore selected. With regard to Berlin and Brussels, their climates are considered Marine West Coast cli-mates and both, yet they exhibit a different cloud coverage throughout the year. In fact, as shown in Table 4.7, Madrid and Athens exhibit the highest annual direct normal irradiance, while the corresponding value for Brussels is almost three times less and slightly lower than in Berlin. Apart from the aforementioned cities, in a similar manner to section 4.1, a case study was assessed for the different climatic zones of Greece, with the same cities, namely Chania (zone A), Thessaloniki (Zone C) and Kozani (Zone D).

Table 4.7. Annual direct normal irradiance for a number of European cities.

City	Athens	Madrid	Rome	Brussels
Value (MWh/m²)	1519,8	1542,3	1204,8	508,9
City	Berlin	Dublin	Warsaw	Copenhagen
Value (MWh/m²)	585,1	577,45	676,5	698,6

The off-design performance of the systems is evaluated with the development and integration of a series of off-design models for all equipment components (solar collectors, thermal energy storage tank, heat exchangers, expander, pump, motor/generator) to accurately simulate their operation under realistic, variable conditions. Furthermore, cost correlations based on literature data and manufacturers' datasheets are used to enable the detailed capital and operational cost estimation. In each case, a GA optimization technique is implemented to determine the optimal solar field area and storage tank capacity with regard to the maximum annual exergy efficiency and minimum LCOE of the solar ORCs.

4.2.1 ORC system modelling

The layout of the investigated solar ORC is illustrated in Fig. 4.11. The HTF is heated in the field of solar collectors and is conveyed to the heat storage tank in the collectors' sub-circuit. Subsequently, and depending on the operating mode of the system, the HTC circulates from the storage tank to the ORC evaporator to provide heat to the cycle.

Depending on the operating conditions, a second expander is considered when the pressure ratio of the cycle is higher than a maximum expansion ratio. Meanwhile, a recuperator is added to recover heat from the expanded superheated vapor for preheating the subcooled liquid after the pump. Finally, the condensation of the working fluid is achieved through a water-cooled condenser.

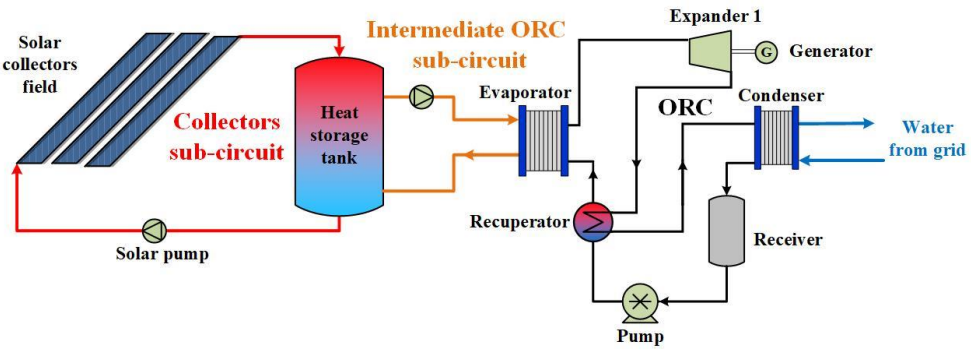

Fig. 4.11. Layout of the investigated solar driven ORC with a recuperator and two in-series expanders system

The solar collectors were modelled based on the equations (2.1)-(2.5), considering the coefficients for PTC-2 and PDC from Table 2.1. For both types of solar collectors, it was decided to consider a sun tracking system to maximize the absorbed solar energy. A single-axis tracking mechanism was considered, in which the collectors are fixed with respect to the north-south axis and rotate around an axis with the direction of east-west.
Correspondingly, the storage tank modelling was based on the analysis of section 2.2. For the heat loss coefficient of the storage tank to its surroundings, U_l of equation (2.13), it was assumed to be equal to 2.5 W m^{-2} K^{-1} [165]. For both sub-circuits interconnected with the storage tank, the same HTF was selected based on the maximum working temperatures. The selected HTF is Therminol VP-1, which is commonly used at temperatures above 250 °C, since its maximum working temperature is approximately 327°C [18, 166].
All the ORC components were modelled based on equations of section 3.5. Since the system was intended for use in medium to high temperatures and the corresponding working fluids results in higher pressure and volume ratios, screw expanders were used in the analysis, and therefore the equations of section 3.5.3 were used for the expander modelling.

4.2.2 Performance parameters

Prior to application of the genetic algorithm, an evaluation of the design point operation was conducted with respect to the ORC. In particular, the net electric efficiency of the system is calculated for a range of driving heat temperatures. Due to the presence of the recuperator, the cycle thermal efficiency is given by the following equation:

$$\eta_{th,orc} = \frac{\dot{W}_{el,gen} - \dot{W}_{el,motor}}{\dot{Q}_{evap} - \dot{Q}_{rec}} \qquad (4.10)$$

In the above formula, the difference in the denominator is the final heat supplied to the evaporator, which is equal from the initially imposed evaporator's heat duty reduced by the heat duty of the recuperator.
The independent design variables of the ORC are the evaporation and condensation pressure as well as the mass flowrate of the working fluid. These variables were selected by taking into account the boundary conditions and constraints that are presented in Table 4.8.

Table 4.8. On-design working parameters of ORC.

Property	Value
Evaporator heat duty (kW)	40.0
Heat exchangers pinch point (K)	5.0÷40
Condenser subcooling (K)	5.0
HTF inlet temperature (°C)	210
HTF inlet pressure (bar)	1.5
HTF mass flow rate (kg/s)	0.8
Single expander pressure ratio (-)	2.4÷6.1
Cooling water inlet temperature (°C)	20.0
Cooling water inlet pressure (bar)	2.0
Cooling water mass flow rate (kg/s)	1.0

Based on the parameters set in Table 4.8, a dedicated single objective optimization algorithm is executed to find the optimal specifications of the ORC cycle for each of the considered working fluids towards the maximization of the cycle's thermal efficiency. Depending on the operating conditions, a second expander is considered when the pressure ratio of the cycle is higher than the maximum expansion ratio of a single expander (set at 6.1). Meanwhile, a recuperator is operational when the temperature difference between the expander outlet temperature and the condensation temperature is great-er than 20 K. Both the second expander and the recuperator can be bypassed if their operating criteria are not met with the addition of two diverting three-way valves.

4.2.3 Working fluid selection

Working fluid selection is based on the critical properties and thermodynamic efficiency. In the present case, the thermodynamic efficiency at the nominal operating point listed above in Table 4.9 was the main selection criterion. In most applications, the maximum efficiency is attained with fluids whose critical temperature is slightly higher than the cycle's driving temperature, in order to achieve maximum heat source utilization [167]. Since the maximum temperature of the solar loop is around 210 ^{o}C, only fluids with critical temperatures higher than this value were examined in the study. Although, fluids with critical temperatures above 300 ^{o}C cannot be effectively coupled with the HTF, some notable fluids with wide commercial application with critical temperatures exceeding this value were also assessed [66] for the sake of completeness. The list of the considered working fluids along with their critical properties and their type in terms of dry, wet or isentropic behavior, are presented in Table 4.9. With regard to fluid type, fluids are divided into dry, wet and isentropic based on the slope of temperature-specific entropy saturation curve in the in the saturated vapor region. In particular, dry fluids have a positive slope (Fig. 4.12), wet fluids a negative slope whereas an almost vertical line appears in isentropic fluids. All considered fluids are dry to avoid droplet formation during expansion and environmentally friendly, i.e. they have negligible Global Warming Potential and zero Ozone Depletion Potential. The fluids that are selected for the main analysis of the study are highlighted in grey. These include the fluids yielding the highest efficiency values, as well as Toluene, which has an extensive use in commercial ORC systems [18]. Since, according to equation (18), expander efficiency is almost constant, exceeding 70%, for pressure ratios higher than 4 and the examined cycles correspond to two-stage cycles with the pressure ratios of both machines above 4, the difference is derived from the isentropic enthalpy difference during expansion and the pump's consumption. The former is a property of the fluid and is maximized for the selected fluids whereas the latter depends on the volume flow rate and the difference between evaporation and condensation pressures. Although the pressure difference is higher for the selected fluids, they exhibit higher expansion enthalpic difference, which outperforms the increased pump consumption.

Table 4.9. Properties and calculated design thermal efficiency of examined organic fluids [151, 168]

Organic fluid	T_{crit} (°C)	P_{crit} (bar)	Fluid type	P_{evap} (bar)	$T_{max,orc}$ (°C)	P_{cond} (bar)	$\dot{W}_{el,net}$ (kW)	$\eta_{th,orc}$ (%)
Isohexane	225	30.4	Dry	20.47	203.2	0.55	5.16	17.01
Acetone	235	47.0	Dry	25.24	199.5	0.68	6.07	15.17
Hexane	235	30.34	Dry	17.18	201.9	0.46	5.14	16.78

Cyclopentane	239	45.71	Dry	24.99	200.7	0.67	6.17	17.24
Methanol	240	82.16	Wet	12.04	204.7	0.32	5.74	14.14
Ethanol	242	62.68	Wet	23.02	204.9	0.62	5.34	12.90
Heptane	267	27.3	Dry	9.10	202.7	0.24	4.70	16.02
Cyclohexane	280	40.82	Dry	12.24	199.2	0.33	5.52	17.02
Benzene	289	48.9	Dry	12.82	198.0	0.34	5.90	16.39
MDM	291	14.1	Dry	2.80	201.3	0.08	3.34	13.77
Octane	296	25.0	Dry	4.93	199.8	0.13	4.35	15.10
Toluene	319	41.3	Dry	6.53	197.4	0.18	5.37	15.71
n-Nonane	321	22.7	Dry	2.80	193.9	0.08	4.05	14.21
p-Xylene	343	35.3	Dry	3.66	196.7	0.09	4.92	14.88

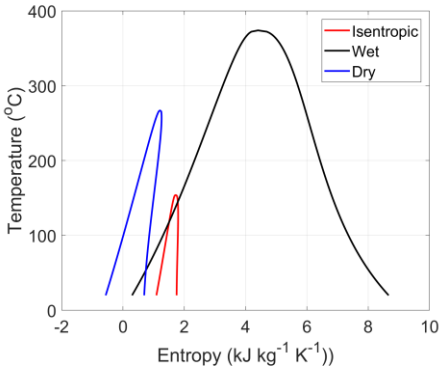

Fig. 4.12. Temperature vs specific entropy saturation curve of dry, wet and isentropic fluids

In order to take into account the fluctuations in the driving temperature, a corresponding modelling of the off-design operation of the system is performed as well. The lowest HTF temperature which is the threshold for the operation of the ORC system is taken equal to 180°C (T_{thr}). Thus, as the HTF varies from 180 °C to 210 °C the power absorbed by the evaporator varies from 20 kWth to up to its nominal heat duty of 40 kWth. For intermediate HTF temperatures between 180 and 210°C, a linear variation of the heat in-put to the ORC is considered.

4.2.4 Results of the GA on medium temperature ORC

Similarly to the case of low temperature ORCs, a multi-objective genetic algorithm was implemented to optimize the system's performance with two objective functions a) the system's exergy efficiency which must be maximized and b) the LCOE which must be minimized. Two independent optimization variables are considered: the collectors' surface (A_{col}) and the storage tank's capacity (V_{st}). The boundaries for the genetic algorithm's variables are listed in Table 4.10. As initial conditions were set a solar field of 120 m² and a storage tank of 3.0 m³, as the ratio of 40 m²/m³ is commonly applied in solar driven applications with TES [63] and the initial setpoint was preferred to have average values for the considered range of evaluation. The population of each generation was equal to 50, which is a sufficient number of offspring for a two-variable problem. The optimization was set to terminate after 20 generations.

Table 4.10. Genetic algorithm boundaries and initial conditions s

Parameter	Range
Solar collectors' field (m²)	10 ÷ 400
Initial solar collectors' surface (m²)	120
Storage tank capacity (m³)	0.2 ÷ 5.0
Initial storage tank capacity (m³)	3.0

Overall, 96 scenarios were evaluated, consisting of the 8 cities, 6 working fluids/ORC nominal designs and 2 types of collectors. With the use of the genetic algorithm, the Pareto fronts are produced for the optimization results in these scenarios, which depict the fluctuations in the optimized objectives, as shown in Fig. 4.13-Fig. 4.14.

The shape of the Pareto fronts illustrates that there is a trade-off between the optimization criteria of exergy efficiency and LCOE [169]. It is obvious that the exergy efficiency and the LCOE are conflicting objectives, since a small unit may achieve effective exploitation of the available solar power, but the produced electricity will not be sufficient in order to cover its investment cost, affecting severely its economic performance. For example, increasing the area of solar collectors enables the ORC to operate closer to its nominal point (and hence at higher efficiencies) for longer periods of time, leading to an increase of the exergy efficiency. However, the increased generated electricity does not necessarily compensate for the higher cost of the solar field. Accordingly, increasing the storage tank volume extends the capacity factor of the system and results in increased exergy efficiencies, but the increased cost of the tank may lead to disproportionately increased capital costs and have a negative influence on the LCOE. The above point is illustrated in Fig. 4.15, which presents an overview of the results of the genetic algorithm in an indicative scenario of Athens with PTCs for all the examined working fluids is presented. In this figure, the variation of the two objectives (n_{ex} and LCOE) with respect to the two variables of the system (A_{col} and V_{st}) is illustrated.

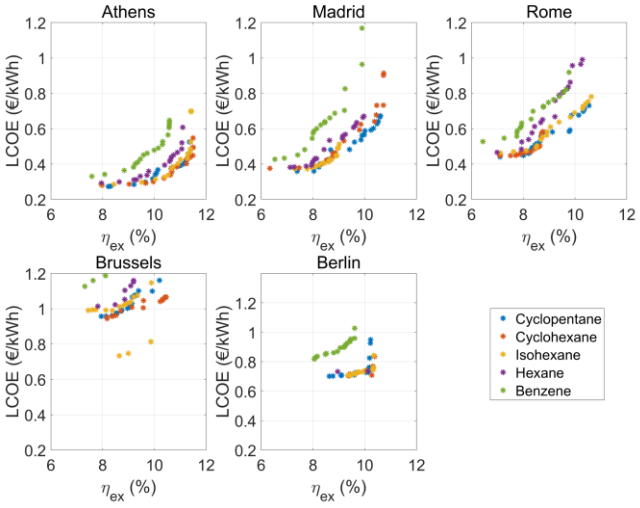

(a)

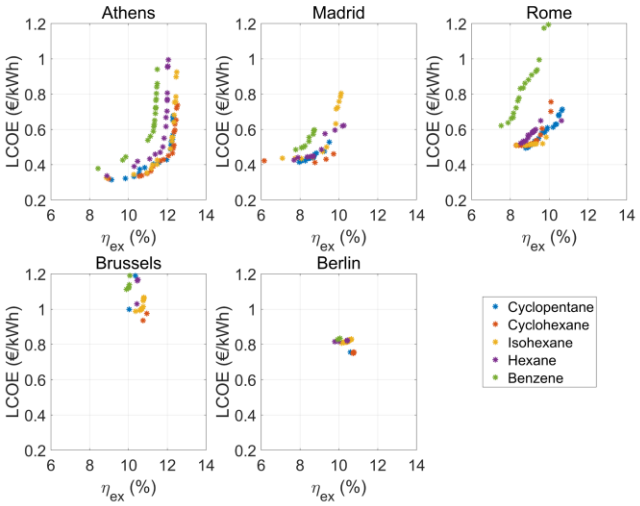

(b)

Fig. 4.13. (a) Pareto fronts for the considered working fluids in the examined European cities in case of PTCs; (b) Pareto fronts for the considered working fluids in the examined cities in case of PDCs

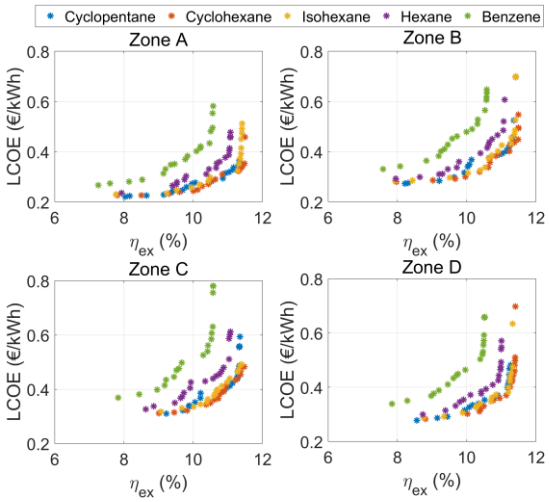

(a)

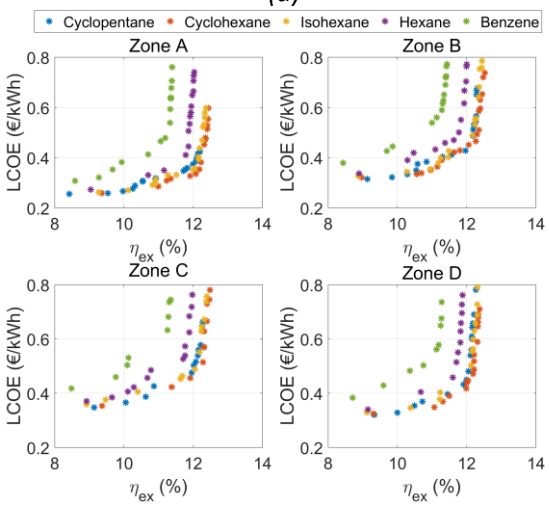

(b)

Fig. 4.14. (a) Pareto fronts for the considered working fluids in the evaluated Greek cities in case of PTCs; (b) Pareto fronts for the considered working fluids in the evaluated Greek cities in case of PDCs

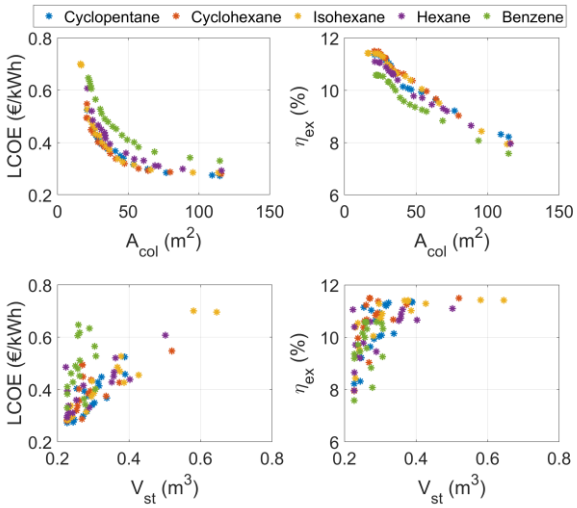

Fig. 4.15. Optimization parameters with respect to input variables for all the working fluids in case of Athens and PTCs

I. Exergy efficiency

It can be observed that comparable exergy efficiencies are obtained in northern and southern regions, both for the case of the European cities as well as the Greek climatic zones. That happens because in the case of the northern cities the available solar energy is limited, which leads to lower thermal input to the ORC. Since in all cases the system works with the same nominal characteristics, in northern regions there is a direct exploitation of solar production and thus the stored energy losses are reduced, counter-balancing the excess of solar irradiance and the higher production of the southern regions.

Concerning the examined working fluids, it can be observed that they do not lead to substantial differences in the calculated efficiencies. As it can be observed in most of the above diagrams, Cyclohexane tends to achieve the highest performance, followed by Cyclopentane and Isohexane. In most cases, Toluene appears to yield slightly inferior efficiencies followed by Benzene. The main factor that influences the system's operation is their thermodynamic performance. The overall maximum exergy efficiency achieved in the studied cities lies between 12.0-12.6%. These values are, in general, lower to similar design studies. However, this is attributed mainly to the fact that this analysis considered in detail the induced losses in the system, including the exergy losses to the ambient, the pump's losses, which often are under-estimated in literature, and the losses in the inverters and generators. Furthermore, it can be observed that the although PDCs appear to lead to slightly higher exergy efficiencies compared to PTCs, the difference in the performance of the systems operating with these two types of collectors is insignificant.

II. LCOE

The influence of the geographical location on the LCOE is much more significant than its influence on the total conversion efficiency. As already mentioned, for southern cities, the available solar energy is higher, leading to higher useful power generation and enabling the

ORC operation for more hours annually and closer to nominal conditions, achieving a corresponding increase in the final power output. The increased electricity generation results in increased cash inflows and in reduced LCOE values, improving the economic viability of the system. More specifically, in the case of Athens, which represents the financially optimal result for the European cities, the cost of electricity for the PTC-Cyclopentane scenario is close to 0.27 €/kWh, whereas the corresponding LCOE in Brussels is 0.73 €/kWh. With respect to the Greek zones, in a similar manner, the optimal performance can be found in the southern climatic zone (zone A), with the case of Chania, reporting an optimum LCOE of 0.22 €/kWh for the PTC-Cyclopentane combination.

Cyclopentane and Cyclohexane present the most profitable results, whereas Toluene, Benzene and Hexane result in the higher cost of the produced energy. Since the studied fluids are all hydrocarbons and have in general similar price, their costs end up to not being a critical parameter in the optimization process. Therefore, the system's operation is again ruled mainly by the thermodynamic performance and the sizing of the equipment components.

As for the influence of the solar collector type on the LCOE, the results present a superiority of PTCs in all the examined scenarios. Since the differences in the thermal and exergy efficiency are close to negligible, the lower cost of PTCs is a major advantage leading to lower LCOE and more viable economic outcomes.

4.2.5 Results interpretation

The correlation between the collecting surface and the optimization objectives is shown minutely in Fig. 4.15. The collecting surface appears to be negatively correlated with both the exergy efficiency as well as with the cost of electricity. When the surface is too small, the useful solar heat is limited which leads to an almost full use of the energy inflow to cover the thermal needs of the ORC, thus yielding high efficiencies due to the reduced storage losses. However, at the same time the generated electrical energy is proportionally limited because the system is operational for fewer hours annually, leading to an increase of the LCOE. As the collecting surface increases, the energy received by the collectors is also increased and thus more energy remains unexploited due to the low size of the ORC, leading to increase in exergy losses. Nevertheless, the ORC operates for longer periods at higher efficiencies, producing more electrical energy and thus the LCOE is reduced. Overall, a negative correlation between the optimization targets and the collectors' surface is observed.

As shown in the figures, the solar field area corresponding to the optimal economic performance is limited to around 150 m². For higher collecting areas, the improvement in the economic competitiveness of the system is negligible, since it simply increases the CAPEX without offering any benefit in terms of energy production. This region is not depicted in the diagrams, since it corresponds to both minimized exergy efficiency and financial performance. The above is a result of the on-design sizing of the system's components. In particular, because the scale of the ORC is relatively small, the heat duty in the evaporator and the ORC thermal capacity are rather low and can be covered with a relatively small collecting surface. Consequently, the addition of more solar collectors only causes the production of excess solar heat, which, for a given storage tank capacity, does not benefit the power production and has a negative impact on the optimization variables.

Concerning the volume of the storage tank, it appears to be positively correlated with the exergy efficiency, since higher volumes result in increased system operating hours and thus

reduced exergy losses. However, given a specific collecting area, an increase in the storage capacity beyond a specific value does not offer any more benefits and even increases the capital cost of the system, resulting in a stall of economic and exergy efficiency.

Additionally, it can be observed that the optimal results are concentrated in a range of relatively small storage tanks. This is justified both in terms of efficiency as well as in terms of economic performance. It is obvious that the higher storage tank volumes increase the CAPEX, while at the same time they increase the thermal inertia of the system. Larger tanks would demand much higher thermal power from the collectors to increase their temperature since they contain larger quantities of HTF and have greater losses towards the environment. Therefore, even though the inspected range is between 0.2-5 m³, in all cases the derived optimal points correspond to tank capacities below 1.2 m³.

Finally, an overall summary of the results is presented in Table 4.11-Table 4.12, in which the combinations of optimal solar field areas and storage tank capacities that lead to the optimization of the two objectives for each city are shown. Concerning the exergy efficiency, the maximum yielded values reached values up to 12.6%

Based on the results, it can be concluded that a major hindrance for the implementation of these types of solar ORCs is their limited financial viability. As shown in the table, the optimum LCOE for each city ranges between 0.22-0.91 €/kWh. In any case, these values are higher than the corresponding price of electricity. That means that in terms of economics solely, it is not profitable to install this system at the time being. Moreover, since the main criterion for the economic feasibility is the total amount of produced energy, it is obvious that the lowest values of LCOE are achieved in the southern locations where the solar availability, and thus the total production, are higher. Of course, it should be noted that in this study, no policy incentives (such as subsidies or premiums) have been taken into account, which are very commonly introduced in RES systems and which could greatly improve the eco-nomic competitiveness of the investigated solar ORC. Moreover, it is expected that the addition of heat utilization step of the condenser's heat rejection will enhance the system's economics at a small penalty of the ORC's electrical efficiency. This is mainly due to the fact that the condensation temperature is already relatively high due to the technical limitations of the expander's pressure ratios and therefore the cooling water outlet temperature from the condenser can be suitable for floor heating applications, with proper modification of its mass flowrate.

Table 4.11. Overview of the optimal working combinations for each city

City/Objective	Working fluid	Collector type	A_{col} (m²)	V_{st} (m³)
Chania – max η_{ex}	Isohexane	PDC	10.06	0.83
Chania – max LCOE	Cyclopentane	PTC	116.16	0.23
Athens – max η_{ex}	Isohexane	PDC	12.69	0.37
Athens – max LCOE	Cyclopentane	PTC	114.66	0.23
Thessaloniki – max η_{ex}	Cyclohexane	PDC	10.12	0.34
Thessaloniki – max LCOE	Cyclopentane	PTC	78.42	0.22
Kozani – max η_{ex}	Cyclohexane	PDC	10.31	0.69
Kozani – max LCOE	Cyclopentane	PTC	106.68	0.23
Madrid – max η_{ex}	Cyclohexane	PDC	20.81	0.33
Madrid – max LCOE	Cyclopentane	PTC	120.84	0.33

Rome – max η_{ex}	Cyclopentane	PDC	29.90	0.37
Rome – max LCOE	Cyclopentane	PTC	150.84	0.30
Brussels – max η_{ex}	Isohexane	PDC	84.22	0.22
Brussels – max LCOE	Hexane	PTC	98.41	0.32
Berlin – max η_{ex}	Cyclohexane	PDC	149.92	0.23
Berlin – max LCOE	Cyclopentane	PTC	211.69	0.26

Table 4.12. Overview of the optimal working combinations' results for each city

City/Objective	**η_{ex} (%)**	**$LCOE$ (€/kWh)**	**NPV (k€)**	**PbP (years)**
Chania – max η_{ex}	12.46	0.801	-19.75	n/a
Chania – max LCOE	8.04	0.221	6.40	18.93
Athens – max η_{ex}	12.52	0.738	-15.83	n/a
Athens – max LCOE	8.22	0.273	-4.86	25.71
Thessaloniki – max η_{ex}	12.64	1.06	-19.13	n/a
Thessaloniki – max LCOE	9.22	0.310	-8.32	31.42
Kozani – max η_{ex}	12.54	1.14	-22.52	n/a
Kozani – max LCOE	9.44	0.278	-5.48	26.45
Madrid – max η_{ex}	10.94	0.742	-15.52	96.68
Madrid – max LCOE	7.39	0.359	-1.89	23.41
Rome – max η_{ex}	10.68	0.714	-16.83	104.67
Rome – max LCOE	7.10	0.441	-16.86	35.91
Brussels – max η_{ex}	10.94	0.976	-29.52	139.90
Brussels – max LCOE	8.64	0.734	-35.22	163.05
Berlin – max η_{ex}	10.93	0.758	-31.91	52.92
Berlin – max LCOE	8.64	0.701	-29.01	45.42

In the case of medium temperature ORCs, given the improved economics in comparison to the low temperature ORC systems, is even more important to assess the impact of the existing feed-in tariff for solar thermal power generation in Greece. In fact, the results presented in Table 4.13, show that the application of a feed-in tariff turns the optimum LCOE systems for all climatic zones into competitive solutions, with PbP as low as 10.63 years for Chania and corresponding NPV of 39.89 k€.

Table 4.13. Overview of the feed-in tariff effect on the optimal solutions in Greece

City/Objective	**η_{ex} (%)**	**$LCOE$ (€/kWh)**	**NPV (k€)**	**PbP (years)**
Chania – max η_{ex}	5.91	1.097	-15.25	108.98
Chania – max LCOE	4.37	0.350	39.89	10.63
Athens – max η_{ex}	5.86	1.374	-11.30	70.69
Athens – max LCOE	4.50	0.468	21.99	13.84
Thessaloniki – max η_{ex}	5.93	1.424	-15.83	n/a
Thessaloniki – max LCOE	4.49	0.511	10.30	16.35
Kozani – max η_{ex}	5.91	1.338	-18.96	n/a
Kozani – max LCOE	4.49	0.402	19.66	14.18

Finally, the contribution of different components into the investment cost is illustrated for a reference the scenario that yields the economically optimal results of Athens for PTC and using Cyclopentane (as shown in Table 4.11) in the two pie charts of Fig. 4.16. At this point it has to

be mentioned, as shown by Fig. 4.16(b) and the specific costs of the HTF in Table I.2, that the selection of Therminol VP-1 has a significant impact on the total costs, owing to the amount used in the solar field. However, for working temperatures that exclude the use of commonly used and "cheap" ethylene or propylene glycol aqueous mixtures, the use of the more expensive HTFs is necessary.

Among the ORC components, the biggest cost contribution is that of the screw ex-panders, followed by the evaporator and pump. When the total system cost is considered, more than half of its cost corresponds to the ORC module, with the solar field also having a strong contribution into the CAPEX.

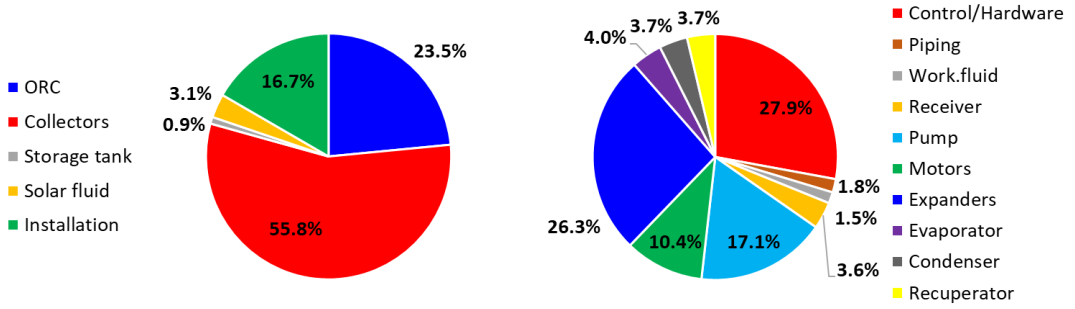

(a) *(b)*

Fig. 4.16. (a) Cost distribution for the ORC system; (b) Cost distribution for the total system, case of Chania-PTC-Cyclopentane for min LCOE (see Table 4.11)

4.2.6 Comparison to relevant studies

In order to properly establish the undertaken optimization procedure, a comparison to similar analyses is carried out. In particular, techno-economic studies oriented towards small- to medium-scale (below 2 MW_e [170]), exclusively solar-driven, medium- to high- temperature (above 150 °C) ORC systems are taken as reference. The summary of the non-exhaustive comparison is reported in Table 4.14, where LCOE values are converted to 2021 equivalent values accounting for inflation rates. It is also stressed that in these studies, similar climates in terms of solar irradiance were investigated, thus neglecting the effect of climate on the results.

As shown, the hereby obtained LCOE (0.221 €/kWh) is higher than most of the others, yet within an acceptable range. First and foremost, it is apparent that economies of scale exist, leading to substantially lower cost of energy in medium-scale systems. In addition, this cost discrepancy is further explained by the different system layouts and operation, as well as the conditions (heat source and heat sink temperature, power range) and assumptions made such as the economic terms (years of evaluation and discount ratio) and the simulation strategy. Namely, the very low LCOE reported by Sun et al. [171] derives mainly from the overestimation of ORC efficiency (15.26%) and the assumption of constant-efficiency ORC operation throughout the evaluation period. On the other hand, the very high LCOE presented in the study of Ciocolanti et al. [172] is expected as it refers to a very small-scale prototype which, additionally, is intended for CHP operation and as a result, a large amount of the available heat is utilized for heating purposes.

Moreover, the comparative works of Desai et al. [173] and Petrollesse and Cocco [174] highlight the importance of TES in the economic feasibility of such systems thanks to the increased operating time. In this context, as shown in the 1 MWe system of Desai and Bandyopadhyay [175], the operation without TES diminishes the positive effect of economies

of scale resulting in similar cost with systems of lower capacity. Ultimately, the 50 kWe system proposed by Patil et al. [176] attained a low LCOE thanks to the combination of increased capacity factor (0.56) and low storage cost.

Concluding, the reported cost has derived from an optimization analysis of a system incorporating TES using detailed off-design modeling in order to properly estimate the net produced electricity. Furthermore, present cost values were included covering all types of system cost. Hence, it appears that the achieved LCOE is acceptable and could be further reduced in a larger-scale application.

Table 4.14. Comparison summary between present work and related studies.

Reference	System type	Heat source temperature (°C)	Design power capacity (kW)	LCOE (€2021/kWh)
Current study	PTC w/ TES	180-210	6.2	0.221
Ciocolanti et al. [172]	LFC w/ TES	210-280	2.0	4.706
Patil et al. [176]	PTC w/ TES	275	50.0	0.171
Sun et al. [171]	LFC w/o TES	210	171.8	0.045
	LFC w/o TES	275	700.0	0.176
Petrollesse and Cocco [174]	LFC w/ TES	275	700.0	0.120
Desai et al. [173]	Polymer-foil CSP w/ TES	165-300	1000.0	0.141
El hamdani et al. [177]	PTC w/ TES	300	1000.0	0.199
Desai and Bandyopadhyay [175]	PTC w/o TES	250	1000.0	0.300

4.2.7 Sensitivity analysis

As the study for medium temperature ORCs is practically an expansion of the work conducted for low temperature ORCs, presented in section 4.1, a sensitivity analysis was carried out also on this case, to identify the influence of the CAPEX reduction, the period of investment, the electricity price and solar and ORC subsystems' efficiencies in the overall system's performance.

I. Reduction in CAPEX

As expected, a reduction in the CAPEX has a positive effect on system's economic performance. Considering only the optimum LCOE scenarios of Table 4.11, evident improvement can be observed by assuming a 10% and 20% reduction of the CAPEX, respectively. More specifically, in the scenario of a 20% reduction of the CAPEX, the optimum system in Chania would record a LCOE of 0.177 €/kWh, while the corresponding value for Athens would be equal to 0.219 €/kWh. An overview of the CAPEX's influence in the system's LCOE for the optimum cases per city can be shown in Fig. 4.17(a).

II. Period of investment

In this analysis, the variation of the LCOE with 20- and 30-years period of investment was considered, in comparison to the base case scenario of 25 years. The results of the analysis are listed in Fig. 4.17(b). As expected, an increase in the years of investment deteriorates the

performance, with the corresponding LCOE for 20 years period of investment and for the optimal case of Chania to be equal to 0.239 €/kWh, while all other reported LCOEs exceed 0.3 €/kWh.

III. Electricity price

Fig. 4.17(c)-(d) present the influence of the electricity prices on the PbP and the NPV, respectively, by considering a potential increase of 10% and 20%. As expected, an increase of 20% in the electricity price, resulted in a significant benefit on the solar ORC performance. In fact, the PbP for the optimum case of Chania was reduced to 15.86 years, while the corresponding PbP for Athens was as low as 21.57 years. The corresponding values for the NPV values of Chania and Athens were 18.23 k€ and 4.62 k€, respectively.

IV. Solar system and ORC efficiency

Possible improvements in the subsystems efficiencies are expected to improve both the LCOE, Fig. 4.17(e), and the system's exergy efficiency, Fig. 4.17(f). As shown in both figures, the ORC performance enhancement has only slightly higher influence on the system's economic and exergetic performance. For instance, in Chania a 10% increase in the ORC's thermal efficiency leads to an LCOE of 0.201 €/kWh, while the corresponding value for a 10% increase in the solar collectors' efficiency is 0.204 €/kWh.

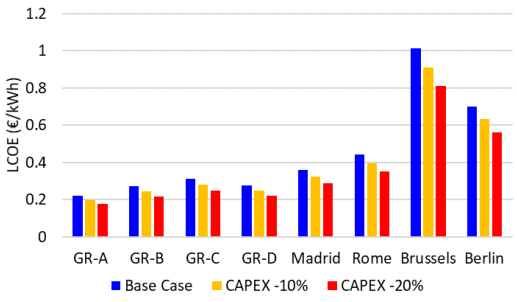

(a)

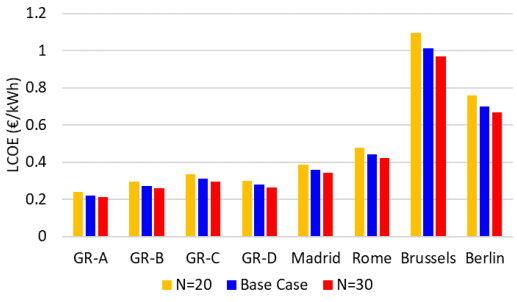

(b)

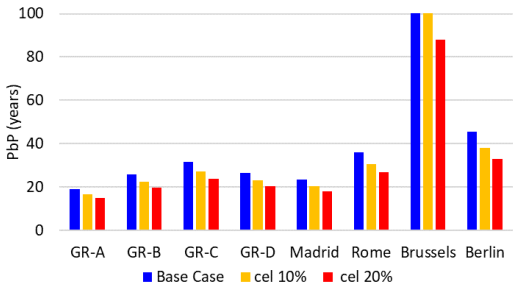

(c)

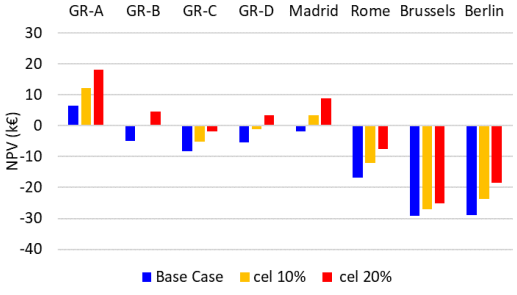

(d)

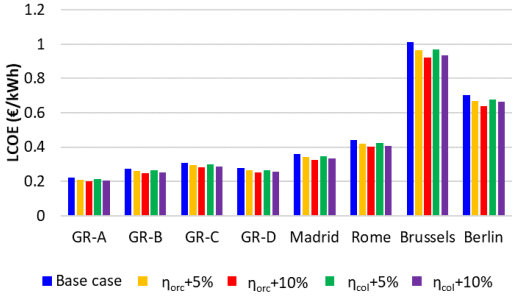

(e)

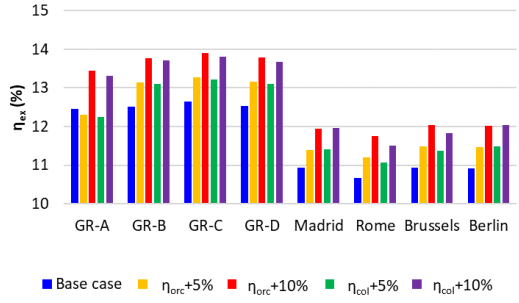

(f)

Fig. 4.17. Results of the sensitivity analyses: (a) influence of the reduction in the CAPEX on the LCOE; (b) influence of the period of investment in the LCOE; influence of the electricity prices (c) on the payback period and (d) on the NPV; influence of the solar system and ORC efficiencies (e) on the LCOE and (f) on the exergy efficiency

4.2.8 Conclusions

In section 4.2, a techno-economic optimization methodology of a small-scale medium-to-high-temperature solar ORC was presented. The system was optimized using a genetic algorithm with respect to the exergy efficiency and the LCOE for five different European cities as well as the Greek climatic zones, considering a number of different working fluids and two types of concentrating solar collectors, PTCs and PDCs. The main conclusions of the study are summarized below:

- The use of concentrating collectors (PTC and PDC) requires the integration of a sun tracking system, which increases the total solar irradiance absorbed by the collectors, by roughly 7.5% in an annual basis.
- Though, there are no great differences in the exergy efficiency between the systems that use different types of collectors, in most cases systems using PDCs perform slightly better. However, PTCs are more profitable from an economic perspective due to their lower purchase costs.
- The selection of the working fluid is strongly correlated to the temperature of the heat source. The optimum performance is achieved in most cases by working fluids which have critical temperature slightly higher than the cycle's top temperature. In the examined system with a driving temperature between 180-210 ^{o}C, Cyclopentane and Cyclohexane give the optimal results
- The maximum exergy efficiency of the systems was around 12.6%. Only substantial differences were found in the exergy efficiency between the examined cities of northern and southern climates.
- The cost of the produced electrical energy was lower for southern locations (e.g. Chania with 0.221 €/kWh) with higher values of the collecting surface and low storage tank capacities. However, its minimum value was found to be higher than the current commercial cost of electricity.
- Higher LCOE is reported than in relevant literature, owing to the small-scale of the system along with the efficiency deterioration in low part load ratios arising from the detailed off-design modeling

4.3 Techno-economic analysis of solar cooling/heating systems

In this study, the techno-economic performance of solar driven absorption and adsorption cooling systems is evaluated. The systems are considered to be used to cover the heating and cooling loads of a residential building. The system performance is evaluated for the four different climatic zones of Greece and thus the thermal loads of section 3.3 were used for the analysis. Two types of non-concentrating solar collectors were evaluated, namely FPCs and ETCs. The investigated systems were optimized with respect to the solar field area and the storage tank's capacity. As objective functions were set the exergy efficiency and the levelized cost of energy. Moreover, for each climatic zone case, additional scenarios were considered for the economic comparison. More specifically, three additional systems were evaluated, a

grid-connected heat pump (HP), a PV-HP with net metering (PV-HP-nm) and a PV-HP with a battery (PV-HP-B).

4.3.1 System description

With respect to the solar ab-/ad-sorption systems, an overview of the considered system configuration is presented in Fig. 4.18(a). According to this schematic, the solar heat is fed into the storage tank -an open-circuit storage tank was considered- and a secondary stream directs a flow from the upper level of the tank towards the HT circuit of the sorption chiller. The integration of the storage tank in series with the sorption chiller, apart from the obvious storage, is dictated by the necessity to "neutralize" the thermal spikes induced by the solar field and provide steadier conditions in the chiller's HT stream. On cooling mode, the MT of the chiller is connected to a dry cooler, modelled based on section 2.3.2, for the heat rejection. Finally, a fan coil system is connected with the LT circuit of the chiller to provide the cooling effect in the building. On heating mode, the MT and LT circuits are reversed so that the heat from the MT to be rejected in the fan coils. All sorption systems, in a similar manner to Zeosol system, in order to be able to meet the thermal loads of the building, at all times, are equipped with a backup HP, which operates in cases of peak loads and during cases of inadequate solar heat to drive the sorption chiller.

The considered building loads were modeled in section 3.3, considering a building constructed in 2001-2010. As described in section 3.3, the reference heating system was realized via a gas condensing boiler with a thermal efficiency of 96.1%, with respect to the higher heating value, and a heating capacity of 10 kW which is the smallest commercially available capacity. The respective cooling loads were considered to be covered by a total of three single-split air-conditioning (a/c) units, with a total capacity of 7.92 kW (3 units of 9000 Btu/h) [126]. The EER of the considered single split units was equal to 10.24 Btu/(W h), which corresponds to a COP of 3.

As a second reference, in terms of the economic analysis, three additional scenarios with a HP were evaluated. The first HP scenario consists simple by the evaluation of a grid connected reversible HP to cover the total amount of building's heating and cooling loads. The second scenario involved the implementation of some PV panels which are supplying their power generation to the grid and a grid-connected HP, considering a net metering to be applied. At this point it has to be mentioned that given the Law 759/2019 [48], the considered feed-in-tariff for the PVs was equal to approximately 0.11 €/kWh. Finally, a third additional scenario involved the implementation of a battery, as shown Fig. 4.18(b), to store the power production of the PV panels and therefore cover part of the reversible HP electric loads from the PV generation.

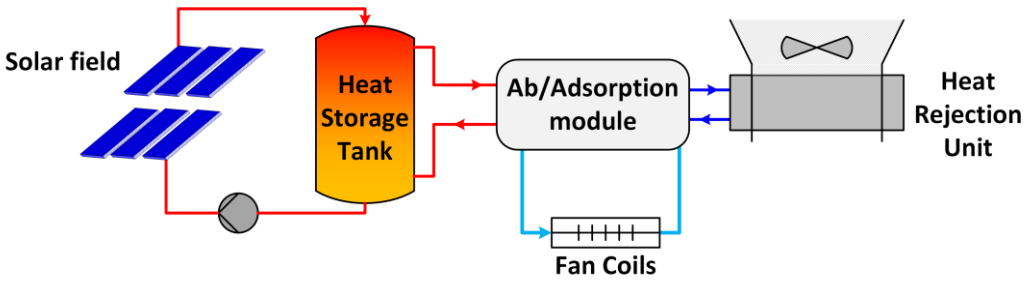

(a)

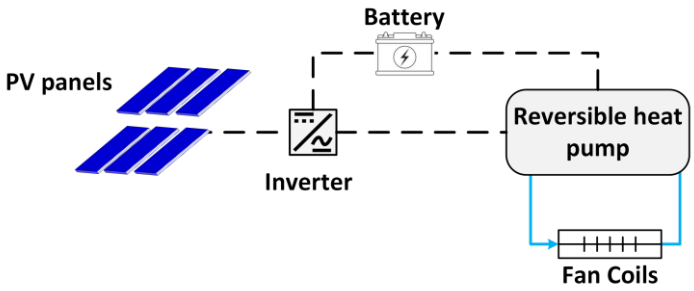

(b)

Fig. 4.18. Schematics of the evaluated systems: (a) solar driven sorption system and (b) PV assisted reversible heat pump with battery

4.3.2 Results of GA optimization

Within the context of the techno-economic optimization, initially a multi-objective GA was applied. As objective functions of the GA were set the exergy efficiency of the system and the levelized cost of energy, defined as listed below:

$$LCOE = \frac{CRF \cdot \left\{C_{tot} + \sum_{t=1}^{20}\left[\frac{C_{main} \cdot (1+r_{om})^{t-1}}{(1+r)^{t}}\right]\right\}}{Q_{heat,an} + Q_{cool,an}} \quad (4.11)$$

With the CAPEX of the solar cooling/heating system to be calculated from.

$$C_{tot} = C_{col} + C_{st} + C_{cpump} + C_{HTF} + C_{abs/ads} + C_{HP} + C_{dc} + C_{fancoil} \quad (4.12)$$

On the other hand, the total exergy efficiency of the system was calculated as following:

$$\eta_{ex} = \frac{\sum \dot{E}x_{o,t}}{\sum(\dot{E}x_{sol,t} + W_{el,HP,t})} \quad (4.13)$$

With the $\dot{E}x_{sol}$ to be calculated as shown in (4.3), $W_{el,HP,t}$ to be the electrical consumption of the backup HP on each hour t of the year and the exergy at the outlet of the chiller, $\dot{E}x_{o}$, to be equal to:

$$\dot{E}x_{o,t} = \dot{m}_{LT,w} \cdot \left[h_{LT,o} - h_{w,ref} - T_{ref} \cdot \left(s_{LT,o} - s_{w,ref}\right)\right] \quad (4.14)$$

The optimization parameters were the solar field area and the storage tank capacity, with ranges of evaluation [2,35] and [0,3], respectively. The lifetime of the system's was considered equal to 20 years in all economic performance indicators.

However, the results of the GAs revealed a negative performance of the system. More specifically, in all evaluated cases a single optimum point was found, which maximized the exergy efficiency and minimized the LCOE. The aforementioned optimum point ranged between 2-4 m^2 of solar field and approximately 0.25-0.4 m^3, highlighting that practically the evaluated systems were not economically viable and the computational result moved towards to the minimization of the sorption chiller's operation, in favor of the backup HP.

Given the abovementioned results, a second analysis was conducted using a single objective GA optimization, in order to assess the performance results of the proposed systems over the

same range for the solar field areas and the storage tank capacities. The reverse Pareto fronts which were calculated from the second analysis for each zone and solar sorption system are presented in Fig. 4.19. As can be seen, the maximum reported exergy efficiency was in Zone D (Kozani) with a value of 16.8% for the case of FPC driven adsorption system. On the other hand, the minimum LCOE was found in Zone C (Thessaloniki) with a value of 0.205 €/kWh for the case of FPC driven absorption. As a general trend, it can be shown that the solar absorption systems are related with the best economic performances, while the adsorption systems tend on most cases to record better exergy efficiencies, owing to the lower driving temperatures that require for their operation. Moreover, in the comparison between ETC and FPC driven systems, in most cases the FPC driven sorption systems have lower LCOEs, mainly associated to the lower costs of the solar collectors; on the other hand, the higher performance of the ETCs on the nominal temperature of the sorption modules result in generally higher exergy efficiencies. Finally, there is a clear trend of better performances in the colder climatic zones. This fact is mainly associated with the fact that the sorption systems operate better on heating mode and therefore better results are obtained in Zones C and D, which as was shown in Fig. 3.8, had significantly higher heating loads.

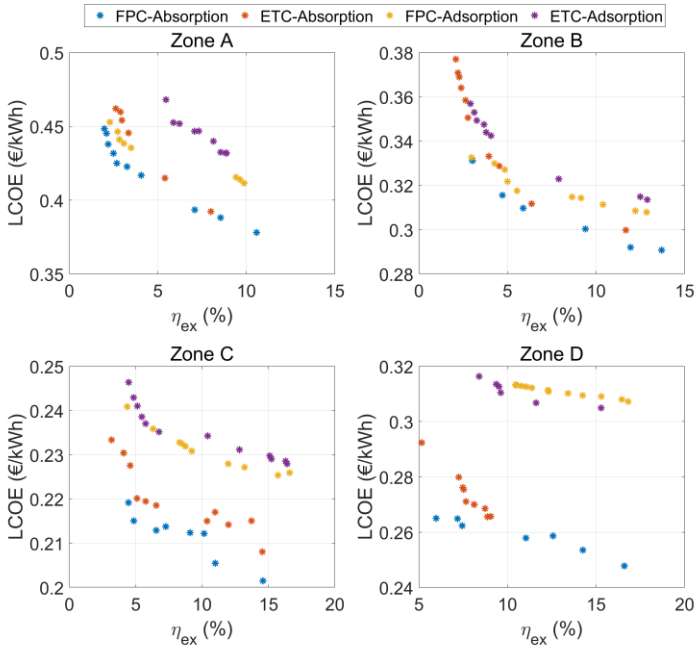

Fig. 4.19. Pareto-wise presentation of the results for the investigated scenarios in the four climatic zones of Greece

A better observation of the investigation results can be shown in Fig. 4.20, where the results of Athens (Zone B) are associated with the considered solar field areas and storage tank's capacities per case. As shown, there is a clear trend of deteriorating performance with increasing solar field areas, a fact which highlights the current in-competitiveness of the proposed solutions, at least for the evaluated residential scale. With respect to the storage tank it can be observed that smaller capacities are favored, with all solutions to be located below 1 m^3. The respective results for the other three regions are listed in the Appendix II (Fig. II.11-Fig. II.13).

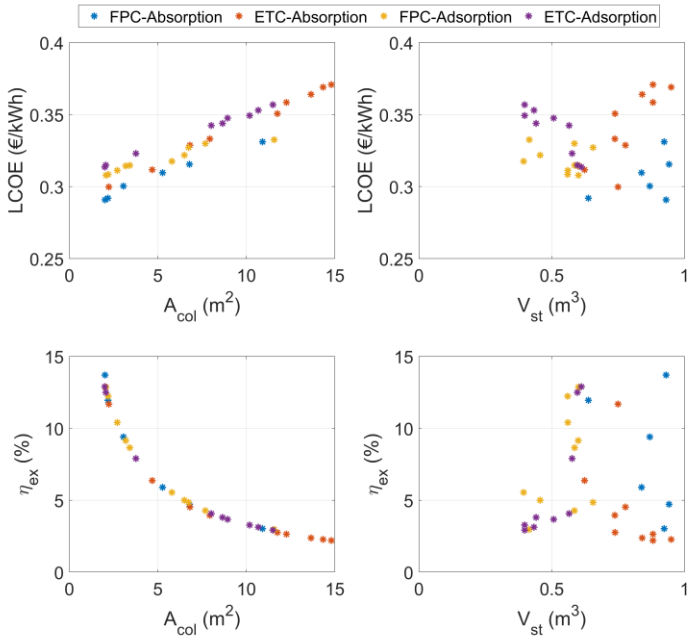

Fig. 4.20. Optimization parameters with respect to input variables for all the considered scenarios in Athens

4.3.3 Economic comparison of solar cooling/heating systems

As shown above, the optimal economic results favor the operation of the HP instead of the use of solar driven sorption module. In order, however, to compare the actual gap of the main available solar cooling/heating technologies, another analysis was conducted, considering for the cases of absorption/adsorption systems the same solar field area of 20 m² and storage tank capacity of 0.5 m³ for the four climatic zones. The obtained results are compared with the three scenarios of HP systems, which were presented in section 4.3.1.

Prior to the presentation of the analysis results, it is worth assessing the contribution of the respective components in the system's CAPEX, based on equation (4.12). Fig. 4.21 presents the CAPEX breakdown for the case of a FPC driven absorption system. As expected, the sorption chiller has the largest share of the CAPEX, with a 39.8%, followed by the installation and the solar collectors, with 20.0% and 18.1%, respectively.

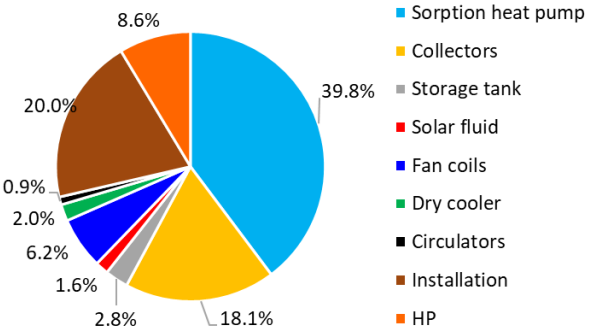

Fig. 4.21. Cost distribution of a solar driven absorption cooling/heating system with 20 m² of FPCs and a 0.5 m³ storage tank

Fig. 4.22 presents the overview of the evaluated scenarios per zone, with respect to the LCOE (Fig. 4.22(a)) and the NPV (Fig. 4.22(b)). As already suggested by the results of the GA, the solar sorption systems have considerably worse performance with LCOEs ranging between

0.280-0.498 €/kWh. The corresponding values for the NPVs ranged between –23.9 to -40.9k€. On the contrary, the three HP scenarios have promising results, with the most favorable case to be the PV-HP-nm, which for the case of Zone C had an LCOE of 0.098 €/kWh and a corresponding NPV of 2.2 k€. Finally, the PV-HP-B scenario had worse performance than the grid connected HP in all four climatic zones, highlighting the existing gap in the PV battery technologies/economics to become competitive for residential applications.

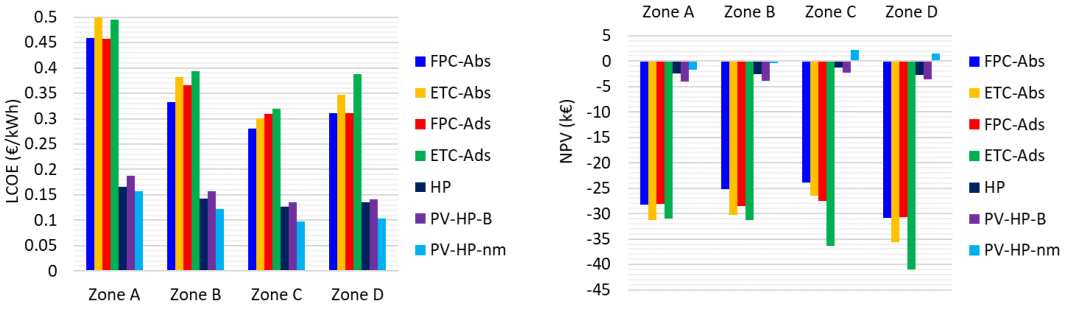

(a) *(b)*

Fig. 4.22. Results of the case study for the Greek climatic zones with respect to: (a) the LCOE and (b) the NPV.

4.3.4 Sensitivity analysis

Similar to ORC optimization studies, a sensitivity analysis was conducted, to identify the influence of the CAPEX reduction and the electricity/natural gas prices in the overall system's economic performance.

I. Reduction in CAPEX

As expected, a reduction in the CAPEX has a positive effect on system's economic performance. Considering scenarios of Table 4.11 previous section for Athens (Zone B), evident improvement can be observed by assuming a 10% and 20% reduction of the CAPEX, respectively. More specifically, in the scenario of a 20% reduction of the CAPEX, the PV-HP-nm system would record a LCOE of 0.101 €/kWh (compared to the 0.123 €/kWh of the base case). Given the significantly higher CAPEXs of solar sorption systems, the reported improvement on these systems is even larger, with a reduction of up to 0.07 €/kWh. An overview of the CAPEX's influence in the system's LCOE for the optimum cases per city can be shown in Fig. 4.23(a).

II. Electricity and natural gas prices

Fig. 4.23(b) presents the influence of the electricity and natural gas prices on the NPV, respectively, by considering a potential increase of 20% and 40% in each one of them, along with a scenario of a combined 20% increase on both electricity and natural gas. As shown, the increase in the electricity price has a negative effect in the proposed systems' performance. This fact is owed to the operation of the HP and the corresponding power consumption which results in added OPEX by a potential electricity price increase. On the contrary, an increase of the natural gas prices would affect only the reference systems' costs and thus the profits of the proposed systems would increase, improving eventually the NPV. The maximum reported values for the NPV, for a 40% natural gas price increase, were equal to -23.0 k€ for the FPC driven absorption system and 1.8 k€ for the PV-HP-nm, respectively. The respective sensitivity analyses' results for the other three regions are listed in the Appendix II (Fig. II.14-Fig. II.16).

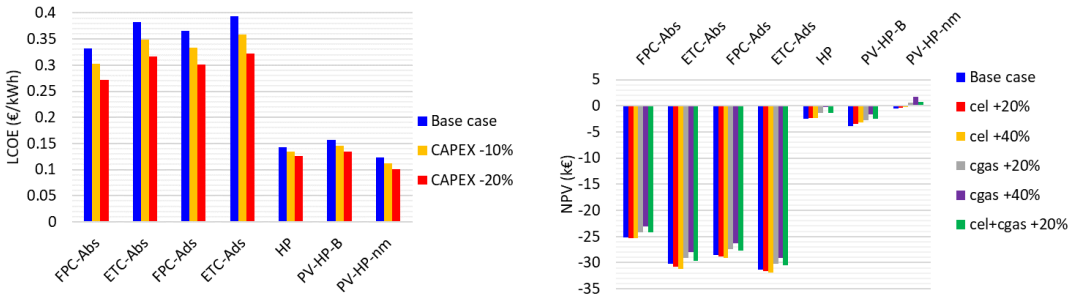

(a) *(b)*

Fig. 4.23. Results of the sensitivity analyses: (a) influence of the reduction in the CAPEX on the LCOE and (b) influence of the electricity and gas prices on the NPV for the case of Athens (Zone B)

4.3.5 Conclusions

In this study, the techno-economic investigations of solar driven absorption/adsorption systems were analyzed. The proposed systems were evaluated for operation a residential application located in the four climatic zones of Greece. The economic performance of the proposed systems was compared to three heat pump-based systems for a more objective overview of the results. The main conclusions of the analysis are summarized below:

- Multi-objective optimization using as objective functions the exergy efficiency and the LCOE is inapplicable for the solar sorption systems in the considered residential application, given that both economics and exergy efficiency deteriorate with increasing fraction of the sorption module's operation to the backup HP operation.
- A single-objective optimization was therefore used instead. The results revealed a general trend of better economic performances for the FPC driven systems compared to the ETC driven systems, mainly due to the lower CAPEX of the FPCs. On the contrary, ETC driven systems recorded better exergy efficiencies, owed to the better performance compared to FPCs, at the driving temperatures range of the sorption chillers. Moreover, the economic performance is enhanced as the site of installation moves to colder climates due to the higher heating loads at which both the sorption module and the backup HP operate more efficiently.
- The analysis of the optimum results with respect to the optimization variables, showed that smaller storage tank capacities were favored in all cases. On the other hand, the increase in the solar field areas worsened both the exergy efficiency and the LCOE.
- For a 20 m^2 FPC field and a 0.5 m^3 storage tank, the CAPEX breakdown of a solar absorption system showed that the sorption chiller contributes the most, with a share of 39.8%, followed by the solar collectors with a 18.1%.
- The solar sorption systems have significantly worse economics in comparison to heat pump-based systems. The LCOEs for solar sorption systems ranged between 0.280-0.498 €/kWh, while the best performing system, a PV-HP system with net metering, recorded an LCOE of 0.098 €/kWh for climatic Zone C.
- The sensitivity analysis revealed that a potential reduction in the CAPEX of 20%, would decrease the LCOEs of the solar sorption systems up to 0.07 €/kWh. An increase in the electricity prices, showed that it would have detrimental effect on the evaluated system's NPVs, due to the induced costs by the power consumption of the heat pumps. On the

contrary, a natural gas price increase is quite beneficial for all systems, as it only affects the expenditure of the reference system.

Chapter 5. Trigeneration systems investigations

In the previous Chapter, the separate production of power and cooling/heating was investigated, showing the potential of the investigated technologies. As a further step in this direction is considered the investigation of a hybrid trigeneration system based on the ORC and the adsorption cycle.

Within the context of a preliminary study in the hybrid ORC-adsorption systems, it is crucial to identify the optimal configuration for the coupling of the two cycles. For this reason, a more simplistic heat source was used, to allow for the preliminary design assessment. Once the optimal configuration is identified, a more detailed case study implementing a solar subsystem is presented in section 5.2. The contents of section 5.1 were published in the study "Integrated ORC-Adsorption cycle: A first and second law analysis of potential configurations" [178].

5.1 Integrated ORC-Adsorption cycle: A first and second law analysis of potential configurations

5.1.1 Introduction

The concept of integrating an ORC with a refrigeration cycle has been already studied in literature. Wang et al. [179] investigated different configurations for combined ORC-VCC systems. The results of the analysis showed that applying both subcooling and cooling recuperation in the VCC, the system's COP could be as high as 0.66 at extreme ambient conditions. Nasir and Kim [180] evaluated a number of working fluids combinations in a combined ORC-VCC system. The study concluded that the use of different fluids for the two cycles allowed for better optimization of the working parameters. Specifically, the use of R134a for the ORC and R600a achieved the optimal performance for the air conditioning application that was

considered, with a thermal efficiency of the ORC of approximately 5.3%, a maximum reported COP of 0.28 and an exergetic efficiency of 27.9%. Zheng et al. [181] proposed the use of zeotropic mixtures in combined ORC-VCC systems. The optimal mixture (R161/R600a with a mass fraction 0.25/0.75) resulted in a significant enhancement of system's performance of more than 39% in comparison to the respective performance of pure fluid operation, using R600a.

In 1998, Yogi Goswami [182] proposed and investigated a hybrid NH_3-H_2O absorption cycle integrated with an ORC, using ammonia (R717) for combined power and refrigeration production. An on design analysis was conducted, revealing a turbine efficiency as high as 90%, for inlet ammonia vapour conditions of 230 °C and 27.6 bar and a pressure ratio of 19.7. Furthermore, it was shown a 2 MW_e power output system would be able to simultaneously produce 176 kW of cooling. Tomków and Cholewiński [183] implemented a combined ORC-absorption cycle in a liquid natural gas re-gasificiation system to enhance the overall system's performance. On the other hand, Mohammadi et al. [184] conducted a first law analysis of a combined gas turbine, ORC and absorption tri-generation system. The results of the analysis indicated that the overall system's efficiency was approximately 67%, with a net power output of 30 kW, a cooling capacity of 8 kW and a heating capacity of 7.2 ton of hot water. Eisavi et al. [185] reported the performance of a solar driven tri-generation system based on an ORC coupled with either a double effect or a single effect LiBr-H_2O absorption chiller. The

integration of a double effect absorption chiller was found to enhance the system's cooling output by almost 49% in comparison to the single effect chiller, while the maximum achieved combined heat and power (CHP) efficiency for the double effect absorption heat pump was as high as 96%.

Chaiyat et al. [186] coupled a 25 kW_e R245fa ORC prototype with a sorption system to lower the condensation temperature of the Organic cycle and enhance its performance. Both a 1 TR absorption chiller and a silica gel-water adsorption chiller of same capacity were evaluated. The experimental evaluation indicated that the ORC-adsorption system performed better than the ORC-absorption one, both in terms of energy and exergy efficiency as well as the estimated levelized cost of electricity. Jiang et al. [187] evaluated a cascade cogeneration system, which integrated an ORC, using R245fa as working fluid, and a two stage $CaCl_2/BaCl_2$-ammonia adsorption cycle. The coupling of the two subsystems was realized by connecting the ORC condenser's jacket water and the hot water that heated the ORC to drive the chiller's adsorption and the desorption phases, respectively. For a hot water temperature of 95 °C, the power production of the ORC was 0.53 kW_e, while the cooling COP was equal to 0.201 (condensation temperature: 30 °C, evaporation temperature: 0 °C). Wang et al. [188] used solar collectors to drive a cogeneration system based on a R600 ORC and a silica gel-water adsorption chiller. For a driving heat of 15 kW, the resulting electrical efficiency of the system was equal to 10-15%, while the adsorption COP was approximately 0.8. The corresponding overall exergy efficiency was ranging between 0.56-0.74.

As it can be observed from the literature review, so far the vast majority of studies on combined ORC-refrigeration systems have been focused on coupling ORCs with either a vapour compression cycle (VCC) or an absorption chiller. On the other hand, the number of studies considering the integration of ORCs with adsorption chillers is very limited. Meanwhile, the conducted investigations have exclusively focused on the energetic/first law analysis of the proposed systems and hence the exergetic/second law analysis, which provides a comprehensive evaluation tool for the performance of combined power and cooling systems, has been overlooked. Furthermore, most studies follow an on-design investigation approach and have not taken into account the implications of off-design performance, which are critical especially in the case of adsorption chiller devices. In addition to this, the assumptions followed regarding the performance of some key equipment components (i.e. the ORC pump and expander) are not in accordance with experimental experience of micro-scale systems, which points to lower actual efficiencies than those that are typically assumed. Considering the above, this study focuses on the comparison of different configurations of a waste heat multigeneration system consisting of an ORC (topping cycle) and an adsorption chiller (bottoming cycle), taking into consideration the off-design technical features of the included sub-components. Furthermore, an innovative silica gel adsorption chiller is considered, which is ideal for low driving heat temperature (at approximately 70 °C) operation. Last but not least, a first and also a second law evaluation approach is followed, to provide a deeper insight into the overall performance of the proposed systems. In each case, the system performance is compared to that of an ORC-VCC reference system with the same cooling output.

5.1.2 System description

In reality, the selection of the optimal design conditions of multigeneration systems can be based on multiple criteria (primary energy/exergy savings, environmental, economic) and depends on the cooling/electrical load profiles of a particular application. Despite constituting an indispensable component for the complete evaluation of such systems, the optimal design based on the coverage of cooling/electrical loads is beyond the scope of the present work, which focuses on the investigation of the performance of the considered systems under a series of various fixed design conditions, as a first level indicator of their comparative performance, before proceeding with detailed part load calculations. As a result, in the present study, starting by considering a fixed available heat input, the system is simulated under different design conditions and the electricity/cooling production potential is subsequently calculated in each case.

I. Organic Rankine Cycle

For the present study, a conventional, subcritical ORC system has been considered. Six working fluids were evaluated: R245fa, R245ca, R114, R600 (butane), cyclopentane and isohexane. For the case of R245fa, a supercritical ORC was additionally investigated. Note that R114 has an ODP of 1 and is listed on the Intergovernmental Panel on Climate Change's list of ozone depleting chemicals, being classified as a Montreal Protocol Class I, group 1 ozone depleting substance [189]. However, it has been included in the study as representative of working fluids featuring similar thermodynamic properties.

The driving heat for the ORC was provided by the hot flue gases of a 300 kW natural gas fired boiler. The mass flow rate of the flue gases was assumed to be 0.4 kg/s. Different flue gas inlet temperatures were considered, ranging from 240 to 340 °C for all considered configurations. Table 5.1 presents an overview of the key assumptions considered, regarding the ORC subsystem. The expander and pump's isentropic efficiencies were considered such, based on actual performance data from an actual small scale ORC installation located in the laboratories premises [133]. The considered values refer to the nominal efficiencies of a scroll type open drive expander and a multi-diaphragm small scale pump; both evaluated using R134a as the working fluid of the test rig.

Table 5.1. List of assumptions regarding the ORC [133]

Parameter	Value
Pump isentropic efficiency, $\eta_{is,p}$	0.50
Expander isentropic efficiency, $\eta_{is,exp}$	0.65
Electro-mechanical generation losses, η_{gen}	0.95
Water inlet temperature (°C)	20
Maximum expander pressure ratio	4.5 [134]
Maximum expander internal built-in volume ratio	4 [134]

II. Adsorption cycle

The adsorption chiller considered for the simulations is a zeolite-water double-bed adsorption chiller. The rated cooling power of the considered chiller is approximately 13 kW_c, which corresponds to a typical nominal cooling load of a multi-family house building. The operating range of the volumetric flow rate and the working temperatures for the three secondary circuits of the chiller are listed in Table 5.2. The model was developed in Simulink [190], using

a relative tolerance for the solver of 10^{-5}. As Refprop was used for the fluids' properties, several solvers faced stability issues due to the interconnection with Refprop's database. For this reason, the ode23s solver was used in the model to enhance system's stability. In terms of the chiller's cycle, it consists of four phases. In the first phase, the adsorption bed 1 is on desorption mode and the adsorption bed 2 is on adsorption mode. In the third phase, the operation is reversed, while on phases 2 and 4, the two beds are in heat recovery mode, transferring heat from the hot bed to the cold one. The methodology of the developed adsorption system's model and the key equations are listed in the respective section of the Appendix III. An overview of the performance maps of the aforementioned chiller can be found in Fig. 5.1, for a chilled water outlet temperature 12 °C, as they were calculated from the simulation model.

Table 5.2. Technical specifications of the adsorption chiller [191]

Parameter	Value
Heat source (water) temperature range (°C)	75-95
Cooling water temperature range (°C)	22-45
Chilled water temperature range (°C)	8-21
Heat source (water) volumetric flowrate (L/h)	1600-2500
Cooling water volumetric flowrate (L/h)	4100-5100
Chilled water volumetric flowrate (L/h)	2000-2900

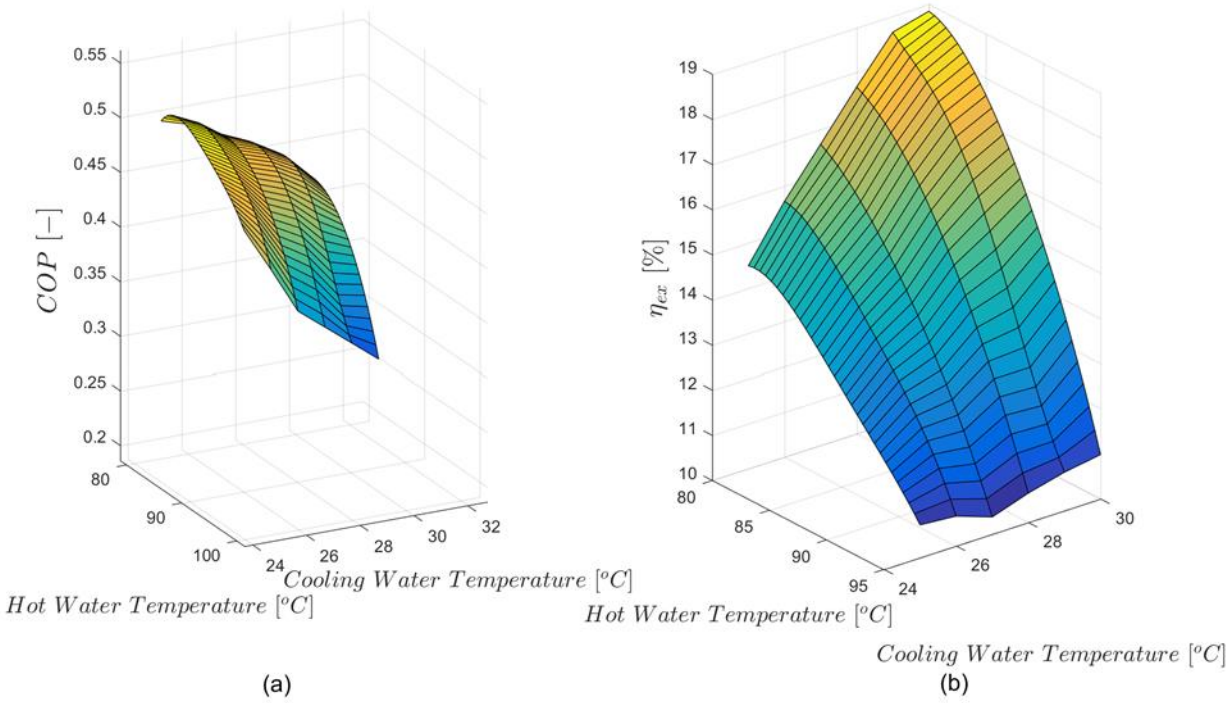

Fig. 5.1. Performance maps for (a) the COP and (b) the exergetic efficiency of the adsorption chiller for a chilled water outlet temperature of 12 °C

III. Investigated configurations

In this section, the considered configurations (Fig. 5.2) are briefly discussed. In the present study, the investigated heat source temperature ranges from 240 °C to 340 °C. Considering the fact that the adsorption chiller operates at driving heat temperatures ranging from 75 °C to 95 °C, positioning the adsorption chiller as a topping cycle would lead to increased exergy

destruction in the intermediate heat exchanger I. On the other hand, the exergy destruction is minimized if the ORC is the topping cycle, since in this case, the working fluid evaporation temperatures can be maximized. An additional benefit attained when positioning the ORC as the topping cycle is the possibility of operating the ORCs under higher pressure ratios, which lead to improved cycle and expansion efficiencies, and hence to higher electrical efficiencies. Meanwhile, positioning the ORC as the topping cycle does not inhibit the performance of the adsorption chiller, since the heat source stream exits the intermediate heat exchanger I at sufficiently high temperatures that enable the optimal operation of the chiller under high COP values. Therefore, in all examined configurations, the ORC is considered as the topping cycle. The above does not preclude that, depending on the heat source temperature and the prioritization of electricity vs cooling production, alternative configurations in which the adsorption chiller is the topping cycle could be favorable.

In configuration (a), the flue gases pass through a first intermediate heat exchanger (IHE1), which serves as the ORC heater. After exiting IHE1, the flue gases are driven to a second heat exchanger (IHE2) to provide the required driving heat for the desorption process of the adsorption chiller. In all cases, the ORC is sized so that the driving temperature in the adsorption chiller is 90 °C.

In configuration (b) the driving heat of the adsorption chiller is supplied by the ORC condenser. Thus, the flue gas stream is used exclusively for providing heat to the ORC (in IHE1). In configuration (c), a double stage ORC is featured. The flue gases are again exclusively used for heating the ORC working fluid. The driving heat of the chiller is provided by the superheated vapor exiting the high-pressure stage of the ORC expander, via a secondary intermediate heat exchanger (IHE2).

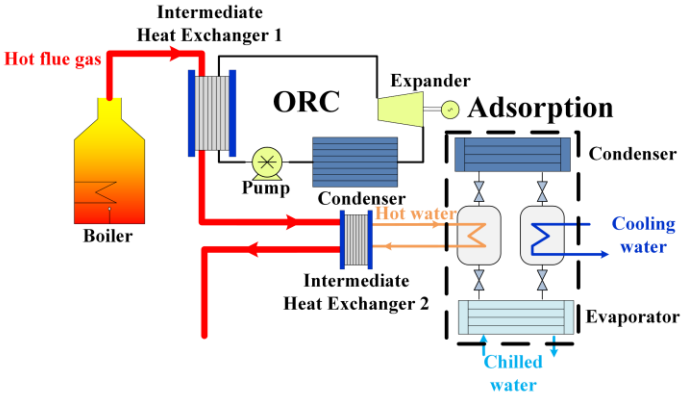

(a)

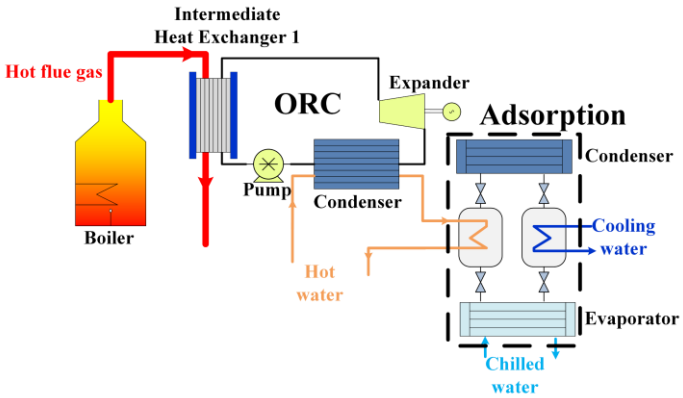

(b)

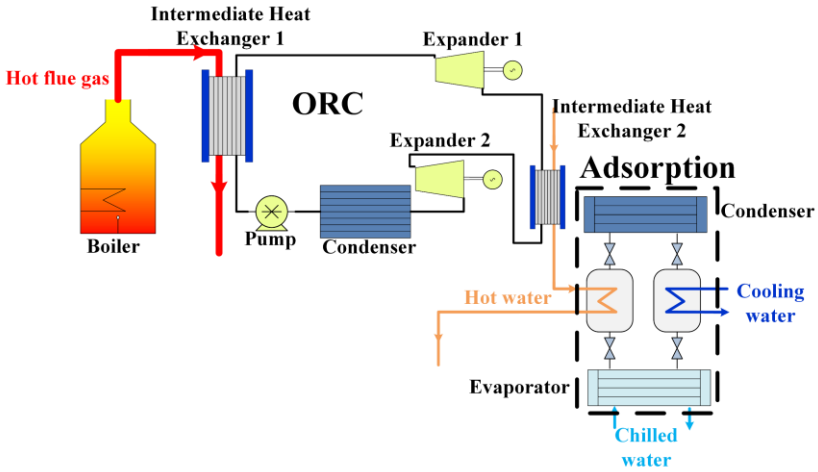

(c)

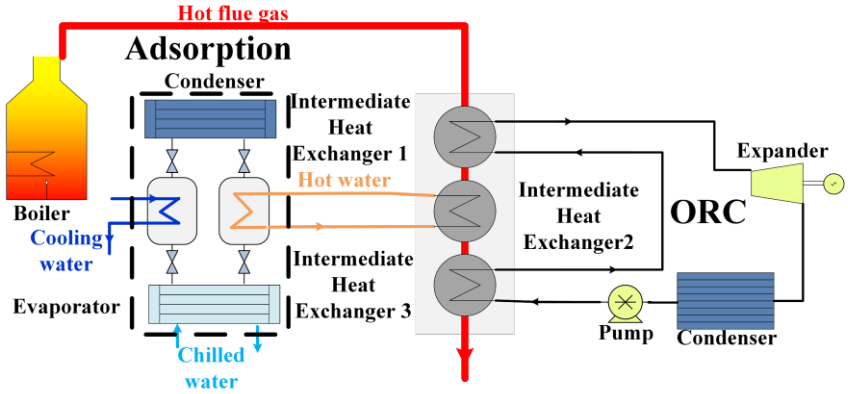

(d)

Fig. 5.2. Schematics of the four evaluated configurations for the integrated adsorption-ORC system

Finally, in configuration (d), a series of three heat exchangers is implemented based on the principle of a heat recovery steam generator. Intermediate heat exchanger 1 (IHE1), as seen in Fig. 5.2(d), serves as the superheater of the ORC, while intermediate heat exchanger 3 (IHE3) serves as the preheater and the evaporator. An additional third heat exchanger (IHE2) is installed between IHE1 and IHE3 to recover heat for driving the adsorption chiller.

Concerning, the combined cooling and power production efficiency, it is calculated as follows:

$$\eta_{CCP} = \frac{\dot{W}_{el,gen} - \dot{W}_{el,motor} + \dot{Q}_{cool}}{\dot{Q}_{fg}} \qquad (5.1)$$

All the systems were evaluated using as reference a combined ORC-VCC system, driven by the same heat source and using the same fluid on both the ORC and the VCC. On the other hand, for a VCC the coefficient of performance was calculated by eq. (2.19).

The second law efficiency for the integrated ORC-VCC reference system was calculated from the following:

$$\eta_{ex,ORC,VCC} = \frac{\dot{W}_{el,gen} - \dot{W}_{el,motor} - \dot{W}_{el,com} + \dot{E}x_{ch,w}}{\dot{E}x_{fg}} \qquad (5.2)$$

with a reference temperature of $T_{ref} = 298\,K$ and reference pressure equal to $p_{ref} = 1.01325\,bar$.

While, the exergy rate of change of the chilled water stream is calculated from the following:

$$\dot{E}x_{ch,w} = \dot{m}_{ch,w} \cdot \left[h_{ch,w,o} - h_{w,ref} - T_{ref} \cdot \left(s_{ch,w,o} - s_{w,ref}\right)\right] \quad (5.3)$$

The exergy rate of change of the flue gases is calculated from the following:

$$\dot{E}x_{fg} = \dot{m}_{fg} \cdot \left[h_{fg,i} - h_{fg,ref} - T_{ref} \cdot \left(s_{fg,i} - s_{fg,ref}\right)\right] \quad (5.4)$$

On the other hand, the corresponding second law efficiency for the integrated ORC-adsorption system is calculated based on the following equation:

$$\eta_{ex,orc,ads} = \frac{\left(\dot{W}_{el,gen} - \dot{W}_{el,motor}\right) + \dot{E}x_{ch,w}}{\dot{E}x_{fg}} \quad (5.5)$$

IV. Potential of CCHP operation of investigated configurations

In the present sub-section, a brief discussion of the potential integration of heating production in the examined configurations is included. At this point has to be stated that no configuration has been tested on heating mode operation as this was exceeding the scope of this study. Heating could be produced from the examined systems via the following was:

- Case 1 Heat source stream exiting Intermediate Heat Exchanger 1 (configurations b and c d) or 2 (configuration a)
- Case 2 ORC condenser (configuration a, c, d)
- Case 3 Adsorption chiller re-cooler (all configurations)

In Cases 1 and 2, the production of heating could lead to a decline of the electrical efficiency of the ORC, as the condensation temperature would have to be increased from 30 °C to 60-80 °C in order to ensure the generation of heat of sufficiently high temperature. This penalty would be more severe at low waste heat source temperatures, exceeding a 5% decrease in the ORC thermal efficiency. An additional constraint regarding Case 1 concerns the acid dew point of the flue gas stream, which is influenced by the sulphur content of the fuel. Furthermore, depending on the water content of the flue gas, a condensing heat exchanger could be used for heat generation, which would nevertheless be associated with increased capital costs. It should also be noted that in configuration (a) less heat would be available to be extracted from the flue gas stream, as it is expected to have a significantly lower temperature compared to the other configurations.

Due to the low re-cooler temperature (which in the present study is taken equal to 25 °C), it is impossible to extract a substantial amount of heat from the re-cooler of the adsorption chiller. However, if this temperature is increased to 45 °C, it would be possible to generate low temperature heat that could be used for domestic hot water or floor heating. Of course, increasing the re-cooler temperature would have a negative impact on the COP of the chiller, which would be less than 50% of its nominal value. Therefore, this operation mode could be a feasible option during spring and autumn, during which the DHW-to-cooling demand ratio is minimized (but not zero).

5.1.3 Results

The configurations were evaluated for a series of hot flue gas inlet temperatures and for two different pinch point values of the intermediate heat exchangers -namely 5 and 10 K-. The performance of each configuration was evaluated for the following fluid cases:

- R114, for a subcritical cycle
- R245fa, for both a supercritical and a subcritical cycle
- R245ca, for a subcritical cycle
- R600 (butane), for a subcritical cycle
- Cyclopentane, for a subcritical cycle
- Isohexane, for a subcritical cycle

I. Pinch Point effect

Fig. 5.3 presents the effect of the pinch point variation on the exergy efficiency for configuration (b). The best and worst performing organic fluids are presented for two heat source temperatures (240 °C and 300 °C) to highlight the pinch point effect. It can be seen that the decrease on the heat exchanger's pinch point temperature improves the overall efficiency as the hot flue gases stream can be more efficiently exploited. For all the next sections, the pinch point was set to be 5 K for all intermediate heat exchangers.

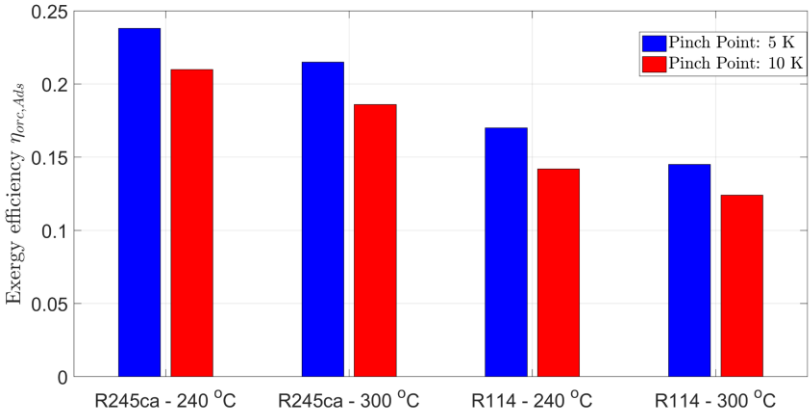

Fig. 5.3. Effect of the intermediate heat exchanger (IHE1) pinch point for configuration (b) on the exergetic efficiency for the cases of R245ca (working fluid) and R114 (worst performing fluid)

II. First law analysis

Given the low capacitance of the flue gases and thus the large temperature difference between the ORC's evaporator and the flue gases stream, the variation in the flue gas inlet temperature does not affect significantly the system's first law performance. The results of the ORC optimization revealed that the system's design points are mainly influenced by the technological restrictions - condensation temperature to drive the sorption system, expansion pressure ratio and built-in volumetric ratio-. Hence, for the considered range of flue gas inlet temperatures, the design point for each case was not varied significantly.

Thus, Fig. 5.4(a) presents an overview on the maximum reported thermal efficiencies of the ORC for each considered working fluid per configuration. As shown, configuration (c) tends to have higher efficiencies for all working fluids, with configuration (d) to be the second most efficient. The highest efficiencies of configuration (c) are mainly attributed to the implementation of a second expander and the heat rejection -to drive the sorption system-

before the inlet of the second expander, allowing the expansion to exploit lower pressures and thus increase the expansion work. In Fig. 5.4(b), the respective maximum combined cooling and power production (CCP) efficiencies are provided. As shown, for all working fluids configuration (b) tends to have the highest efficiency, mainly due to the fact that on this case the adsorption chiller is solely driven by the heat rejected by the ORC's condenser, without neither increasing further the heat input from the hot flue gases -configuration (a) and (d)- nor decreasing the power output of the ORC -configuration (c)-. The cyclic hydrocarbons have the highest efficiencies on this case, thanks to their thermodynamic properties which allow for sufficient expansion even if the condensation temperature is as high as 90 °C. On the other hand, Fig. 5.4(c), reports the cooling to power ratios corresponding to the values of Fig. 5.4 (a)-(b). As shown, all configurations favor the production of cooling, except configuration (c), during which the cooling to power ratio has values in the range 0.61-0.75. On the other hand, the highest ratios are reported in configurations (b) and (d), with values of 5.55 and 6.47, respectively.

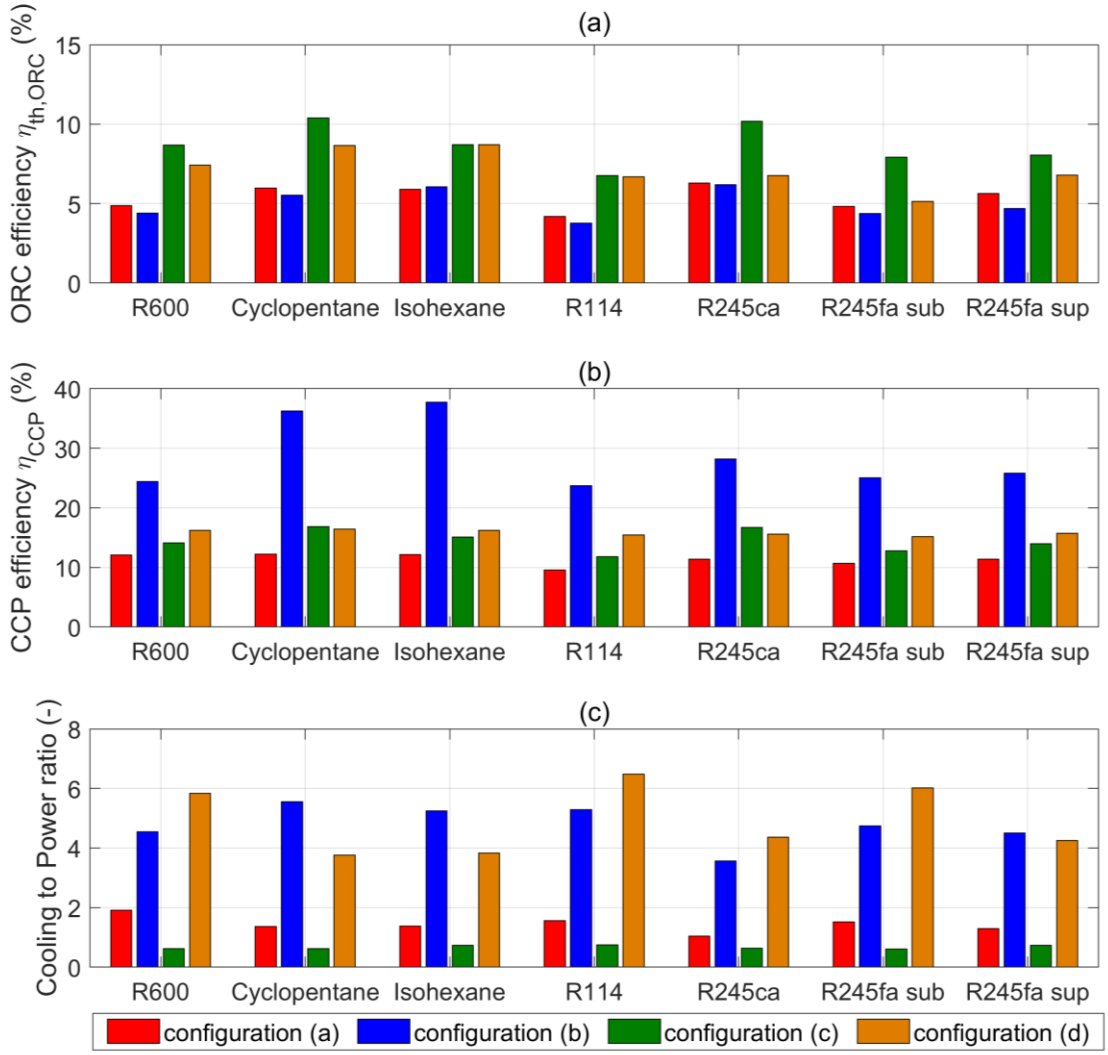

Fig. 5.4. (a) Maximum reported thermal efficiencies of the involved ORC (b)corresponding combined cooling and power efficiencies and (c) cooling to power ratios for each configuration and working fluid (sup: supercritical, sub: subcritical)

III. Second law analysis

In this section are discussed the results with respect to the second law analysis, as defined by equations (11)-(14). As shown in Fig. 5.5, the best performing working fluid for configuration (a) was found to be R245ca with a maximum reported exergy efficiency of 21.3% with a flue gas temperature of 240 °C, while the worst performance was identified to occur when R114 was used with a value of 15.8%. In general, it was observed that the highest efficiencies were achieved at the lowest flue gas temperatures, mainly, justified by the fact that the use of a single expander on this module did not allow for maximum expansion.

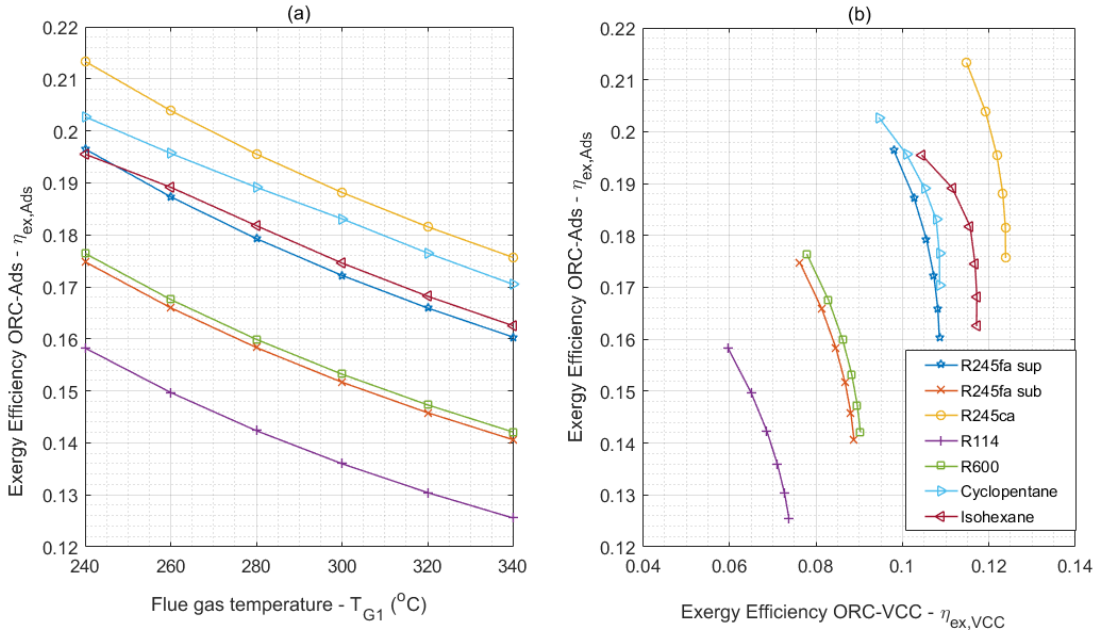

Fig. 5.5. Exergy analysis results for configuration (a) as a function of (a) the flue gas inlet temperature and (b) the exergy efficiency of the respective ORC-VCC system

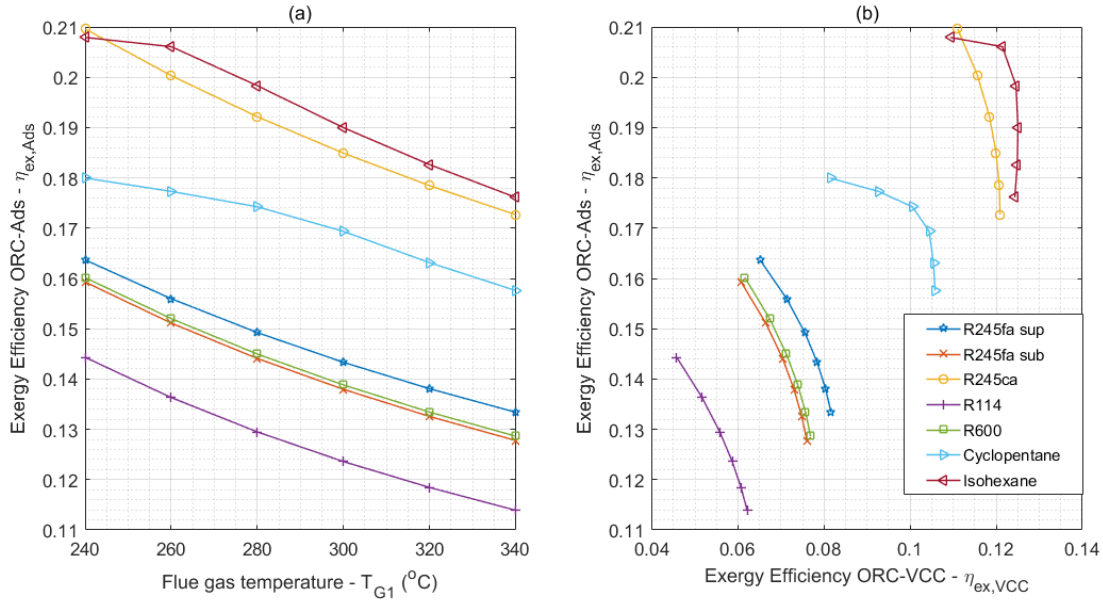

Fig. 5.6. Exergy analysis results for configuration (b) as a function of (a) the flue gas inlet temperature and (b) the exergy efficiency of the respective ORC-VCC system

In a similar manner to configuration (a), the results of configuration (b) reveal a decreasing trend of the exergy efficiency with increasing flue gas temperature. On this case, the main restriction is introduced by the condensation temperature and thus the cycle's low pressure. This results in a demand for higher pressures at the inlet of the expander to maximize the produced work. Hence, working fluids which have higher critical points and allow for higher maximum temperatures and pressures at a subcritical cycle, tend to perform better on this case. Hence, as shown in Fig. 5.6, at temperatures higher than 240 °C, isohexane is the best performing working fluid ($T_{crit} = 224.5$ °C, $P_{crit} = 30.4\ bar$ [192]).

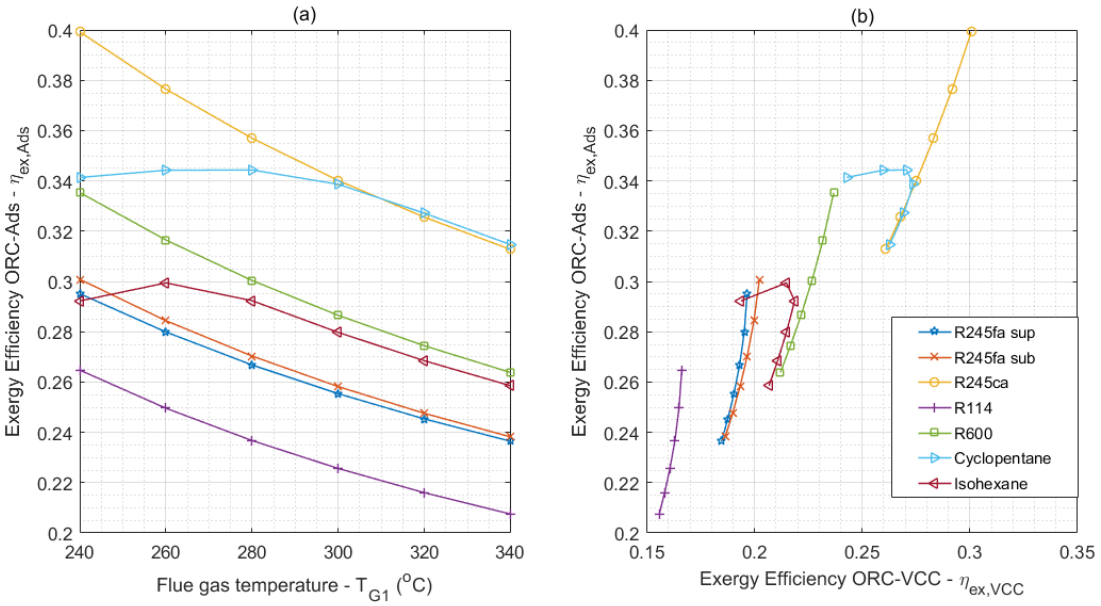

Fig. 5.7. Exergy analysis results for configuration (c) as a function of (a) the flue gas inlet temperature and (b) the exergy efficiency of the respective ORC-VCC system

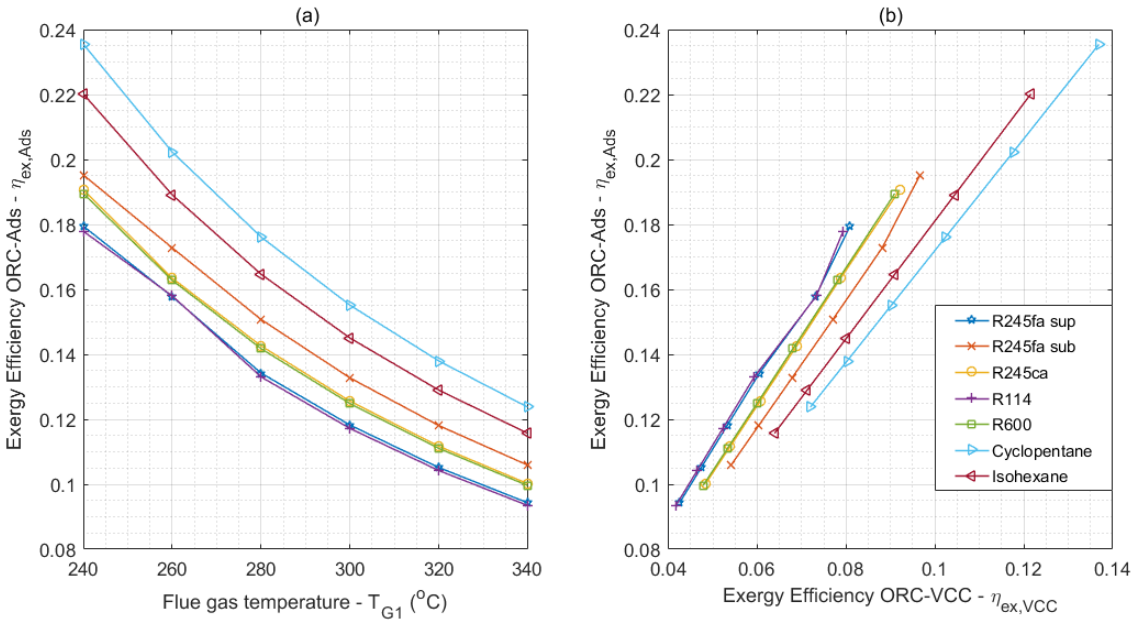

Fig. 5.8. Exergy analysis results for configuration (d) as a function of (a) the flue gas inlet temperature and (b) the exergy efficiency of the respective ORC-VCC system

In configuration (c), Fig. 5.7, the behavior of the considered cyclic hydrocarbons is significantly varying from the rest considered working fluids. This is mainly justified by the fact that for higher flue gas temperatures the maximum pressure of the ORC cannot be further increased due to the limitation of the maximum allowable expanders' pressure ratios not allowing full exploitation of the heat source's potential. On the other hand, the significantly lower temperature that is reported at a subcritical ORC with R245ca as working fluid, results in larger decline in the exergy efficiency at higher temperatures. Hence, at flue gas temperatures higher than 300 °C, cyclopentane tends to perform better than the rest considered fluids.
Lastly, with respect to configuration (d), Fig. 5.8 shows that cyclic hydrocarbons tend to perform better mainly due to the stepwise exploitation of the heat source by means of the three intermediate ("heat recovery steam generator" like) heat exchangers. However, the absence of a second expander does not allow for efficient exploitation of the heat source at higher temperatures, resulting in a decrease in the exergy efficiency with increasing heat source temperatures for all fluids.

IV. Overview

In this section are presented the overview figures for the best performing fluids per configuration, with respect to the reference ORC-VCC exergy efficiency, Fig. 5.9.
In Fig. 5.9, the optimized exergetic efficiency of the investigated integrated ORC-adsorption configurations is compared to that of the reference ORC-VCC system. As shown, for all configurations and heat source temperatures, the ORC-adsorption systems result in higher exergy efficiencies. This is partly justified by the fact that the temperature levels at which the heat is transferred from the flue gases to the cooling cycle are more suitable for an adsorption cycle. Lowering the condensation temperature and thus increasing the expansion ratio of the ORC expanders, might simultaneously increase the cycle efficiencies of the ORC and the VCC and thus the overall system's efficiency.

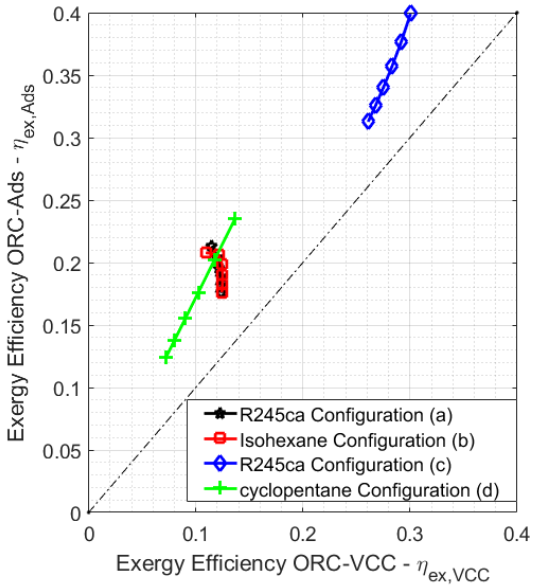

Fig. 5.9. Optimized exergy efficiency of the integrated ORC-adsorption configurations as a function of the exergy efficiency of the respective ORC-VCC system

5.1.4 Conclusions

In this study, the performance of four integrated ORC-adsorption configurations powered by waste heat from hot flue gases was investigated. The configurations were evaluated for different ORC working fluids and driving temperatures, for both subcritical and supercritical cycles. In each case, the optimized exergy efficiency was calculated and compared to the efficiency of a reference ORC-VCC system.

Firstly, it was determined that lower pinch point values in the flue gas/ORC working fluid heat exchangers lead to an increase of the exergetic efficiency of all investigated systems, as they promote the heat source utilization effectiveness. The thermal efficiency of the ORC module is maximized in configuration (c), which involves a two-stage expansion process. In this configuration, the driving heat to the chiller is extracted from de-superheating vapor between the two expanders and not from the ORC condenser, thus permitting higher expansion ratios and overall work production. In all configurations, for a given ORC working fluid, increasing the flue gas inlet temperature leads to a drop of the overall exergetic efficiency, as the limited expansion ratio of the ORC leads to higher condensation temperatures and thus higher flue gas exergy losses. For this reason, configuration (c), which involves two-serially connected expanders, exhibits the highest exergetic efficiency. Furthermore, it was found that the ORC-adsorption systems have fewer exergy losses and perform better than the conventional ORC-VCC systems, mainly due to the mismatch of the temperature levels of the latter. Lastly, it was concluded that the implementation of double expander ORCs and the heat recovery before the inlet of the second expander to drive the adsorption module resulted in higher exergetic performance mainly due to the fact that this configuration allowed for larger expansion and subsequently to lower condensation pressures, increasing thus the expansion work for a given mass flowrate.

5.2 Integrated ORC-adsorption with solar energy

Having conducted a more generic approach, with respect to the heat source, for the trigeneration systems, it is worth as a next step to evaluate the techno-economic potential of a combined orc-adsorption system driven by solar energy. Of course, one has to take into account that the unfavorable economics of solar sorption cooling/heating systems, which as a result reduce the expectations for an economically viable trigeneration solution. Nonetheless, it is worth assessing the current status from both a technical and an economic viewpoint, a study which will be presented in the following sections.

5.2.1 System description

In an attempt to evaluate a solar analogue system of the evaluated configurations of section 5.1, the design temperature of the solar collectors was set at 240 °C. Hence, the considered solar collectors were selected to be PTC, given their favorable economics. With respect to the ORC system, the models implemented for the GA on medium temperature ORCs, section 4.2, were used. Fig. 5.11 presents an overview of the first and second law efficiencies as a function of the cycle's high temperature (and thus the high pressure of the ORC) for a number of working fluids with critical temperatures close to the set driving temperature. Eventually for the analysis were selected three of the shown working fluids, namely, isohexane, cyclopentane and cyclohexane. In fact, according to design results of Fig. 5.11 cyclohexane is the best performing working fluid, with a maximum thermal efficiency of 13.8% and a corresponding exergy efficiency of 51.7%. Cyclopentane and isohexane perform slightly worse

than other tested working fluids, however they were favored due to the involved low pressures (also shown in Fig. 5.11(a)).

The developed system was designed to cover the heating and cooling loads of a residential building for the four climatic zones of Greece, with the corresponding loads to be presented in section 3.3.

In the analysis of section 5.1, the best performing configuration consisted in driving the sorption chiller by a heat recovery step between the two expanders. However, in order to provide the chiller with sufficient driving heat with this configuration, which for all cases corresponds to approximately 10-15 kW, would require a significantly larger scale in the integrated ORC, which is out of the current scope. Therefore, the implemented, in this study, configuration utilized the heat rejection from the condenser to drive the chiller. In order to ensure the optimal design of the cycle, as target outlet temperature of secondary stream from the condenser was set to be 85 °C which is a close to optimal temperature to drive the sorption chiller. An overview of the investigated system can be found in Fig. 5.10.

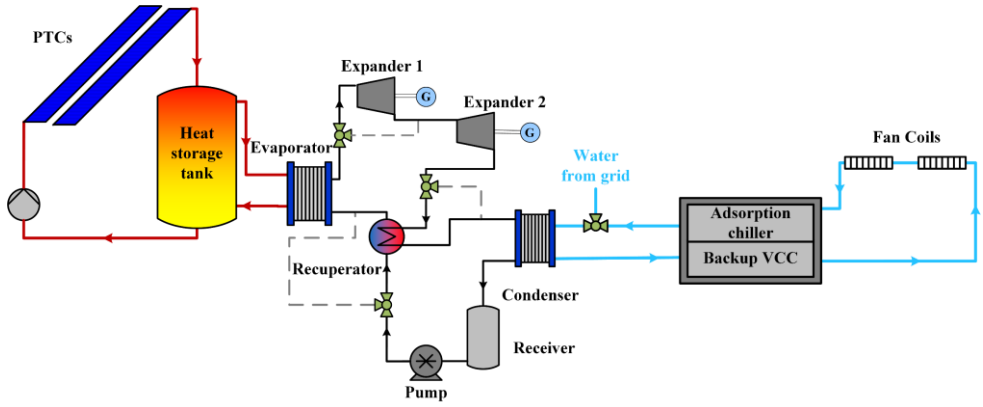

Fig. 5.10. Schematic of the evaluated system

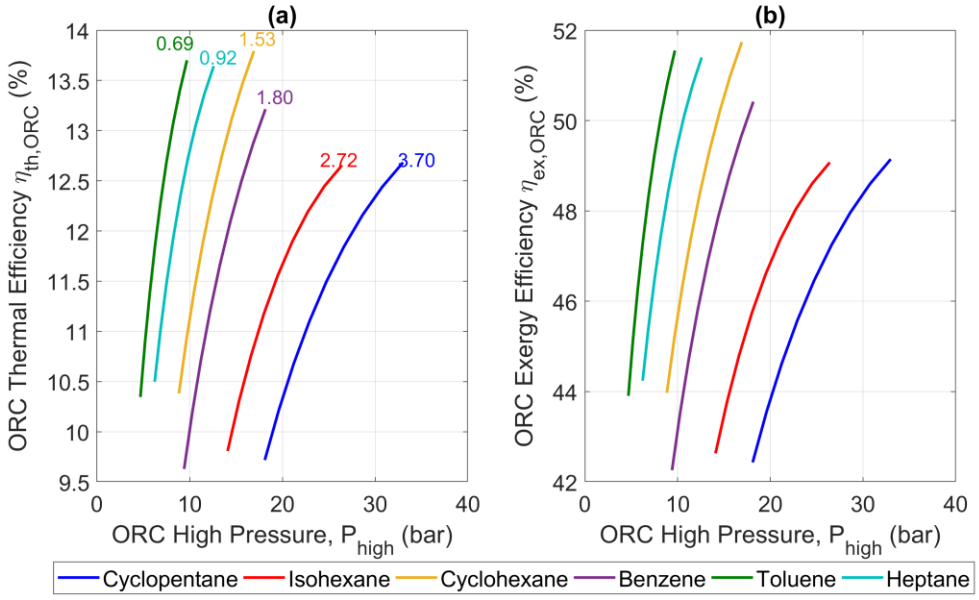

Fig. 5.11. (a) ORC thermal efficiency and (b) ORC exergy efficiency of the evaluated working fluids as a function of the cycle's high pressure

5.2.2 Optimization results

For the techno-economic optimization a multi-objective GA optimization was applied with respect to the exergy efficiency of the system and the levelized cost of energy, similarly to the previous analyses. However, given the complex nature of the system, both objective functions have to be redefined for the trigeneration concept. Hence, the exergy efficiency of the system is calculated below:

$$\eta_{ex,sorc-ads} = \frac{\left(\dot{W}_{el,gen} - \dot{W}_{el,motor}\right) + \dot{E}x_{ch,w}}{\dot{E}x_{sol} + \dot{W}_{el,HP,t}} \quad (5.6)$$

With the $\dot{E}x_{sol}$ to be calculated from eq.(4.3) and the $\dot{E}x_{ch,w}$ to be calculated from eq. (5.3). On the other hand, the levelized cost of energy for the trigeneration system was defined as shown below:

$$LCOE = \frac{CRF \cdot \left\{C_{tot} + \sum_{t=1}^{20}\left[\frac{C_{main} \cdot (1 + r_{om})^{t-1}}{(1+r)^t}\right]\right\}}{Q_{heat,an} + Q_{cool,an} + P_{el,an}} \quad (5.7)$$

With the CAPEX of the solar trigeneration system to be calculated from.

$$C_{tot} = C_{col} + C_{st} + C_{cpump} + C_{HTF} + C_{abs/ads} + C_{HP} + C_{dc} + C_{fancoil} + C_{orc} \quad (5.8)$$

And the ORC system CAPEX, C_{orc}, to be calculated from eq. (4.6).

As design variables for the optimization were set the PTC field surface and the storage tank capacity, with ranges [5,40] and [0.3,2], respectively.

As mentioned above, three working fluids were evaluated along with four cities scenarios, corresponding to the four climatic zones of Greece.

The Pareto fronts of the applied GA for the evaluated scenarios are listed in Fig. 5.12. The exploitation of the heat rejection by the ORC to drive the chiller is depicted in enhanced exergy efficiencies compared to the solar ORC tested in Chapter 4, with values as high as 27.8% for the case of cyclohexane in Kozani (Zone D). The minimum LCOE was also reported in Kozani (Zone D), however with isohexane as working fluid of the ORC and with a value of 0.29 €/kWh. In all cases, the LCOEs are higher than corresponding values of energy prices in Greece, however the small differences that are reported, remark the potential of such systems.

Towards the further enhancement of the economic viability of such systems it is worth analyzing the share of each separate component of the trigeneration setup in the CAPEX. Fig. 5.13 presents the CAPEX breakdown for the system with the optimum LCOE in Athens (Zone B). As shown, the ORC has the highest contribution in the CAPEX with a 29.3%, followed by the adsorption chiller with a 28.1%, while the collectors account for 14.0% of the CAPEX.

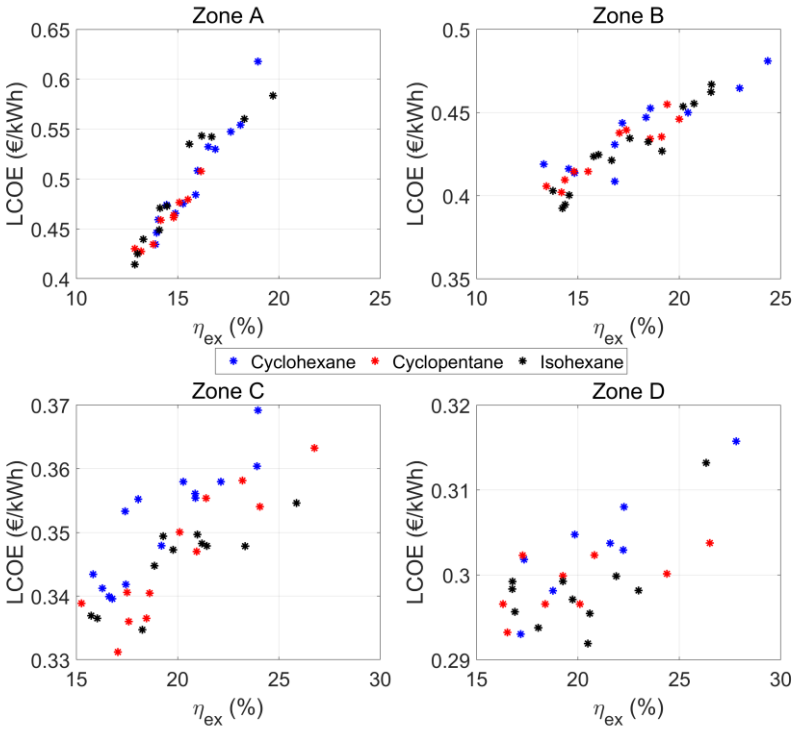

Fig. 5.12. Pareto fronts for the considered working fluids in the four climatic zones of Greece

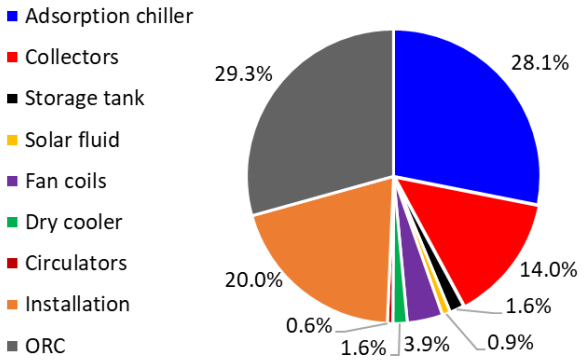

Fig. 5.13. Cost breakdown for a system with 27.5 m² of PTCs, a 0.45 m³ storage tank and an ORC with Isohexane as working fluid

Fig. 5.14 presents the profiles of the objective functions with respect to the two optimization variables for the case of Athens (Zone B). Similarly to all previous optimization studies, there is a clear trend of decreasing exergy efficiency with increasing solar field areas. In the same manner, an increase in the solar field area enhances the economic performance, by reducing the LCOE. With respect to the storage tank capacities, the optimal solutions are located in capacities lower than 0.8 m³, which highlights the trend towards minimum storage tank capacities for the maximization of the system's performance.

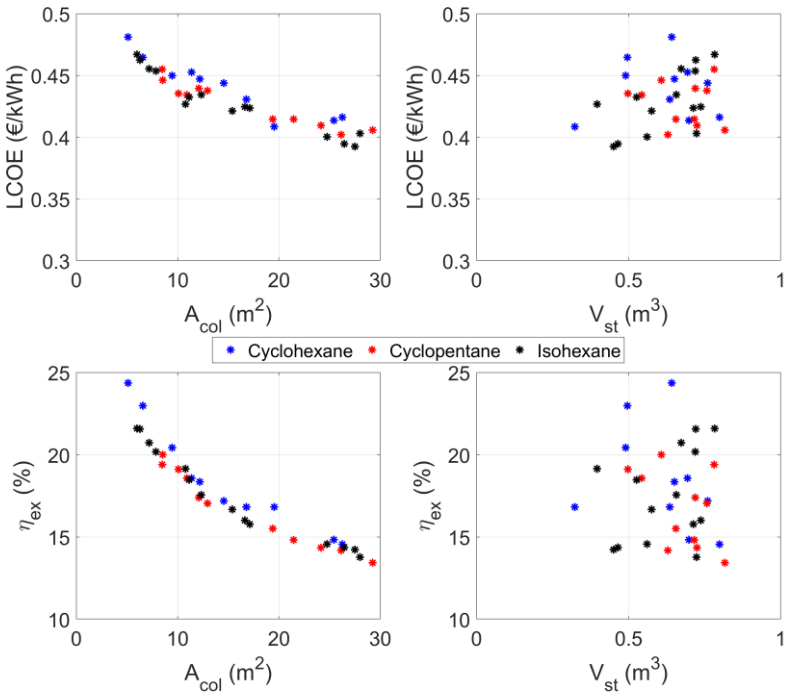

Fig. 5.14. Overview of genetic algorithm results for the case of Athens for the considered working fluids

Table 5.3 and Table 5.4 present an overview of the optimal combinations for the exergy efficiency and the LCOE, respectively, for all considered regions. Detailed plots of the GA's results for the rest three zones are listed in Appendix II (Fig. II.17-Fig. II.19). Moreover, Table 5.4 presents the corresponding NPV and PbP for the optimal solutions. As shown, only a few solutions have a positive cashflow and still the calculated PbP are quite high. In a similar manner, all reported NPVs are negative ranging between -41.2 k€ to -30.7.

Table 5.3. Overview of the optimal combinations in the tested cities

City/Objective	Working fluid	A_{col} (m²)	V_{st} (m³)
Chania – max η_{ex}	Isohexane	5.9	0.34
Chania – max LCOE	Isohexane	34.4	0.37
Athens – max η_{ex}	Cyclohexane	5.1	0.64
Athens – max LCOE	Cyclohexane	32.5	1.12
Thessaloniki – max η_{ex}	Cyclohexane	5.3	0.38
Thessaloniki – max LCOE	Cyclohexane	28.7	0.54
Kozani – max η_{ex}	Isohexane	6.1	0.70
Kozani – max LCOE	Cyclohexane	29.9	0.31

Table 5.4. Overview of the optimal combinations' results in the tested cities

City/Objective	η_{ex} (%)	$LCOE$ (€/kWh)	NPV (k€)	PbP (years)
Chania – max η_{ex}	19.70	0.584	-33.42	n/a
Chania – max LCOE	12.89	0.414	-30.72	102.5
Athens – max η_{ex}	24.35	0.481	-35.16	n/a
Athens – max LCOE	13.32	0.419	-36.54	221.1
Thessaloniki – max η_{ex}	31.65	0.368	-40.50	n/a

Thessaloniki – max LCOE	15.84	0.343	-41.16	n/a
Kozani – max η_{ex}	30.40	0.315	-31.20	n/a
Kozani – max LCOE	17.15	0.293	-30.58	98.7

5.2.3 Sensitivity analysis

In order to have a complete overview of the evaluated scenarios a brief sensitive analysis was also conducted with respect to the systems' economics. Within the sensitive analyses, shown in Fig. 5.15, are listed only the optimum LCOE systems of Table 5.3.

I. Reduction in CAPEX

The reduction in the CAPEX has a positive effect on the trigeneration system's economic performance. For the case of Athens (Zone B), the improvement observed by assuming a 20% reduction of the CAPEX, corresponds to a LCOE of 0.335 €/kWh. On the other hand, for the optimum scenario of Zone D, the LCOE under a CAPEX reduction of 20% was reported as low as 0.234 €/kWh. An overview of the CAPEX's influence in the system's LCOE can be shown in Fig. 5.15(a).

II. Investment lifetime

In Fig. 5.15(b) is depicted the effect of the considered lifetime of the investment in the system's LCOE. Extending the period of investment is naturally improving system's LCOE; the minimum LCOE was recorded in Zone D for a 25-year period of investment with a value of 0.271 €/kWh.

III. Electricity and natural gas prices

Fig. 5.15(c)-(d) present the influence of the electricity and natural gas prices on the PbP and the NPV, respectively. As shown, the increase in both prices has a positive effect on system's economics, with both the NPV and the PbP to be more sensitive in the electricity prices, mainly owed to the fact that a percentage increase in the electricity price corresponds to higher absolute values of the price raise. The optimal results again are obtained for Zone D. More specifically, a 20% increase in the electricity price results in a 74.2 years PbP and a corresponding NPV of -28.3 k€.

IV. Feed-in tariff

The main analysis of section 5.2.2 was conducted considering that the produced electricity by the system is used to cover consumptions of the residential building and therefore a price equal to the electricity price for residential users was considered. However, for solar thermally driven systems in Greece, a feed-in tariff exists, which is equal to 0.248 €/kWh, for systems with absence of a storage tank system that can expand the operation for at least two hours. In this perspective, Fig. 5.15(e)-(f) present the corresponding PbP and NPV results for the base case and the scenario of the feed-in tariff. In fact, the application of a feed-in tariff enhances considerably the economic performance of the system, with a minimum PbP of 42.7 years, for the case of Zone A, while the corresponding NPV was -21.6 k€. As shown, the economic performance of the trigeneration system is still not competitive, however the reduced PbP highlight the potential of the technology, should certain improvements occur in system CAPEX or other influential for the economics figures.

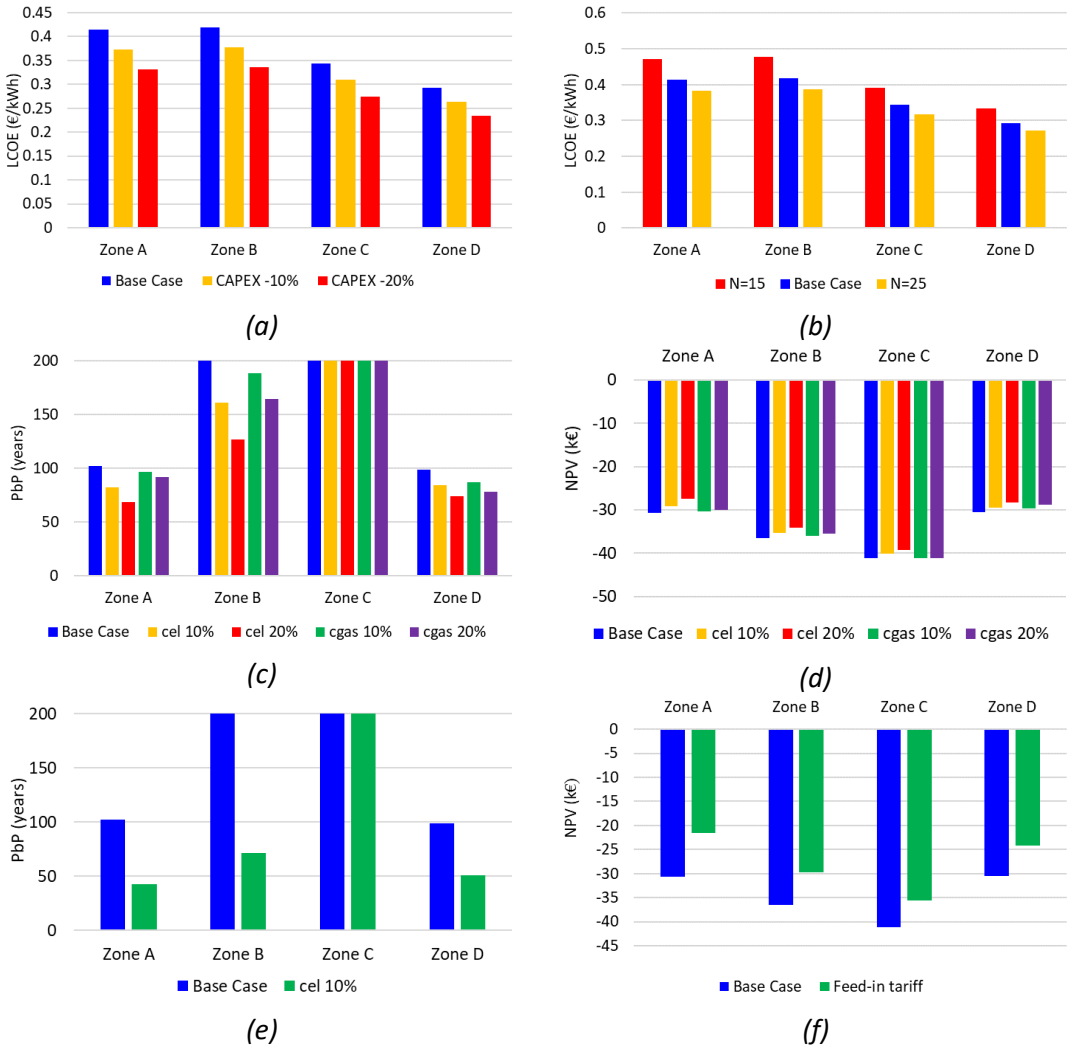

Fig. 5.15. Results of the sensitivity analyses: (a) influence of the reduction in the CAPEX on the LCOE; (b) influence of the period of investment in the LCOE; influence of the electricity prices (c) on the payback period and (d) on the NPV; influence of the application of feed-in tariff (e) on the payback period and (f) on the NPV

5.2.4 Conclusions

In this section, the techno-economic performance of a solar driven trigeneration system based on ORC and adsorption cycle was investigated and optimized via a multi-objective GA. Based on the results of the analysis, the following can be concluded:

- Exergy efficiencies as high as 27.8% were reported, with the higher values to be reported in the colder climatic zones.
- The minimum reported LCOE was equal to 0.29 €/kWh, with the lower values to be mostly reported also in colder climatic zones.
- A components breakdown of the system's CAPEX revealed that the largest shares were attributed to the ORC and the adsorption chiller, with the corresponding values for the reported case study to be 29.3% and 28.1%, respectively.
- There is a clear trend of reducing LCOE values with increasing solar field areas. On the contrary, exergy efficiency is deteriorating with larger solar fields. With respect to the storage tank, both for the exergy efficiency and the LCOE, the optimal values were recorded for smaller tank's capacities.

- Despite relatively low LCOEs, the corresponding PbP and NPVs are pessimistic with PbP as high as 98.7 years and NPVs of at least -30 k€.
- The application of a feed-in tariff enhances significantly system's economics, with the minimum PbP to be 42.7 years and the corresponding NPV to be -21.6 k€.

Chapter 6. Environmental performance investigations

In this section, the systems analyzed and evaluated techno-economically in the previous sections will be assessed from an environmental viewpoint. For the needs of the environmental analysis, the methodology of Life Cycle Analysis (LCA) will be applied in order to have a common well-acknowledged assessment tool for all the cases. Prior to the presentation of the conducted LCA studies, in the following section will be presented a brief introduction in the main aspects of an LCA.

6.1 Introduction to life cycle analysis

Life Cycle Analysis (LCA) is an assessment method developed to quantify the environmental impact of a product, by taking into account its entire life cycle, from the raw materials production to the waste management [193, 194].

LCA is a methodology already applied since 1960s, mainly to assess the raw materials and energy resources consumption in products and processes [195, 196]. Since that period, several standards have been issued mainly by the International Organization for Standardization and the Society for Environmental Toxicology and Chemistry towards the standardization of the LCA process. According to the most well-known ISO 14040-14044/2006 [193], a LCA consists mainly of four interactive stages (Fig. 6.1):

- Goal and scope definition
- Inventory analysis
- Impact assessment
- Interpretation of results

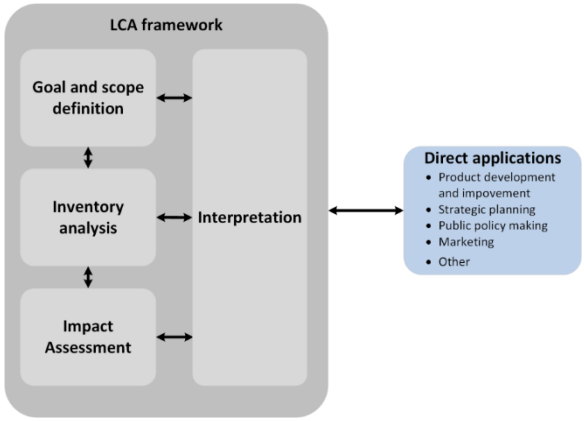

Fig. 6.1. Phases of LCA as defined in ISO 14040 [193]

6.1.1 Goal and scope definition

The definition of the goal and the scope of the LCA is the first step in every such analysis. The goal statement must be clearly indicating the field of application, the reasons for conducting the LCA, the community that addresses and the potential dissemination of the results. The scope is a list of qualitative and quantitative information, including the functional unit(s), system boundaries, and the inventory and/or impact assessments to be tracked [197].

6.1.2 Inventory analysis

In this stage, all inputs and outputs of all involved processes over the entire life cycle of the investigated system are listed and quantified. Due to the high diversity of LCA studies and the

respective inventories, the inputs/outputs are not thoroughly documented within the ISO. In the simplest version, the inputs include the key raw materials and energy requirements, while the outputs list the main gas emissions, solid wastes and water pollutants. As realized from this definition, the accurate listing of the energy use and the detailed list of the consumed raw materials is not always possible, leading the LCA experts to necessary assumptions to compensate for the missing data. What is evident from the above is that the more accurate and detailed a life cycle inventory (LCI) is, the smaller is the uncertainty of the LCA calculations.

6.1.3 Impact assessment

In this stage of the LCA the impact of the previously collected LCA inventory is quantified. This process is realized via a number of sub-processes which are briefly presented below:

- Classification: The results are classified in different categories based on their environmental impact and the used method.
- Characterization: Certain factors are introduced to quantify the results per category.
- Normalization: this optional sub-step introduces per category a weight factor to allow the comparison of different sets of inputs.
- Grouping: another optional sub-step which groups certain categories to simplify the interpretation of the results [198]
- Weighting: an optional sub-step, in which the results are weighted based on the prioritization of the LCA expert. At this point is important to mention that ISO 14040 [193] mentions that weighting should not be applied for comparative studies planned to be published.

6.1.4 Interpretation of results

The final step of an LCA consists of the presentation of the results and the consequent discussion on potential modifications/improvements based on the results of the previous stages as well as a discussion on the limitations of the study. Moreover, at this stage are commonly applied case studies and sensitivity analyses to enhance the study' validity and assess the influence of certain parameters in the investigated system's/product's environmental performance.

6.1.5 Introduction to LCA procedures, databases and softwares

As it is clear, the development of a detailed LCI is a rather demanding and time-consuming process. However, in all cases the collection of all necessary data is almost impossible, mainly due to certain challenges during this procedure, including products and processes that are not precisely accounted by the respective manufacturers and mainly due to confidentiality rights related to certain commercial products and processes. In order to compensate for certain inadequacies of the LCI, different databases have been developed. One of the most well-known and widely recognized database is the ecoinvent database, which is used for a wide range of applications for both industrial and educational purposes, including over 34000 datasets [199]. Ecoinvent database was used also in all LCA studies of this dissertation, with the specific version per study to be defined in the respective section.

As the data processing and impact assessment of systems/products with complex LCIs is rather challenging, dedicated softwares are introduced to conduct the LCA. Two of the most common softwares are the openLCA [200]and the SimaPro [201] softwares. In this dissertation, the SimaPro software was used due to its advantage to allow the user either use

datasets available in the connected databases (e.g., ecoinvent, Agri-footprint) or to create his own datasets based on data collected from manufacturers. The same software can carry out all the involved stages of an LCA, from the creation of the dataset to the impact assessment and sensitivity analysis.

6.1.6 The ReCiPe 2016 method of environmental impact assessment

ReCiPe is the most recent, harmonized method of environmental impact assessment. ReCiPe 2016 is an up-to-date and extensive version of ReCiPe 2008, developed by the Royal Institute of Public Health and the Netherlands (RIVM), the Radboud University in the Netherlands, CML and PRé Sustainability BV.

ReCiPe 2016 focused on providing characterization factors that are representative for the global scale, while maintaining the possibility for a number of impact categories to implement characterization factors at a country and continental scale and improving the methods applied to model midpoint-to-endpoint factors [202].

Depending on the level of the impact characterization, ReCiPe provides results in the form of either 18 midpoint indicators or 3 endpoint indicators, with the relationship between the two levels shown in Fig. 6.2. Midpoint level focuses on single environmental problems, e.g., global warming or ozone layer depletion. On the other hand, endpoint level analysis groups the environmental impact on three higher level indicators namely: (i) the damage to human health, (ii) damage to ecosystems and (iii) the resource availability. Obviously, the reduction from midpoint level to endpoint allows for easier interpretation of the LCA results, with the drawback of increasing the uncertainty on the predictions.

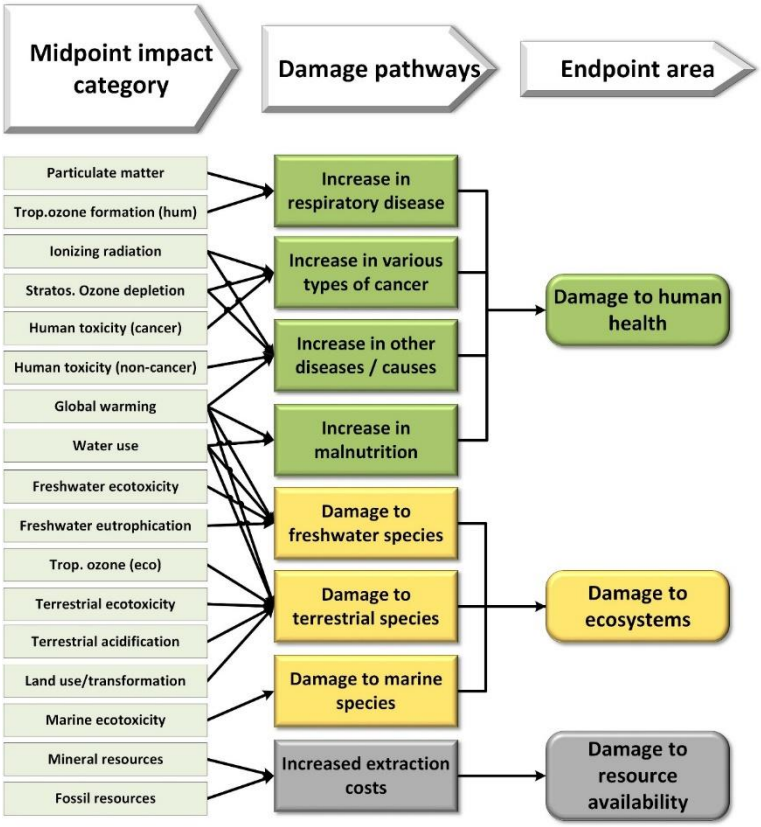

Fig. 6.2. Overview of ReCiPe method

6.2 The Life Cycle Analysis of ZEOSOL system

This section contains information and results published in the study "Life cycle analysis of ZEOSOL solar cooling and heating system" [63]. In the first sub-section, a brief literature review is presented on the key relevant publications, while the next sub-sections include the stages of the conducted LCA and the results of the study.

6.2.1 Literature review on solar cooling/heating LCA studies

Although, as shown in previous Chapters, the solar adsorption-based cooling/heating concept has been thoroughly investigated both theoretically and experimentally from technical and economical viewpoints, its environmental impact had not been, prior to this study, evaluated in detail.

Batlles et al. [203] investigated also a solar driven cooling/heating system, with the difference of using flat plate collectors (FPC) and an absorption chiller. The inventory was composed based on manufacturer data, the ecoinvent database and relevant literature and the reference system was a conventional heat pump, similarly to the present study. However, a different impact assessment method (CML 2001) was used in SimaPro software for the analysis, while as functional unit the thermal loads of the considered building were used. Koroneos and Tsarouhis [204] conducted an exergy and life cycle analysis for solar driven heating, cooling and domestic hot water (DHW) systems in the building sector for the region of northern Greece. Similarly, to the present study, 1 kWh of cooling/heating was used as functional unit. Moreover, the analysis was conducted using evacuated tube collectors (ETC) as ZEOSOL system, however in this case geothermal heat and PVs were used as the backup scenarios. Among the evaluated systems, the solar driven absorption heat pump was found to have the worst environmental performance, while the minimum footprint was found when using a photovoltaic system. Beccali et al. [205] investigated the life cycle of solar driven water-ammonia absorption chiller. The system was evaluated in different locations, similarly to this study, using meteorological data of Palermo, Italy, and Zurich, Switzerland. Using a cradle-to-grave approach, the LCA showed that the use phase has the largest impact in the environmental impact of the system, with a contribution of 73.5% for Palermo and 90.4% for Zurich, respectively. Again 1 kWh of cooling/heating was selected as the functional unit and the environmental impacts of the system was investigated using the Cumulative Energy Demand and EPD LCIA methodologies. However, it has to be stated that the aforementioned report did not take into account any data for transportation, installation and maintenance stages. Jing et al. [206] analyzed the environmental performance of a solar driven combined cooling, heating and power (CCHP) system. The LCIA stage of the study was based on the grey relation theory. The results showed that when the system followed the electric load of the considered building, the environmental impact was lower than in the case of following the thermal load. Moreover, the impact breakdown revealed the significant contribution of materials, operation and fuel stages in comparison to transportation and manufacturing phases. Bukoski et al. [207] conducted a LCA for a large scale solar assisted air conditioning system used to cover the demands of a stadium in Bangkok, Thailand. The LCI was compiled based on the ecoinvent database, while in the present study the ecoinvent database was mainly used for the background processes. The system consisted of 2000 m² compound parabolic concentrator solar collectors driving a 560 kW absorption chiller. Similarly, to ZEOSOL system, a vapor compression chiller (VCC) is also considered as a backup. The

performance of the proposed system is compared to three 1758 kW primary VCC units and a backup unit of similar capacity. The impact assessment stage was conducted using CML2 Baseline 2000 method, a method that investigates ecotoxicity categories usually affected by waste management. However, the updated ReCiPe 2016 midpoint method followed in the present study includes a larger set of distinct environmental indicators, leading to more in-depth impact assessment results. The solar assisted air conditioning system was found to reduce the GWP by 26%, while the corresponding improvements in the categories of acidification and eutrophication were 58% and 34%, respectively.

An analysis on ETC driven absorption chiller has also been conducted by Longo et al. [208] using cradle to grave approach. As in most cases, a conventional heat pump was used as reference. The analysis, however, was conducted in ELISA tool software and used IPCC2013 and Cumulative Energy Demand impact assessment methods. Furthermore, the case studies included evaluated the performance of a PV driven heat pump and not the solar thermal system, contrary to the present study.

The only LCA study of adsorption systems the authors are aware of is the one by Longo et al. [209]. In that study the LCA methodology was applied, in order to assess the environmental impact in terms of Global Energy Requirement (GER) and GWP (thus only consisting of a carbon footprint evaluation, rather than a complete LCA study) of a solar driven adsorption cooling/heating system for domestic applications, using as reference system a conventional reversible heat pump. The system was analyzed for different locations, as ZEOSOL system, while the functional unit was set as "a system with a useful life of 10 years, that provides cooling and heating for the selected reference building, considering a cooling solar fraction of about 0.85". The results of the analysis showed that for all evaluated locations, the solar driven system performed worse than the conventional system, mainly due to the significant impact of the manufacturing phase, even though the analysis did not consider transportation, installation and maintenance data. These results are also highly dependent on the assessment method of the LCA tool that was used for the analysis.

In Table 6.1 is provided an overview of LCA studies on thermally driven cooling systems with details provided for the system type, applied methodology and investigated scenarios. The literature review mainly focuses on LCA studies of absorption, adsorption and desiccant cooling systems. In most cases, vapor compression cycles/heat pumps are considered as suitable reference systems. Moreover, similarly to this study, most analyses follow the cradle to grave approach; while the majority of them also uses SimaPro software to conduct the calculations, even though with other impact assessment methods. Further information on LCA studies on different types of residential heat pumps can be found in Marinelli et al. [210].

Table 6.1. Non exhaustive list of LCA studies on thermally driven cooling/heating systems

System	LCA boundaries	Functional unit	Reference system	Study
FPC driven H_2O-LiBr absorption chiller, backup gas boiler and additional PV field	Production of the installed equipment, transport to the site, operation, maintenance and disposal	Cooling and heating annual loads of considered building	Conventional HP	[203]

Absorption chiller with solar thermal/ geothermal heat and PV	Cradle-to-grave	1 kWh of cooling/ heating	Comparison between assessed units	[204]
Vacuum tubes collector's driven NH_3-H_2O absorption chiller	Cradle-to-grave (excl. transportation, installation and maintenance)	a) overall SHC system b) 1 kW of absorption chiller installed c) 1 kWh of cooling and heating	HP (summer) Gas boiler (winter)	[205]
CCHP system with absorption chiller operating with solar heat and waste heat from gas engine	System construction (incl. raw materials), transportation and operation phase	Tri-generation system through its lifetime	• -	[206]
Single/double effect H_2O-LiBr absorption chiller driven by CPCs / back-up HP	Cradle-to-grave	Overall system through its lifetime (for chilled water production)	• HP (grid-connected)	[207]
• **PV-HP** • **ETC driven AHP**	Cradle-to-grave	Overall system through its lifetime	• Air-water HP	[208]
Adsorption chiller (10 kW) driven by solar thermal collectors and back-up boiler	Cradle-to-grave (excl. transportation, installation and maintenance processes)	Overall system through its lifetime (for heating and cooling)	• Water-water HP	[209]
Absorption chiller with solar thermal collectors	Cradle-to-grave (excl. transportation, installation and maintenance)	Overall system through its lifetime	• HP (grid connected PV) HP (stand-alone powered by PV)	[211]
Single effect H_2O-LiBr absorption chiller (100 kW)	Operation phase (no construction step included)	Chiller cooling capacity	-	[212]
Biomass driven CCHP	Fuel extraction, pre-treatment, transportation, combustion & manufacturing and disposal of all components	1 h of operation	Conventional system with: • Fossil fuel boiler (heating) • HP (cooling) Reference power plant	[213]
Small scale solar driven absorption chillers / PV driven HPs	Production, operation and end-of-life (excl. transportation, system installation and maintenance)	Considered systems	Grid connected HP	[214]

Double-effect H_2O-LiBr absorption chiller with solar thermal collectors	Cradle-to-grave	Cooling energy consumed by the building over its lifetime	Water-water HP and NG boiler (for large-sized building) Packaged a/c unit and NG furnace (for medium-sized building)	[215]
Solar assisted CCHP using an absorption chiller	Cradle-to-grave	-	One of considered cases	[216]
PV/T driven desiccant evaporative cooling system (2.7 kW)	Cradle-to-grave (excl. transportation, installation and maintenance processes)	Overall system through its lifetime (for heating and cooling)	HP	[217]
NH_3-H_2O absorption chiller (12 kW) driven by solar thermal collectors	Cradle-to-grave	Overall system through its lifetime (for heating and cooling)	HP with NG burner and solar PV	[218]
Hybrid energy plant consisting of solar thermal and PV field and CCHP system with absorption chiller	Cradle-to-gate	-	-	[219]
CPC driven ORC – Absorption chiller system	Raw materials extraction, manufacturing and operation (excl. decommissioning and disposal)	1 kWh of equivalent primary energy	-	[220]
PTC driven absorption air-conditioning system	Construction, operation and end-of-life	114.4 MW_c (cooling during entire lifespan)	Conventional a/c unit	[221]

AHP: Absorption heat pump CPC: Compound parabolic concentrators ETC: Evacuated tube collectors FPC: Flat plate collectors PTC: Parabolic trough collectors PV/T: Photovoltaic thermal collectors

Within this context, the ZEOSOL project aims to develop a fully commercial solar driven hybrid adsorption heating/cooling system able to solely cover the cooling and heating needs of a residential building with an enhanced thermal efficiency and competitive specific costs of less than 2,000 €/kWc.

The LCI was structured with high level of detail, using data from manufacturers, the literature and measurements from the demo plant, including precise data for life cycle stages like transportation, installation and maintenance, which are often not taken into account in other studies or are listed in a quite rough approach and is in fact not listed before in a LCA study of solar adsorption systems. The system's environmental performance over a wide variety of

impact categories was evaluated and compared to the one of a conventional reversible heat pump. The base scenario evaluated the system life cycle considering its operation to be in Athens, Greece. However, the impact of different parameters has been investigated via various case studies, like the comparison of the performance of the system based on the working mode (cooling mode only and for entire year operation), a comparison which has not been discussed in the existing literature. Given that at the time of the analysis, only cooling mode experiments were conducted, the main focus was on that mode, while a section on both cooling and heating mode was also added and discussed with on a latter date.
With respect to the system description, it is thoroughly presented in a previous section. Hereby is listed a brief overview for completion of the LCA.

6.2.2 System brief description

The key concept of ZEOSOL setup consists in the coupling of high performance solar thermal collectors with a hybrid adsorption chiller to solely cover the heating and cooling needs of a building. The schematic of the demo plant that was commissioned and tested at the Laboratory of Steam Boilers Thermal Plants of National Technical University of Athens is shown in Fig. 6.3. The solar field of the ZEOSOL system consists of three rows of evacuated tube collectors, manufactured by AKOTEC, with a total surface of approximately 40 m^2. The tilt angle of the collectors is approximately 30 ^oC, with a south orientation. The working fluid of the solar collectors, is an aqueous mixture of propylene glycol. Heat storage is realized in the system via a 1 m^3 water tank equipped with coils through which the tank is heated from the solar sub-circuit.
The hot water from the storage tank is then used to drive the zeolite-water adsorption chiller, which has a cooling capacity of up to 12.5 kW, with a maximum thermal COP of 0.65. The chiller, manufactured by Fahrenheit GmbH, is coupled with a backup heat pump to enhance part load operation of the system. The backup heat pump has a similar cooling capacity to the adsorption chiller, so that it can fully cover the loads of the building in days with no solar irradiance. The heat rejection of the hybrid system is realized via a V type dry cooler, retrofitted for the specific application by CNR-ITAE.

6.2.3 System modelling

Most components modelling has been presented already in previous Chapters along with its experimental validation. However, for the needs of the LCA study, data was needed for the use phase of the ZEOSOL system in a reference building. Given the scale of the demo plant, a reference building model was developed with a total floor surface of 550 m^2, such that the peak cooling load was equal to 12.5 kW using EnergyPlus software and simulated with Athens meteorological data [222]. The thermal properties of the building's elements were derived from ISO 6946 [223]. Specifically, the heat transfer coefficients for the walls, roof and floor were 0.447 W m^{-2} K^{-1},0.181 W m^{-2} K^{-1}, and 0.283 W m^{-2} K^{-1}, respectively. The corresponding heat transfer coefficient for the windows was considered 3.78 m^{-2} K^{-1}. Regarding the temperature setpoints were set at 20 °C for heating, while the respective value for cooling mode was equal to 25 °C. Finally, regarding the heating/cooling schedule it was considered to operate between 16.00-08.00 during week, and continuously during the weekend. An overview of the cooling load profile for the cooling period is shown in Fig. 6.4.

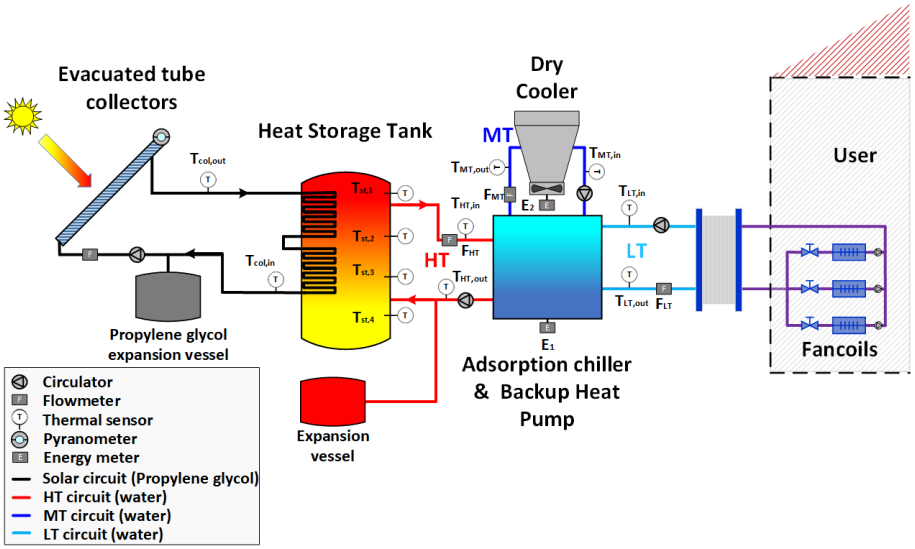

Fig. 6.3. Schematic of ZEOSOL setup considered for the LCA study

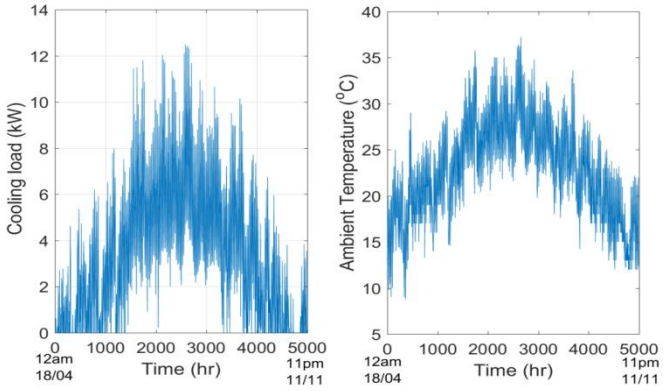

Fig. 6.4. Overview of the cooling load as calculated by EnergyPlus and the respective ambient temperature in Athens over the cooling period

By implementing all the aforementioned sub-models and setting the solar collectors' area to be 40 m², the model was executed for the meteorological data of Athens. The final results over the cooling load covered by ZEOSOL and thus the electricity consumption of ZEOSOL due to the operation of the backup heat pump was estimated, as shown in Fig. 6.5. The operational strategy of the developed model is similar to the actual setup. In this context, the solar cooling system is used to cover partially or totally the loads of the test building whenever there is sufficient heat to drive the adsorption chiller. The temperature threshold for this case was set at 85 °C during summer and 80 °C during spring and autumn, values that were identified as optimal by the chiller's actual operation. In cases that the solar heat is not sufficient or the loads are exceeding the capacity of the adsorption chiller, the backup heat pump is used to cover the thermal needs of the building. Hence, for a peak cooling load of 12.5 kW, the overall cooling load of the building was estimated by EnergyPlus to be 18,654 kWh which corresponded to 4,896 kWh of electricity for the reference heat pump. At this point, has to be stated that the performance of the reference system, was based on performance data from a commercial reversible heat pump [224], thus its operation was modelled on hourly basis based on the ambient condition and the target water temperature for the cooling of the building. Based on the results of the simulation, the seasonal cooling COP of the reference

system was equal to 3.81. On the other hand, for ZEOSOL a solar fraction of up to 65% is achieved, resulting in power consumption savings of 3,230 kWh. In terms of system's performance, the seasonal energy efficiency ratio (EER) of the sorption part was equal to 18.6, while the seasonal COP of the backup heat pump was equal to 5.68.

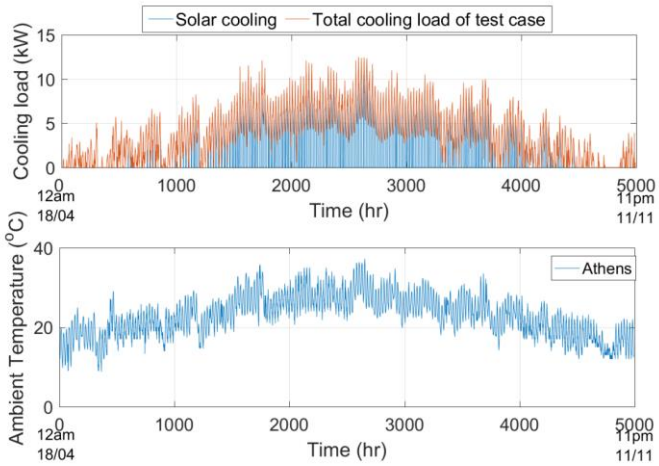

Fig. 6.5. Final results of the Matlab modelling for ZEOSOL performance

6.2.4 Application of LCA methodology

The stages of the LCA study, towards the quantification of the environmental impact of the ZEOSOL system, are listed in this subsection following the order of ISO14040, as presented in Section 6.1.

I. Goal and scope definition

The main goal of this LCA study is to assess the environmental performance of ZEOSOL system installed in Athens, Greece, in order to provide space cooling in domestic scale and its comparison with a conventional heat pump of equal nominal capacity. The study also aims at identifying the components and the processes which contribute the most to the total impact of the overall system. The analysis includes all the parts of the ZEOSOL system and the conventional heat pump respectively, whereas it does not include the distribution system of the building installed, which is considered the same for both setups. A cradle-to-grave approach is followed; since all stages from raw material extraction, manufacturing, transportation, operation, maintenance to the end-of-life were taken into account. Fig. 6.6 illustrates the process flow schematically, illustrating with a broken line the system boundaries. The useful life of both systems is considered to be 20 years. Finally, the functional unit used throughout the study was chosen to be 1 kWh of cooling provided by the system.

II. Inventory analysis

The life cycle inventory has been developed such to list all the inputs and outputs of the investigated system, in terms of the involved materials and the energy consumption over the entire life cycle. More specifically the inventory includes:

- All the components and their technical specifications, including maintenance as provided by the manufacturers. As this data is property of the respective manufacturer, is subjected to confidentiality and therefore could not be presented in this study.
- Due to lack of detailed data, the scroll compressor of ZEOSOL's backup heat pump was modelled using the study of Shi et al. [225].

- The reference heat pump was modelled based on the study of Greening and Azapagic [226]
- The inventory does not include components like electronics or automation systems due to lack of data.
- Piping, valves and miscellaneous used for the hydraulic connections was measured prior to the installation of the demonstrator (Table 6.2).

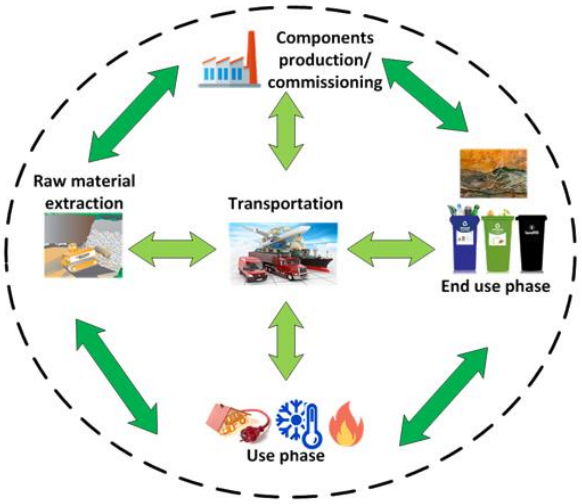

Fig. 6.6. Process flow diagram and system boundaries for the investigated system

Table 6.2. Inventory list for the pipelines/miscellaneous fittings used during the commissioning of the system

Component	Input	Value/Units	Corresponding listing in ecoinvent
Copper pipeline	Copper (OD:22)	3.19 kg	Copper (GLO)| market for
	Copper (OD:35)	19.95 kg	Copper (GLO)| market for
	Copper Transformation	23.14 kg	Wire drawing, copper (RER)| processing
Multilayer tubes	HDPE (OD:26)	17.10 kg	Polyethylene, high density, granulate (GLO)| market for
	HDPE (OD:16)	2.50 kg	Polyethylene, high density, granulate (GLO)| market for
	Polyethylene Transformation	19.60 kg	Extrusion, plastic pipes (RER)| production
Brass fittings (Total weight 40.1 kg)	Brass	90.36 kg	Brass (RoW)| market for brass
	Brass transformation	50.26 kg	Brass removed by drilling, computer numerical controlled (RER)| brass drilling, computer numerical controlled
Copper fittings	Copper	3.14 kg	Copper (GLO)| market for
	Copper Transformation	3.14 kg	Metal working, average for copper product manufacturing (RER)| processing
Transportation (to Athens)	Transportation distance of brass fittings	84.20 tn·km	Transport, freight, lorry >32 metric ton, EURO5 (RER)| transport, freight, lorry >32 metric ton, EURO5

- Refrigerant losses are considered equal to 3%, at the manufacturing stage of the compressors.
- Data has been elaborated using ecoinvent 3.4.

- The base case scenario evaluated the performance of the two systems over the cooling period in Athens (from 18th April to 11th November). The period was determined by the cooling needs of a typical building in Athens, as derived from the EnergyPlus software [222]
- With respect to its operation, the reference heat pump was modeled based on performance charts from Carrier [224].
- During operation, annual refrigerant losses equal to 6% of the total charge of the compressors.
- Transportation of the various components from the production to the installation site as well as from the installation site to the waste treatment site.
- All the components made of copper (tubes and fittings) are considered to be bought from Greece, as they were actually produced, and therefore their transportation is considered negligible. Brass fittings are imported from northern Italy and a transportation distance of 2100 km by lorry is considered for shipping to Athens.
- Dismantling of the setups is not taken into account as was consider that is performed by hand.
- Losses of refrigerant from mechanical compression devices during dismantling are taken into account, considered as equal to 20% of the total refrigerant's mass [227].
- Regarding end-life, 90% of the R-134a refrigerant is recovered and reused, while the remaining 10% is sent for combustion -assumption made in accordance with the ecoinvent analysis- [228].
- Full recovery and recycling of all metals is assumed. For all non-metallic materials, such as plastic and lubricating oils, combustion was considered.
- The cut-off system model of ecoinvent has been used throughout the study.

III. Impact assessment

The impact assessment methods that have been chosen for this study, as mentioned already, are ReCiPe 2016 Midpoint v.1.02 and ReCiPe 2016 Endpoint v.1.02 under Hierarchist, H perspective. The results are presented in all impact categories available by the method.

6.2.5 Results

In the base case scenario, the environmental impact of ZEOSOL cooling system is compared to a conventional heat pump for the reference scenario, i.e., operation in Athens, Greece, and a solar collector field of 40 m². As shown in Fig. 6.7, ZEOSOL system has a better performance in most categories, including global warming and ozone depletion, with a 51.2% and a 37.4% decrease of the equivalent emissions of two impact categories, respectively. The main reason for the better environmental performance of ZEOSOL system is its lower electricity consumption compared to the conventional heat pump, given the dominant role of fossil fuels in the electricity mix in Greece.

On the other hand, there is a number of categories on which the reference heat pump tends to perform better, including the land use and the mineral resources scarcity. More specifically, the impact of the conventional heat pump is less than 61% of the respective impact of ZEOSOL system in the mineral resources scarcity. This mainly due to the use of copper-based materials for the pipelines and the solar field. A quantitative overview of the two systems comparison is provided in Table 6.3 and Fig. 6.7.

Table 6.3. Quantitative results of impact assessment for ZEOSOL system and reference heat pump per functional unit for key impact categories

Impact category	ZEOSOL system	Reference heat pump
Global warming (kg CO_{2eq})	1.37·10-1	2.81·10-1
Stratospheric ozone depletion (kg CFC-11_{eq})	0.67·10-7	1.07·10-7
Water consumption (m^3)	1.02·10-3	1.62·10-3
Land use (m^2)	1.68·10-3	8.78·10-4
Mineral resource scarcity (kg Cu_{eq})	2.40·10-3	3.96·10-4

Fig. 6.8 presents a breakdown of the component's contribution in each impact parameter. As can be seen, electricity consumption for backup heat pump's compressor operation has a large impact on ozone depletion, water consumption and global warming, in the latter accounting for more than 50% of the total impact. In fact, the high impact of electricity on the aforementioned impact categories is related to the energy mix of Greece dominated by lignite power generation [229]. Significant contribution on global warming and ozone depletion has also the backup heat pump, which is mainly attributed to the refrigerant (R-134a) used. This is explained by the high global warming potential (GWP) of R-134a, which is equal to 1430 [151]. Regarding ozone depletion, other substances emitted during the refrigerants' life cycle, such as monochloro-tetrafluoroethane (R-124) and trichlorotrifluoroethane (R-113), have an impact on ozone depletion [226]. As a result, R-134a is responsible for 95% of the total impact of the backup heat pump in the ozone depletion indicator.

On the contrary, electricity has a relatively small influence on land use and mineral resources scarcity, with rates of 14.8% and 2.3%, respectively. In these categories, the main impact is due to the large masses of metals, and in particular copper, contained in the system. Hence, on these impact categories the influence of pipelines and fitting equipment is more significant, given that they mainly consist of copper and brass. Similarly, in land use and mineral resources scarcity, evacuated tube collectors have a significant contribution with 37.5% and 24.3%, respectively. The impact of collectors on the different categories depends on many factors as it is a component of the system, which consists of a large mass of raw materials, and their construction involves high electricity consumption, according to the data provided by the manufacturers.

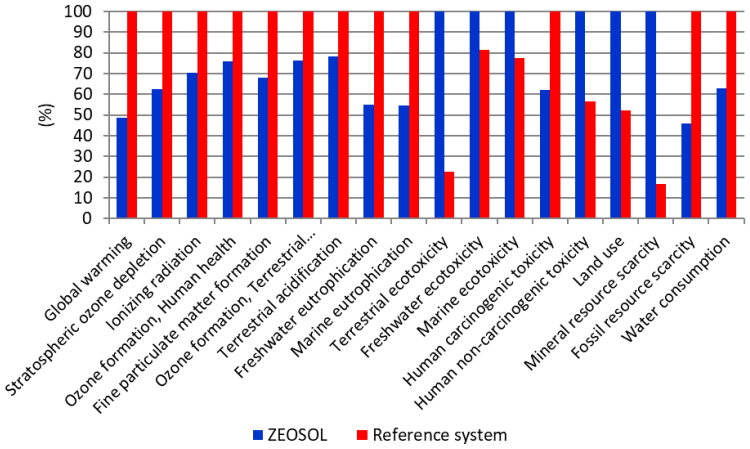

Fig. 6.7. Comparative Impact Assessment results of ZEOSOL system in respect with a conventional heat pump using Midpoint Level

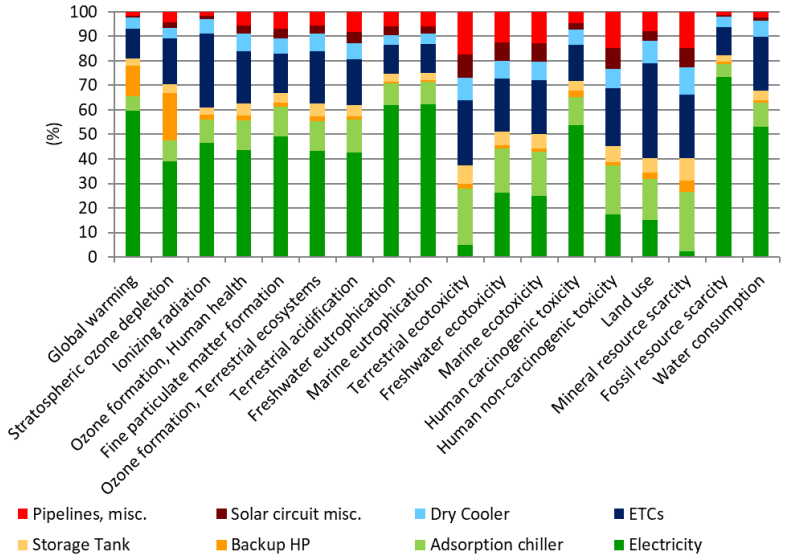

Fig. 6.8. Components impact on overall results of ZEOSOL system using Midpoint Level analysis

Fig. 6.9 and Fig. 6.10 provide the respective results with regards to endpoint categorization. At this point, it has to be stated that for the endpoint analysis all 18 midpoint level impact categories were used in ReCiPe 2016 method. In fact, ZEOSOL system was favorable in 12 categories, justifying the reduced impact shown in all three cumulative indicators of Fig. 6.9. As presented in Fig. 6.10, electricity has a dominant role in the overall system's performance, accounting between 40.0-51.2% in the three impact categories. The impact of the copper and the used glass is also visible by the contribution of the pipelines and the evacuated tube collectors in all categories.

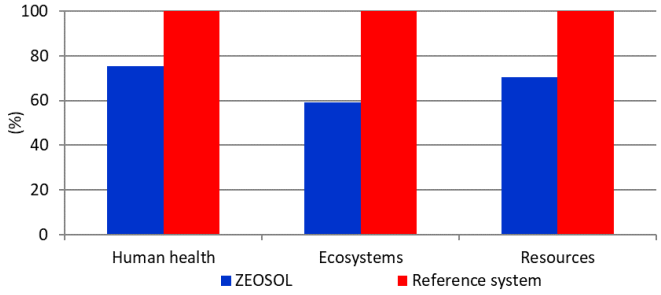

Fig. 6.9. Comparative Impact Assessment results of ZEOSOL system in respect with a conventional heat pump using Endpoint Level.

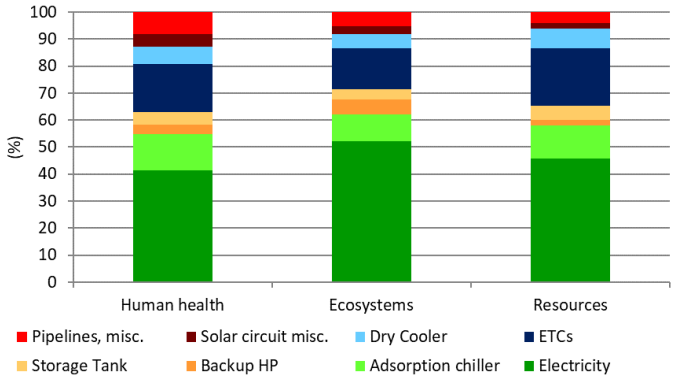

Fig. 6.10. Components impact on overall results of ZEOSOL system using Endpoint Level analysis.

6.2.6 Influence of solar field

In the section 6.2.5, it was shown the significant impact of the solar field in many impact categories, including the mineral resources scarcity and the land use. For this reason, a sensitivity analysis was conducted to evaluate the importance of reducing the solar field surface on the environmental performance of the overall system. Two alternative scenarios were analyzed; namely the reduction of the solar field down to 30 and 15 m², respectively. The reduction of the solar fraction, a direct consequence of the smaller amount of harvested solar energy, resulted in an increase in electrical consumption from the backup heat pump.

The results of the analysis revealed that system tends to perform in a similar manner to the base case investigated above. In this way, an increase in the environmental footprint of the system is observed in all the impact categories, which are mainly affected by the electricity consumption. In any case, however, the environmental impact on those categories is still smaller than the conventional heat pump, as shown in Fig. 6.12 and Fig. 6.11. Respectively, due to the reduction in the raw materials of the system there is a resulting decrease in the impact on the categories that are mainly affected by the mass of the system.

In the marine ecotoxicity and freshwater ecosystems categories, as shown in Fig. 6.11, the impact of the solar field and electricity consumption are comparable. Moreover, it is observed that eventually there is an increase in the environmental footprint of the system on these categories, which implies that the reduction in the solar field and the consequent raw materials reduction yields less environmental benefit than the negative effect of the increased electricity consumption. This effect becomes more apparent for a collector field of 15 m². At the endpoint level (Fig. 6.12), a deteriorating in the environmental performance of all three damage categories is observed as the surface area of the solar field decreases, while even for a field of 15 m² the system's impact is less than that of the conventional heat pump.

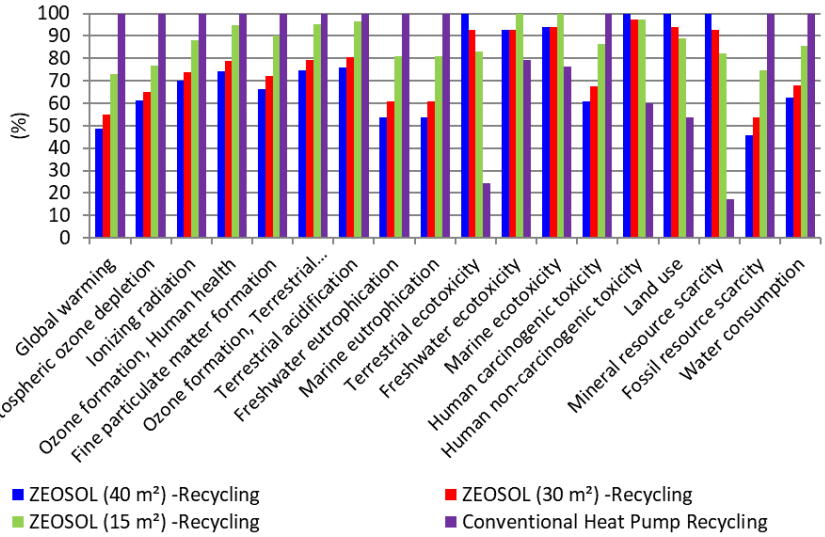

Fig. 6.11. Comparative Impact Assessment results of ZEOSOL system using Midpoint Level for different solar field areas.

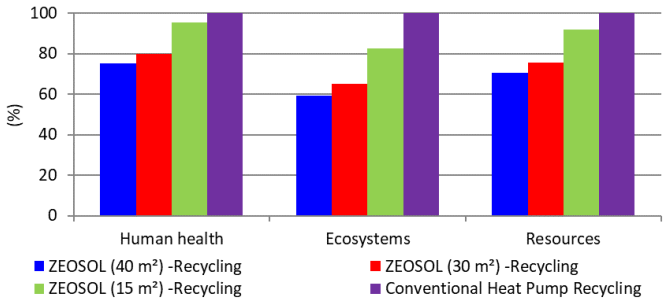

Fig. 6.12. Comparative Impact Assessment results of ZEOSOL system using Endpoint Level for different solar field areas.

6.2.7 Annual performance of solar heating/cooling setup

In the last case study, it was decided to evaluate the performance of the ZEOSOL system over an entire year for both cooling and heating operation. The general assumptions of the study remain the same, with two adaptations to facilitate the heating mode operation on both the ZEOSOL setup and the reference heat pump:

With respect to its operation, the same datasheets -for heating mode performance data- were used for the reference heat pump from Carrier [224]. Heating is realized in ZEOSOL by either harvesting the medium temperature heat rejection from the adsorption chiller or operating the backup heat pump on heating mode, in absence/insufficiency of solar irradiance to drive the adsorption chiller. The functional unit used was chosen to be 1 kWh of thermal energy (both cooling and heating). As expected, the expansion of the system's operation for heating purposes as well, improves the environmental performance, mainly due to the fact that there is further reduction of the electricity consumption. In fact, the footprint of ZEOSOL in most categories has been reduced by 5-8%, with respect to the reference heat pump, compared to the respective results of the "cooling-only" operation. On the other hand, impact categories with worse performance, including land use and minerals resource scarcity, have improved up to 20%, owing to the extended use of the system -without any modifications in the manufacturing phase- (Fig. 6.13).

In a similar manner, the comparative performance of ZEOSOL has improved in all three indicators at endpoint level. More specifically, the results of the "cooling-only" mode revealed an impact of 75%, 59% and 71% compared to the reference heat pump, for the human health, ecosystems and resources indicator, respectively. On the other hand, in the heating/cooling scenario discussed in this section, as shown in Fig. 6.14, the respective results were reduced to 66%, 53% and 62%, respectively. This effect is again attributed to the further reduction of the electricity dependence, the higher COPs of the hybrid system on heating mode and the overall extended use of the system, without any additional manufacturing/energy cost. The small difference between the two reference systems in combined cooling/heating operation and the "cooling-only" mode, is owed to the slightly different performance between heating and cooling in terms of COP, with heating seasonal average COP to be slightly lower, due to worse off-design performance of the evaluated commercial heat pump.

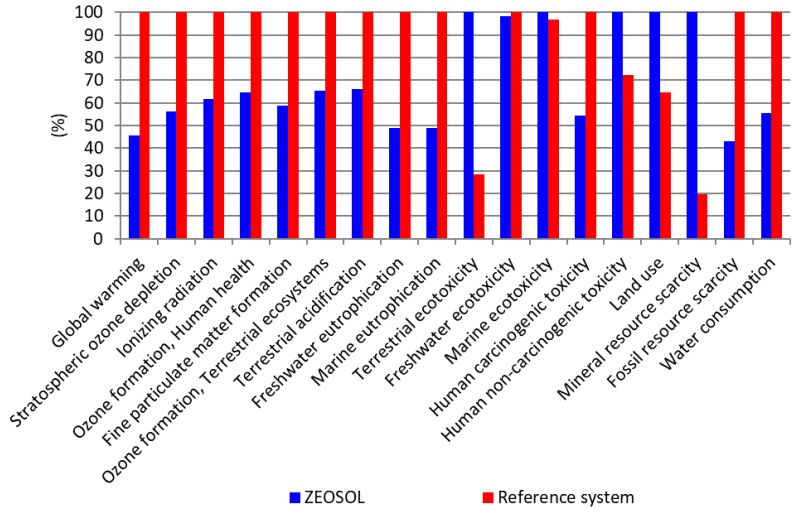

Fig. 6.13. Comparative Impact Assessment results of ZEOSOL system over an entire year (cooling/heating operation) in respect with a conventional heat pump at midpoint level.

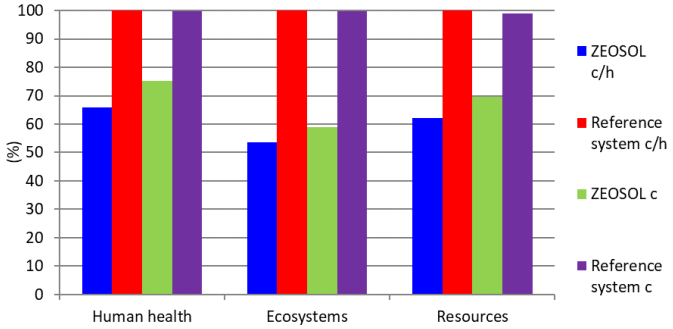

Fig. 6.14. Comparative Impact Assessment results of ZEOSOL system over an entire year (denoted as c/h in the legend) in comparison to the reference system in both entire year and cooling-only (denoted as c in the legend) operation.

6.2.8 Influence of site of installation

The results of this section quantitatively show the effect of different cooling demands on the location of the installation, the country's electricity mix and the different transport distance of the ZEOSOL components from their manufacturing location to the location of the installation. It is worth mentioning that in the majority of cases, the most important factor influencing the impact of the system on each impact category is the electricity consumption, as shown in Fig. 6.15 and Fig. 6.16.

The system's highest impact on global warming and the depletion of mineral resources for installation in Greece and Cyprus is particularly noticeable. This is mainly due to the two countries' electricity mix, which is mostly fossil fuel-based, resulting in higher carbon dioxide (CO_2) emissions (Fig. 6.18). In the case of Cyprus, there is also a significantly higher impact on ozone formation, due to the production of electricity from internal combustion engines, which results in the emission of NOx and ozone depletion, from emissions during oil production [230]. Similarly, Greece has the highest impact on eutrophication of ecosystems as well as human carcinogenic toxicity, mainly due to the lignite combustion [231].

On the other hand, Spain has the highest impact on ionizing radiation, ecotoxicity of ecosystems, human non-carcinogenic toxicity and the depletion of minerals. As far as ionizing

radiation is concerned, the higher impact is related to the use of nuclear energy for the production of electricity in Spain and the emissions of radioactive particles during uranium mining. For the latter categories, which are mainly affected by copper, it should be noted that the results are presented per cooling kWh and given that Spain is the country with the lowest cooling load, each kWh corresponds to a higher weight of raw material and hence more copper, which is responsible for the largest proportion of the impact in these categories. Finally, Italy has the highest impact on water use, which is linked to the production of electricity from hydroelectric stations with a reservoir. A more visible overview of the significant impact of the electricity production mix of each country in the final results of the analysis, is also shown in Fig. 6.17, summarizing the aforementioned discussion. Finally, at the endpoint level (Fig. 6.15), the impacts of different countries on human health and ecosystems vary by less than 30%, with Italy showing the best performance and Spain and Greece showing the worst in human health and ecosystems, respectively. As far as mineral resources are concerned, Cyprus has a significantly worse performance than the rest of the countries, with a 62% difference from the second worse, while Portugal has the best performance.

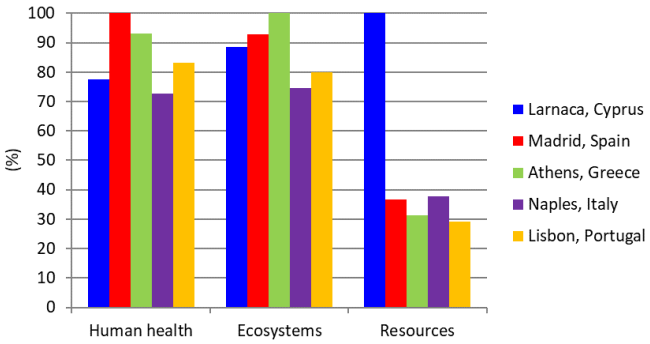

Fig. 6.15. Comparative Impact Assessment results of ZEOSOL system using Endpoint Level for different installation sites.

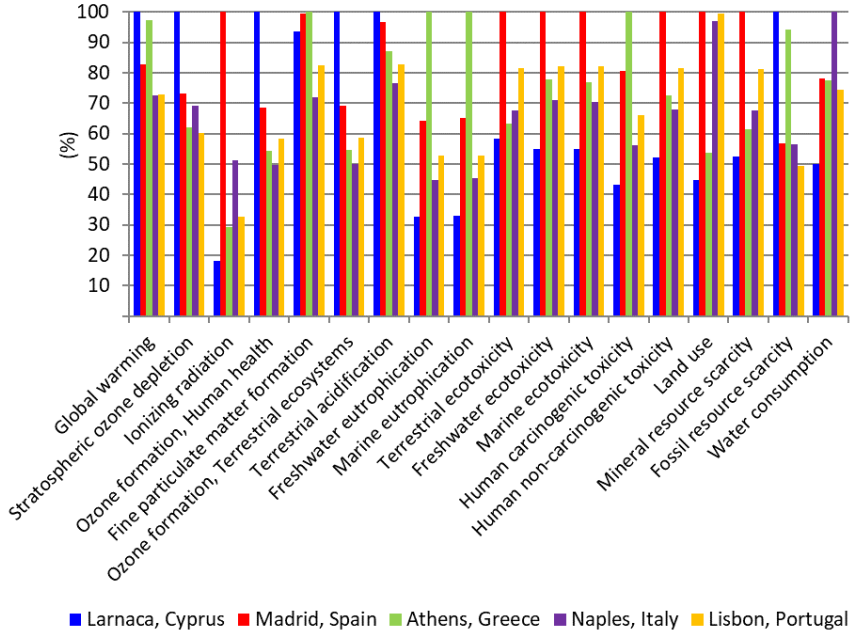

Fig. 6.16. Comparative Impact Assessment results of ZEOSOL system using Midpoint Level for different installation sites.

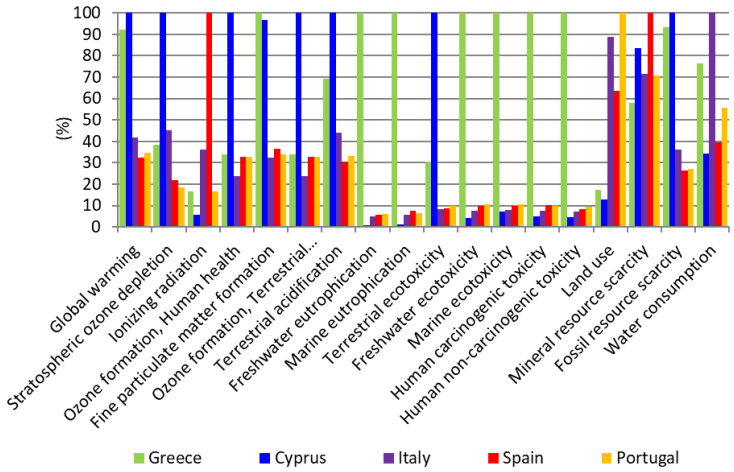

Fig. 6.17. Comparative Impact Assessment results at midpoint level for the electricity mixes of the five considered countries using ReCiPe 2016 method.

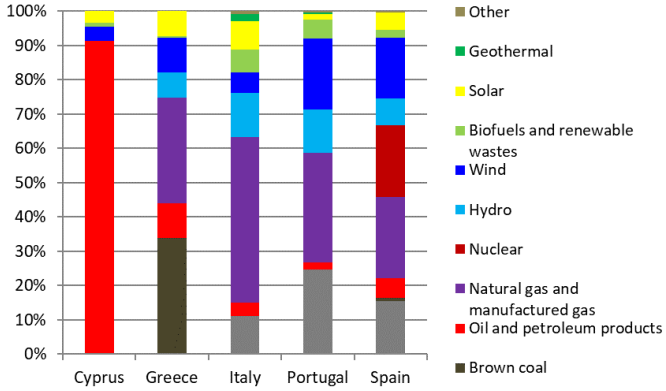

Fig. 6.18. Electricity mix of the considered countries based on data for 2017 from Directorate-General for Energy [232].

6.2.9 Conclusions of ZEOSOL system LCA study

In this study, the environmental performance of the ZEOSOL system prototype has been discussed. The results were analyzed with respect to a conventional heat pump supplied with power from the grid, using the ReCiPe 2016 method. The key conclusions of the analysis are listed below:

With regard to several impact categories, including global warming, water consumption and ozone depletion, the ZEOSOL system has a significantly lower impact than the conventional heat pumps, thanks to reduced electricity consumption. Specifically for global warming and ozone depletion, it was reported a 51.2% and a 37.4% decrease of the equivalent emissions of two impact categories, respectively.

On the other hand, the system presents a significantly higher footprint on the ecotoxicity of ecosystems and the depletion of the mineral resources, mainly due to the use of copper and glass.

With respect to the endpoint level, ZEOSOL system was found to be performing better in all three impact indicators, mainly due to the reduction of electrical consumption.

The reduction of the solar field, results in deteriorating all the categories that are affected by the increase in the dependency from the electrical driven backup heat pump, while there is a small decrease in the impact of those categories (mineral resources, ecotoxicity of ecosystems etc.) which are directly affected by the mass of the system.

Due to the use of the ecoinvent cut-off system model, the impact of landfill in comparison to recycling is not quite visible for the investigated case, despite a small improvement even on this case by the use of recycling for most of the involved materials.
The site of installation has a significant impact on the overall footprint of the system, as the electricity production mix of each country and the deviation in the meteorological conditions per case directly affect most of the impact categories. The more a country is based on non-sustainable sources (e.g., Cyprus) the better the performance of the system is found to be.
Finally, the use of the ZEOSOL system also for heating further decreases the dependency on the electricity and thus enhances the benefits per produced thermal kWh up to a 9%.
Based on the above, it is concluded that to further enhance the system's environmental performance it is of major importance to focus on strategies to reduce the mass of the used metals and perhaps to replace the copper of certain components of the system with other metals or materials.

6.3 Life Cycle Analysis of solar cooling/heating alternatives: Residential scale

The LCA in section 6.2 evaluated a system dedicated for utility or large domestic applications, based on the size of the demo site installed at National Technical University of Athens. However, given the focus of the dissertation on smaller scale systems, it was considered crucial to expand the previous analysis into residential applications. In this perspective, the key solar cooling/heating alternatives were evaluated for use in the simulated buildings used also for the solar cooling/heating GA investigations. The considered alternatives included both conventional systems and solar driven systems More specifically, the considered systems were the following:

- the existing systems consisting of single-split a/c units and a condensing natural gas fired boiler
- an air-water electric heat pump (HP)
- an air-water electric heat pump with PVs and a battery (PV-HP-B)
- Solar hybrid adsorption, based on the LCI of Zeosol system with proper downscaling
- Solar hybrid absorption

6.3.1 Literature review on heat pump related LCA studies

Prior to the presentation of the LCA stages of ISO14040, a brief literature review is listed with main LCA studies related to HP based systems. The literature review and the development of the LCI for the grid connected HP and the PV driven HP is part of the study "Life cycle analysis of a photovoltaic driven reversible heat pump" [126]. In literature, there are many studies and researches regarding the improvements, advantages and emissions reductions related to the PV-driven heat pumps; however, to the authors knowledge, recent and comprehensive LCA studies of the same systems are still missing. Shah et al. [233] were among the first in the USA to make a comparison among three different technologies used with the aim of both heating and cooling a domestic dwelling, varying the geographical location of installation: an air furnace and air conditioner, a water boiler and air conditioner and an air source heat pump (ASHP). The study revealed that the heat pump has the highest impacts in almost all regions mainly due to the electricity mix.
Eicher et al. [234] considered a solar heat pump (SHP) to produce domestic hot water and space heating, avoiding again cooling demand which showed less impact than the

conventional heat pump and electric boiler. Nitkiewicz and Sekret [235] considered three different systems aimed at providing a seasonal heat demand. The several options consisted of a water-water electric heat pump, an absorption water-water heat pump, both using low temperature geothermal water as the low temperature heat sink, and a natural gas-fired boiler. The study shows that heating plants using a low-temperature geothermal source have a lower impact than a gas boiler unit. In the comparison of the two heat pumps, the absorption heat pump has a lower environmental impact rather than electric heat pump. Li [236] conducted an LCA about an ASHP working with different refrigerant fluids to satisfy both heating and cooling demand. Huang and Mauerhofer [237] compared a ground source heat pump (GSHP) with an ASHP and found out that the GSHP has lower environmental impact providing heating and cooling. The results indicated that R410a presented better results than R22 refrigerant, while two capacity heat pumps had a reduction of approximately 5% in CO_2 emissions compared to the single speed ones.

Zhao et al. [238], carried out an optimization study of a solar (PV) assisted hybrid power gas heat pump system (SHPGHP) with respect to the total normalized environmental impact of the system during its whole life cycle. The parameters considered were the photovoltaic ratio, namely the maximum power of the PVs with respect to the one of the gas engine, the transmission ratio, which is the ratio of the gas engine rotational speed to the one of the heat pump compressor and the mixing degree, which reflects the ratio of the actual power provided by the engine and the PVs to the compressor. From the results it is concluded that the best environmental performance is achieved for a photovoltaic ratio of 0.4, while it deteriorates with the increase of the transmission ratio and improves with the increase of the mixing degree.

A techno-economic and environmental impact assessment study of different configurations for providing space heating, DHW and cooling was conducted by Litjens et al. [239]. The investigated systems included a GSHP with a gas boiler (reference case), a GSHP combined with PVs with the incorporation or not of batteries and systems solely comprised of PVs or PVs combined with batteries. From the results it was found that the GSHP system presents the lowest greenhouse gas emissions PBP, compensating for the emissions from manufacturing and installation. A sensitivity analysis was also conducted in respect to the rate of decarbonization (zero emissions) of the electricity mix. As indicated, the faster this is achieved the lower the emissions avoided by PV and battery energy storage system (BESS) systems and the higher by GSHP system.

From all abovementioned studies, it is possible to deduce that heat pumps represent a valid solution to abate greenhouse gases (GHG) emissions but in none of these papers a detailed LCA study on PV-driven heat pump for residential applications was conducted. Existing literature focuses on the CO_2 emissions of relevant systems, without discussion on other environmental parameters. Nowadays, Wang et al. [240] wrote a paper about the growing attention that HPs assisted by solar energy are obtaining, owing to their great feasibility in buildings for space heating/cooling and hot water purposes. Motivated by a lack of comparisons in the literature review, they conducted a performance evaluation of ASHP systems powered by three main solar sources, such as solar thermal (ST), photovoltaic and hybrid photovoltaic/thermal (PV/T). The comparison result indicates that the PV-ASHP system has the best techno-economic performance with a coefficient of performance (COP) of around 3.75.

Similarly, to Table 6.1 of section 6.2, in Table 6.4 is provided an overview of LCA studies on heat pump systems with relevant details for the specifications of each analysis. As in most cases the systems under investigation are used to cover the space heating needs of buildings, natural gas fired boilers are considered as suitable reference systems. Further documentation about LCA studies on residential heat pumps is listed in Marinelli et al. [210] and Wang et al. [240].

Table 6.4. Non exhaustive list of LCA studies on thermally driven cooling/heating systems

System	LCA boundaries	Functional unit	Reference system	Study
• **Central NG furnace/ central AC** • **NG hydronic heating/ central AC** • **ASHP**	Cradle-to-grave	Cooling and heating needs of building over lifetime	-	[233]
• **GSHP / electric boiler** • **GSHP / 10 m² STCs**	Cradle-to-grave	DHW and heating demands of a building over lifetime	Brine water HP + 2 m² STCs	[234]
• **GSHP** • **Geothermal AHP**	Production, operation and transportation (excl. end of life)	Seasonal heat demand for district heating	NG boiler	[235]
ASHP	Cradle-to-grave	Cooling and heating needs of building over lifetime	-	[236]
GSHP	Production, construction, transportation and operation (excl. end of life)	1 kW of installed power	-	[241]
Electric HP	Manufacturing, operation and end of life	Cooling and heating needs of building over lifetime	NG boiler	[242]
PV assisted hybrid gas HP	Cradle-to-grave	Cooling and heating needs of building over lifetime	-	[238]
Waste water HP	Only operation	Total seasonal heating needs of considered building	• Coal boiler • NG boiler	[243]

AC: air-conditioning AHP: Absorption heat pump CCHP: Combined Cooling, Heating and Power DHW: Domestic hot water ETC: Evacuated tube collectors FPC: Flat plate collectors GSHP: Ground source heat pump GWP: Global warming potential LCCP: Life Cycle Climate Performance LCI: Life Cycle Inventory NG: natural gas STC: solar thermal collectors

6.3.2 Systems description

As mentioned above, this generic LCA will include five types of systems. The solar hybrid adsorption will be based on the ZEOSOL system with proper scaling, as defined by the manufacturing companies involved in ZEOSOL. More specifically, the proposed system for residential (single-family) buildings the solar collectors' field will be reduced to half (20 m^2)

and hence the storage tank was respectively reduced to half (0.5 m^3). The electric chiller will have a nominal capacity of 7.5 kW and the adsorption chiller module will have a 5 kW cooling capacity. As suggested, the scaling factor used for the electric chiller was equal to 0.7 ($\cong 1/\sqrt{2}$), while the adsorption chiller inputs were reduced to half of the ones accounted for the ZEOSOL LCI. Finally, the dry cooler will also have 20 kW heat rejection capacity and therefore a scaling factor of 0.7 was considered. The pipelines and commissioning were also considered 0.5 of ZEOSOL's LCI, as the covered distances in residential applications are quite shorter than the circuits constructed in the Laboratory of Steam Boilers and Thermal Plants.

The solar hybrid absorption system was considered to have identical structure with the solar adsorption system, with the only difference to be the substitution of the adsorption chiller with an absorption chiller of 7.5 kW cooling capacity. With respect to the conventional system, it was considered to consist of a gas condensing boiler with a thermal efficiency of 95%, with respect to the higher heating value, and a capacity of 10 kW, which is the smallest capacity found by commercial suppliers. Performance data for the gas boiler was extrapolated from a commercial model, namely Riello gas condensing boiler model 20 IS-E [125]. The respective cooling loads were considered to be covered by a total of three single-split air-conditioning (a/c) units, with a total capacity of 7.92 kW (3 units of 9000 Btu/h) [126]. The EER of the considered single split units was equal to 10.24 Btu/(W h), which corresponds to a COP of 3, as stated in section 3.3. Finally, the HP was modeled based on performance charts from Carrier for the 30AW heat pump model [224]. The HP interacts with the environment via an air-cooled heat exchanger, and with the interior of the building through a water-refrigerant heat exchanger. The results were coupled with the thermal loads of the considered building, as described in section 3.3, to estimate the total electrical consumption of the considered heat pump. Considering that in every moment of the year, the system has to be able to satisfy the load, the heat pump was sized at 8 kW. As mentioned above, the PVs are considered connected to a battery-inverter module.

In all systems, except from the conventional one, two fan coil units were assumed with a cooling capacity of 3.77 kW each. In a similar manner, for the conventional systems, three central heating panel radiators are also implemented [244].

6.3.3 System modelling

The considered building's loads, used in this LCA, are already presented in section 3.3. With respect to the calculation of the systems' use phases, all were based in the presented models of Chapter 2 and 3. More specifically, the use phases for both sorption systems were based on the used models of the solar cooling/heating GA analysis (section 4.3.3), implementing on both cases a solar field of 20 m^2 of ETCs and a 0.5 m^3 storage tank, in order to have a fairer comparison between the two competing technologies. For the PV driven heat pump, the model presented in section 3.4 was used, while for the grid connected heat pump, the model of section 3.2 was implemented. The simulations were conducted for the four climatic zones of Greece, in a similar manner to the analysis of section 4.3.3, for the weather/load data of Chania, Athens, Thessaloniki and Kozani.

An overview of the annual use phase consumptions calculated per system and implemented in the Simapro software for the analysis, is presented in Table IV.1-Table IV.5.

6.3.4 Application of LCA methodology

In a similar manner to the previous life cycle study, the stages of the LCA are listed in the following subsection according to the order of ISO14040, as presented in Section 6.1.

I. Goal and scope definition

The main goal of this LCA study is to assess the environmental performance of the conventional cooling/heating systems and compare them in a homogeneous analysis with the main solar driven cooling/heating alternatives, within the Greek region. For this reason, the performance of the studied systems is evaluated for the four different climatic zones of Greece, considering their use to cover the heating and cooling loads of a residential building, located per case in a city of each climatic zone. Given the different distribution systems of conventional heating systems to the rest, unlike the LCA of Zeosol system, in this case the distribution systems were taken into account in the inventory. A cradle-to-grave approach is followed; since all stages from raw material extraction, manufacturing, transportation, operation, maintenance to the end-of-life were taken into account. The useful life of both systems is considered to be 20 years. Finally, 1 kWh of thermal energy (sum of annual total cooling and heating loads covered by each system) was chosen to be the functional unit for the analysis.

II. Inventory analysis

As in previous study, the life cycle inventory has been developed such to list all the inputs and outputs of the investigated system, in terms of the involved materials and the energy consumption over their entire life cycle. With respect to the Zeosol system, in its inventory the same assumptions were considered as in section 6.2.4. However, given the lower loads of the residential application, a scaling factor of 0.7 was applied. With respect to the rest of the considered systems, the inventory includes:

- The ecoinvent v 3.5 database, under the cut-off system model, is used in order to model the respective flows, namely the materials, energy and emissions of the systems throughout the study.
- Regarding the photovoltaic panels the inventory and technical specifications are taken from the study of Fu et al. [245]. This approach was mandated by the fact that the existing listing, in the ecoinvent database, is rather obsolete and towards a more objective evaluation of the system, a more detailed LCI was favored. During modelling with ecoinvent some assumptions were made regarding used materials. For instance, instead of nitric acid 35%, nitric acid 50% was used and instead of gaseous nitrogen, liquid nitrogen was selected, as the latter ones were the only available in the database. Regarding transportations, the panels are considered to be manufactured in China and transported to Europe by sea before reaching the port of Piraeus, Greece and eventually via lorries reach their final destination. Lorries of Euro 4 and Euro 5 technology are considered for road transport in China and Europe respectively, while a freight ship is considered for sea transport. Finally, for the end of life (EoL) treatments, it is considered that most of the materials such as glass, aluminum and plastics are reclaimed and recycled, whereas other materials like waste acid or silicon carbide are considered to be transported with municipal waste collection lorries in order to be incinerated [246, 247].
- The bill of materials and energy input for the manufacturing of conventional heat pumps, which was selected to be an air-water one, are received from the study of Greening and

Azapagic [226] and are adjusted proportionally to the power of the heat pump in this work. Regarding the operational phase, annual refrigerant losses are assumed 6% of the total charge, while the heat pump is considered maintenance-free, only requiring a top-up of refrigerant [248]. In fact, there is a high deviation in the predicted refrigerant losses in such systems, with Koronaki et al. [249] reporting a range of 4-10%. However, as the study by Heberle et al. [250] revealed by conducting a sensitivity analysis on the refrigerant losses' impact, for low GWP fluids, this variation has negligible impact on the system's overall footprint. Other refrigerant losses accounted are 3% and 20% of the total mass during the manufacturing phase and dismantling of the heat pump after the end of its life respectively [251, 252]. All the components are assumed to be manufactured in Europe, hence transportation via trains and Euro 5 trucks is considered for the refrigerant and lubricating oil. Regarding the end-of-life phase, all the materials of the heat pump including the refrigerant are considered to be reclaimed, except from for a fraction equal to 15% of the lubricating oil which is considered to be transported by municipal waste collection lorries for incineration. These assumptions come from the Italian law regarding waste refrigerant and oil disposal [253-255].

- The compressor considered is the Copeland ZB66KCE-TDF hermetic scroll compressor. The data for the inventory are received from the study of Shi et al. [225] and adjusted accordingly in proportion to the weight, due to lack of data for the actual compressor. 1,3,3,3-Tetraflouropropene, also known as R-1234ze(E) is used as the refrigerant for the compressor, which is modelled as a mixture of n-olefins and fluorine due to lack of data in ecoinvent. Since the component is manufactured in Europe, Euro 5 trucks are considered for road transportation. Regarding refrigerant losses and EoL treatments, the same assumptions made for the conventional heat pump are adopted.
- The list of materials and their quantities for the evaporator and the condenser is taken from the LCA study of ZEOSOL project [63], proportionally to the weight of each heat exchanger. More specifically, the condenser weighs 7.16 kg and consists of 65 plates, while the evaporator weighs 6.1 kg and consists of 80 plates. The energy consumption for manufacturing and the electricity consumption for the copper brazing process are taken from the studies of Adolfsson and Rashid [256] and Reisgen et al. [257], respectively. Transportation from the manufacturing site in Europe to the installation site by Euro 5 lorry is considered. Regarding the end-of-life phase, since the specific components are made entirely of metals, it is assumed that these are fully reclaimed and recycled.
- The inventory for the dry cooler comes from data from manufacturers in the context of ZEOSOL project [258]. The data were adjusted based on the thermal capacity of the condenser. The dry cooler is manufactured in South Germany, so transportation with Euro 5 lorries from the factory to the installation site is considered. The useful life of this component is 10 years, so it is accounted twice over the 20 years lifetime of the system. After the end of its life, all the materials of the dry cooler, which are mostly metals like steel, copper and aluminum and some plastics, are assumed to be recycled.
- For the gas boiler the respective ecoinvent process was selected, since it is a mature technology and the data provided by ecoinvent are considered sufficient. In this case, similarly to other components the data are scaled up proportionally to the power of the

boiler. Transportation from manufacturer to installation site is neglected, as local suppliers are considered per case.

- The absorption chiller was modelled based on the respective ecoinvent process, given the absence of detailed data. In a similar manner to previous cases, a downscaling of the chiller was required for the considered application.
- The multi split a/c units are modelled based on the study of Boustani et al.[259] The units are assumed to be manufactured in Europe, so transportation from the factory to the installation site, as well as transportation of other materials, like the refrigerant, used for the ac unit to the factory, with Euro 5 trucks is considered. Regarding the operational phase 1% annual losses of the total mass of the refrigerant (R-134a) are considered [252]. Regarding the end-of-life phase, consistently to the Italian legislation and the disposal common methods in Italy, 97.5% of the AC units are recycled while the rest is sent to incinerator facilities.
- The fan coils were modelled based on data from Prek [260] and the datasheet of a commercial model [261]. In total two fan coil units were assumed with a cooling capacity of 3 kW each. Fan coils are considered only in the base case, since the conventional systems do not include any. In all case studies, as all considered systems do need the same number of fan coils, they are excluded from the inventory for simplicity. In a similar manner, for the conventional systems, three central heating panel radiators are also implemented [244]. For their modelling 30.22 kg of unalloyed steel were considered per panel, along with average metal working process for the manufacturing of the same amount of mass.
- The inventory for all the considered components does not include the dismantling process, since it considered to be performed by hand and therefore negligible.
- Electronics and automation systems of respective systems are not included in the inventory due to lack of data.
- The Greek electricity mix considered in this study is based on the data from Eurostat for year 2018[262]. An overview of the electricity mix is shown in Fig. 6.19. As shown, 40% of the electricity production in 2018 was provided by renewable sources and biofuels, which results in smaller footprint of the electricity from the grid, compared to other fossil-dependent countries.

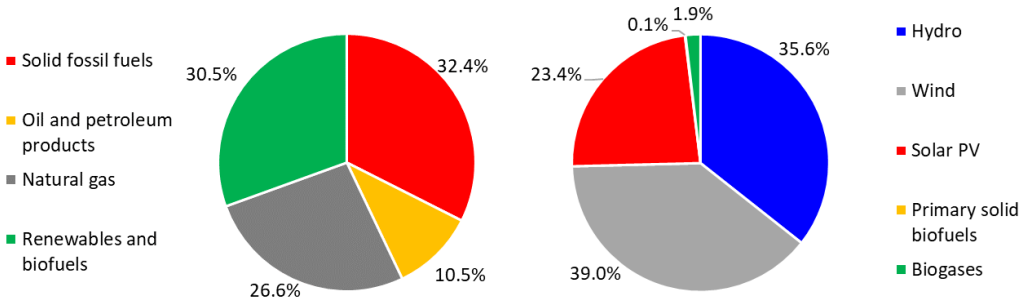

Fig. 6.19. (a) Electricity production in the Greek grid during 2018 and (b) breakdown of the renewable sources and biofuels

III. Impact assessment

The impact assessment methods that have been chosen for this study, as mentioned already, are ReCiPe 2016 Midpoint v.1.02 and ReCiPe 2016 Endpoint v.1.02 under Hierarchist, H perspective. The results are presented in all impact categories available by the method.

6.3.5 Comparative analysis

In Fig. 6.20 are presented the results of the comparative analysis of the investigated systems for the case of Athens (Zone B), Greece, both at Midpoint level, Fig. 6.20(a), and Endpoint Level, Fig. 6.20(b). With respect to Midpoint level, it is worth highlighting the significant reduction of at least 20% in the global warming impact category by all proposed systems compared to the conventional ones. In fact, the best-performing system in the global warming category was solar absorption, reporting 44.9% of the corresponding global warming emissions of the conventional systems. The second best-performing system in this category was solar adsorption system, with a 62.4% of the corresponding conventional systems' global warming impact. On the other hand, the two sorption systems are the worst systems in terms of the mineral resource scarcity impact category, with the conventional system to record 63.8% less equivalent emissions.

On endpoint level, the solar absorption system has the lowest impact on human health and ecosystems categories, which is mainly related to the reduced dependence on the grid, compared to the HP based system and the smaller amounts of materials consisting its inventory, compared to the solar adsorption system. On the other hand, the larger masses of minerals for the solar field and the overall installation, result in the two sorption systems to be performing worse than the HP based ones. The considerably worse performance of the conventional systems in the resources category is owed to the consumption of natural gas and the lower COP of the a/c units for cooling. Finally, with respect to the HP system, the high values on the human health and the ecosystems, are mainly due to the extensive power consumption from the grid, while the comparable performance of the PV-HP-B is due to the fact that the impact induced by the PV inventory counterbalances the benefits by the power savings.

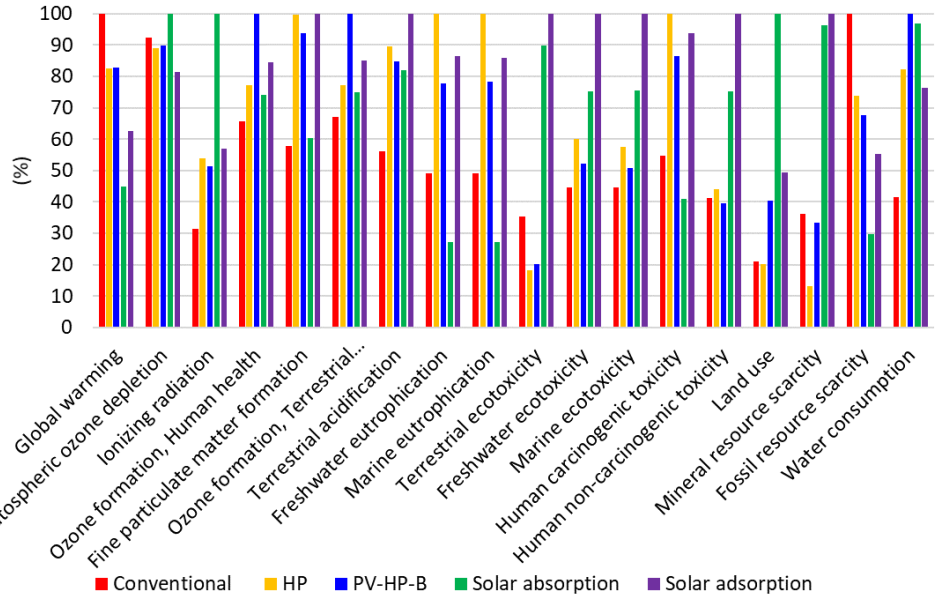

(a)

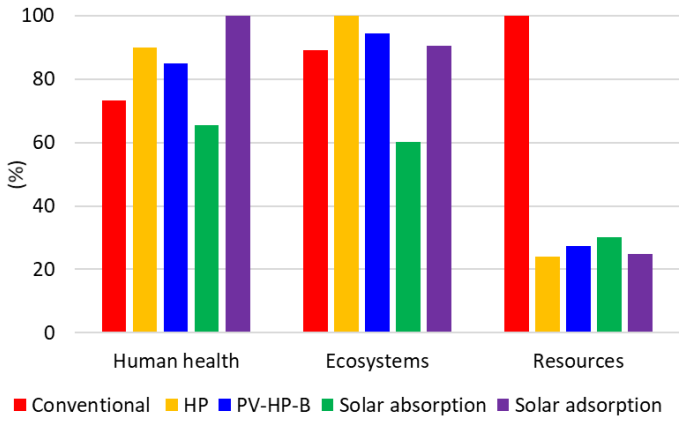

(b)

Fig. 6.20. Comparative Impact Assessment results of residential cooling/heating systems at (a) Midpoint Level and (b) Endpoint Level for the case of Athens (Zone B), Greece.

6.3.6 Components contribution on PV-HP-B

As mentioned in section 6.3.5, the estimated impact of PV-HP-B is largely owed to the high power consumption of the HP and the added impact of the PV inventory. To further justify this statement, in Fig. 6.21 is presented the components contribution on the total system's footprint of the PV-HP-B. As expected, the used electricity from the grid is by far the most contributing factor in the PV-HP-B total impact, with a share of more than 50% on most impact categories on Midpoint level. Significant is also the contribution of the PVs, with shares in the range of 10-30%. More specifically, the PVs reported a share of 22.6% in the global warming impact category, which is mainly attributed to the Chinese electricity mix, used during PV manufacturing, as well as the fact that the production of a PV module requires a large amount of hard coal in the initial phase of processing, in order to obtain metallurgical silicon through smelting [245]. With respect to the 56.2% PV share in the mineral resource scarcity, the impact is mainly due to the use of nitric acid and nylon-6 and the exploitation of ferronickel, silver, bauxite [263]. A notable contribution in the global warming and ozone depletion is attributed also in the HP, with shares of 13.1% and 25.8%, respectively. A similar behavior can be observed on Endpoint level, with the electricity having a share of 61-72% on all categories. On the other hand, PVs are responsible for 32.8% of the total impact on the resources, mainly due to the large mass of copper-based materials.

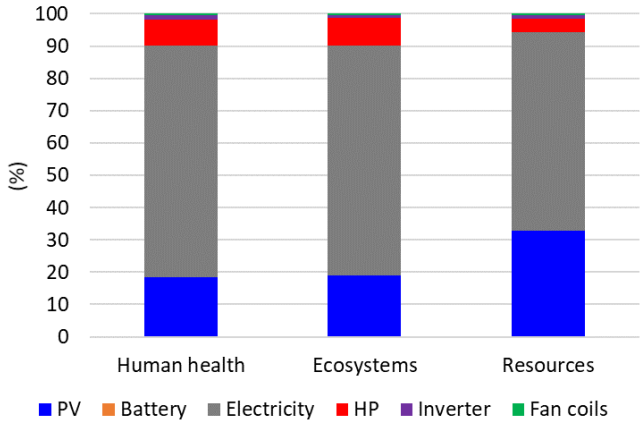

(a)

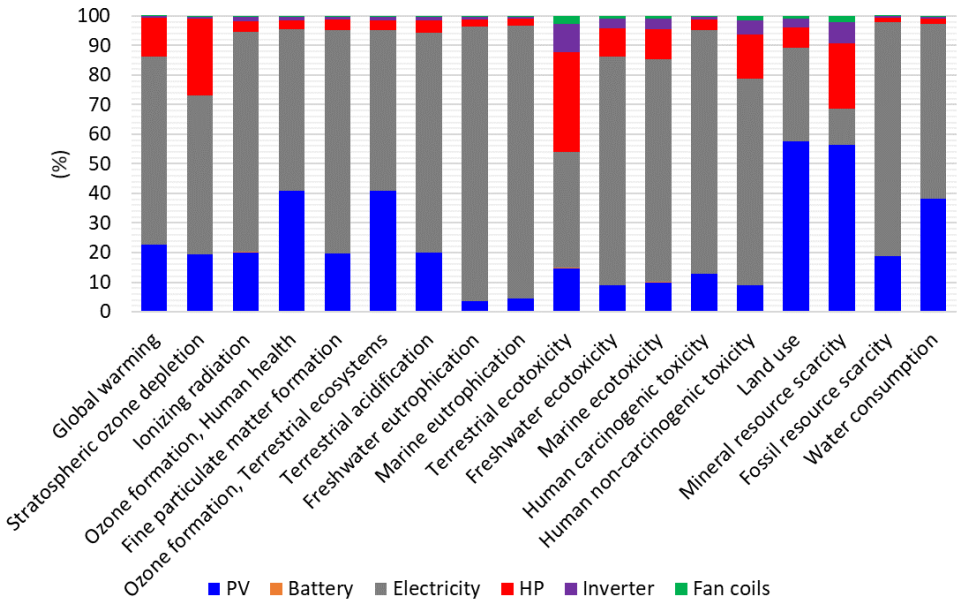

(b)

Fig. 6.21. Components' contribution of the considered PV driven HP system (a) at Endpoint Level and (b) at Midpoint Level.

6.3.7 Components contribution on solar hybrid absorption system

A similar analysis as the one for the PV-HP-B, is conducted for the case of solar absorption system, with the results presented in Fig. 6.22. Similarly to the Zeosol case of section 6.2, the electricity consumption has a very high impact on many categories, including global warming and ozone depletion, with shares of 50.9 and 52.9%, respectively. This behavior is highly connected to the used Greek electricity mix, which is largely based on lignite, as shown in Fig. 6.19. The second highest shares on global warming and ozone depletion categories were reported by the backup HP, mainly due to the use of R134a in the considered inventory, and the implications that were already discussed in section 6.2.5. On the other hand, for impact categories such as mineral resources scarcity and marine ecotoxicity, the solar collectors and the installation inventory (fittings, piping, etc.,) have the highest contributions, mainly due to the extensive use of copper-based materials. On Endpoint level, the influence of electricity is reduced, apart from the resources category, which is largely based on the fossil fuels consumption of the grid.

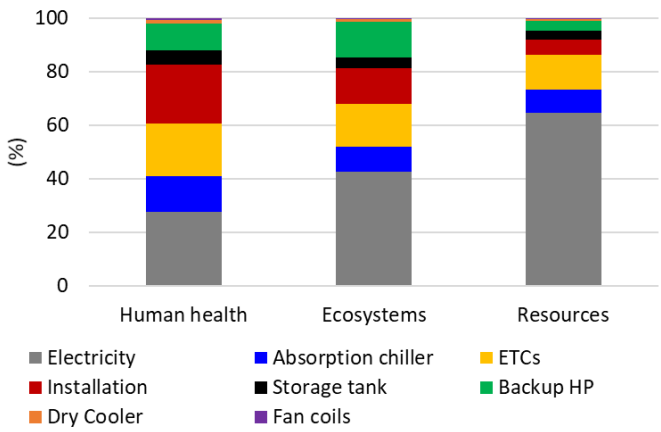

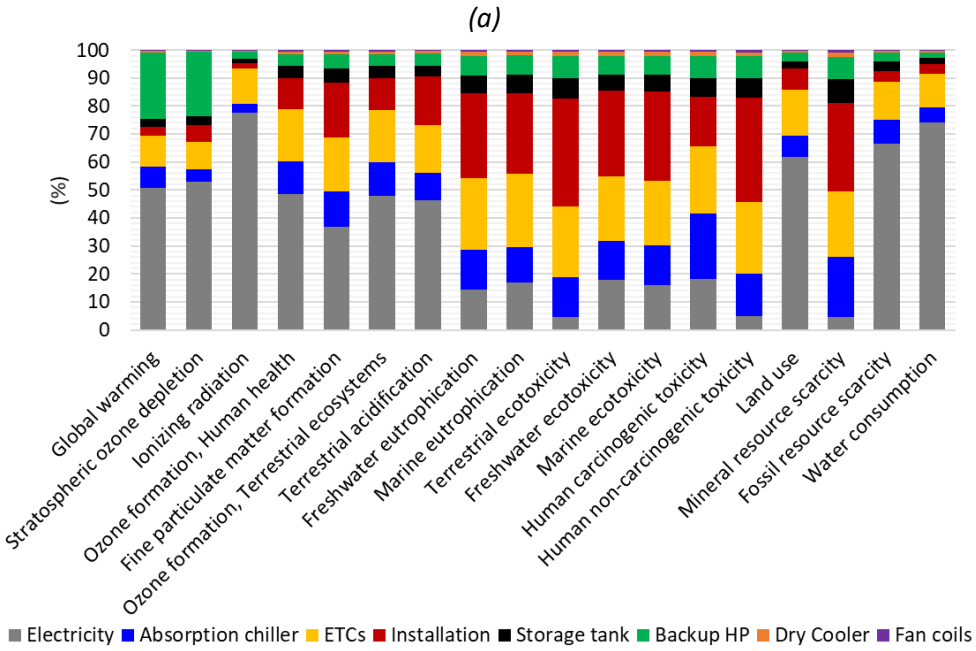

Fig. 6.22. Components' contribution on overall results of considered solar absorption system (a) at Endpoint Level and (b) at Midpoint Level.

6.3.8 Conclusions on LCA of residential scale solar cooling/heating systems

In this section, a LCA of the main available solar cooling/heating systems on residential scale was conducted using as reference the conventional heating/cooling systems of a building built in 2001-2010 in Greece. The main conclusions of the analysis can be summarized below:

- All evaluated systems record an at least 20% reduction in the equivalent global warming emissions compared to the conventional heating/cooling system. In fact, the best performing system, solar hybrid absorption cooling, reported a reduction of 55% in the global warming equivalent emissions compared to the conventional system.
- Solar driven sorption systems have worse performance on categories that are affected by the extensive use of copper-based materials such as the mineral resource scarcity and the marine ecotoxicity, having more than double emissions compared to the other evaluated systems.
- The large impact of the PV panels counterbalances in many impact categories the emissions reduction which are connected to the savings by the PV power generation.
- With respect to the PV-HP-B system, the electricity from the grid is responsible for more than 50% of the total impact on most categories, followed by the PV which reported shares in the range of 10-30%. In particular for global warming and ozone depletion impact categories, the HP has also notable contribution, with shares of 13.15 and 26%, respectively.
- The impact of the solar hybrid absorption system is also greatly affected by the used electricity to drive the backup HP. With respect to the global warming and ozone depletion impact categories, the electricity has shares of 51% and 53%, respectively.

6.4 Life Cycle Analysis of a small-scale ORC system

This study was presented in the ORC2021 conference, under the title “Environmental analysis of a small-scale marine ORC” [264].

6.4.1 Introduction

Based on the study from International Maritime Organization [265], shipping accounted for almost 2.9% of the global greenhouse gas (GHG) emissions in 2018, which corresponded to a value of 1,076 million tonnes CO_2. In order to reduce the emissions, a number of improvements has been suggested, including energy-efficiency measures and the increase in the penetration of near-zero carbon footprint fuels. In this perspective, the implementation of waste heat recovery (WHR) can lead to considerable emission savings, given the excessive heat losses in the exhaust gases and the jacket cooling water [266]. Taking into consideration the relatively low temperatures of the aforementioned waste heat, Organic Rankine Cycle (ORC) is one of the best candidates to exploit such heat streams towards power production and the consequent increase in the overall system’s efficiency. In fact, reviews on waste heat recovery on marine applications propose as main candidate for WHR the steam Rankine cycle, the ORC and the Kalina cycle, with the ORC being the only, so far, proposed option for WHR from heat sources below 100 °C in maritime applications [267, 268].. Several studies have focused on the optimization of the ORC system for marine applications on energy, exergy and economic level [269, 270].

However, to the best of the authors’ knowledge, there are only a few studies discussing the environmental impact of ORC systems and none, in particular, for WHR in marine applications ORCs. Life Cycle Analysis (LCA) is an assessment method developed to quantify the environmental impact of a product, by taking into account its entire life cycle, from the raw materials production to the waste management [193, 194].

Walsh and Thornley [271] conducted an LCA for an ORC driven by WHR in the production of metallurgical coke. The net power output of the proposed ORC system was estimated to be 550 kW. However, the environmental impacts on the life cycle basis were improved by less than 1%. Liu et al. [272] used a simplified model, proposed by the Ecological Environment Research Center of Chinese Academy, to analyze the environmental performance of a conventional subcritical ORC dedicated for WHR, taking into consideration the use of different working fluids. The authors concluded that, in most impact categories, R113 was the best performing working fluid. A similar approach was followed by Wang et al. [154] for a 10 kW subcritical ORC, designed to be driven by the WHR from cement production. A first detailed LCA on ORCs was published by Heberle et al. [250], analyzing the environmental performance of different geothermal ORC plant configurations and working fluids. The results indicated that the use of ultra-low GWP fluids (e.g., R1233zd) can decrease the GWP impact by 4 times compared to the use of conventional working fluids (e.g., R245fa). This statement is also confirmed by the analysis of Dawo et al. [273], in which the usage of R1233zd(E) was found to decrease the CO_2-equivalent emissions of a large scale geothermal ORC by 67.1% compared to the case that R245fa was used as working fluid.

In this study, the environmental performance of an experimental small-scale ORC unit for marine applications (marine ORC), developed in the National Technical University of Athens (NTUA), Greece, is investigated. The analysis is conducted in Simapro software, following the procedure of ISO 14040:2006, as discussed more thoroughly in the following sections.

6.4.2 System description

The marine ORC prototype is a small-scale subcritical ORC. The system is operating with R134a and has a nominal power output of 5 kWe. As the system was developed to exploit the waste heat from the jacket cooling water of a ship's auxiliary internal combustion engine (ICE), the heat source for the lab experiments was simulated by a gas boiler with a nominal thermal output of 90 kW. The heat source temperature ranges between 80-90 °C, which corresponded to an ORC evaporation pressure of 25 bar. The design pressure ratio was set at 2.3. The mass flows determined for the design power production, dictated the use of two scroll expanders in parallel to have feasible volumetric flow rates and rotational speeds per expander for the rated power output. Considering that the expanders resulted from the modification of off-the-shelf open-drive scroll compressors, a limited range was available in terms of volumetric displacement, leading to the selection of two expanders to handle the design volumetric flow rates. This configuration also allows for a smoother control of the system during startup in conjunction with the capability of part-load operation, further enhancing its control. Each expander drives an asynchronous generator by means of a belt-pulley [274]. Moreover, a subcooler was installed to cool down the stream coming from the receiver and ensure cavitation free operation of the multi-diaphragm pump [275]. With respect to the types of the used heat exchangers, the evaporator is a plate heat exchanger, while the subcooler and the condenser are of shell and tube type [156]. Finally, the total volume of working fluid used for the initial charging of the system was 50 lt (0.05 m^3).

A simplified schematic of the marine ORC prototype, which was considered for the LCA,was already presented in the pump modelling section, in Fig. 3.10, while Table 6.5 provides some key technical specifications of the main ORC components.

Table 6.5. Technical specifications of marine ORC key components, based on data from [131] and [274]

Component	Manufacturer	Model	Technical data
Scroll expander	Sanden	TRSA12	Design rotational speed (rpm): 1,450 Volumetric displacement (cm^3): 121.1
Diaphragm pump	Hydra Cell	G-10X	Design rotational speed (rpm): 960 Maximum global efficiency (%): 48
Evaporator	Alfa Laval	CB60	Number of plates (-): 90
Condenser	Bitzer	K573HB	Heat transfer area (m^2): 1.33 Nominal pressure drop (kPa): 59
Subcooler	Bitzer	K123HB	Heat transfer area (m^2): 0.3 Nominal pressure drop (kPa): 28

6.4.3 LCA modelling

According to ISO 14040:2006 the LCA can be divided in four main phases: (i) goal and scope definition, (ii) inventory analysis, (iii) impact assessment and (iv) interpretation. The following sections are discussing the application of the ISO methodology in the marine ORC LCA.

I. Goal and scope definition

Main aim of the LCA study is the assessment of the environmental footprint of the marine ORC prototype and its comparison to the production of the power surplus entirely by the existing ICE. In this perspective, the analysis will allow to have a quantitative view of possible

benefits by the implementation of a WHR ORC as well as identify the key components that require further optimization towards the minimization of the system's environmental impact. A cradle-to-grave approach is applied, considering all stages from raw material extraction, system manufacturing and commissioning, use phase to the end-of-life, including all transportations. The base case analysis took into consideration all the components of the marine ORC prototype, including the ICE from which the waste heat was extracted. The lifetime of the system was selected to be 20 years, which is common for such systems [63, 126, 276]. Finally, the functional unit was set to be 1 kWh of produced net electricity.

II. Inventory analysis

The inventory included a detailed listing of all the available data for inputs and outputs of materials/processes and energy consumptions over the life cycle of the investigated system. A number of components, including the receiver tank, the piping, the mass of the working fluid and the shell and tube heat exchangers of the marine ORC prototype (condenser and subcooler) were modelled based on data from manufacturers and collected data during the prototype commissioning. For the rest of the system's components, ecoinvent v3.6 database was used along with a number of assumptions, the most important of which are listed below:

- Refrigerant losses due to leakages are estimated to be 2% on annual basis [249, 250].
- Given that the lubricant is mixed with the refrigerant during operation a 2% annual loss is also considered for the lubricant on both the cases of pump and expanders.
- Maintenance is neglected, as it is mainly considered to involve the refrigerant refilling, already considered within the respective fluid listing. Furthermore, maintenance issues are mostly assigned to the ICE itself, which is common for the investigated and the reference system. In this framework, the ORC hosts cathodic protection to address the issue of corrosion due to the utilization of seawater, thus preventing the main cause of failures and maintenance for the ORC. Moreover, the two shell and tube heat exchangers (condenser, subcooler) of the system have a seawater resistant design, with tubes made of copper nickel 90-10, to minimize corrosion mechanisms with the seawater.
- The ICE was modeled based on an existing dataset in ecoinvent and appropriate scaling. For the scale of the marine ORC, the corresponding ICE capacity was equal to 150 kWe.
- As cooling water in the condenser and the subcooler are both rejected back to the sea, no water consumption was considered in the respective components use phase. Freshwater of the hot side of the evaporator is circulating in a closed loop, therefore apart from subsystem filling, no further water consumption takes place during use phase.
- With respect to the reference system, no water consumption is considered during use phase as the jacket water heat rejection is realized via a heat exchanger using seawater which is then rejected back to the sea, similarly to the ICE-ORC.
- The plate heat exchanger (evaporator) consists mainly of stainless steel, copper and brass, while the consumed energy for its manufacturing was assumed to be 0.4014 MJ/kg [256].
- The pump was considered to be made of 21 kg of brass, 20.3 kg of stainless steel (pump's metallic head) and 1 kg of lubricant. Secondary materials were neglected due to significantly smaller masses.

- With respect to the two scroll expanders, they were disassembled and weighed before the system's commissioning. The main body was made of stainless steel (31.6 kg per expander). 0.3 kg of lubricant was also measured per expander.
- For the calculation of the diesel consumption by the ICE, the fuel oil specific consumption of ship diesel engines was taken equal to 181 g/kWhe [156]. The rest data for the use phase is presented below in Table 6.6. At this point has to be clarified, that the waste heat recovery is considered to not influence the fuel oil specific consumption.

Table 6.6. Use phase data, based on Pallis et al. [156]

Operating hours per year	ORC average electrical efficiency (%)	Average ORC net power output (kW)	Annual ORC power production (kWh)	ORC/ICE power ratio	Annual fuel savings (kg of fuel oil)
6252	4.51	4.06	25123	2.68 %	4365.5

- All transportations were considered from the manufacturing site, each of the prototype's components was actually sent to the installation site of the prototype in Athens. Most components were constructed within Greece, with the exception of the scroll expanders sent from France, the diaphragm pump manufactured in the United Kingdom and the R134a which is produced in the Netherlands. All international transportations were considered to be realized with >32 metric tons lorries; all domestic transportations were realized with <3.5 metric tons lorries.
- Metals are assumed to be fully recovered, while non-metals are considered to be combusted at the end of their life. For the refrigerant R134a, in accordance with ecoinvent, 90% is assumed to be recovered, while the rest 10% is combusted [63, 228].

III. Impact assessment

For the midpoint level, the ReCiPe 2016 Midpoint v.1.02 was used as a commonly applied impact assessment method. On endpoint level, ReCiPe 2016 Endpoint v.1.02 was selected, respectively.

6.4.4 Comparison to reference system

In the base case scenario, the considered ICE-ORC system is compared with the operation of the ICE at higher loads to cover the power production by the operation of the ORC. This comparison targeted to identify the key challenges of the ORC system, at prototype level, to out-perform on environmental basis the conventional ICE. In fact, the results at midpoint level (Fig. 6.23(a)) show that despite the large amounts of materials used for the construction of the ORC system, the avoided fuel oil consumption results in an improvement in 10 out of 18 impact categories. The largest improvement is identified in the categories of fossil resource scarcity, ionizing radiation and ozone formation in terrestrial ecosystems, which record an improvement of 2-3% mainly due to avoidance of the fuel oil combustion and the respective emissions. As the oil savings by the use of the ORC account for only 2.7% of the total oil consumption on annual basis and an additional footprint is added by the R134a, the effect in the, highly sensitive to fossil fuel emissions, global warming and ozone depletion categories is minimal. This small improvement of 1% in the aforementioned categories comes in agreement with other relevant studies in literature [154, 271] and highlights the necessity for a scale up

of the system, which could possibly enhance its environmental performance due to both reduction in materials per kW of produced power as well as the enhanced efficiencies [156]. The absolute values of some key impact categories for the two systems on midpoint level are reported in Table 6.7.

On the other hand, the use of ferrous and (mainly) non-ferrous metals for the realization of the ORC has a negative effect in categories, directly affected by metal use and the corresponding emissions, including freshwater, marine and terrestrial ecotoxicity [272].

With respect to endpoint level, a similar performance can be observed in Fig. 6.23(b). In all three categories, the ICE-ORC has a better performance than the reference system, however the improvement is between 1-2.7%. In human health and ecosystems, the improvement by only 1%, is mainly affected by the global warming and ozone depletion categories and the corresponding high fuel oil consumption. The largest improvement is identified in the resources category, with a 2.7% decrease compared to the reference, which is mainly attributed to the oil reduction. The respective absolute values on endpoint level are reported in Table 6.8.

Table 6.7. Quantitative results of impact assessment for ICE-ORC system and reference system per functional unit for key impact categories, at Midpoint Level

Impact category	Reference system	ICE-ORC system
Global warming (kg $CO_{2,eq}$)	0.665	0.651
Stratospheric ozone depletion (kg CFC-11_{eq})	$1.66 \cdot 10^{-7}$	$1.66 \cdot 10^{-7}$
Water consumption (m^3)	$2.09 \cdot 10^{-4}$	$2.07 \cdot 10^{-4}$
Fossil resource scarcity (kg oil_{eq})	0.211	0.205
Mineral resource scarcity (kg Cu_{eq})	$2.07 \cdot 10^{-4}$	$2.15 \cdot 10^{-4}$

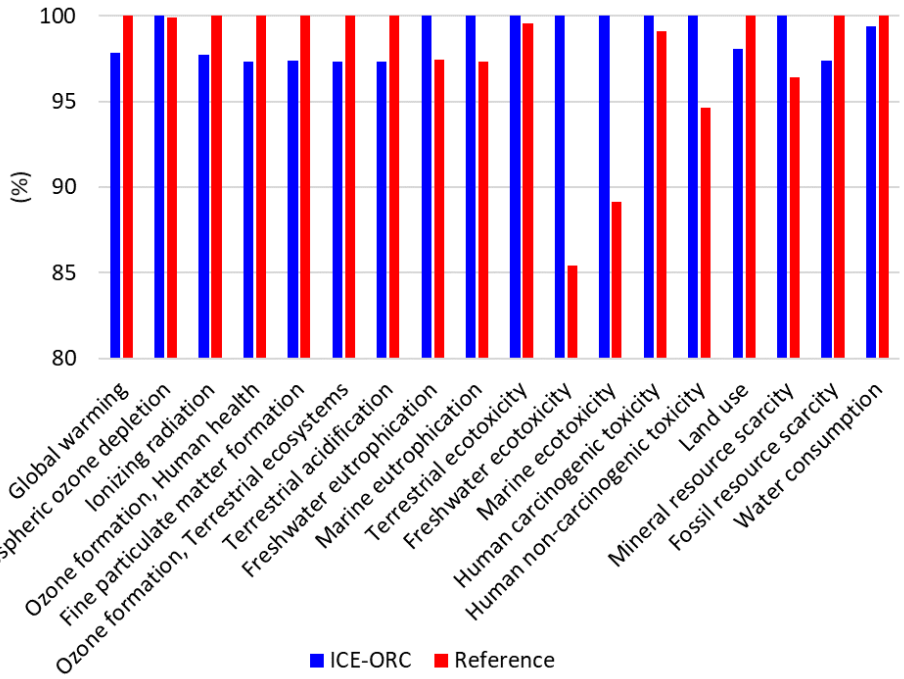

(a)

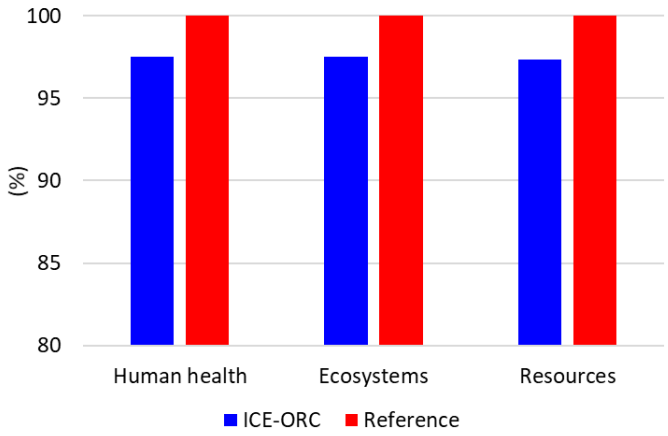

(b)

Fig. 6.23. Comparative Impact Assessment results of ICE-marine ORC system in respect with the reference ICE using (a) Midpoint Level and (b) Endpoint Level

Table 6.8. Quantitative results of impact assessment for ICE-ORC system and reference system per functional unit for key impact categories, at Endpoint Level

Impact category	Reference system	ICE-ORC system
Human health (DALY)	$2.61 \cdot 10^{-6}$	$2.55 \cdot 10^{-6}$
Ecosystems (species.yr)	$5.80 \cdot 10^{-9}$	$5.66 \cdot 10^{-9}$
Resources (USD2013)	$9.48 \cdot 10^{-2}$	$9.23 \cdot 10^{-2}$

6.4.5 ORC breakdown

Looking deeper into the comparison of the marine ORC with the ICE, it is worth analyzing the contribution of the ORC's components in the total impact of the prototype over its entire life cycle, as shown at midpoint level in Fig. 6.24 and at endpoint level on Fig. 6.25. In this analysis, the ICE and consequently the emissions related to the waste heat generation are excluded from the inventory. The exclusion of the ICE was dictated by the scale of the ORC prototype, which accounts for only a small fraction of the combined ICE-ORC system as was clearly shown by the results of section 4.1. As expected, the use of R134a, with a global warming potential (GWP) of 1430 [62], results in a 91.6% share in the global warming category, shown in Fig. 6.24. On the other hand, the 95.9% share of R134a in ozone depletion is mainly due to the emissions of R113 and R124 during the life cycle of R134a [226] Both R113 and R124 are intermediate products, during the production of R134a, according to the used dataset of ecoinvent [277].

Despite the substantial impact of the refrigerant, the system was, firstly, constructed in 2015 when low-GWP refrigerants and compatible commercial components, such as valves, were scarcely available. Besides, the retrofit of the unit to operate with an environmentally friendly refrigerant would require major modifications such as the replacement of components and piping in order to maintain proper flow conditions. Finally, R134a replacements such as R1234yf and R1234ze(E) are classified as A2L refrigerants, exhibiting flammability issues which, by the time of construction, made them inappropriate for a marine environment. With respect to global warming, the pump's motor and the two generators have also a considerable impact, with a 4.9% share. This is due to the large metal masses of these components, with a total metal mass of 172 kg, in comparison to the 97 kg of the heat exchangers, the 41 kg of the pump and the 32 kg of the scroll expanders. The large masses of electrical steel and copper

used in the construction of the system's motor/generators result in large shares on the total impacts on most categories ranging between 30-70%. The considerable mass of the heat exchangers results in high contributions also in several impact categories. The comparable contribution to the motor/generators of approximately 27% of the total impact in freshwater, marine and terrestrial ecotoxicity is mainly justified by the higher copper content in the heat exchangers [278]. Finally, pump accounts for approximately 10-15% each, on categories such as mineral resource scarcity and terrestrial ecotoxicity, due to their brass content [279].

On endpoint level, the high impact of R134a in global warming and ozone depletion, result in 59.5% and 79.1% shares in human health and ecosystems impact categories, respectively. The large metal mass of motor/generators result in a considerable contribution in human health and ecosystems impact categories, with a share of 14.5% and 8.9%, respectively. Moreover, the high metal content of generators/motor results in a 45.0% contribution on resources, followed by the 20.1% of the R134a and the 13.6% of the diaphragm pump. Ultimately, scroll expanders account for less than 1% contribution with respect to resources and human health, implying the low impact of the two expanders configuration on the environmental footprint of the system. Given that the relative contribution is considered, even the use of a –fictitious– single machine would not halve their influence, supporting this assertion.

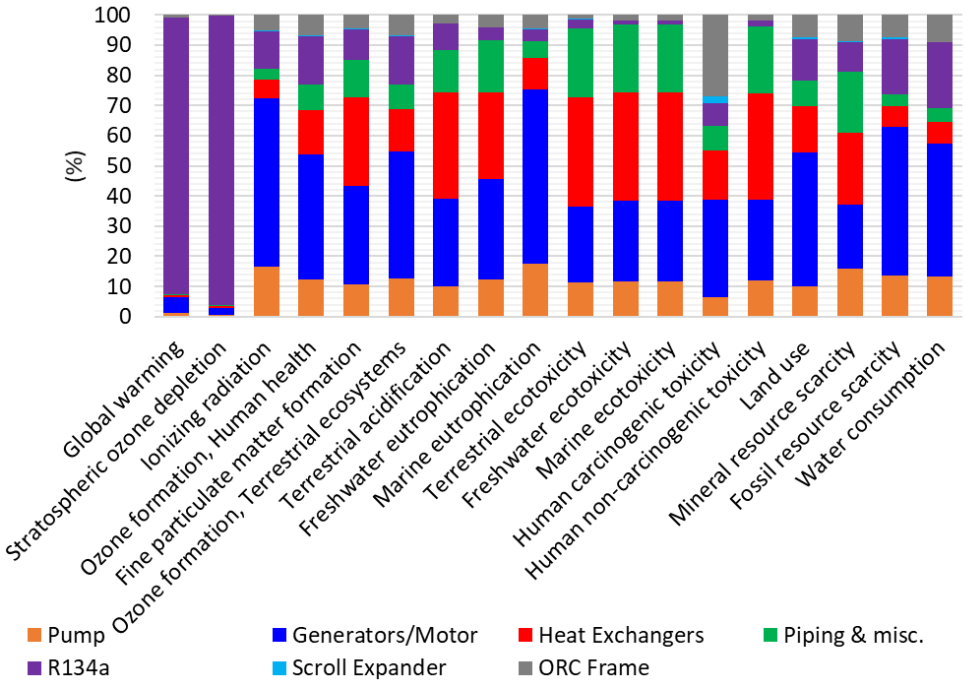

Fig. 6.24. Components contribution on overall results of marine ORC prototype at Midpoint Level.

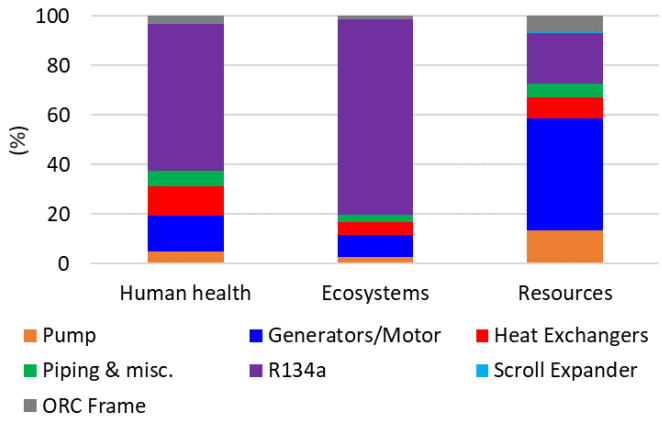

Fig. 6.25. Components contribution on overall results of marine ORC prototype at Endpoint Level

6.4.6 Fluid replacement

Considering the large contribution of R134a in many impact categories, it was decided to conduct a case study with a working fluid substitution. The considered scenario involved the replacement of R134a with the ultra-low GWP working fluid, R1234ze. The new fluid was assumed to be used in the marine ORC prototype and thus all components of the inventory apart from the fluid were left unmodified. Taking into consideration the constant volume of the test rig, the added new fluid was assumed to be of equal volume with R134a, thus the added mass of R1234ze was estimated using the density of the liquid R1234ze at 20 °C and 10 bar. By applying a design simulation of the developed models of section 3.5, the net power production of the marine ORC prototype was estimated to be equal to 4.35 kW, corresponding to a net electrical efficiency of 4.83%. Considering that the system operates annually for 6252 hours, as in the base case (see Table 6.6), the marine ORC with R1234ze was found to produce 1801 kWh more than the R134a prototype, on annual basis.

Based on the above input, the results of the comparative LCA for the ORC prototypes operating with the two different fluids are presented in Fig. 6.26. As expected, the combination of the enhanced performance and the implementation of a ultra-low GWP working fluid, resulted in significant reduction of the environmental impact in most categories. In fact, in the global warming category, with the new fluid, the system has less than 10% of the R134a equivalent emissions. Similarly, the ozone depletion potential with R1234ze accounts only for 5% of the respective of the marine ORC with R134a. With respect to most of the other Midpoint level impact categories, the reduction is mainly attributed to the enhanced performance of the marine ORC prototype with R1234ze.

Similar behavior can be observed at Endpoint level. In fact, in human health and ecosystems, which are affected by the global warming Midpoint level impact category, the reduced impact accounts for less than 50% of the corresponding impact for the marine ORC with R134a. The reduction in the resources category is mainly owed to the additional power production of the R1234ze ORC system.

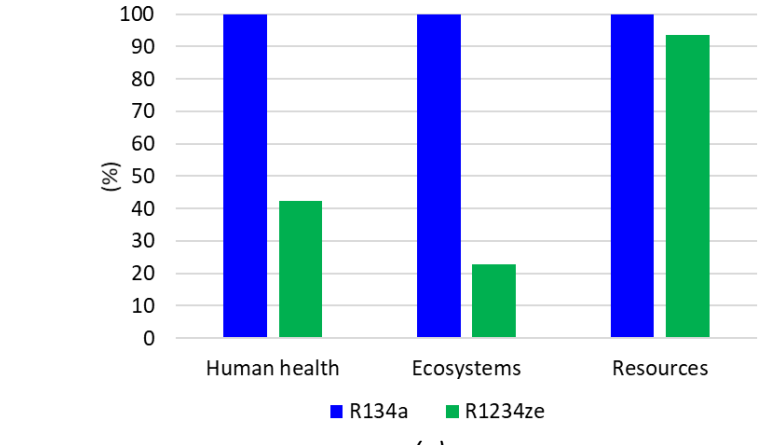

(a)

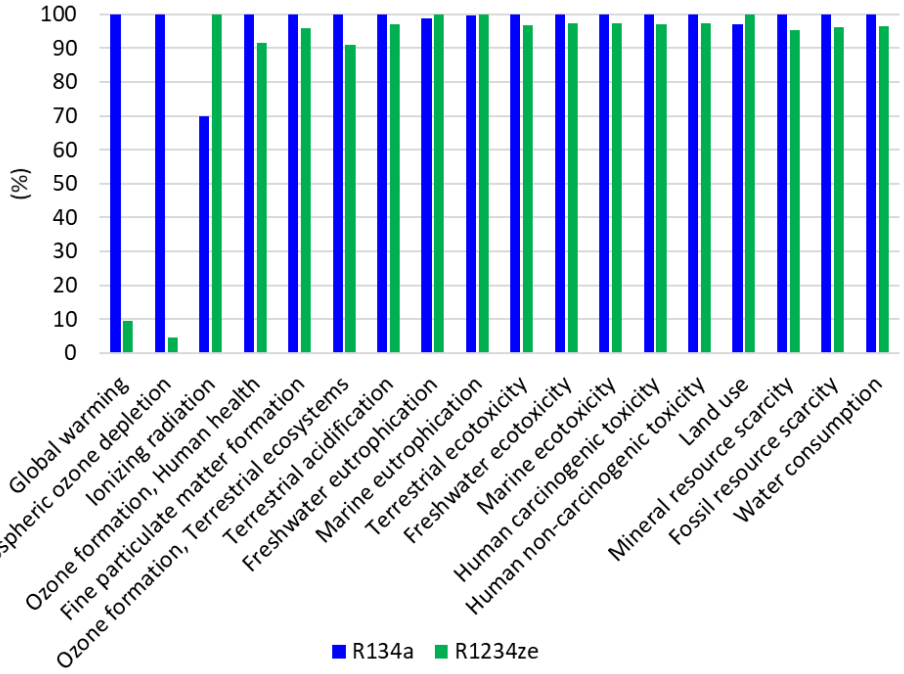

(b)

Fig. 6.26. Comparative Impact Assessment results of the marine ORC system on prototype scale operating with R134a in respect with the case of using R1234ze (a) Endpoint Level and (b) Midpoint Level

6.4.7 Case study of a Solar ORC

Having developed the ORC inventory for a small-scale system and having also actual data for a number of solar components, it was decided to couple the relevant listings into a single assembly in Simapro, in order to evaluate the performance of a small-scale low temperature solar driven ORC. For the analysis, the data for a solar ORC from the techno-economic optimization of section 4.1 was selected. Namely the selected system was the optimal LCOE solution for the case of Chania (Zone A), Greece, as listed in Table 4.4. The considered system consisted of 52.39 m^2 of FPC, a 0.36 m^3 storage tank and the ORC's working fluid was R152a. The developed system was assessed for operation in the four climatic zones of Greece. The calculated, by the simulations of section 4.1, annual electricity production of the system per climatic zone of operation are listed in Table 6.9. As a reference system for the analysis was considered 1 PV panel, similar to the ones assessed in section 6.3. The corresponding annual

electricity production of the PV panel for each climatic zone is listed in Table 6.10. The lifetime of the two systems was assumed to be 20 years, while the functional unit was selected to be 1 kWh of produced electricity.

Table 6.9. Annual electricity production of the solar ORC for the Greek climatic zones

Component	Zone A	Zone B	Zone C	Zone D
Annual electricity production (kWh)	5918.39	3315.69	3684.62	5056.58

Table 6.10. Annual electricity production of a single PV panel for the Greek climatic zones

Component	Zone A	Zone B	Zone C	Zone D
Annual electricity production (kWh)	667.82	558.29	543.26	572.83

The results of the LCA for the comparative analysis of the FPC driven ORC in respect with a PV panel installed in Athens (Zone B) are shown in Fig. 6.27. The corresponding results for the other climatic regions of Greece are listed in the Appendix IV (Fig. IV.4-Fig. IV.6). As shown in Fig. 6.27, the PV panel has a lower impact on all categories, with the exception of water consumption, in which the ORC has 18% less impact, mainly due to the high amounts of water consumed during the manufacturing phase of PV panels. The significantly higher total mass of copper-based and in general metal-based materials of the ORC is a key factor that results in the worse performance in most categories, involving mineral resources scarcity and marine ecotoxicity. Moreover, the GWP of R152a, which according to Table 4.1 is equal to 124, along with the energy intensive manufacturing of FPCs are considered the main reasons the PV panel has 20% and 42% less impact on global warming and ozone depletion, respectively. A similar behavior can be observed on Endpoint level, with the human health impact of the PV to be only 32.4% of the corresponding solar ORC value. With respect to ecosystems and resources, there is also a clear advantage of the PV panel, with 50% and 33% reduced impact, respectively.

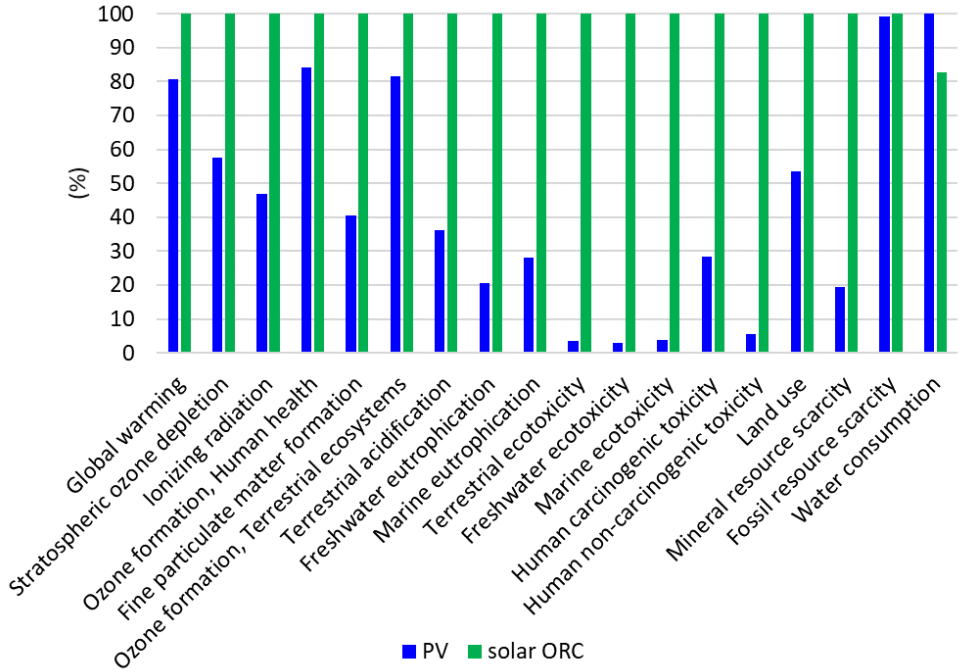

(a)

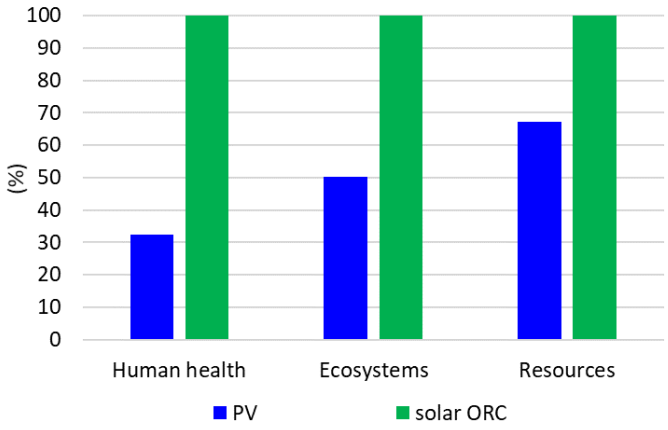

(b)

Fig. 6.27. Comparative Impact Assessment results of FPC driven ORC system operating with R152a in respect with a PV panel at (a) Midpoint Level and (b) Endpoint Level for the case of Athens, Greece.

In order to look in depth to the main contributors to the less attractive performance of the solar ORC, a component' impact breakdown was conducted. The results of the solar ORCs components' contribution are listed in Fig. 6.28. As expected, the FPCs are responsible for the largest share in almost all impact categories on Midpoint level, taking also into account the large solar field surface of the considered scenario. Notable is the contribution of the pump's motor and the expander's generator in the total solar ORC's impact, with shares ranging from 8.5-36.9%. This is justified mainly by the large masses of electrical steel and copper used for the construction of these components.

At Endpoint level, the share of the FPCs ranges between 49.5-55.9%, followed by the generator/motor with shares of 12.8-24.7%. Notable contribution have also the heat exchangers, in particular on human health, with a share of 10.4%.

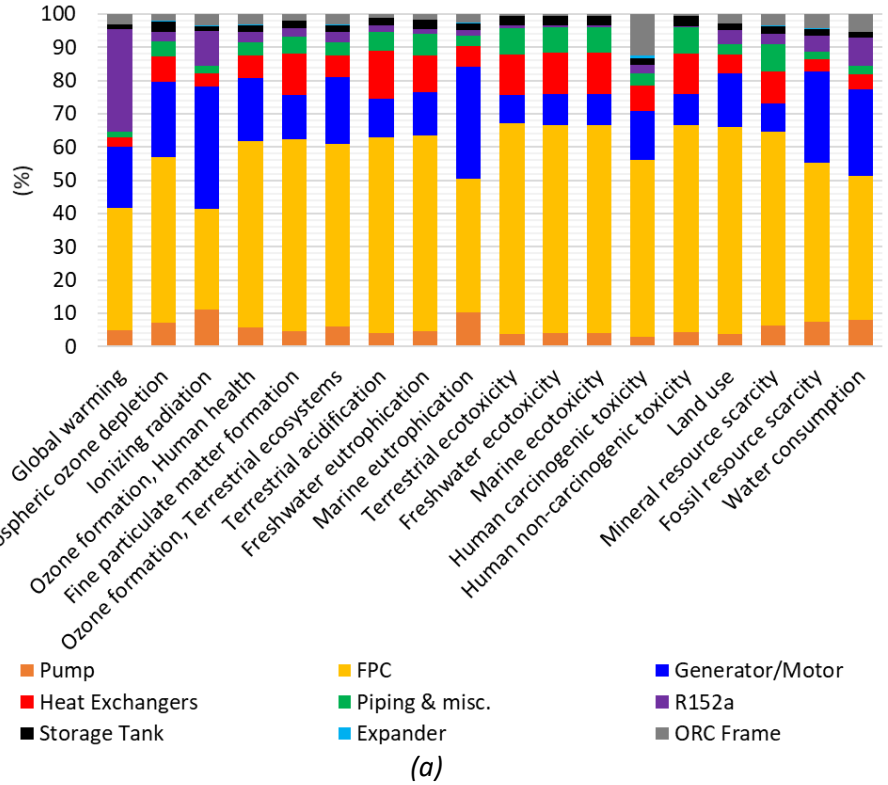

(a)

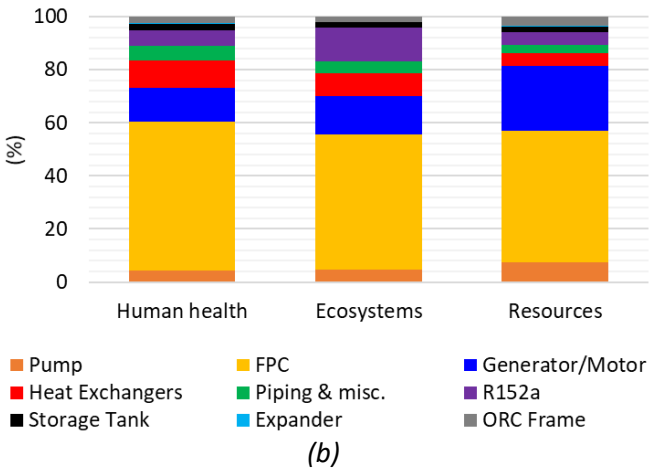

(b)

Fig. 6.28. Components contribution on overall results of marine ORC prototype at (a) Midpoint Level and (b) Endpoint Level.

6.4.8 Conclusions

In this study, the life cycle analysis of a small-scale ORC prototype was investigated. The system was designed for WHR from jacket water of marine ICEs. The analysis was based on data collected during the commissioning of the system and was analyzed in Simapro software. The main conclusions of the study are summarized below:

- The reduced oil consumption by the introduction of the ORC leads to an improvement in both midpoint and endpoint level. However, the improvement is in the range of 1-3% due to the high contribution of the ICE and the corresponding oil consumption in the overall system's impact.
- With respect to the ORC components contribution, the working fluid R134a has a 78% share in the global warming impact category and a 91% in ozone depletion.
- In most midpoint level impact categories, the motor/generators have the largest share of up to 60% of the total ORC's contribution.
- At endpoint level, R134a has a 38% and 59% share in human health and ecosystems impact categories, respectively. On the other hand, motor/generators have the largest contribution in the resources category with a value of 55%.
- The large contribution of R134a on global warming and ozone depletion dictates the evaluation of a fluid replacement towards the optimization of the system's environmental performance.
- The ORC system scale-up is expected to enhance the environmental performance of the ICE-ORC system due to further reduction in fuel oil consumption, as suggested also in other relevant studies [154, 156].
- The replacement of the R134a with an ultra-low GWP fluid, such as R1234ze, resulted in significant deduction of the ORC system's environmental footprint. Specifically, with respect to the global warming impact category, the equivalent emissions with the new fluid were less than 10% of the ORC with R134a equivalent emissions.
- The comparison of an FPC driven small scale ORC, with R152a as working fluid, with a PV panel revealed that the PV panel has significantly smaller impact per kWh of produced electricity, mainly due to the high shares of the solar field and the motor/generator in the ORCs total impact.

Chapter 7. General conclusions and future work

7.1 Key remarks

Towards the energy transition to a more sustainable basis, solar driven systems are expected to gain further interest and play an important role both on larger scale as well as on small - residential scale. Within this context, this dissertation aimed at analyzing both experimentally, whenever possible, and by simulations the potential and the challenges of solar driven systems for cooling/heating and/or power generation.

The key remarks by the studies presented in the dissertation are listed below:

- The experimental characterization of the novel direct flow type ETCs revealed a promising performance, which, within the accuracy limitations of the field measurements, was comparable to the performance of the standard heat pipe ETCs.
- The experimental validation of the solar collectors' model estimated the absolute daily error in terms of accumulative solar harvested energy to be approximately 2.5%.
- The experimental validation of the storage model showed a good agreement between the simulation results and the measured data. A minimum number of 30 nodes was found to be required for the simulation model discretization in order to maximize the model's accuracy.
- The experimental characterization of the Zeosol system revealed a promising performance on adsorption only mode, with a maximum reported COP of 0.535 and a maximum measured EER of 7.4($\pm$0.8). Towards the maximization of the solar adsorption system's performance, a dedicated control strategy has to be applied. Moreover, the experiments revealed that on hot days, higher driving temperatures are required by the chiller to operate efficiently. In order this to be achieved from a design viewpoint, either additional heat should be supplied, with the enlargement of the solar field, or the storage tank's volume has to be decreased in order to reach higher temperature at a given solar heat input.
- The follow-up measurements on Wassermod2 chiller further proved the statement of the driving heat insufficiency for operation on hot days. In fact, the monitoring of the room temperature in two chilled offices showed that the system was unable to achieve thermal comfort when ambient temperatures are high due to the absence of additional heat. On the other hand, the boiler tests conducted in July 2021, showed that once the chiller is provided with the missing driving heat it can hold thermal comfort conditions in the chilled rooms.
- In the techno-economic optimization of low temperature solar ORCs, exergy efficiencies as high as 7% were reported, while the corresponding minimum LCOEs were in the range of 0.35 €/kWh. Lower purchase costs refrigerants were associated with lower LCOEs, highlighting the importance of not neglecting the working fluids costs in relevant studies. Moreover, higher solar field areas were reported to have better economic performance in regions with high solar availability; on the contrary, an increase in the solar field area reduces the exergy efficiency. Finally, with respect to storage tank capacities, the optimal performances are identified for smaller tanks which serve purely as thermal buffers.
- For higher temperatures, in the range of 180-210 °C, flammable fluids, such as cyclopentane and cyclohexane were reported to have the optimum performance. The maximum calculated exergy efficiency for the medium temperature ORCs was equal to

12.6%, while the minimum reported LCOE was equal to 0.221 €/kWh in the southern climatic zone of Greece (city of Chania). Finally, the application of a feed-in tariff results in considerable improvement of the system's economic performance, with the minimum reported PbP in this case to be 10.6 years, compared to the corresponding 18.9 years of the base case scenario for the same region.

- Solar cooling/heating systems are not economically viable in none of the Greek climatic zones, mainly due to their high CAPEX and the relatively low electricity and natural gas prices for residential users in the country. Among the solar driven sorption systems, the absorption ones tend to have the better economic performance, while the adsorption systems tend to record higher exergy efficiencies. In terms of the used solar collectors, systems with FPCs were more competitive economically, while the ETC driven systems were associated with higher exergy efficiencies. Similarly to solar ORCs, the optimum scenarios in solar driven sorption systems were reported for small storage tank capacities. Heat pump-based systems have considerably better economic performance than solar sorption ones, with the case of PV-HP with net metering to have an LCOE as low as 0.098 €/kWh, compared to the 0.28 €/kWh at the minimum for solar absorption systems. A general trend was identified with enhanced economics at northern climates, mainly due to the more efficient operation of both electric heat pumps and sorption ones on heating mode.
- An allocation study for the optimal coupling of a waste heat recovery ORC with an adsorption chiller showed that the optimal configuration consisted in a heat recovery step to drive the adsorption chiller between the ORC's two expanders. The maximum reported exergy efficiency of 40%, while the respective value of a cascade ORC-VCC system was approximately 30%.
- The optimization of a solar driven trigeneration system based on the coupling of an ORC and an adsorption chiller driven by the heat rejection of the ORCs condenser reported exergy efficiencies as high as 27.8% on annual basis. The corresponding minimum LCOE was 0.29 €/kWh. However, given the large CAPEX of the system, the corresponding PbP and NPVs are not attractive with PbP as high as 98.7 years and NPVs of at least -30 k€. The application of a feed-in tariff for the electricity production is crucial for the improvement of the system's economic performance, resulting in a minimum PbP of 42.7 years and a corresponding NPV to be -21.6 k€.
- On environmental level, the Zeosol system was found to have smaller impact than a conventional heat pump, with a 51.2% and a 37.4% decrease of the equivalent emissions of global warming and ozone depletion categories, respectively. On the other hand, Zeosol system presents a significantly higher footprint on the ecosystems ecotoxicity and the mineral resources scarcity categories, mainly due to the use of copper-based materials. The site of installation has a significant impact on the overall footprint of the Zeosol system, mainly due to the significant impact of the respective electricity production mix of each country. As expected, when the share of non-sustainable sources is higher, the Zeosol system performs better than a conventional heat pump, mainly due to the reduction of the electricity consumption from the grid.
- With respect to the analysis of the main solar cooling/heating systems on residential scale, all systems were found to have at least 20% less equivalent global warming emissions compared to the conventional heating/cooling system. In line with the

conclusions of the LCA on Zeosol, solar driven sorption systems have worse performance on categories that are affected by the extensive use of copper-based materials. On the contrary, the reduced electricity consumption of solar sorption systems results in better performance on the global warming impact category than both heat pump-based systems. The coupling of PVs with a HP has in most categories similar performance to the grid connected HP, because the large impact of the PV panels the induced benefits by the savings of the PV power generation. In fact, for the case of the PV driven HP, the PVs account for 10-30% on most categories, with the largest share of more than 50% to be attributed to the electricity from the grid. Solar absorption systems' environmental performance is also greatly dependent on the backup HP electricity consumption, with share of 51% of the total impact on the global warming category.

- Finally, with respect to the LCA of a small-scale marine ORC, the working fluid R134a was found to account for 78% of the system's total global warming emissions. The corresponding share for the ozone depletion category was as high as 91%. The pump's motor and the expander's generator have a large contribution on most impact categories with shares of up to 60%. The replacement of the R134a with an ultra-low GWP fluid improved considerably the system's environmental performance, with the global warming equivalent emissions of the new system to be less than 10% of the respective emissions of the R134a ORC. Finally, by assessing the environmental performance of an FPC driven ORC in comparison to a PV panel, it was found that the ORC has considerably higher impact on most categories, mainly due to the extensive footprint of the solar field and the motor/generator.

7.2 Innovative work

The aspects of the thesis that contribute to knowledge are summarized below:

- On field comparison experiments between commercial heat pipe and direct flow evacuated tube collectors for use in space heating and domestic hot water residential application.
- Detailed modelling and experimental characterization of a 12.5 kW hybrid solar adsorption unit used to cover the thermal loads of five offices at the laboratory, with parallel monitoring of the room temperature and the corresponding thermal comfort in the chilled offices.
- Development and experimental validation of all the components used in a solar adsorption system.
- Application of a multi-objective genetic algorithm for the techno-economic optimization of low and medium temperature solar driven Organic Rankine Cycle systems for small scale applications in the European territory, with particular focus on the Greek climatic zones.
- Techno-economic optimization of solar driven sorption systems for residential applications with detailed modeling of the building loads and comparison with heat pump based systems.
- Development and techno-economic optimization of trigeneration system based on adsorption cycle for use in a residential building in Greece
- Development and calibration of updated cost functions for the estimation of system's CAPEX based on recent (within 2021) data from the Greek and European market.

- Detailed environmental assessment of the solar adsorption unit and a detailed comparison from a life cycle perspective of the main available renewable driven cooling/heating systems in comparison to electric heat pumps and conventional heating and cooling residential systems.
- Detailed life cycle assessment of solar driven ORC system with real data from a respective test rig.

7.3 Future work

Based on the studies presented in this dissertation and the key remarks from the previous section, a number of future work fields can be identified:

- With respect to the enhancement of the solar adsorption cooling/heating available systems, there was identified significant room for improvement towards the effective coupling of the solar subsystems with the sorption module. Advanced control strategies could therefore be evaluated for integration on solar adsorption applications towards the maximization of the solar fraction and the further improvement of the overall system's performance.
- The considered solar cooling/heating study evaluated the techno-economic performance on the Greek climatic zones, revealing limited economic potential. It is therefore important to identify and evaluate other countries with more suitable building's consumption profiles and combination of higher electricity and natural gas prices, which would eventually lead to more attractive results for the solar cooling/heating systems.
- With respect to the ORC systems, there is a growing interest towards flammable fluids, with the medium temperature ORC studies revealing a great potential for such fluids. However, it is worth analyzing such fluids experimentally, not only to monitor their real time performance but to assess also the involved hazards and the eventual added costs for the mitigation measures against the flammability risks.
- In the case of the LCA studies, there is a knowledge gap in the existing literature for larger scale ORCs. The development of a relevant analysis, based on real data from manufacturers for the accurate construction of the LCI is crucial to assess the environmental performance of such systems.

List of relevant publications

Book

*Karellas, S., **Roumpedakis, T.C.**, Tzouganatos, N., and Braimakis, K. 2018. Solar Cooling Technologies. CRC Press. ISBN 9781138060173.*

Book Chapter

*Karellas, S. and **T.C. Roumpedakis**, Chapter 7 - Solar thermal power plants, in Solar Hydrogen Production, F. Calise, et al., Editors. 2019, Academic Press. p. 179-235.*

Journal publications

***Roumpedakis, T.C**., T. Christou, E. Monokrousou, K. Braimakis, and S. Karellas, Integrated ORC-Adsorption cycle: A first and second law analysis of potential configurations. Energy, 2019. 179: p. 46-58.*

***Roumpedakis, T.C.**, G. Loumpardis, E. Monokrousou, K. Braimakis, A. Charalampidis, and S. Karellas, Exergetic and economic analysis of a solar driven small scale ORC. Renewable Energy, 2020. 157: p. 1008-1024.*

***Roumpedakis, T.C.**, G. Kallis, D. Magiri-Skouloudi, D. Grimekis, and S. Karellas, Life cycle analysis of ZEOSOL solar cooling and heating system. Renewable Energy, 2020. 154: p. 82-98.*

***Roumpedakis, T.C.**, S. Vasta, A. Sapienza, G. Kallis, S. Karellas, U. Wittstadt, M. Tanne, N. Harborth, and U. Sonnenfeld, Performance Results of a Solar Adsorption Cooling and Heating Unit. Energies, 2020. 13(7): p. 1630.*

*Riva, C., **T.C. Roumpedakis**, G. Kallis, M.V. Rocco, and S. Karellas, Life cycle analysis of a photovoltaic driven reversible heat pump. Energy and Buildings, 2021: p. 110894.*

***Roumpedakis, T.C.**, N. Fostieris, K. Braimakis, E. Monokrousou, A. Charalampidis, and S. Karellas, Techno-Economic Optimization of Medium Temperature Solar-Driven Subcritical Organic Rankine Cycle. Thermo, 2021. 1(1): p. 77-105.*

*Pallis, P., K. Braimakis, **T.C. Roumpedakis**, E. Varvagiannis, S. Karellas, L. Doulos, M. Katsaros, and P. Vourliotis, Energy and economic performance assessment of efficiency measures in zero-energy office buildings in Greece. Building and Environment, 2021: p. 108378.*

*Pallis, P., E. Varvagiannis, K. Braimakis, **T. Roumpedakis**, A.D. Leontaritis, and S. Karellas, Development, experimental testing and techno-economic assessment of a fully automated marine organic rankine cycle prototype for jacket cooling water heat recovery. Energy, 2021. 228: p. 120596.*

*Volpato, G., S. Rech, A. Lazzaretto, **T.C. Roumpedakis**, S. Karellas, and C.A. Frangopoulos, Conceptual development and optimization of the main absorption systems configurations. Renewable Energy, 2021.*

Conference papers

***Roumpedakis, T.C.**, T. Christou, K. Braimakis, E. Varvagiannis, and S. Karellas, Integrated ORC-Adsorption cycle: A first and second law analysis of potential configurations, in ECOS 2018. 2018: Guimaraes, Portugal.*

*Kallis, G., **T.C. Roumpedakis**, D. Magiri-Skouloudi, and S. Karellas, Environmental performance of ZEOSOL solar cooling setup, in ECOS 2019 - The 32nd International conference on Efficiency, Cost, Optimization, Simulation and environmental impact of energy systems. 2019: Wroclaw, Poland.*

***Roumpedakis, T.C**., G. Loumpardis, and S. Karellas, Exergetic and Economic Analysis of a Solar Driven Small Scale ORC, in ORC2019. 2019: Athens, Greece.*

***Roumpedakis, T.C**., S. Karellas, S. Vasta, U. Wittstadt, and N. Harborth. Performance results of a solar adsorption cooling and heating unit. in Proceedings of the ISES Solar World Congress 2019 and IEA SHC International Conference on Solar Heating and Cooling for Buildings and Industry 2019. 2020.*

***Roumpedakis, T.C.**, G. Kallis, Z. Koutantzi, P. Pallis, A. Charalampidis, and S. Karellas. Environmental analysis of a small scale marine ORC. in ORC2021. 2021. Munich, Germany.*

References

1. European Parliament and Council of the European Union, *Directive 2009/28/EC of the European Parliament and of the Council of 23 April 2009 on the promotion of the use of energy from renewable sources and amending and subsequently repealing Directives 2001/77/EC and 2003/30/EC.* Official Journal of the European Union, 2009. **5**: p. 2009.
2. European Parliament and Council of the European Union, *Directive (EU) 2018/2001 of the European Parliament and of the Council of 11 December 2018 on the promotion of the use of energy from renewable sources*. 2018, Official Journal of the European Union.
3. European Parliament and Council of the European Union, *Directive (EU) 2018/2002 of the European Parliament and of the Council of 11 December 2018 amending Directive 2012/27/EU on energy efficiency* 2018, Official Journal of the European Union.
4. Ministry of Environment and Energy - Hellenic Republic, *National Energy and Climate Plan (NECP)*. 2019.
5. Stavrakas, V., N. Kleanthis, and A. Flamos, *An Ex-Post Assessment of RES-E Support in Greece by Investigating the Monetary Flows and the Causal Relationships in the Electricity Market.* Energies, 2020. **13**(17): p. 4575.
6. Goffman, E., *Why not the sun? Advantages of and problems with solar energy.* Journal of ProQuest Discovery Guides, 2008.
7. Eurostat. *Simplified energy balances*. 2021 May 2021]; Available from: https://ec.europa.eu/eurostat/databrowser/view/nrg_bal_s/default/table?lang=en.
8. Eurostat. *Electricity prices, second half of year, 2020*. 2020 April 2021]; Available from: https://ec.europa.eu/eurostat/statistics-explained/index.php/Electricity_price_statistics.
9. Eurostat. *Natural gas prices (including taxes) for household consumers, second half 2020*. 2021 Φεβρουάριος 2019]; Available from: https://ec.europa.eu/eurostat/statistics-explained/index.php?title=Natural_gas_price_statistics.
10. Eurostat. *Energy consumption in households by type of end-use*. 2021 May 2021]; Available from: https://ec.europa.eu/eurostat/statistics-explained/index.php?title=Energy_consumption_in_households.
11. © 2021 The World Bank Group. *Population, total - Greece*. 2021; Available from: https://data.worldbank.org/indicator/SP.POP.TOTL?locations=GR.
12. Solar Heat Europe ESTIF, *Solar Heat Markets in Europe - Trends and Market Statistics 2019*. 2021.
13. Weiss, W. and F. Mauthner, *Solar heat worldwide*, in *Global Market Development and Trends in 2019. Detailed Market Data 2018*, IEA Solar Heating & Cooling Programme, Editor. 2020.
14. International Energy Agency (IEA), *The Future of Cooling Opportunities for energy efficient air conditioning*. 2018.
15. Neyer, D. and U. Jakob. *Solar Cooling for the Sunbelt Regions – a new IEA SHC Task*. in *EuroSun 2020: 13th International Conference on Solar Energy for Buildings and Industry*. 2020.
16. Delgado-Torres, A.M. and L. García-Rodríguez, *Analysis and optimization of the low-temperature solar organic Rankine cycle (ORC).* Energy Conversion and Management, 2010. **51**(12): p. 2846-2856.
17. Casati, E., A. Galli, and P. Colonna, *Thermal energy storage for solar-powered organic Rankine cycle engines.* Solar Energy, 2013. **96**: p. 205-219.
18. Karellas, S. and T.C. Roumpedakis, *Chapter 7 - Solar thermal power plants*, in *Solar Hydrogen Production*, F. Calise, et al., Editors. 2019, Academic Press. p. 179-235.

19. Tartière, T. and M. Astolfi, *A World Overview of the Organic Rankine Cycle Market.* Energy Procedia, 2017. **129**(Supplement C): p. 2-9.
20. Petrollese, M., G. Cau, and D. Cocco, *The Ottana solar facility: dispatchable power from small-scale CSP plants based on ORC systems.* Renewable Energy, 2020. **147**: p. 2932-2943.
21. ©Aalborg CSP 2015. *16.6MWTH CSP FOR COMBINED HEAT AND POWER GENERATION, DENMARK*. 2021; Available from: https://www.aalborgcsp.com/projects/166mwth-csp-for-combined-heat-and-power-generation-denmark/.
22. Mascuch, J., V. Novotny, J. Spale, V. Vodicka, and Z. Zeleny, *Experience from set-up and pilot operation of an in-house developed biomass-fired ORC microcogeneration unit.* Renewable Energy, 2021. **165**: p. 251-260.
23. Tocci, L., T. Pal, I. Pesmazoglou, and B. Franchetti, *Small Scale Organic Rankine Cycle (ORC): A Techno-Economic Review.* Energies, 2017. **10**(4): p. 413.
24. ©Ingeco Clean Energy Systems, *Sistemi di generazione a Ciclo Combinato Vapore + ORC di piccola taglia ad alta efficienza*. 2015.
25. ©Climeon. *How it works: The heat power process*. 2021 May 2021]; Available from: https://climeon.com/how-it-works/.
26. ©2021 ElectraTherm. *PRODUCTS POWER+ GENERATOR*. 2021 May 2021]; Available from: http://electratherm.com/power-generator/.
27. ©Enertime. *ORC Modules*. 2021 May 2021]; Available from: https://www.enertime.com/en/technology/solutions/orc-modules.
28. ©2014 - 2018 Entropea Labs. *Products*. 2021 May 2021]; Available from: http://entropea.com/technology/.
29. ©E-rational. *PRODUCTS ORC ULTRA HIGH TEMPERATURE (130°C - 175°C)*. 2021 May 2021]; Available from: https://e-rational.net/products/orc-uht.html.
30. ©Exergy International Srl. *ORC INSTALLATIONS REFERENCE LIST /APR 2021*. 2021; Available from: https://www.exergy-orc.com/upload/pages/282/exergy-ExergyReferencelistApr_2021.pdf.
31. ©General Electric Company, *Clean Cycle II J-Series Technical Specification*. 2014.
32. ©KaishanUSA. *ORC Power Generation*. 2021 May 2021]; Available from: https://kaishanusa.com/products/orc-power-expander/.
33. ©Orcan Energy AG. *Products*. 2021 May 2021]; Available from: https://www.orcan-energy.com/en/#solutions.
34. ©Rank®, *Rank®LT1*. 2018.
35. ©TAS. *WASTE HEAT/GEO THERMAL*. 2021 May 2021]; Available from: http://turbineairsystems.com/waste-heat-geo-thermal/.
36. ©Triogen. *Our products - Triogen e-box*. 2021 May 2021]; Available from: http://www.triogen.nl/technology/triogen-our-products.
37. ©Turbiden S.p.A. *ORC System*. 2021 May 2021]; Available from: https://www.turboden.com/products/2463/orc-system.
38. ©2019 ZE International Group. *Clean electricity generation using the ORC process*. 2021 May 2021]; Available from: https://www.zeintlplc.com/?page_id=463.
39. ©2020 Zuccato Energia srl. *Products*. 2021 May 2021]; Available from: https://zuccatoenergia.it/en/products/.
40. Sarzynski, A., J. Larrieu, and G. Shrimali, *The impact of state financial incentives on market deployment of solar technology.* Energy Policy, 2012. **46**: p. 550-557.
41. Simpson, G. and J. Clifton, *Testing Diffusion of Innovations Theory with data: Financial incentives, early adopters, and distributed solar energy in Australia.* Energy Research & Social Science, 2017. **29**: p. 12-22.

42. The President of the Hellenic Republic, *Institutional framework for the establishment of private investment aid schemes for the regional and economic development of the country* in *4399/2016* 2016, Official Greek Government Gazette.
43. EFEPAE. *Calls - Quality Modernization [4/6/2018]*. 2018 May 2021]; Available from: http://www.antagonistikotita.gr/epanek_en/prokirixeis.asp?id=24&cs=.
44. Ministry of Development and Investments - Hellenic Republic, *Competitiveness Toolkit for Small and Very Small Businesses* 2021.
45. Ministry of Environment and Energy - Hellenic Republic, *Application guide for program "energy saving-autonomize"*. 2021.
46. The President of the Hellenic Republic, *Tax reform with a development dimension for tomorrow's Greece.*, in *4646/2019* 2019, Official Greek Government Gazette.
47. Ministry of Environment and Energy - Hellenic Republic, *Ministerial Decision ΥΠΕΝ/ΔΑΠΕΕΚ/30971/1190/2020*. 2020.
48. Ministry of Environment and Energy - Hellenic Republic, *Ministerial Decision ΥΠΕΝ/ΔΑΠΕΕΚ/15084/382*. 2019.
49. Public Power Corporation S.A.-Hellas. *Residential Tariff - Γ1*. 2021; Available from: https://www.dei.gr/en/oikiakoi-pelates/timologia-1-jan-2021/oikiako-timologio-xwris-xronoxrewsi-g1jan2021.
50. The President of the Hellenic Republic, *Modernization of Spatial and Urban Planning Legislation and other provisions.*, in *4759/2020*. 2020, Official Greek Government Gazette.
51. Ministry of Environment and Energy - Hellenic Republic, *Approval of energy performance of buildings regulation.*, in *ΦΕΚ 2367/Β/2017*. 2017.
52. The President of the Hellenic Republic, *Energy Efficiency of Buildings - Harmonization with Directive 2010/31/EU of the European Parliament and of the Council and other provisions*, in *4122/2013*. 2013, Official Greek Government Gazette.
53. Eurostat. *Electricity price statistics*. 2021 May 2021,]; Available from: https://ec.europa.eu/eurostat/statistics-explained/index.php?title=Electricity_price_statistics.
54. Gestore dei Servizi Energetici GSE S.p.A. *Efficienza energetica -Conto Termico*. 2021 May 2021,]; Available from: https://www.gse.it/servizi-per-te/efficienza-energetica/conto-termico.
55. Paradigma Italia S.p.A., *Guida 2021: Conto Termic 2.0 - Superbonus110% - Ecobonus - Bonus Ristrutturazione*. 2021.
56. Ministry of Economic Development and Ministry of the Environment and Protection of Natural Resources and the Sea, *DECRETO 4 luglio 2019 Incentivazione dell'energia elettrica prodotta dagli impianti eolici on shore, solari fotovoltaici, idroelettrici e a gas residuati dei processi di depurazione*. 2019.
57. Gestore dei Servizi Energetici GSE S.p.A. *Fotovoltaico - Scambio sul posto*. 2021 May 2021,]; Available from: https://www.gse.it/servizi-per-te/fotovoltaico/scambio-sul-posto.
58. Il presidente della republica, *DECRETO LEGISLATIVO 3 marzo 2011, n. 28 Attuazione della direttiva 2009/28/CE sulla promozione dell'uso dell'energia da fonti rinnovabili, recante modifica e successiva abrogazione delle direttive 2001/77/CE e 2003/30/CE. (11G0067)*. 2011.
59. Il presidente della republica, *DECRETO-LEGGE 30 aprile 2019, n. 34 Misure urgenti di crescita economica e per la risoluzione di specifiche situazioni di crisi. (19G00043) (GU Serie Generale n.100 del 30-04-2019)*. 2019.
60. Ministry of Economic Development, Ministry of the Environment and Protection of Natural Resources and the Sea, and M.o.I.a. Transport, *Integrated National Energy and climate plan - Italy*. 2019.

61. Kalogirou, S.A., *Solar energy engineering : processes and systems*. 2014, Elsevier/Academic Press: Amsterdam :.
62. Roumpedakis, T.C., G. Loumpardis, E. Monokrousou, K. Braimakis, A. Charalampidis, and S. Karellas, *Exergetic and economic analysis of a solar driven small scale ORC.* Renewable Energy, 2020. **157**: p. 1008-1024.
63. Roumpedakis, T.C., G. Kallis, D. Magiri-Skouloudi, D. Grimekis, and S. Karellas, *Life cycle analysis of ZEOSOL solar cooling and heating system.* Renewable Energy, 2020. **154**: p. 82-98.
64. Roumpedakis, T.C., N. Fostieris, K. Braimakis, E. Monokrousou, A. Charalampidis, and S. Karellas, *Techno-Economic Optimization of Medium Temperature Solar-Driven Subcritical Organic Rankine Cycle.* Thermo, 2021. **1**(1): p. 77-105.
65. Kalogirou, S.A., *Solar thermal collectors and applications.* Progress in Energy and Combustion Science, 2004. **30**(3): p. 231-295.
66. Roumpedakis, T., *Techo-economic investigations of a solar driven ORC-sorption system for combined cooling, heating and power*. 2018, TU Delft.
67. Infante Ferreira, C. and D.-S. Kim, *Techno-economic review of solar cooling technologies based on location-specific data.* International Journal of Refrigeration, 2014. **39**(Supplement C): p. 23-37.
68. Drück, H., S. Fischer, and H. Müller-Steinhagen. *Solar keymark testing of solar thermal products*. in *Proceedings of ISES World Congress 2007 (Vol. I–Vol. V)*. 2008. Springer.
69. ©Viessmann Luxembourg sarl. *VITOSOL 300-F*. 2019; Available from: https://www.viessmann.lu/de/wohngebaeude/solarsysteme/Flachkollektoren/vitosol-300-f.html.
70. ©AkoTec. *OEM Vario 1000 Solar Keymark certificate*. 2014; Available from: https://akotec.eu/wp-content/uploads/16-03-17-df-SolarKeymarkErklaerung.pdf.
71. Kasaeian, A., S. Daviran, R.D. Azarian, and A. Rashidi, *Performance evaluation and nanofluid using capability study of a solar parabolic trough collector.* Energy Conversion and Management, 2015. **89**: p. 368-375.
72. Loni, R., A. Kasaeian, E.A. Asli-Ardeh, B. Ghobadian, and S. Gorjian, *Experimental and numerical study on dish concentrator with cubical and cylindrical cavity receivers using thermal oil.* Energy, 2018. **154**: p. 168-181.
73. Essa, M.A., M. Asal, M.A. Saleh, and R. Shaltout, *A comparative study of the performance of a novel helical direct flow U-Tube evacuated tube collector.* Renewable Energy, 2021. **163**: p. 2068-2080.
74. Abokersh, M.H., M. El-Morsi, O. Sharaf, and W. Abdelrahman, *An experimental evaluation of direct flow evacuated tube solar collector integrated with phase change material.* Energy, 2017. **139**: p. 1111-1125.
75. Garg, H., S. Mullick, and V.K. Bhargava, *Solar thermal energy storage*. 2012: Springer Science & Business Media.
76. Sarbu, I. and C. Sebarchievici, *A Comprehensive Review of Thermal Energy Storage.* Sustainability, 2018. **10**(1): p. 191.
77. Raccanello, J., S. Rech, and A. Lazzaretto, *Simplified dynamic modeling of single-tank thermal energy storage systems.* Energy, 2019. **182**: p. 1154-1172.
78. Salomoni, V.A., C.E. Majorana, G.M. Giannuzzi, A. Miliozzi, R. Di Maggio, F. Girardi, D. Mele, and M. Lucentini, *Thermal storage of sensible heat using concrete modules in solar power plants.* Solar Energy, 2014. **103**: p. 303-315.
79. Cabeza, L.F., I. Martorell, L. Miró, A.I. Fernández, and C. Barreneche, *1 - Introduction to thermal energy storage systems*, in *Advances in Thermal Energy Storage Systems (Second Edition)*, L.F. Cabeza, Editor. 2021, Woodhead Publishing. p. 1-33.
80. Palomba, V. and A. Frazzica, *Recent advancements in sorption technology for solar thermal energy storage applications.* Solar Energy, 2019. **192**: p. 69-105.

81. H Abedin, A. and M. A Rosen, *A critical review of thermochemical energy storage systems.* The open renewable energy journal, 2011. **4**(1).
82. Lahmidi, H., S. Mauran, and V. Goetz, *Definition, test and simulation of a thermochemical storage process adapted to solar thermal systems.* Solar Energy, 2006. **80**(7): p. 883-893.
83. Morofsky, E. *History of thermal energy storage*. 2007. Dordrecht: Springer Netherlands.
84. Ter-Gazarian, A., E. Institution of, and Technology, *Energy storage for power systems*. 2011, Institution of Engineering and Technology: Stevenage, U.K. :.
85. Chidambaram, L.A., A.S. Ramana, G. Kamaraj, and R. Velraj, *Review of solar cooling methods and thermal storage options.* Renewable and Sustainable Energy Reviews, 2011. **15**(6): p. 3220-3228.
86. Alva, G., Y. Lin, and G. Fang, *An overview of thermal energy storage systems.* Energy, 2018. **144**: p. 341-378.
87. Gil, A., M. Medrano, I. Martorell, A. Lázaro, P. Dolado, B. Zalba, and L.F. Cabeza, *State of the art on high temperature thermal energy storage for power generation. Part 1—Concepts, materials and modellization.* Renewable and Sustainable Energy Reviews, 2010. **14**(1): p. 31-55.
88. Tian, Y. and C.Y. Zhao, *A review of solar collectors and thermal energy storage in solar thermal applications.* Applied Energy, 2013. **104**: p. 538-553.
89. Hasan Ismaeel, H. and R. Yumrutaş, *Investigation of a solar assisted heat pump wheat drying system with underground thermal energy storage tank.* Solar Energy, 2020. **199**: p. 538-551.
90. Syed, A., M. Izquierdo, P. Rodríguez, G. Maidment, J. Missenden, A. Lecuona, and R. Tozer, *A novel experimental investigation of a solar cooling system in Madrid.* International Journal of Refrigeration, 2005. **28**(6): p. 859-871.
91. Karim, A., A. Burnett, and S. Fawzia, *Investigation of Stratified Thermal Storage Tank Performance for Heating and Cooling Applications.* Energies, 2018. **11**(5): p. 1049.
92. Pintaldi, S., S. Sethuvenkatraman, S. White, and G. Rosengarten, *Energetic evaluation of thermal energy storage options for high efficiency solar cooling systems.* Applied Energy, 2017. **188**: p. 160-177.
93. Jung, W., D. Kim, B.H. Kang, and Y.S. Chang, *Investigation of Heat Pump Operation Strategies with Thermal Storage in Heating Conditions.* Energies, 2017. **10**(12): p. 2020.
94. Che, D., Y. Liu, and C. Gao, *Evaluation of retrofitting a conventional natural gas fired boiler into a condensing boiler.* Energy Conversion and Management, 2004. **45**(20): p. 3251-3266.
95. ©RIELLO SPA. *RESIDENCE| CONDENSING WALL HUNG BOILERS - RESIDENCE 25 KIS*. 2021; Available from: https://www.riello.com/international/products/heating-catalogue-products/residence_R-EX-PL-0011659?k=Product+Line%7CR-EX-PL-0004110%7C-.
96. European Committee for Standardization (CEN), *EN 13203-2:2018 Gas-fired domestic appliances producing hot water Part 2: Assessment of energy consumption*. 2018: Brussels.
97. Pallis, P., N. Gkonis, E. Varvagiannis, K. Braimakis, S. Karellas, M. Katsaros, P. Vourliotis, and D. Sarafianos, *Towards NZEB in Greece: A comparative study between cost optimality and energy efficiency for newly constructed residential buildings.* Energy and Buildings, 2019. **198**: p. 115-137.
98. Attia, S., *Chapter 1 - Introduction to NZEB and Market Accelerators*, in *Net Zero Energy Buildings (NZEB)*, S. Attia, Editor. 2018, Butterworth-Heinemann. p. 1-20.

99. Chapra, S.C. and R.P. Canale, *Numerical methods for engineers*. 3rd ed. 2011: Mcgraw-hill New York.
100. Wischhusen, S. *An enhanced discretization method for storage tank models within energy systems*. in *Proc. of the 5-th International Modelica Conference*. 2006.
101. Lemmon, E.W.H., M.L. and M.O. McLinden, *NIST Standard ReferenceDatabase 23: Reference Fluid Thermodynamic and Transport Properties - REFPROP. 9.0.* 2010.
102. Nash, A.L., A. Badithela, and N. Jain, *Dynamic modeling of a sensible thermal energy storage tank with an immersed coil heat exchanger under three operation modes.* Applied Energy, 2017. **195**: p. 877-889.
103. Frazzica, A., V. Brancato, and B. Dawoud, *Unified Methodology to Identify the Potential Application of Seasonal Sorption Storage Technology.* Energies, 2020. **13**(5): p. 1037.
104. Roumpedakis, T.C., S. Vasta, A. Sapienza, G. Kallis, S. Karellas, U. Wittstadt, M. Tanne, N. Harborth, and U. Sonnenfeld, *Performance Results of a Solar Adsorption Cooling and Heating Unit.* Energies, 2020. **13**(7): p. 1630.
105. Palomba, V., U. Wittstadt, A. Bonanno, M. Tanne, N. Harborth, and S. Vasta, *Components and design guidelines for solar cooling systems: The experience of ZEOSOL.* Renewable Energy, 2019. **141**: p. 678-692.
106. Sapienza, A., V. Palomba, G. Gullì, A. Frazzica, and S. Vasta, *A new management strategy based on the reallocation of ads-/desorption times: Experimental operation of a full-scale 3 beds adsorption chiller.* Applied Energy, 2017. **205**: p. 1081-1090.
107. Sharonov, V.E. and Y.I. Aristov, *Chemical and adsorption heat pumps: Comments on the second law efficiency.* Chemical Engineering Journal, 2008. **136**(2–3): p. 419-424.
108. Meunier, F., P. Neveu, and J. Castaing-Lasvignottes, *Equivalent Carnot cycles for sorption refrigeration: Cycles de Carnot équivalents pour la production de froid par sorption.* International Journal of Refrigeration, 1998. **21**(6): p. 472-489.
109. San, J.-Y. and H.-C. Hsu, *Performance of a multi-bed adsorption heat pump using SWS-1L composite adsorbent and water as the working pair.* Applied Thermal Engineering, 2009. **29**(8–9): p. 1606-1613.
110. Chan, K.C., C.Y.H. Chao, G.N. Sze-To, and K.S. Hui, *Performance predictions for a new zeolite 13X/CaCl2 composite adsorbent for adsorption cooling systems.* International Journal of Heat and Mass Transfer, 2012. **55**(11–12): p. 3214-3224.
111. Allouhi, A., T. Kousksou, A. Jamil, T. El Rhafiki, Y. Mourad, and Y. Zeraouli, *Economic and environmental assessment of solar air-conditioning systems in Morocco.* Renewable and Sustainable Energy Reviews, 2015. **50**: p. 770-781.
112. Du, S.W., X.H. Li, Z.X. Yuan, C.X. Du, W.C. Wang, and Z.B. Liu, *Performance of solar adsorption refrigeration in system of SAPO-34 and ZSM-5 zeolite.* Solar Energy, 2016. **138**: p. 98-104.
113. Quoilin, S., R. Aumann, A. Grill, A. Schuster, V. Lemort, and H. Spliethoff, *Dynamic modeling and optimal control strategy of waste heat recovery Organic Rankine Cycles.* Applied Energy, 2011. **88**(6): p. 2183-2190.
114. Bergman, T.L. and F.P. Incropera, *Fundamentals of heat and mass transfer*. 7th ed. / ed. 2011, Hoboken, NJ :: Wiley.
115. Donowski, V.D. and S.G. Kandlikar. *Correlating evaporation heat transfer coefficient of refrigerant R-134a in a plate heat exchanger*. in *Engineering Foundation Conference on Pool and Flow Boiling, Alaska*. 2000.
116. Focke, W.W., J. Zachariades, and I. Olivier, *The effect of the corrugation inclination angle on the thermohydraulic performance of plate heat exchangers.* International Journal of Heat and Mass Transfer, 1985. **28**(8): p. 1469-1479.

117. Infante Ferreira, C.A. and T.C. Roumpedakis, *Solar driven Organic Rankine Cycle – ab/adsorption cogeneration systems*, in *The 25th IIR International Congress of Refrigeration*. 2019: Montreal, Canada.
118. Kim, D.S. and C.A. Infante Ferreira, *Analytic modelling of steady state single-effect absorption cycles.* International Journal of Refrigeration, 2008. **31**(6): p. 1012-1020.
119. Gordon, J.M. and K.C. Ng, *Cool thermodynamics : the engineering and physics of predictive, diagnostic and optimization methods for cooling systems*. 2000, Cambridge :: Cambridge International Science Publishing.
120. Nkwetta, D.N. and J. Sandercock, *A state-of-the-art review of solar air-conditioning systems.* Renewable and Sustainable Energy Reviews, 2016. **60**(Supplement C): p. 1351-1366.
121. Azhar, M. and M.A. Siddiqui, *Exergy analysis of single to triple effect lithium bromide-water vapour absorption cycles and optimization of the operating parameters.* Energy Conversion and Management, 2019. **180**: p. 1225-1246.
122. Beausoleil-Morrison, I., G. Johnson, and B.P. Kemery, *The experimental characterization of a lithium bromide–water absorption chiller and the development of a calibrated model.* Solar Energy, 2015. **122**: p. 368-381.
123. *TABULA WebTool*. 2019.
124. Pallis, P., K. Braimakis, T.C. Roumpedakis, E. Varvagiannis, S. Karellas, L. Doulos, M. Katsaros, and P. Vourliotis, *Energy and economic performance assessment of efficiency measures in zero-energy office buildings in Greece.* Building and Environment, 2021: p. 108378.
125. ©RIELLO SPA. *RESIDENCE| CONDENSING WALL HUNG BOILERS - RESIDENCE 20 IS*. 2020; Available from: https://www.riello.com/international/products/heating-catalogue-products/residence_R-EX-PL-0011659?k=Product+Line%7CR-EX-PL-0004110%7C-.
126. Riva, C., T.C. Roumpedakis, G. Kallis, M.V. Rocco, and S. Karellas, *Life cycle analysis of a photovoltaic driven reversible heat pump.* Energy and Buildings, 2021: p. 110894.
127. ©Suzhou Talesun Solar Technologies Co. Ltd. *Talesun TP660P*. 2021; Available from: https://www.talesun-solar.com/wp-content/uploads/2020/04/PIPRO-TP660P-20200415.pdf.
128. © 2011 Fronius™. *FRONIUS Galvo*. 2020; Available from: https://www.evolveindia.in/doc/inverters/Fronius%20Inverter/Data%20sheet/SE_DS_Fronius_Galvo_EN.pdf.
129. De Soto, W., S.A. Klein, and W.A. Beckman, *Improvement and validation of a model for photovoltaic array performance.* Solar Energy, 2006. **80**(1): p. 78-88.
130. Varvagiannis, E., A. Charalampidis, G. Zsembinszki, S. Karellas, and L.F. Cabeza, *Energy assessment based on semi-dynamic modelling of a photovoltaic driven vapour compression chiller using phase change materials for cold energy storage.* Renewable Energy, 2021. **163**: p. 198-212.
131. Pallis, P., *Experimental investigation and economic assessment of a fully automated organic Rankine cycle for waste heat recovery from marine engine jacket cooling water*, in *School of Mechanicla Engineering*. 2020, National Technical University of Athens: Greece.
132. Wanner Engineering, I. *D10 Series Specifications Datasheet*. 2014; Available from: http://www.hydra-cell.com/product/D10-hydracell-pump.html.
133. Roumpedakis, T.C., S. Chapaloglou, P. Pallis, A.-D. Leontaritis, K. Braimakis, S. Karellas, and P. Vourliotis, *Experimental Investigation and CFD Analysis of Heat Transfer in Single Phase Subcooler of a Small Scale Waste Heat Recovery ORC.* Energy Procedia, 2017. **129**: p. 487-494.

134. Quoilin, S., M.V.D. Broek, S. Declaye, P. Dewallef, and V. Lemort, *Techno-economic survey of Organic Rankine Cycle (ORC) systems.* Renewable and Sustainable Energy Reviews, 2013. **22**: p. 168-186.
135. Dumont, O., R. Dickes, and V. Lemort, *Experimental investigation of four volumetric expanders.* Energy Procedia, 2017. **129**: p. 859-866.
136. Declaye, S., S. Quoilin, L. Guillaume, and V. Lemort, *Experimental study on an open-drive scroll expander integrated into an ORC (Organic Rankine Cycle) system with R245fa as working fluid.* Energy, 2013. **55**: p. 173-183.
137. Lemort, V., S. Declaye, and S. Quoilin, *Experimental characterization of a hermetic scroll expander for use in a micro-scale Rankine cycle.* Proceedings of the Institution of Mechanical Engineers, Part A: Journal of Power and Energy, 2011. **226**(1): p. 126-136.
138. Ziviani, D., S. Gusev, S. Lecompte, E.A. Groll, J.E. Braun, W.T. Horton, M. van den Broek, and M. De Paepe, *Characterizing the performance of a single-screw expander in a small-scale organic Rankine cycle for waste heat recovery.* Applied Energy, 2016. **181**: p. 155-170.
139. Lemort, V., L. Guillaume, A. Legros, S. Declaye, and S. Quoilin. *A comparison of piston, screw and scroll expanders for small scale Rankine cycle systems*. in *Proceedings of the 3rd international conference on microgeneration and related technologies*. 2013.
140. Hsu, S.-W., H.-W. Chiang, and C.-W. Yen, *Experimental investigation of the performance of a hermetic screw-expander organic Rankine cycle.* Energies, 2014. **7**(9): p. 6172-6185.
141. Wang, W., L.-l. Shen, R.-m. Chen, Y.-t. Wu, and C.-f. Ma, *Experimental Study on Heat Loss of a Single Screw Expander for an Organic Rankine Cycle System.* Frontiers in Energy Research, 2020. **8**(273).
142. Lemort, V., S. Quoilin, C. Cuevas, and J. Lebrun, *Testing and modeling a scroll expander integrated into an Organic Rankine Cycle.* Applied Thermal Engineering, 2009. **29**(14–15): p. 3094-3102.
143. Giuffrida, A., *Improving the semi-empirical modelling of a single-screw expander for small organic Rankine cycles.* Applied Energy, 2017. **193**: p. 356-368.
144. Kakaç, S. and H. Liu, *Heat exchangers : selection, rating, and thermal design*. 2nd ed. ed. 2002, Boca Raton :: CRC Press.
145. Laval, A., *Alfa Laval CB60/CBH60*. 2016.
146. Dickes, R., O. Dumont, and V. Lemort, *Infrared imaging of a multi-zone condenser for heat transfer coefficients assessment.* Proceedings of ECOS 2019, 2019.
147. Chemieingenieurwesen, V.D.-G.V.u., *VDI heat atlas*. 2010, Springer: Berlin ;.
148. Yan, Y.Y. and T.F. Lin, *Evaporation Heat Transfer and Pressure Drop of Refrigerant R-134a in a Plate Heat Exchanger.* Journal of Heat Transfer, 1999. **121**(1): p. 118-127.
149. Yan, Y.-Y., H.-C. Lio, and T.-F. Lin, *Condensation heat transfer and pressure drop of refrigerant R-134a in a plate heat exchanger.* International Journal of Heat and Mass Transfer, 1999. **42**(6): p. 993-1006.
150. Gunantara, N., *A review of multi-objective optimization: Methods and its applications.* Cogent Engineering, 2018. **5**(1): p. 1502242.
151. Braimakis, K., T.C. Roumpedakis, A.-D. Leontaritis, and S. Karellas, *Comparison of Environmentally Friendly Working Fluids for Organic Rankine Cycles*, in *Advances in New Heat Transfer Fluids: from Numerical to Experimental Techniques*, A.A. Minea, Editor. 2016, CRC Press: Boca Raton. p. 377-426.
152. European Committee for Standardisation (CEN), *Refrigerating systems and heat pumps - Safety and environmental requirements - Part 3: Installation site and personal protection*. 2020.

153. Kalogirou, S.A., S. Karellas, V. Badescu, and K. Braimakis, *Exergy analysis on solar thermal systems: A better understanding of their sustainability.* Renewable Energy, 2016. **85**: p. 1328-1333.
154. Wang, H., J. Xu, X. Yang, Z. Miao, and C. Yu, *Organic Rankine cycle saves energy and reduces gas emissions for cement production.* Energy, 2015. **86**: p. 59-73.
155. Tzivanidis, C., E. Bellos, and K.A. Antonopoulos, *Energetic and financial investigation of a stand-alone solar-thermal Organic Rankine Cycle power plant.* Energy Conversion and Management, 2016. **126**: p. 421-433.
156. Pallis, P., E. Varvagiannis, K. Braimakis, T. Roumpedakis, A.D. Leontaritis, and S. Karellas, *Development, experimental testing and techno-economic assessment of a fully automated marine organic rankine cycle prototype for jacket cooling water heat recovery.* Energy, 2021. **228**: p. 120596.
157. He, Z., Y. Zhang, S. Dong, H. Ma, X. Yu, Y. Zhang, X. Ma, N. Deng, and Y. Sheng, *Thermodynamic analysis of a low-temperature organic Rankine cycle power plant operating at off-design conditions.* Applied Thermal Engineering, 2017. **113**: p. 937-951.
158. Saheb, Y., H. Ossenbrink, S. Szabo, K. Bódis, and S. Panev. *Energy transition of Europe's building stock. Implications for EU 2030. Sustainable Development Goals*. in *Annales des Mines-Responsabilite et environnement*. 2018. FFE.
159. Rentizelas, A., S. Karellas, E. Kakaras, and I. Tatsiopoulos, *Comparative techno-economic analysis of ORC and gasification for bioenergy applications.* Energy Conversion and Management, 2009. **50**(3): p. 674-681.
160. Li, L., L. Tao, Q. Li, and Y. Hu, *Experimentally economic analysis of ORC power plant with low-temperature waste heat recovery.* International Journal of Low-Carbon Technologies, 2020. **16**(1): p. 35-44.
161. Leibowitz, H., I.K. Smith, and N. Stosic. *Cost Effective Small Scale ORC Systems for Power Recovery From Low Grade Heat Sources*. in *ASME 2006 International Mechanical Engineering Congress and Exposition*. 2006.
162. Zahedi, R., A. Ahmadi, and R. Dashti, *Energy, exergy, exergoeconomic and exergoenvironmental analysis and optimization of quadruple combined solar, biogas, SRC and ORC cycles with methane system.* Renewable and Sustainable Energy Reviews, 2021. **150**: p. 111420.
163. Sterrer, R., S. Schidler, O. Schwandt, P. Franz, and A. Hammerschmid, *Theoretical Analysis of the Combination of CSP with a Biomass CHP-plant Using ORC-technology in Central Europe.* Energy Procedia, 2014. **49**(Supplement C): p. 1218-1227.
164. Peel, M.C., B.L. Finlayson, and T.A. McMahon, *Updated world map of the Köppen-Geiger climate classification.* Hydrology and earth system sciences, 2007. **11**(5): p. 1633-1644.
165. Bellos, E., C. Tzivanidis, and K.A. Antonopoulos, *Exergetic, energetic and financial evaluation of a solar driven absorption cooling system with various collector types.* Applied Thermal Engineering, 2016. **102**: p. 749-759.
166. Abed, N., I. Afgan, A. Cioncolini, H. Iacovides, and A. Nasser, *Assessment and evaluation of the thermal performance of various working fluids in parabolic trough collectors of solar thermal power plants under non-uniform heat flux distribution conditions.* Energies, 2020. **13**(15): p. 3776.
167. Quoilin, S., S. Declaye, B.F. Tchanche, and V. Lemort, *Thermo-economic optimization of waste heat recovery Organic Rankine Cycles.* Applied thermal engineering, 2011. **31**(14-15): p. 2885-2893.
168. Maraver, D., J. Uche, and J. Royo, *Assessment of high temperature organic Rankine cycle engine for polygeneration with MED desalination: A preliminary approach.* Energy Conversion and Management, 2012. **53**(1): p. 108-117.

169. Deb, K., A. Pratap, S. Agarwal, and T. Meyarivan, *A fast and elitist multiobjective genetic algorithm: NSGA-II.* IEEE transactions on evolutionary computation, 2002. **6**(2): p. 182-197.
170. Desai, N.B. and S. Bandyopadhyay, *Thermo-economic analysis and selection of working fluid for solar organic Rankine cycle.* Applied Thermal Engineering, 2016. **95**: p. 471-481.
171. Sun, K., T. Zhao, S. Wu, and S. Yang, *Comprehensive evaluation of concentrated solar collector and Organic Rankine cycle hybrid energy process with considering the effects of different heat transfer fluids.* Energy Reports, 2021. **7**: p. 362-384.
172. Cioccolanti, L., R. Tascioni, and A. Arteconi, *Mathematical modelling of operation modes and performance evaluation of an innovative small-scale concentrated solar organic Rankine cycle plant.* Applied Energy, 2018. **221**: p. 464-476.
173. Desai, N.B., H. Pranov, and F. Haglind, *Techno-economic analysis of a foil-based solar collector driven electricity and fresh water generation system.* Renewable Energy, 2021. **165**: p. 642-656.
174. Petrollese, M. and D. Cocco, *A multi-scenario approach for a robust design of solar-based ORC systems.* Renewable Energy, 2020. **161**: p. 1184-1194.
175. Desai, N.B. and S. Bandyopadhyay, *Thermo-economic comparisons between solar steam Rankine and organic Rankine cycles.* Applied Thermal Engineering, 2016. **105**: p. 862-875.
176. Patil, V.R., V.I. Biradar, R. Shreyas, P. Garg, M.S. Orosz, and N.C. Thirumalai, *Techno-economic comparison of solar organic Rankine cycle (ORC) and photovoltaic (PV) systems with energy storage.* Renewable Energy, 2017. **113**: p. 1250-1260.
177. El hamdani, F., S. Vaudreuil, S. Abderafi, and T. Bounahmidi, *Techno-Economic Evaluation of a Concentrating Solar Power Plant Driven by an Organic Rankine Cycle.* Journal of Solar Energy Engineering, 2020. **142**(6).
178. Roumpedakis, T.C., T. Christou, E. Monokrousou, K. Braimakis, and S. Karellas, *Integrated ORC-Adsorption cycle: A first and second law analysis of potential configurations.* Energy, 2019. **179**: p. 46-58.
179. Wang, H., R. Peterson, and T. Herron, *Design study of configurations on system COP for a combined ORC (organic Rankine cycle) and VCC (vapor compression cycle).* Energy, 2011. **36**(8): p. 4809-4820.
180. Nasir, M.T. and K.C. Kim, *Working fluids selection and parametric optimization of an Organic Rankine Cycle coupled Vapor Compression Cycle (ORC-VCC) for air conditioning using low grade heat.* Energy and Buildings, 2016. **129**: p. 378-395.
181. Zheng, N., J. Wei, and L. Zhao, *Analysis of a solar Rankine cycle powered refrigerator with zeotropic mixtures.* Solar Energy, 2018. **162**: p. 57-66.
182. Yogi Goswami, D., *Solar thermal power technology: present status and ideas for the future.* Energy Sources, 1998. **20**(2): p. 137-145.
183. Tomków, Ł. and M. Cholewiński, *Improvement of the LNG (liquid natural gas) regasification efficiency by utilizing the cold exergy with a coupled absorption – ORC (organic Rankine cycle).* Energy, 2015. **87**: p. 645-653.
184. Mohammadi, A., A. Kasaeian, F. Pourfayaz, and M.H. Ahmadi, *Thermodynamic analysis of a combined gas turbine, ORC cycle and absorption refrigeration for a CCHP system.* Applied Thermal Engineering, 2017. **111**: p. 397-406.
185. Eisavi, B., S. Khalilarya, A. Chitsaz, and M.A. Rosen, *Thermodynamic analysis of a novel combined cooling, heating and power system driven by solar energy.* Applied Thermal Engineering, 2018. **129**: p. 1219-1229.
186. Chaiyat, N., Y. Wakaiyang, and X. Inthavideth, *Enhancement efficiency of organic Rankine cycle by using sorption system.* Applied Thermal Engineering, 2017. **122**(Supplement C): p. 368-379.

187. Jiang, L., L. Wang, R. Wang, P. Gao, and F. Song, *Investigation on cascading cogeneration system of ORC (Organic Rankine Cycle) and CaCl2/BaCl2 two-stage adsorption freezer.* Energy, 2014. **71**: p. 377-387.
188. Wang, L., A.P. Roskilly, and R. Wang, *Solar Powered Cascading Cogeneration Cycle with ORC and Adsorption Technology for Electricity and Refrigeration.* Heat Transfer Engineering, 2014. **35**(11-12): p. 1028-1034.
189. Karakosta, C., M. Flouri, S. Dimopoulou, and J. Psarras, *Analysis of renewable energy progress in the western Balkan countries: Bosnia–Herzegovina and Serbia.* Renewable and Sustainable Energy Reviews, 2012. **16**(7): p. 5166-5175.
190. The MathWorks Inc., *Simulink-Matlab R2016b*. 2016: Natick,MA.
191. Fahrenheit©. *Fahrenheit: eZea*. 2018 January 2017]; Available from: https://fahrenheit.cool/en/zeo/.
192. Lemmon, E.W., M.L. Huber, and M.O. McLinden, *NIST Standard ReferenceDatabase 23: Reference Fluid Thermodynamic and Transport Properties - REFPROP. 9.0.* 2010.
193. ISO, *ISO 14040 International Standard. In: Environmental Management –Life Cycle Assessment – Principles and Framework*, I.O.f. Standardization, Editor. 2006: Geneva, Switzerland.
194. Finnveden, G., M.Z. Hauschild, T. Ekvall, J. Guinée, R. Heijungs, S. Hellweg, A. Koehler, D. Pennington, and S. Suh, *Recent developments in Life Cycle Assessment.* Journal of Environmental Management, 2009. **91**(1): p. 1-21.
195. Ayres, R.U. and L. Ayres, *A handbook of industrial ecology*. 2002: Edward Elgar Publishing.
196. You, S. and X. Wang, *Chapter 20 - On the Carbon Abatement Potential and Economic Viability of Biochar Production Systems: Cost-Benefit and Life Cycle Assessment*, in *Biochar from Biomass and Waste*, Y.S. Ok, et al., Editors. 2019, Elsevier. p. 385-408.
197. Cabeza, L.F., L. Rincón, V. Vilariño, G. Pérez, and A. Castell, *Life cycle assessment (LCA) and life cycle energy analysis (LCEA) of buildings and the building sector: A review.* Renewable and Sustainable Energy Reviews, 2014. **29**(Supplement C): p. 394-416.
198. Matthews, H.S., *The Life-Cycle Assessmentv and Industrial Ecology Communities.* Journal of Industrial Ecology, 2007. **11**(4): p. 1-4.
199. Moreno Ruiz, E., L. Valsasina, D. FitzGerald, A. Symeonidis, J. Müller, N. Minas, G. Bourgault, C. Vadenbo, D. Ioannidou, and G. Wernet, *Documentation of changes implemented in ecoinvent database v3. 7. ecoinvent Association.* Zürich, Switzerland, 2020.
200. Ciroth, A., S. Winter, and G. Berlin, *openLCA 1.4 overview and first steps.* GreenDelta, Berlin, 2014.
201. PRé Sustainability B.V., *SimaPro v.9.0*. 2020.
202. Huijbregts, M.A.J., Z.J.N. Steinmann, P.M.F. Elshout, G. Stam, F. Verones, M. Vieira, M. Zijp, A. Hollander, and R. van Zelm, *ReCiPe2016: a harmonised life cycle impact assessment method at midpoint and endpoint level.* The International Journal of Life Cycle Assessment, 2017. **22**(2): p. 138-147.
203. Batlles, F.J., S. Rosiek, I. Muñoz, and A.R. Fernández-Alba, *Environmental assessment of the CIESOL solar building after two years operation.* Environmental science & technology, 2010. **44**(9): p. 3587-3593.
204. Koroneos, C. and M. Tsarouhis, *Exergy analysis and life cycle assessment of solar heating and cooling systems in the building environment.* Journal of Cleaner Production, 2012. **32**: p. 52-60.
205. Beccali, M., M. Cellura, S. Longo, B. Nocke, and P. Finocchiaro, *LCA of a solar heating and cooling system equipped with a small water–ammonia absorption chiller.* Solar Energy, 2012. **86**(5): p. 1491-1503.

206. Jing, Y.-Y., H. Bai, J.-J. Wang, and L. Liu, *Life cycle assessment of a solar combined cooling heating and power system in different operation strategies.* Applied Energy, 2012. **92**: p. 843-853.
207. Bukoski, J., S.H. Gheewala, A. Mui, M. Smead, and S. Chirarattananon, *The life cycle assessment of a solar-assisted absorption chilling system in Bangkok, Thailand.* Energy and Buildings, 2014. **72**: p. 150-156.
208. Longo, S., M. Beccali, M. Cellura, and F. Guarino, *Energy and environmental life-cycle impacts of solar-assisted systems: The application of the tool "ELISA".* Renewable Energy, 2020. **145**: p. 29-40.
209. Longo, S., V. Palomba, M. Beccali, M. Cellura, and S. Vasta, *Energy balance and life cycle assessment of small size residential solar heating and cooling systems equipped with adsorption chillers.* Solar Energy, 2017. **158**(Supplement C): p. 543-558.
210. Marinelli, S., F. Lolli, R. Gamberini, and B. Rimini, *Life Cycle Thinking (LCT) applied to residential heat pump systems: A critical review.* Energy and Buildings, 2019.
211. Beccali, M., M. Cellura, P. Finocchiaro, F. Guarino, S. Longo, and B. Nocke, *Life Cycle Assessment performance comparison of small solar thermal cooling systems with conventional plants assisted with photovoltaics.* Energy Procedia, 2012. **30**: p. 893-903.
212. Gebreslassie, B.H., E.A. Groll, and S.V. Garimella, *Multi-objective optimization of sustainable single-effect water/Lithium Bromide absorption cycle.* Renewable energy, 2012. **46**: p. 100-110.
213. Maraver, D., A. Sin, F. Sebastián, and J. Royo, *Environmental assessment of CCHP (combined cooling heating and power) systems based on biomass combustion in comparison to conventional generation.* Energy, 2013. **57**: p. 17-23.
214. Beccali, M., M. Cellura, P. Finocchiaro, F. Guarino, S. Longo, and B. Nocke, *Life cycle performance assessment of small solar thermal cooling systems and conventional plants assisted with photovoltaics.* Solar Energy, 2014. **104**(Supplement C): p. 93-102.
215. Hang, Y., M. Qu, R. Winston, L. Jiang, B. Widyolar, and H. Poiry, *Experimental based energy performance analysis and life cycle assessment for solar absorption cooling system at University of Californian, Merced.* Energy and Buildings, 2014. **82**: p. 746-757.
216. Wang, J., Y. Yang, T. Mao, J. Sui, and H. Jin, *Life cycle assessment (LCA) optimization of solar-assisted hybrid CCHP system.* Applied Energy, 2015. **146**(Supplement C): p. 38-52.
217. Finocchiaro, P., M. Beccali, M. Cellura, F. Guarino, and S. Longo, *Life Cycle Assessment of a compact Desiccant Evaporative Cooling system: The case study of the "Freescoo".* Solar Energy Materials and Solar Cells, 2016. **156**: p. 83-91.
218. Beccali, M., M. Cellura, S. Longo, and F. Guarino, *Solar heating and cooling systems versus conventional systems assisted by photovoltaic: Application of a simplified LCA tool.* Solar Energy Materials and Solar Cells, 2016. **156**: p. 92-100.
219. Bahlawan, H., M. Morini, M. Pinelli, W.-R. Poganietz, P.R. Spina, and M. Venturini, *Optimal design of a hybrid energy plant by accounting for the cumulative energy demand.* Energy Procedia, 2019. **158**: p. 2834-2840.
220. Cioccolanti, L., S. Rajabi Hamedani, and M. Villarini, *Environmental and energy assessment of a small-scale solar Organic Rankine Cycle trigeneration system based on Compound Parabolic Collectors.* Energy Conversion and Management, 2019. **198**: p. 111829.
221. Solano–Olivares, K., R.J. Romero, E. Santoyo, I. Herrera, Y.R. Galindo–Luna, A. Rodríguez–Martínez, E. Santoyo-Castelazo, and J. Cerezo, *Life cycle assessment of a solar absorption air-conditioning system.* Journal of Cleaner Production, 2019. **240**: p. 118206.

222. EnergyPlus Development Team, *EnergyPlus engineering reference: The reference to EnergyPlus calculations. EnergyPlus Version 8.8.*, U.D.o. Energy, Editor. 2017.
223. EN ISO, *6946: 2017 "Building Components and Building Elements*. 2017.
224. Carrier, *Reversible Air to Water Heat Pump:30AW*. 2013.
225. Shi, J., T. Li, H. Zhang, S. Peng, Z. Liu, and Q. Jiang, *Energy consummation and environmental emissions assessment of a refrigeration compressor based on life cycle assessment methodology.* The International Journal of Life Cycle Assessment, 2015. **20**(7): p. 947-956.
226. Greening, B. and A. Azapagic, *Domestic heat pumps: Life cycle environmental impacts and potential implications for the UK.* Energy, 2012. **39**(1): p. 205-217.
227. Heck, T., *Wärmepumpe* in *Sachbilanzen von Energiesystemen: Grundlagen für den ökologischen Vergleich von Energiesystemen und den Einbezug von Energiesystemen in Ökobilanzen für die Schweiz* R. Dones, Editor. 2007, Swiss Centre for Life Cycle Inventories: Dübendorf, Switzerland.
228. Lenova, T., *treatment of used refrigerant R134a, reclamation, GLO, Allocation cut-off*, in *ecoinvent database version 3.4*. 2018.
229. El-Khozondar, B. and M.A. Koksal. *Investigating the water consumption for electricity generation at Turkish power plants*. in *E3S Web of Conferences*. 2017. EDP Sciences.
230. Chrysostomou, C., A. Kylili, D. Nicolaides, and P.A. Fokaides, *Life Cycle Assessment of concrete manufacturing in small isolated states: the case of Cyprus.* International Journal of Sustainable Energy, 2017. **36**(9): p. 825-839.
231. Korre, A., Z. Nie, and S. Durucan, *Life cycle modelling of fossil fuel power generation with post-combustion CO2 capture.* International Journal of Greenhouse Gas Control, 2010. **4**(2): p. 289-300.
232. Directorate-General for Energy, *Energy datasheets: EU-28 countries*. 2019.
233. Shah, V.P., D.C. Debella, and R.J. Ries, *Life cycle assessment of residential heating and cooling systems in four regions in the United States.* Energy and Buildings, 2008. **40**(4): p. 503-513.
234. Eicher, S., C. Hildbrand, A. Kleijer, J. Bony, M. Bunea, and S. Citherlet, *Life Cycle Impact Assessment of a Solar Assisted Heat Pump for Domestic Hot Water Production and Space Heating.* Energy Procedia, 2014. **48**: p. 813-818.
235. Nitkiewicz, A. and R. Sekret, *Comparison of LCA results of low temperature heat plant using electric heat pump, absorption heat pump and gas-fired boiler.* Energy Conversion and Management, 2014. **87**: p. 647-652.
236. Li, G., *Comprehensive investigations of life cycle climate performance of packaged air source heat pumps for residential application.* Renewable and Sustainable Energy Reviews, 2015. **43**: p. 702-710.
237. Huang, B. and V. Mauerhofer, *Life cycle sustainability assessment of ground source heat pump in Shanghai, China.* Journal of Cleaner Production, 2016. **119**: p. 207-214.
238. Zhao, S., G. Xu, J. Wang, and X. Zhang, *Life cycle assessment optimization of hybrid power gas heat pump integrated with photovoltaic.* Energy Procedia, 2017. **122**: p. 1141-1146.
239. Litjens, G.B.M.A., E. Worrell, and W.G.J.H.M. van Sark, *Lowering greenhouse gas emissions in the built environment by combining ground source heat pumps, photovoltaics and battery storage.* Energy and Buildings, 2018. **180**: p. 51-71.
240. Wang, X., L. Xia, C. Bales, X. Zhang, B. Copertaro, S. Pan, and J. Wu, *A systematic review of recent air source heat pump (ASHP) systems assisted by solar thermal, photovoltaic and photovoltaic/thermal sources.* Renewable Energy, 2020. **146**: p. 2472-2487.
241. Koroneos, C.J. and E.A. Nanaki, *Environmental impact assessment of a ground source heat pump system in Greece.* Geothermics, 2017. **65**: p. 1-9.

242. Choi, S., J. Oh, Y. Hwang, and H. Lee, *Life cycle climate performance evaluation (LCCP) on cooling and heating systems in South Korea.* Applied Thermal Engineering, 2017. **120**: p. 88-98.
243. Chengmin, C., Z. Yufeng, and M. Lijun, *Assessment for central heating systems with different heat sources: A case study.* Energy and Buildings, 2012. **48**: p. 168-174.
244. E.C.A. *Standard Panel Radiator - Type 11*. 2020; Available from: https://www.eca.com.tr/heating-cooling/radiators/panel-radiators/standard-panel-radiators/type-11.
245. Fu, Y., X. Liu, and Z. Yuan, *Life-cycle assessment of multi-crystalline photovoltaic (PV) systems in China.* Journal of Cleaner Production, 2015. **86**: p. 180-190.
246. Huang, B., J. Zhao, J. Chai, B. Xue, F. Zhao, and X. Wang, *Environmental influence assessment of China's multi-crystalline silicon (multi-Si) photovoltaic modules considering recycling process.* Solar Energy, 2017. **143**: p. 132-141.
247. Xu, L., S. Zhang, M. Yang, W. Li, and J. Xu, *Environmental effects of China's solar photovoltaic industry during 2011–2016: A life cycle assessment approach.* Journal of Cleaner Production, 2018. **170**: p. 310-329.
248. Johnson, E.P., *Air-source heat pump carbon footprints: HFC impacts and comparison to other heat sources.* Energy Policy, 2011. **39**(3): p. 1369-1381.
249. Koronaki, I.P., D. Cowan, G. Maidment, K. Beerman, M. Schreurs, K. Kaar, I. Chaer, G. Gontarz, R.I. Christodoulaki, and X. Cazauran, *Refrigerant emissions and leakage prevention across Europe – Results from the RealSkillsEurope project.* Energy, 2012. **45**(1): p. 71-80.
250. Heberle, F., C. Schifflechner, and D. Brüggemann, *Life cycle assessment of Organic Rankine Cycles for geothermal power generation considering low-GWP working fluids.* Geothermics, 2016. **64**: p. 392-400.
251. Heck, T., *Overview and Methodology - Data v2.0*. 2007.
252. Hundy, G.F., *Refrigeration, air conditioning and heat pumps*. 2016: Butterworth-Heinemann.
253. ISPRA, *https://www.isprambiente.gov.it/it/pubblicazioni/rapporti/studio-sulle-alternative-agli-idrofluorocarburi-hfc-in-italia*, in *286/2018*. 2018.
254. Mancini, M. and G. Zampetti, *Legambiente, I gas refrigeranti in Italia*, CUEIM, Editor. 2010.
255. Consorzio Nazionale per la Gestione. *Smaltimento olio lubrificante*. Available from: https://www.conou.it/it/raccolta/smaltimento/.
256. Adolfsson, M. and S. Rashid, *Life Cycle Assessment and Life Cycle Cost of Heat Exchangers: A Case for Inter Terminals Sweden AB Located in Port of Gothenburg*, in *Department of Energy and Environment*. 2016, Chalmers University of Technology.
257. Reisgen, U., M. Angerhausen, A. Pipinikas, T. Twiehaus, V. Wesling, and J. Barthelmie, *The effect of arc brazing process parameters on the microstructure and mechanical properties of high-strength steel HCT780XD using the copper-based filler metal CuAl8.* Journal of Materials Processing Technology, 2017. **249**: p. 549-558.
258. Roumpedakis, T.C., G. Kallis, D. Magiri-Skouloudi, D. Grimekis, and S. Karellas, *Life cycle analysis of ZEOSOL solar cooling and heating system.* Renewable Energy, 2020.
259. Boustani, A., S. Sahni, T. Gutowski, and S. Graves, *Appliance remanufacturing and energy savings.* Management, 2010.
260. Prek, M., *Environmental impact and life cycle assessment of heating and air conditioning systems, a simplified case study.* Energy and Buildings, 2004. **36**(10): p. 1021-1027.
261. Olimpia Splendid S.p.A. *Bi2 SL 800*. 2020; Available from: https://www.olimpiasplendid.com/hydronic-systems/fan-coils-fan-radiators/bi2-sl-smart.

262. Eurostat. *Energy balance sheets-Greece*. 2021 January 2021]; Available from: https://ec.europa.eu/eurostat/web/energy/data/energy-balances/.
263. Kang, D., N. Sgriccia, S. Selke, and R. Auras, *Comparison of bacon packaging on a life cycle basis: a case study.* Journal of Cleaner Production, 2013. **54**: p. 142-149.
264. Roumpedakis, T.C., G. Kallis, Z. Koutantzi, P. Pallis, A. Charalampidis, and S. Karellas. *Environmental analysis of a small scale marine ORC*. in *ORC2021*. 2021. Munich, Germany.
265. International Maritime Organization, *Fourth IMO GHG Study 2020*. 2021, INTERNATIONAL MARITIME ORGANIZATION: London, United Kingdom.
266. Hoang, A.T., *Waste heat recovery from diesel engines based on Organic Rankine Cycle.* Applied Energy, 2018. **231**: p. 138-166.
267. Singh, D.V. and E. Pedersen, *A review of waste heat recovery technologies for maritime applications.* Energy Conversion and Management, 2016. **111**: p. 315-328.
268. Zhu, S., K. Zhang, and K. Deng, *A review of waste heat recovery from the marine engine with highly efficient bottoming power cycles.* Renewable and Sustainable Energy Reviews, 2020. **120**: p. 109611.
269. Song, J., Y. Song, and C.-w. Gu, *Thermodynamic analysis and performance optimization of an Organic Rankine Cycle (ORC) waste heat recovery system for marine diesel engines.* Energy, 2015. **82**: p. 976-985.
270. Yang, M.-H. and R.-H. Yeh, *Analyzing the optimization of an organic Rankine cycle system for recovering waste heat from a large marine engine containing a cooling water system.* Energy Conversion and Management, 2014. **88**: p. 999-1010.
271. Walsh, C. and P. Thornley, *The environmental impact and economic feasibility of introducing an Organic Rankine Cycle to recover low grade heat during the production of metallurgical coke.* Journal of Cleaner Production, 2012. **34**: p. 29-37.
272. Liu, C., C. He, H. Gao, H. Xie, Y. Li, S. Wu, and J. Xu, *The environmental impact of organic Rankine cycle for waste heat recovery through life-cycle assessment.* Energy, 2013. **56**: p. 144-154.
273. Dawo, F., J. Fleischmann, F. Kaufmann, C. Schifflechner, S. Eyerer, C. Wieland, and H. Spliethoff, *R1224yd(Z), R1233zd(E) and R1336mzz(Z) as replacements for R245fa: Experimental performance, interaction with lubricants and environmental impact.* Applied Energy, 2021. **288**: p. 116661.
274. Carraro, G., P. Pallis, A.D. Leontaritis, S. Karellas, P. Vourliotis, S. Rech, and A. Lazzaretto, *Experimental performance evaluation of a multi-diaphragm pump of a micro-ORC system.* Energy Procedia, 2017. **129**(Supplement C): p. 1018-1025.
275. Leontaritis, A.-D., P. Pallis, S. Karellas, A. Papastergiou, N. Antoniou, P. Vourliotis, N.M. Kakalis, and G. Dimopoulos. *Experimental study on a low temperature ORC unit for onboard waste heat recovery from marine diesel engines*. in *3rd International Seminar on ORC Power Systems*. 2015.
276. Li, G., *Organic Rankine cycle environmental impact investigation under various working fluids and heat domains concerning refrigerant leakage rates.* International Journal of Environmental Science and Technology, 2019. **16**(1): p. 431-450.
277. Heck, T. and E. Moreno Ruiz, *Refrigerant R134a production RER (Europe)*. 2011.
278. Huijbregts, M.A., Z.J. Steinmann, P.M. Elshout, G. Stam, F. Verones, M. Vieira, A. Hollander, M. Zijp, and R. van Zelm, *ReCiPe2016. A harmonized life cycle impact assessment method at midpoint and endpoint level. Report I: characterization. RIVM Report 2016–0104.* National Institute for Human Health and the Environment, Bilthoven, 2016.
279. Meshram, R.B., N. Haldar, and K.L. Sahoo, *Environmental impacts of brass melting: an Indian case study.* Procedia CIRP, 2021. **98**: p. 500-504.

280. ©Inflation Tool 2021. *Inflation calculator - Euro*. 2021; Available from: https://www.inflationtool.com/euro.
281. Kurup, P. and C. Turchi, *Parabolic Trough Collector Cost Update for the System Advisor Model (SAM)*. 2015.
282. Mancini, T., P. Heller, B. Butler, B. Osborn, W. Schiel, V. Goldberg, R. Buck, R. Diver, C. Andraka, and J. Moreno, *Dish-Stirling systems: An overview of development and status.* Journal of Solar Energy Engineering, 2003. **125**(2): p. 135-151.
283. Poullikkas, A., G. Kourtis, and I. Hadjipaschalis, *Parametric analysis for the installation of solar dish technologies in Mediterranean regions.* Renewable and Sustainable Energy Reviews, 2010. **14**(9): p. 2772-2783.
284. ©2021 Nobel. *Forced Circulation Tanks*. 2021 April 2021]; Available from: https://nobel.bg/product/forced-circulation-tanks/.
285. © ASSOS BOILERS. *Vertical Storage Tank - Hot Water Boilers*. 2021 April 2021]; Available from: https://www.assosboilers.com/en/hot-water-storage-tanks/hot-water-boiler-tanks.html.
286. © 2020 AKOTEC, *Product Information Sheet: Solarliquid VT51 hp -30°C*. 2021.
287. Zauba_Technologies. *Import & Export Data, Available from: https://www.zauba.com/importanalysis-therminol-vp-1-report.html*. 2018.
288. Astolfi, M., M.C. Romano, P. Bombarda, and E. Macchi, *Binary ORC (organic Rankine cycles) power plants for the exploitation of medium–low temperature geothermal sources – Part A: Thermodynamic optimization.* Energy, 2014. **66**: p. 423-434.
289. Zauba_Technologies. *Import & Export Data, Available from: https://www.zauba.com/importanalysis-cyclopentane-report.html*. 2018.
290. Zauba_Technologies. *Import & Export Data, Available from: https://www.zauba.com/importanalysis-cyclohexane-report.html*. 2018.
291. Zauba_Technologies. *Import & Export Data, Available from: https://www.zauba.com/importanalysis-isohexane-report.html*. 2018.
292. Zauba_Technologies. *Import & Export Data, Available from: https://www.zauba.com/importanalysis-hexane-report.html*. 2018.
293. Zauba_Technologies. *Import & Export Data, Available from: https://www.zauba.com/importanalysis-benzene-report.html*. 2018.
294. Zauba_Technologies. *Import & Export Data, Available from: https://www.zauba.com/importanalysis-toluene-report.html*. 2018.
295. Quoilin, S., S. Declaye, B.F. Tchanche, and V. Lemort, *Thermo-economic optimization of waste heat recovery Organic Rankine Cycles.* Applied Thermal Engineering, 2011. **31**(14): p. 2885-2893.
296. ©Alfa Laval, *Price list - HVAC and General industry – 2020*. 2020.
297. Astolfi, M., *An innovative approach for the techno-economic optimization of organic rankine cycles*. 2014, Italy.
298. Lecompte, S., H. Huisseune, M. van den Broek, S. De Schampheleire, and M. De Paepe, *Part load based thermo-economic optimization of the Organic Rankine Cycle (ORC) applied to a combined heat and power (CHP) system.* Applied Energy, 2013. **111**: p. 871-881.
299. Zilmet USA, *Zilmet USA List Price Catalog*. 2016.
300. Martínez, P.J., P. Martínez, V.M. Soto, L.A. Bujedo, and J. Rodriguez, *Design of a 35 kW solar cooling demonstration facility for a hotel in spain.* Applied Sciences, 2020. **10**(2): p. 496.
301. Henning et al. *SUMMERHEAT: Cooling in SUMMER by applying HEAT from cogeneration*. 2009; Available from: https://www.euroheat.org/our-projects/summerheat/.

302. Lu, Y., A.P. Roskilly, and C. Ma, *A techno-economic case study using heat driven absorption refrigeration technology in UK industry.* Energy Procedia, 2017. **123**: p. 173-179.
303. Gabbrielli, R., P. Castrataro, and F. Del Medico, *Performance and economic comparison of solar cooling configurations.* Energy Procedia, 2016. **91**: p. 759-766.
304. Alahmer, A., X. Wang, R. Al-Rbaihat, K.C. Amanul Alam, and B.B. Saha, *Performance evaluation of a solar adsorption chiller under different climatic conditions.* Applied Energy, 2016. **175**: p. 293-304.
305. Jäger-Waldau, A., *PV status report 2019.* Publications Office of the European Union: Luxembourg, 2019.
306. Kayal, S., S. Baichuan, and B.B. Saha, *Adsorption characteristics of AQSOA zeolites and water for adsorption chillers.* International Journal of Heat and Mass Transfer, 2016. **92**: p. 1120-1127.
307. Llano-Restrepo, M. and M.A. Mosquera, *Accurate correlation, thermochemistry, and structural interpretation of equilibrium adsorption isotherms of water vapor in zeolite 3A by means of a generalized statistical thermodynamic adsorption model.* Fluid Phase Equilibria, 2009. **283**(1–2): p. 73-88.
308. Mette, B., H. Kerskes, H. Drück, and H. Müller-Steinhagen, *Experimental and numerical investigations on the water vapor adsorption isotherms and kinetics of binderless zeolite 13X.* International Journal of Heat and Mass Transfer, 2014. **71**: p. 555-561.
309. Liu, Y. and K.C. Leong, *Numerical modeling of a zeolite/water adsorption cooling system with non-constant condensing pressure.* International Communications in Heat and Mass Transfer, 2008. **35**(5): p. 618-622.
310. Wu, W.-D., H. Zhang, and D.-W. Sun, *Mathematical simulation and experimental study of a modified zeolite 13X–water adsorption refrigeration module.* Applied Thermal Engineering, 2009. **29**(4): p. 645-651.
311. Saha, B.B., A. Chakraborty, S. Koyama, and Y.I. Aristov, *A new generation cooling device employing CaCl2-in-silica gel–water system.* International Journal of Heat and Mass Transfer, 2009. **52**(1–2): p. 516-524.
312. Sayılgan, Ş.Ç., M. Mobedi, and S. Ülkü, *Effect of regeneration temperature on adsorption equilibria and mass diffusivity of zeolite 13x-water pair.* Microporous and Mesoporous Materials, 2016. **224**: p. 9-16.
313. Habib, K., B.B. Saha, A. Chakraborty, S. Koyama, and K. Srinivasan, *Performance evaluation of combined adsorption refrigeration cycles.* International Journal of Refrigeration, 2011. **34**(1): p. 129-137.
314. Askalany, A.A., S.K. Henninger, M. Ghazy, and B.B. Saha, *Effect of improving thermal conductivity of the adsorbent on performance of adsorption cooling system.* Applied Thermal Engineering, 2017. **110**: p. 695-702.
315. Chua, H.T., K.C. Ng, A. Malek, T. Kashiwagi, A. Akisawa, and B.B. Saha, *Modeling the performance of two-bed, sillica gel-water adsorption chillers.* International Journal of Refrigeration, 1999. **22**(3): p. 194-204.
316. Rezk, A.R.M. and R.K. Al-Dadah, *Physical and operating conditions effects on silica gel/water adsorption chiller performance.* Applied Energy, 2012. **89**(1): p. 142-149.
317. Yang, P.-z., *Heat and mass transfer in adsorbent bed with consideration of non-equilibrium adsorption.* Applied Thermal Engineering, 2009. **29**(14–15): p. 3198-3203.
318. Wang, D.C., Z.Z. Xia, and J.Y. Wu, *Design and performance prediction of a novel zeolite–water adsorption air conditioner.* Energy Conversion and Management, 2006. **47**(5): p. 590-610.

Appendix I. Cost correlations

In this section are presented all the components' cost correlations used to estimate the various economic performance indicators in the techno-economic optimizations of the dissertation. Whenever possible, new cost correlations are introduced based on data from local suppliers, while in cases of zero or insufficient number of quotes, commonly used correlations from literature are used. Apart from the cases which is clearly stated otherwise, the correlations below are shown in Euros2021. In cases, of quotes or price estimations used from previous years, inflation has been taken into consideration based on historical data from [280].

I.1 Solar collectors

With respect to the solar collector's cost, on most cases in literature a specific cost is used per unit of surface. This approach is applied also in this study, with data from local suppliers and literature, whenever a quote was not available.

Table I.1. Specific costs for the different types of solar collectors

Type of collectors	FPC[1]	ETC[2]	PTC [281]	PDC [282, 283]
Specific price (€/m²)	210	295	188	268

[1] Price referring to model Cosmosolar EPI 25 CS (base included in price)
[2] Price delivered by AKOTEC Produktionsgesellschaft mbH

I.2 Storage tank

With respect to the storage tanks, there should be a distinction between simple (open-circuit) storage tanks and storage tanks with coils, which allow for system separation between the solar collectors and the storage/downdraft sub-system and therefore are relatively more expensive. Both purchase prices used for the construction of the respective cost correlations were collected/updated in April 2021. The data for the simple storage tanks was with reference to the Nobel Glass series tanks [284], while the coiled storage tanks' data was based on Assos BL series [285].

The developed correlation for simple storage tanks is shown below:

$$C_{st} = 1{,}129.0\, V_{st} + 82.825 \qquad (I.1)$$

The respective cost correlation for the purchase of storage tanks with coils with respect to their volumetric capacity is listed below:

$$C_{st*} = -836.69\, V_{st}^2 + 1{,}783.9\, V_{st} + 182.06 \qquad (I.2)$$

An overview of the fitting between the purchase prices and the proposed correlation along with the estimated coefficient of determination, R^2, is shown in Fig. I.1.

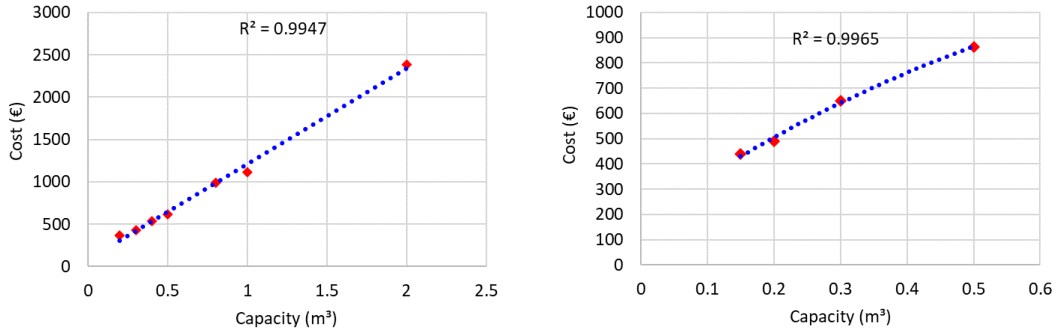

(a) *(b)*

Fig. I.1. Data fitting for the development of cost correlations (blue line) based on purchase prices from quotes (red dots) (a) for storage tanks without coils and (b) with coils

I.3 Circulator pumps

The costs correlation used for the estimation of the purchase costs of a circulating pump was based on quotes received in the period January to March 2021 for pumps of the series UPS2 and ALPHA2 of manufacturing company Grundfos. For circulating pumps it is common in literature to use cost correlations as a function of their power consumption. However, at least for the case of circulating pumps, as shown in Fig. I.2 (b) one such correlation yields only an R^2 of less than 0.6. On the other hand, as shown in Fig. I.2 (a), there is a stronger correlation with the maximum volumetric flowrate of each model and therefore a relevant correlation was developed:

$$C_{cpump} = 83.167 \exp\left(0.1934\, \dot{V}_{max}\right) \tag{I.3}$$

With the maximum volumetric flowrate, $\dot{V}_{max}$, to be in m³/h.

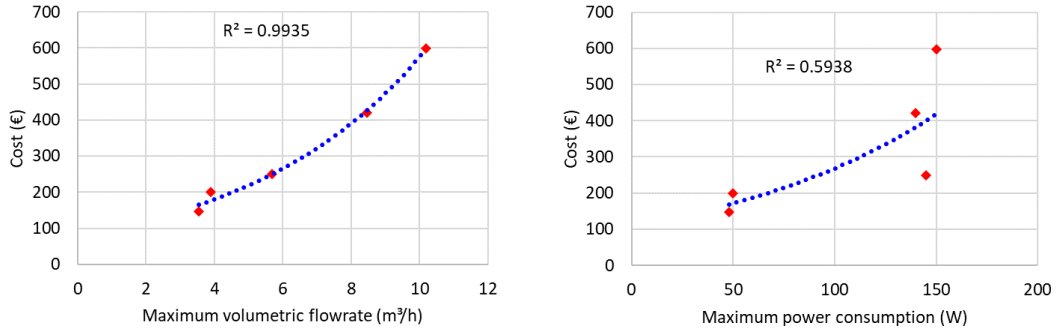

(a) *(b)*

Fig. I.2. Data fitting for the development of cost correlations (blue line) based on retail prices (red dots) for commercially available circulator pumps (a) based on maximum allowable volumetric flowrate and (b) based on maximum power consumption

I.4 Heat transfer fluid

In cases of higher collectors' temperatures (>100 °C), it is common practice to avoid the use of pure water and the corresponding issues of local boiling that may damage irreparably the collectors' pipelines as well as the collectors themselves. Based on the working temperature range of the application, different heat transfer fluids are used. For low temperature applications (<150 °C) an aqueous mixture of a glycol (usually propylene glycol) is used at

concentrations of 5-35%. The use of glycol protects the systems also from freezing, reducing the freezing point well below 0 ^{o}C, e.g., according to the datasheet of Solarliquid VT51 hp [286], which as a 33% v/v glycol content, the freezing point is -30 ^{o}C. In higher temperatures, normally thermal oils or other types of HTFs are used. For the considered applications in this study, two heat transfer fluids were considered: (i) an aqueous mixture of propylene glycol at a 20% v/v glycol content, for the low temperature solar ORC and the solar cooling/heating scenarios, and Therminol VP-1, for the medium temperature solar ORC. The specific costs for the purchase of the aforementioned fluids are listed in Table I.2.

Table I.2. Specific costs for the different HTFs

Type of collectors	**Aqueous mixture of propylene glycol**	**Therminol VP-1 (HTF) [287]**
Specific price (€/lt)	0.49	4.77

I.5 ORC working fluids

In a similar manner to the HTF, specific costs are introduced for the purchase of ORC working fluids. In fact, there are many studies neglecting the working fluid's costs, as having minor contribution to the total capital costs [288]. However, the evaluation of different types of working fluids, therefore with varying purchase costs, dictated the consideration of these costs, as well, towards a more precise estimation of the ORC capital costs. Table I.3 provides the list of the specific costs for the considered working fluids of the dissertation's analyses.

Table I.3. Specific costs for the different ORC working fluids [62, 64]

Working fluid	**Cyclopentane [289]**	**Cyclohexane [290]**	**Isohexane [291]**
Specific price (€/lt)	1.32	2.84	0.85
Working fluid	**Hexane [292]**	**Benzene [293]**	**Toluene [294]**
Specific price (€/lt)	0.82	1.09	0.92
Working fluid	**R134a**	**R245fa**	**R227ea**
Specific price (€/lt)	6.88	25.16	54.97
Working fluid	**R152a**	**R236ea**	**R1234ze(E)**
Specific price (€/lt)	5.47	43.21	13.92

I.6 Plate heat exchangers

With respect to the used heat exchangers, the excessive variation in the types of heat exchangers (shell and tube. Plate, air finned heat exchangers etc.) results in respective large deviations in the cost correlations and therefore is not correct to use a common equation for all types. In terms of the ORC economic analyses, it is common to estimate the purchase costs of a plate heat exchanger via a linear correlation with the heat exchanger's total heat transfer area, as proposed by Quoilin et al. [295]. However, comparing this correlation with retail prices for common commercial series of plate heat exchangers it is shown that there is a considerable under-prediction of the costs, as shown in Fig. I.3. Hence, it is suggested to use a linear correlation per series of plate heat exchangers. For the cases of Alfa Laval's CB60 and CB110 series, the cost correlations used in the study are shown below in equations *(I.4)* and *(I.5)*, respectively.

$$C_{phex-CB60} = 19.055\ N_{pl} + 315.06 \qquad (I.4)$$

$$C_{phex-CB110} = 51.083\ N_{pl} + 783.33 \qquad (I.5)$$

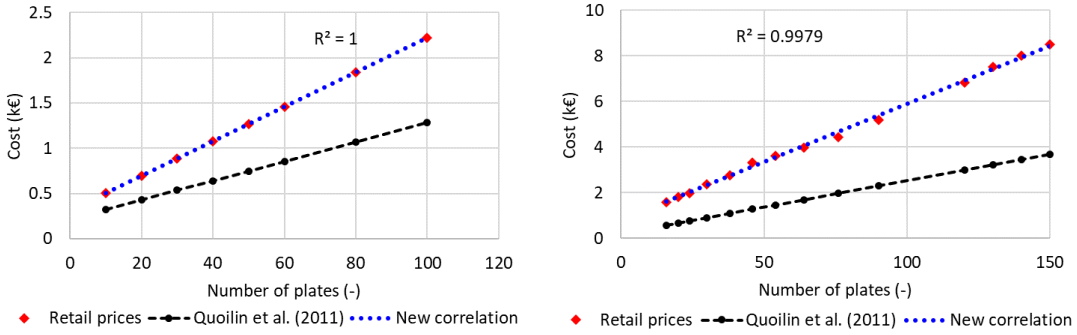

(a) *(b)*

Fig. I.3. Data fitting for commercial model series of plate heat exchangers manufactured by company Alfa Laval. Retail prices derived from [296] and comparison to cost correlation from Quoilin et al. [295] (a) for CB60 series and (b) for CB110 series

Additionally, are presented also the correlations for smaller series of plate heat exchangers CB20 and CB30, for the cases of lower heat duties:

$$C_{phex-CB20} = 11.856\ N_{pl} + 195.21 \qquad (I.6)$$

$$C_{phex-CB30} = 11.452\ N_{pl} + 292.68 \qquad (I.7)$$

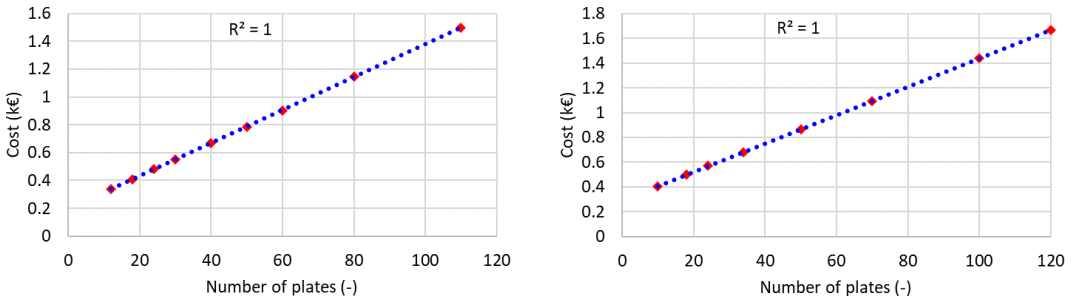

(a) *(b)*

Fig. I.4. Data fitting for commercial model series of plate heat exchangers manufactured by company Alfa Laval. (a) for CB20 series and (b) for CB30 series

I.7 Shell and tube heat exchangers

Shell and tube heat exchangers are the most commonly used heat exchangers thanks to their technological maturity, wide range of pressure and temperature applications and robust design [144]. The cost correlation developed for this type of heat exchangers is based on retail prices for the commercial model series of Bitzer K-type condensers, as shown in Fig. I.5 (a):

$$C_{sthex} = 30.474\ A_{sthex}^3 - 368.45 A_{sthex}^2 + 1{,}697.8 A_{sthex} + 58.54 \qquad (I.8)$$

Equation (I.8) is referring to shell and tube heat exchangers with conventional materials for the shell and the tubes used for freshwater or other non-corrosive fluids' applications For the

case of seawater applications, corrosion resistant materials have to be used and therefore the costs of the heat exchanger increase, based on a correction factor with respect to the heat exchanger's heat transfer area:

$$cf_{sthex} = -0.001\, A_{sthex}^3 + 0.0089 A_{sthex}^2 - 0.0292 A_{sthex} + 1.5434 \qquad (I.9)$$

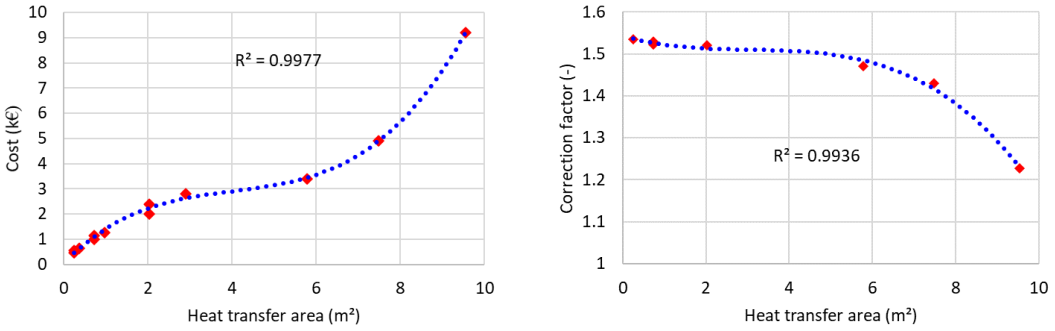

(a) *(b)*

Fig. I.5. Data fitting (a) for the cost of commercial model series of shell and tube heat exchangers for freshwater applications manufactured by company Bitzer and (b) correction factor in cases of seawater applications

I.8 Air-cooled heat exchangers / Dry coolers

Air-cooled finned tube heat exchangers are commonly used as heat rejection units in VCC systems, while they can be used as well for the same purpose in sorption machines, in order to reject the heat of the exothermic ab-/adsorption process. Given the low heat transfer coefficient of air, one or more fans are integrated in their structure in order to improve the heat transfer via forced circulation of the air. Therefore, it is common to express the cost of these heat exchangers as a function of either the heat transfer area or the fans' power. In fact, for the case of the model series of air-cooled finned tube heat exchangers Frigoplast CFR, there is a strong correlation between the cost of the heat exchanger and the fans power, as shown in Fig. I.6, yielding an R^2 equal to 0.9909 for a second order polynomial, listed below:

$$C_{ahex} = -0.4685 \left(\frac{\dot{W}_{el,fan}}{1000}\right)^2 + 0.12344\, \dot{W}_{el,fan} - 25.656 \qquad (I.10)$$

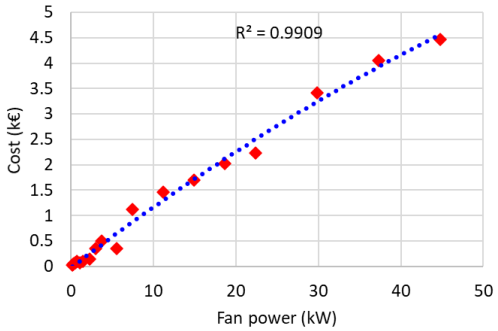

Fig. I.6. Data fitting for the cost of commercial model series of air-cooled finned tube heat exchangers

I.9 Expander/compressor

Within this dissertation, two types of volumetric expanders/compressor were considered: screw and scroll types. With respect to the scroll expanders/compressors, quotes from local suppliers were collected for commercial model series ZR manufactured by Copeland. Based on the collected data, a second order polynomial correlation is extracted as a function of the machine's swept volume, which is presented below:

$$C_{scroll} = -0.0084 V_{sw,scroll}^2 + 21.857\, V_{sw,scroll} - 180.43 \qquad (I.11)$$

With the swept wolume of the compressor/expander, $V_{sw,scroll}$, to be in cc/rev, as also shown in Fig. I.7.

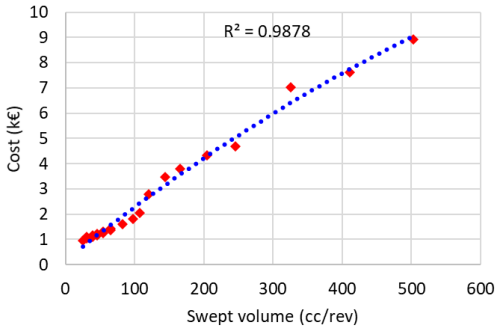

Fig. I.7. Data fitting for the cost of commercial model series of scroll expanders/compressors

Screw expanders are used in larger power capacities than the scroll compressors (>10 kWe) and tend to have considerably higher prices. Due to lack of price quotes for the construction of a fitting correlation, for the cases that screw expanders were investigated, a correlation used in relevant literature was adopted, as proposed by Astolfi [297]. The correlation was referring to USD2013 and therefore inflation between 2013 and 2021 was taken into account:

$$C_{screw} = 205{,}988\, V_{sw,screw} + 2{,}977 \qquad (I.12)$$

With the swept wolume of the compressor/expander, $V_{sw,screw}$, to be in cc/rev.

I.10 ORC Pump

The ORC pump is one of the ORC components with considerable purchase costs and, in particular for smaller scales, there is only a limited range of commercially available models. Therefore, no sufficient number of quotes could be collected for the development of a dedicated cost correlation. As a consequence, a commonly used correlation proposed by Lecompte et al. [298] was adopted. As the proposed equation was in EUR2013, inflation has been taken into consideration, modifying accordingly the equation's constant:

$$C_p = 954.7 \left(\frac{\dot{W}_{mech,p}}{300}\right)^{0.25} \qquad (I.13)$$

I.11 Motor/Generator

Motors and generators are used in the ORC for the driving of the pump and the power generation in coupling with the expanders, respectively. Cost data was derived based on quotes from local suppliers for model series of four-pole three-phase motors and a dedicated linear correlation with the motor's nominal power was derived. In Fig. I.8 is presented to collected cost data in comparison to the proposed correlation:

$$C_{motor} = 0.0586\, \dot{W}_{el,motor} + 80.563 \qquad (I.14)$$

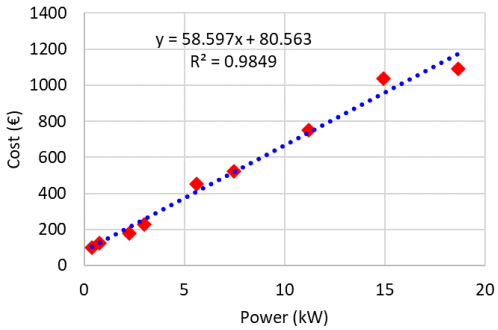

Fig. I.8. Data fitting for the cost of commercial model series of three phase 4-pole motors

I.12 Liquid receiver

Liquid receiver tanks are also necessary components in an ORC setup both to serve as an expansion tank as well as ensuring, along with the use of subcooler, that the inlet stream of the pump is droplet free and avoid cavitation issues. The cost data was derived from a cost datasheet by manufacturing company Zilmet [299] and is presented in Fig. I.9. A linear correlation was constructed by the cost data with respect to the receiver's capacity, as shown below:

$$C_{rt} = 4{,}701.1\, V_{rt} + 157.99 \qquad (I.15)$$

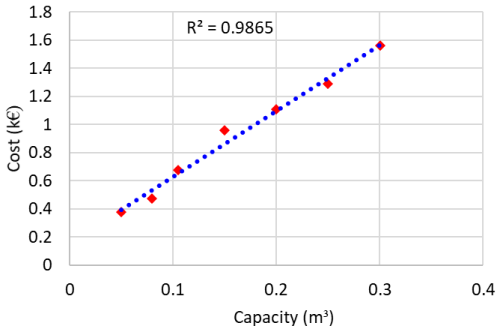

Fig. I.9. Data fitting for the cost of commercial model series of liquid receiver tanks

I.13 Conventional (electric) heat pump

In the cases that a conventional (electric) heat pump is investigated, a dedicated cost function is considered based on cost data collected by quotes from local suppliers. For a uniform profile, costs data was based on commercial model series EHBX from manufacturing company Daikin. A second order cost correlation was derived, with respect to the cooling capacity, as shown below:

$$C_{HP} = 2.5233 \cdot 10^{-6}\, \dot{Q}_{HP}^{2} + 0.18783\, \dot{Q}_{HP} + 2{,}903 \qquad (I.16)$$

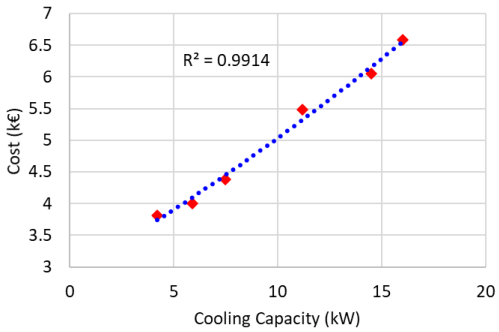

Fig. I.10. Data fitting for the cost of commercial model series of electric heat pumps

I.14 Absorption heat pumps

Absorption heat pumps market is expanding significantly over the last years, resulting in respective decreases in the purchase costs for small and medium scale units. Due to the still limited market in Greece, there were only two quotes for absorption heat pumps units collected. Therefore, the derived cost correlation was based on a combination of the aforementioned quotes and cost data from recent literature, as shown in Fig. I.11. The developed correlation is estimating the specific cost of an absorption heat pump per kW of cooling capacity as a function of the cooling capacity, given also in kW, similarly to the case of electric heat pumps, however, in this case a power type data fitting was used:

$$C_{abs-HP} = 3596.2\, \dot{Q}_{abs-HP}^{-0.415} \qquad (I.17)$$

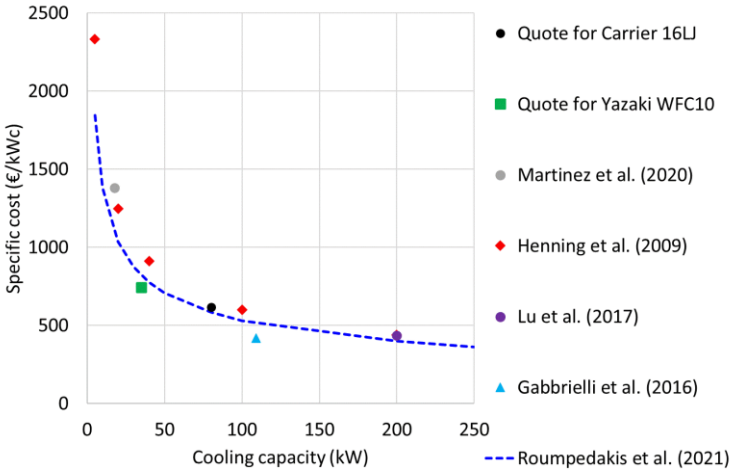

Fig. I.11. Data fitting for the cost of absorption heat pumps [300-303]

I.15 Adsorption heat pumps

Cost data is also limited for the case of adsorption hat pumps, resulting in large deviations in the dedicated economic analyses in literature [67, 304]. In the case of adsorption chillers, cost data from a manufacturer was used, considering a 2075 €/kW.

I.16 Photovoltaic modules

Due to the rapid expansion of the PV market, their purchase costs are steadily decreasing over the last decade. According to Jäger-Waldau [305], the specific costs for the purchase of PV modules was at 1300 €/kWp excluding VAT, including, on the other hand, installation and auxiliary equipment. Recent data (January 2021) from the local Greek market, reveals a further increase in the total purchase costs (including all equipment and installation), with a specific cost of 7,610 € for a 6.1 kWp system, corresponding to 1,247.5 €/kWp including VAT, a value which was adopted in the dissertation's analyses.

I.17 Fan coils

In the cases of replacing a conventional cooling/heating system with either an electric heat pump or a sorption heat pump, apart from the main costs for the acquisition of the heat pump itself, a number of fan coils have to be installed as the terminal units of cooling/heating system, which have a considerable cost. Quotes for the fan coils were collected, in January 2021, from a local supplier for the model series SL from the manufacturer Olympia Splendid. The best fitting for the cost estimation was achieved with a second order polynomial of the fan coils maximum cooling capacity, as shown in Fig. I.12.

$$C_{fancoil} = 2.2956 \cdot 10^{-5}\ \dot{Q}_{fancoil}^{2} - 0.014665\ \dot{Q}_{fancoil} + 448.43 \qquad (I.18)$$

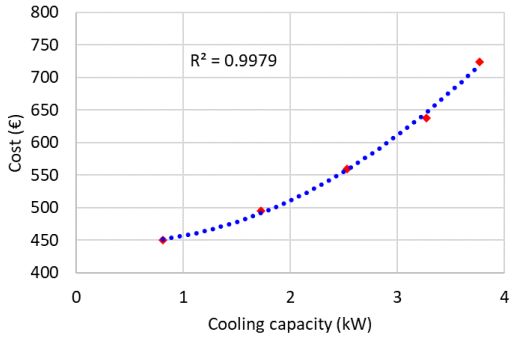

Fig. I.12. Data fitting for the cost of commercial model series of fan coils

I.18 Miscellaneous equipment and installation

Additionally to the aforementioned equipment, installation and miscellaneous equipment (piping, valves etc.) has a considerable share of the total costs for the development of solar driven systems. Therefore, in agreement to many relevant studies, installation is considered to sum up for 20% of the total capital costs [134]. Moreover, for the case of the ORC, additional hardware equipment is considered for the monitoring and control of the system. According to Quoilin et al. [134], a 800 € was considered. However, experience from a prototype ORC [156] led to the conclusion that such a value is rather optimistic and even in more standardized cases of small scale ORC systems, a budget of approximately 2,500 €, should be allocated for such equipment.

Appendix II. Complementary data on conducted studies

II.1 Pareto fronts from GA in low temperature ORCs

Owing to the large number of tested cases in the multi-objective GAs applied and presented in section 4.1, it was selected to include in the main discussion of the results concentrated figures with the optimal scenarios per case. Hereby are presented the detailed Pareto fronts for all tested cities.

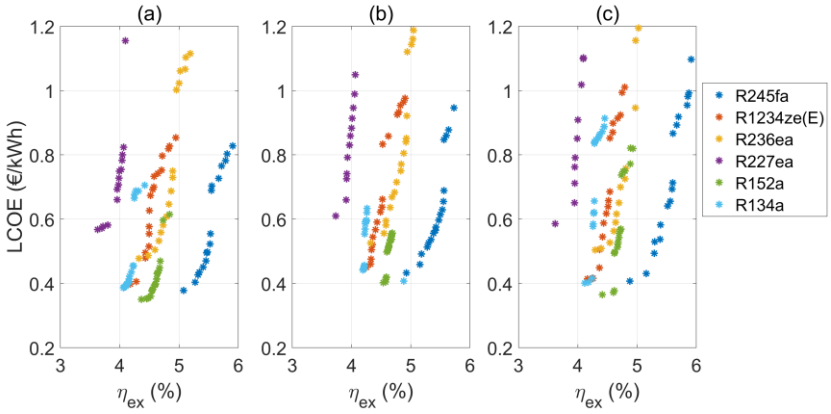

Fig. II.1. Pareto fronts for the considered working fluids in Zone A (Chania) using (a) FPCs, (b) ETCs and (c) PTCs.

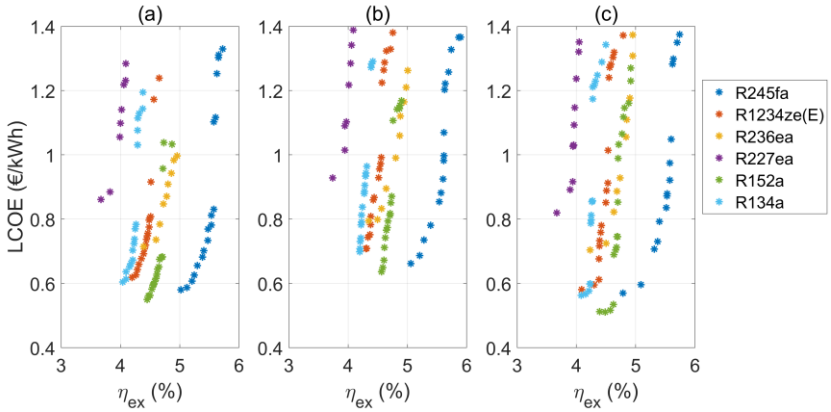

Fig. II.2. Pareto fronts for the considered working fluids in Zone C (Thessaloniki) using (a) FPCs, (b) ETCs and (c) PTCs.

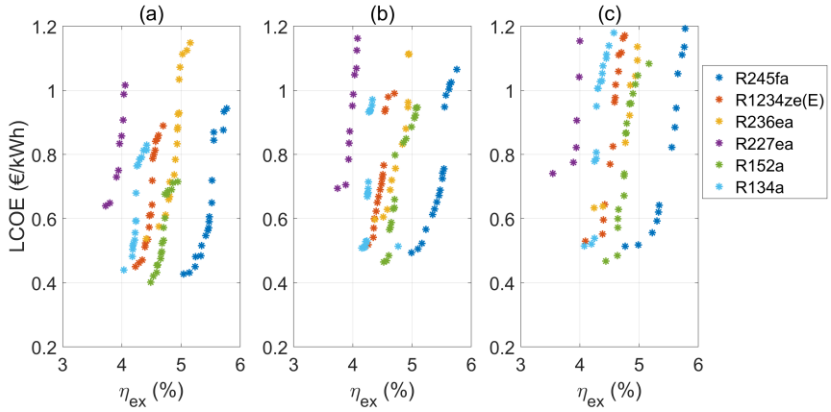

Fig. II.3. Pareto fronts for the considered working fluids in Zone D (Kozani) using (a) FPCs, (b) ETCs and (c) PTCs.

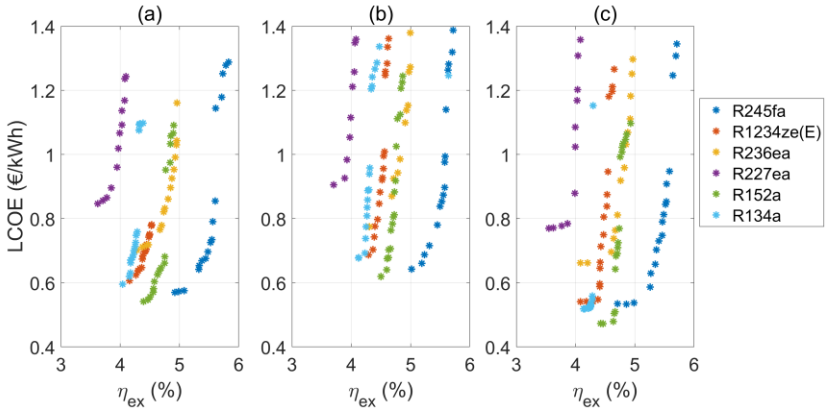

Fig. II.4. Pareto fronts for the considered working fluids in Madrid using (a) FPCs, (b) ETCs and (c) PTCs.

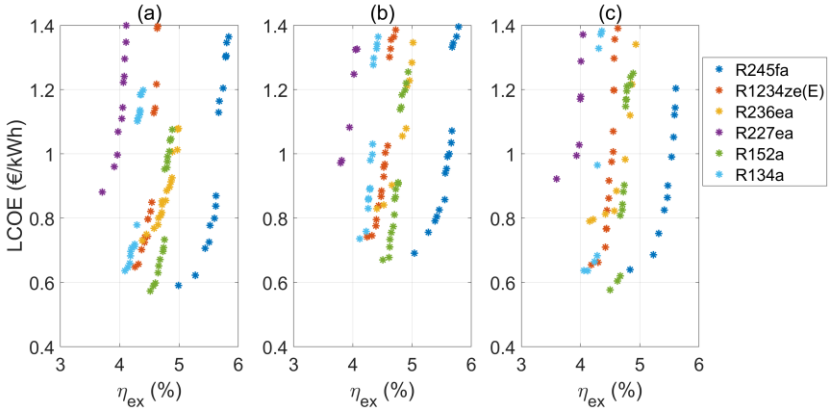

Fig. II.5. Pareto fronts for the considered working fluids in Rome using (a) FPCs, (b) ETCs and (c) PTCs.

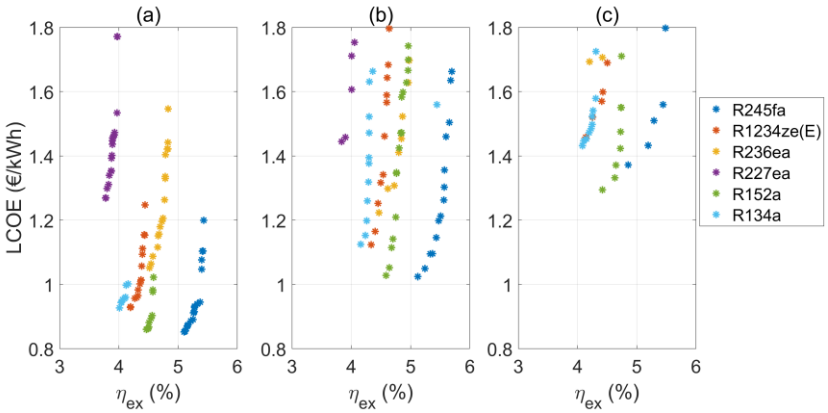

Fig. II.6. Pareto fronts for the considered working fluids in Brussels using (a) FPCs, (b) ETCs and (c) PTCs.

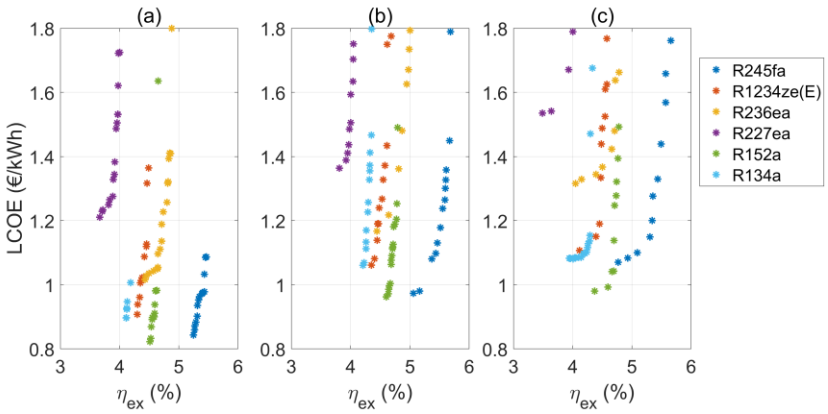

Fig. II.7. Pareto fronts for the considered working fluids in Berlin using (a) FPCs, (b) ETCs and (c) PTCs.

II.2 Medium temperature ORC modelling strategies

The implementation of the solar subsystem model is based on the independent operation of the collectors' loop and the intermediate heat transfer loop, both of which are coupled or decoupled from the total system depending on the prevailing conditions, as shown below in the flow chart. Consequently, it needs to be ensured that for every hourly point the sum of the total accumulated heat by the collectors, up to this moment, is greater than the corresponding sum of the total heat absorbed by the ORC system.

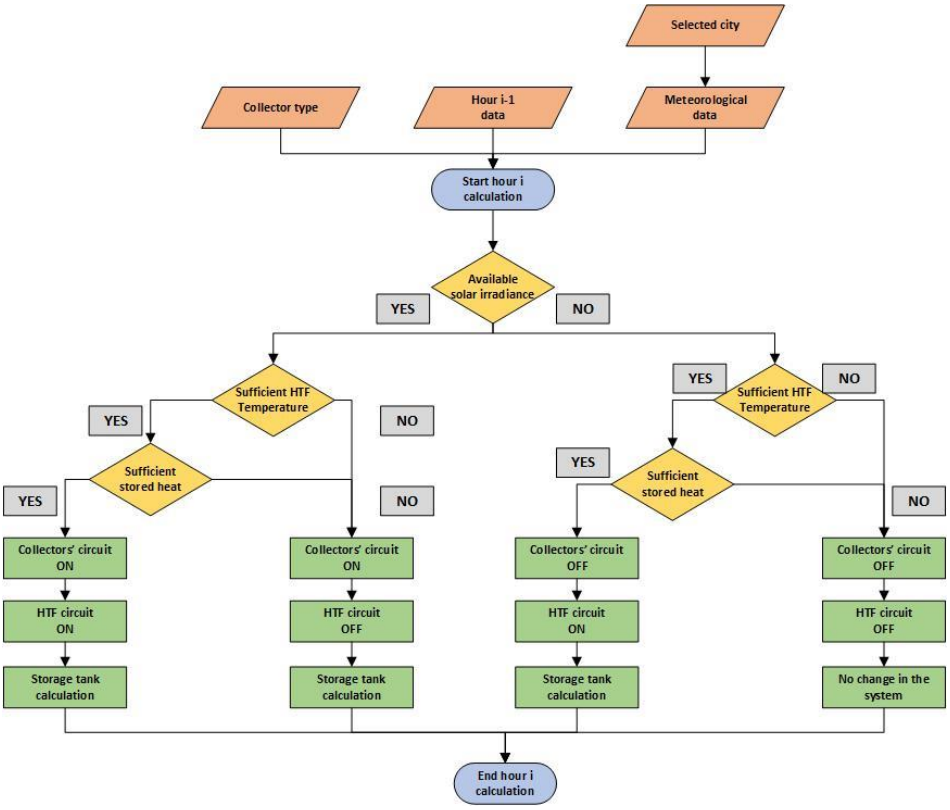

Fig. II.8. Flowchart of the solar subsystem modelling procedure

In Fig. II.9 is illustrated the on-design procedure for the ORC circuit which leads to the final sizing of its components. In this process for dry working fluids, the evaporation and condensing temperatures are defined from the HTF and cooling water streams along with the

selected pinch points. However, in case of wet working fluids, is estimated the minimum value of superheating that leads to a single-phase state at the expander's out-put.

With respect to the off-design modeling of the ORC, for each temperature step are calculated the evaporation and condensation pressure of the ORC by applying a 5 K and 10 K pinch point in the evaporator and condenser respectively. Concerning the integration of the expanders, three scenarios are discerned. For pressure ratios lower than the maxi-mum value, a single expander is utilized; for higher values of pressure ratio two expanders are functioning together with the same pressure ratio. At the same time their rotational speeds are regulated in order to achieve their gradual insertion to the system until they reach the maximum power load.

Based on the data deriving from the aforementioned analysis, the solar and the ORC sub-systems can be coupled in order to model the operation of the overall system for each hour step within an annual period. As shown in Fig. II.10, for a given temperature and solar data, the solar loop is activated and is operating in case there is available direct solar irradiance. The collectors absorb heat and transfer it gradually to the storage tank. In case of absence of solar irradiance, the collectors are decoupled from the storage system, to minimize the heat losses. Regarding the ORC sub-system, its function depends on the temperature of the tank's top zone, as well as on the availability of stored heat. With temperature higher than T_{thr} and sufficient stored heat, the HTF flows towards the evaporator heating up the working fluid. Depending on the driving temperature, a polynomial fitting on the off-design data is performed and derive the cycle's output parameters. In other case, the ORC loop is deactivated with no heat transferred to the evaporator.

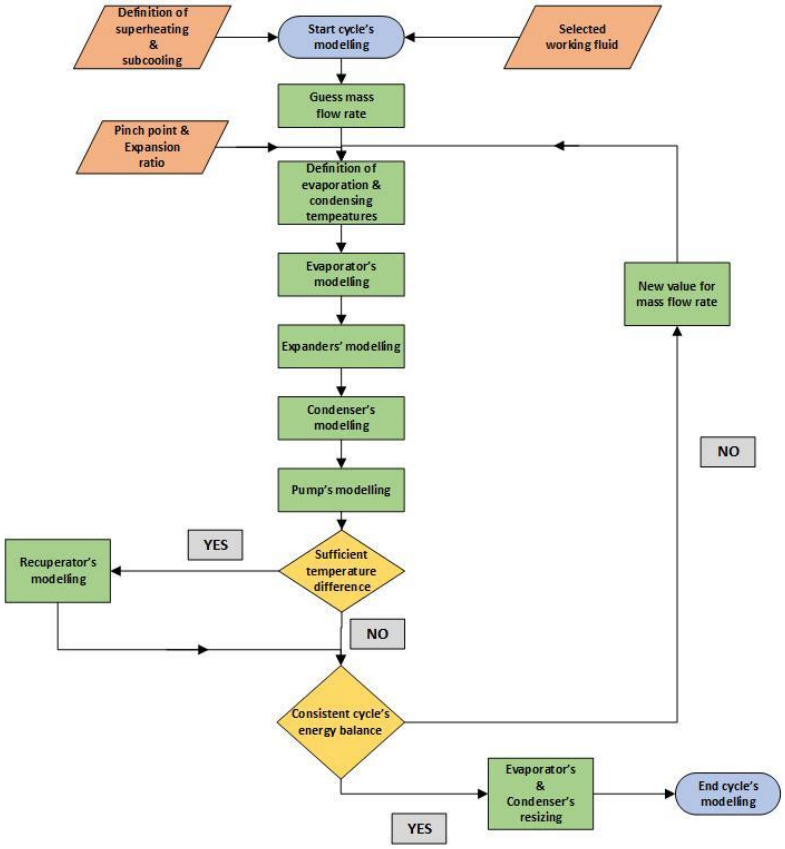

Fig. II.9. Flowchart of the ORC on-design modelling procedure

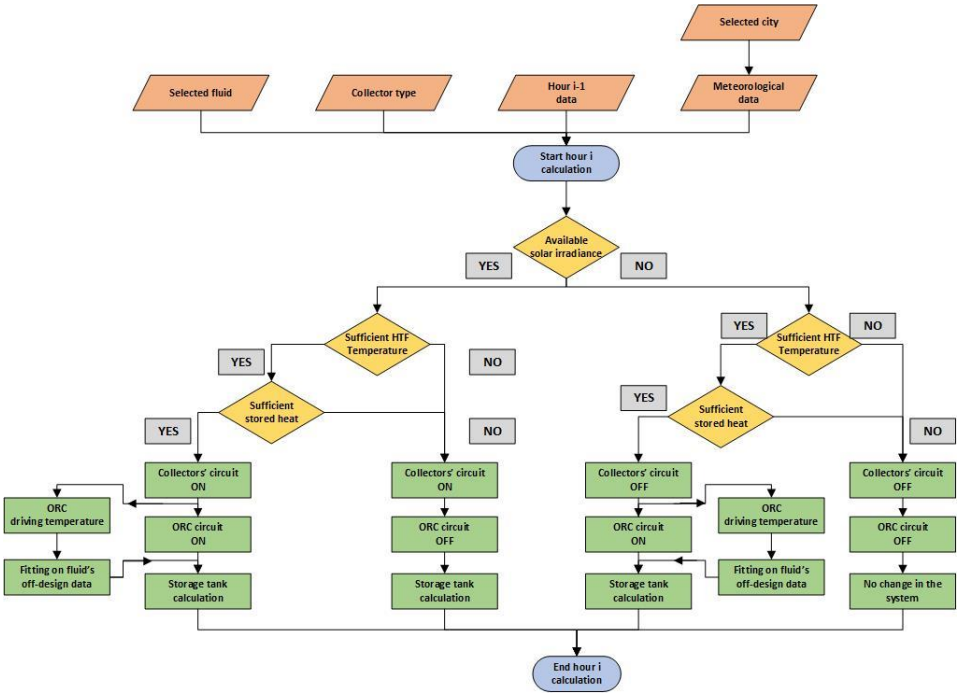

Fig. II.10. Flowchart of the overall system off-design modelling procedure

II.3 Solar cooling/heating study: complementary data

Hereby are listed the additional plots for the solar cooling/heating study, section 4.3, for Zones A, C and D.

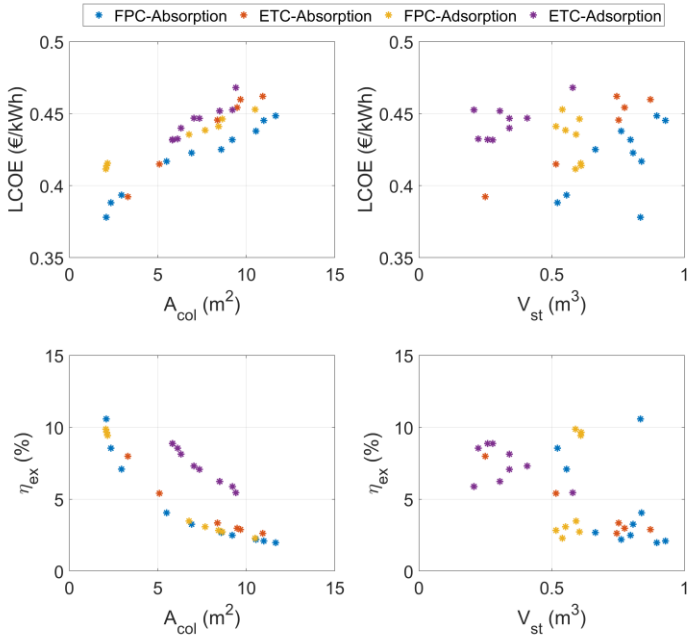

Fig. II.11. Optimization parameters with respect to input variables for all the considered scenarios in Chania.

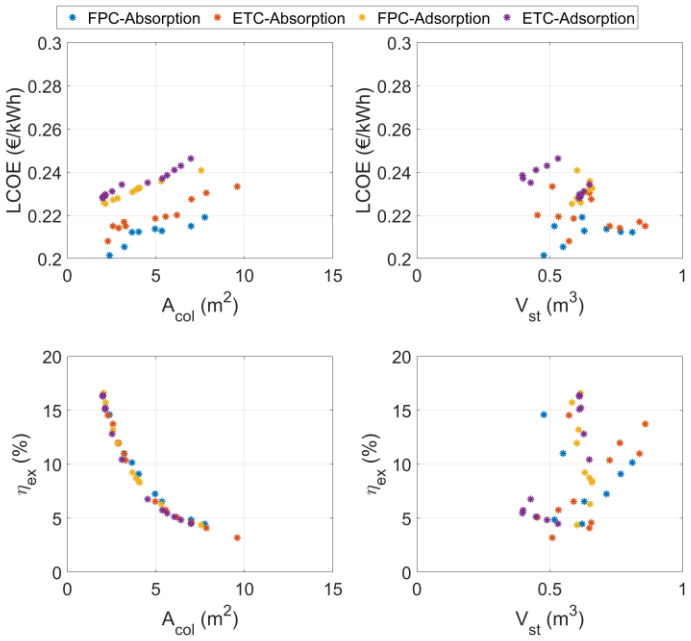

Fig. II.12. Optimization parameters with respect to input variables for all the considered scenarios in Thessaloniki.

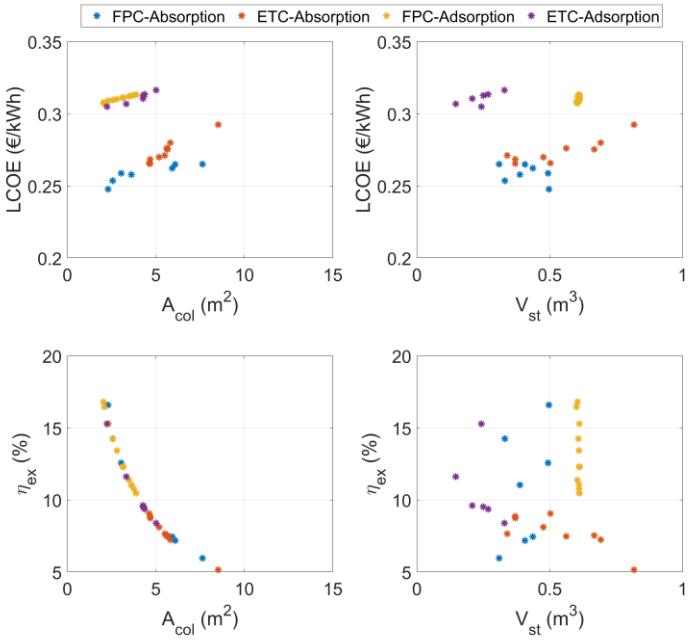

Fig. II.13. Optimization parameters with respect to input variables for all the considered scenarios in Kozani.

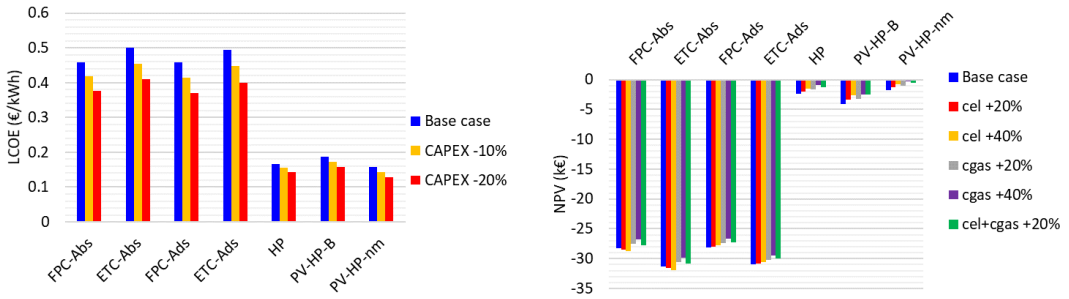

(a) *(b)*

Fig. II.14. Results of the sensitivity analyses: (a) influence of the reduction in the CAPEX on the LCOE and (b) influence of the electricity and gas prices on the NPV for the case of Chania (Zone A)

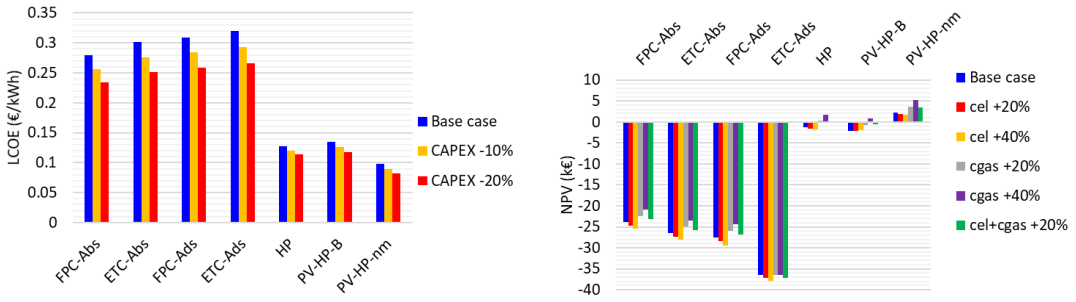

(a) *(b)*

Fig. II.15. Results of the sensitivity analyses: (a) influence of the reduction in the CAPEX on the LCOE and (b) influence of the electricity and gas prices on the NPV for the case of Thessaloniki (Zone C)

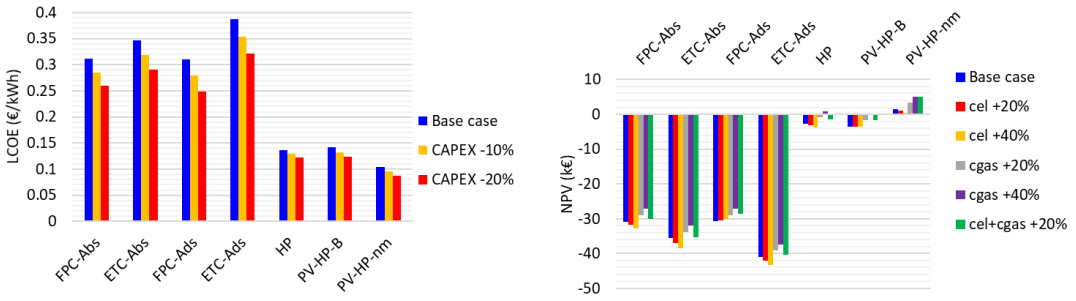

(a) *(b)*

Fig. II.16. Results of the sensitivity analyses: (a) influence of the reduction in the CAPEX on the LCOE and (b) influence of the electricity and gas prices on the NPV for the case of Kozani (Zone D)

II.4 Complementary data of trigeneration GA

Below are presented the additional figures for the techno-economic optimization of the trigeneration system, discussed in section 5.2, for climatic zones A, C and D.

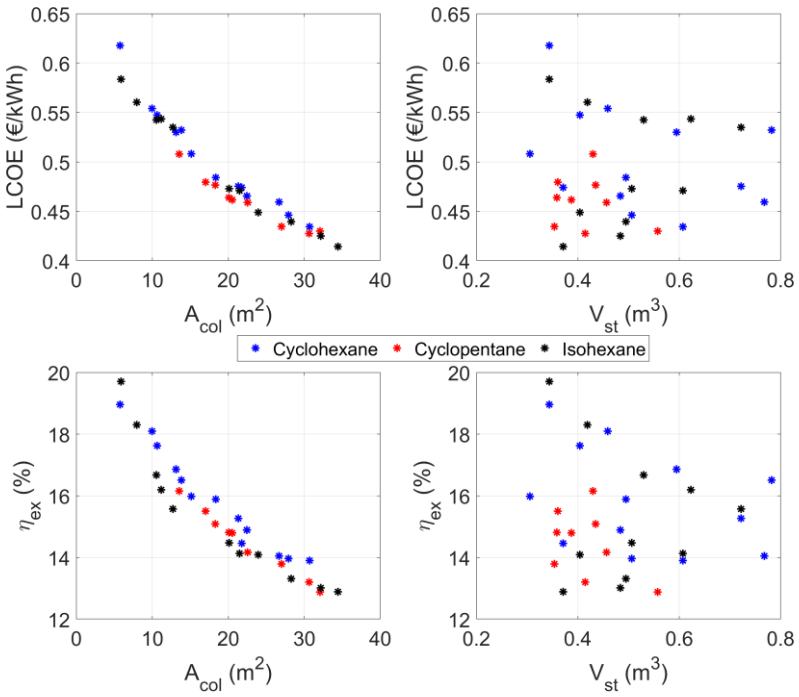

Fig. II.17. Optimization parameters with respect to input variables for all the considered scenarios in Chania.

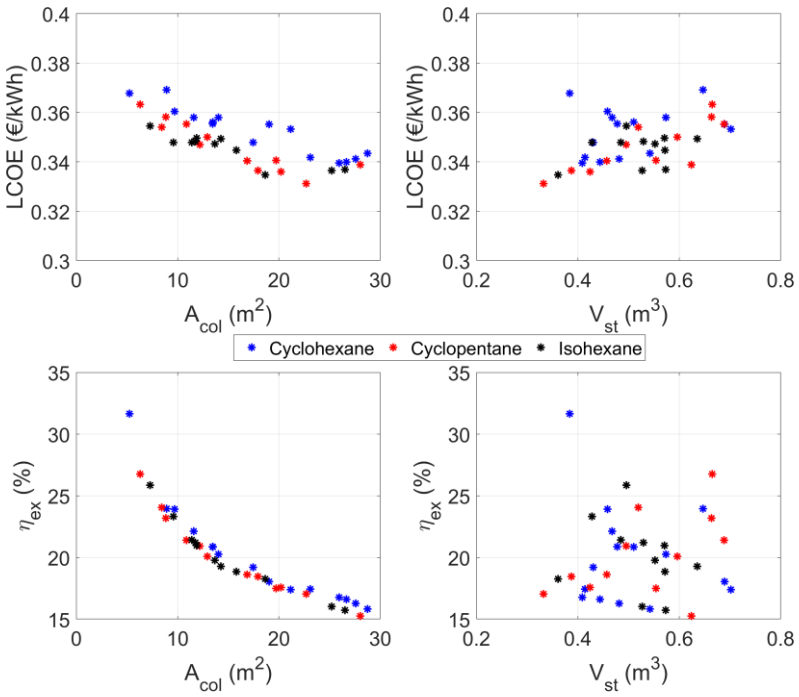

Fig. II.18. Optimization parameters with respect to input variables for all the considered scenarios in Thessaloniki.

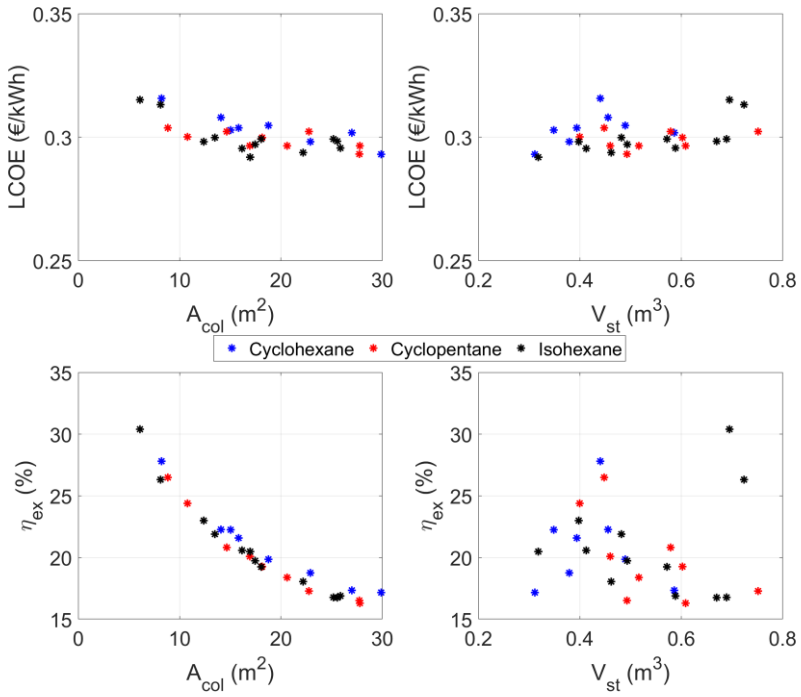

Fig. II.19. Optimization parameters with respect to input variables for all the considered scenarios in Kozani.

Appendix III. Adsorption chiller modelling

Hereby are presented the key features of the adsorption chiller model used in the design studies of Chapter 5. The contents of this section were published in the study "Integrated ORC-Adsorption cycle: A first and second law analysis of potential configurations" [178].

An overview of the general concept of the developed system's operation in Simulink is provided in Fig. III.1.

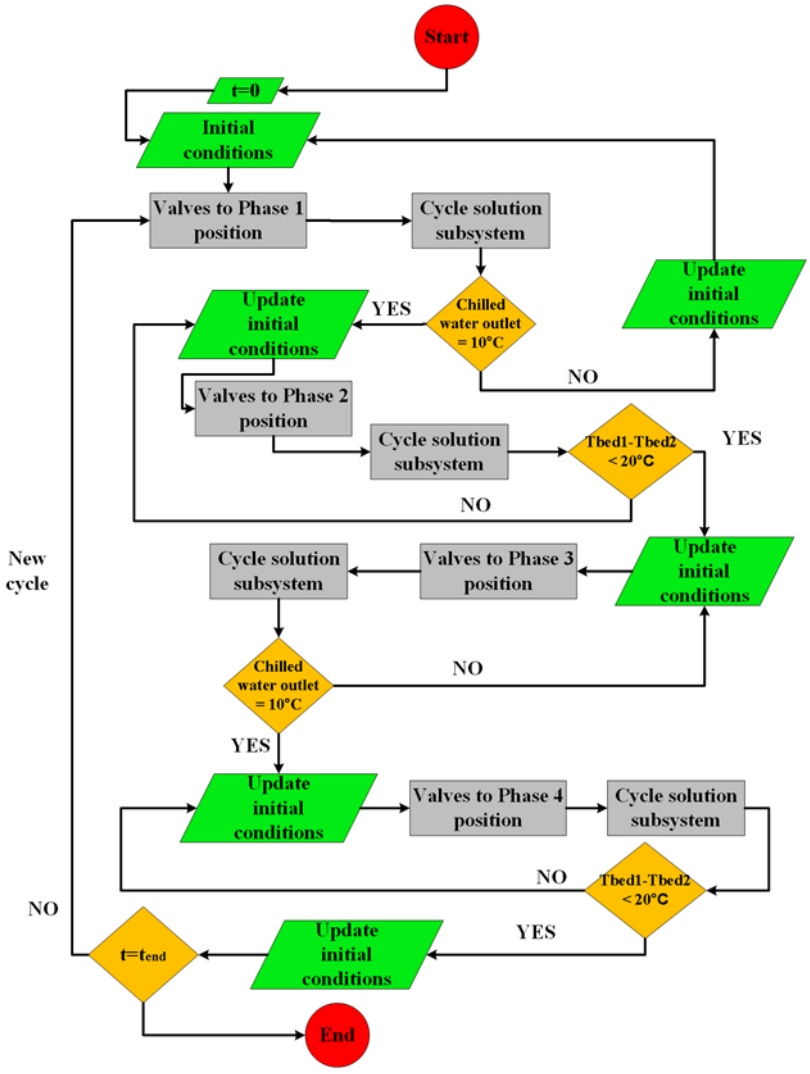

Fig. III.1. Flowchart of the overall system off-design modelling procedure

The equilibrium uptake of water-zeolite working pair will be estimated using the Dubinin-Astakhov model [306, 307]:

$$\frac{x^*}{x_o} = exp\left\{-\left[\frac{R \cdot T}{E_a} ln\left(\frac{p_s}{p_w}\right)\right]^n\right\} \qquad (III.1)$$

For the investigated working pair, the activation energy, E_a, was considered equal to 1192.3 kJ/kg [308], the limiting adsorbate uptake, x_o, was equal to 0.21 kg/kg, while the heterogeneity constant, n, is equal to 5 [306]. The adsorption rate was calculated using the linear driving force (LDF) model [309-311]:

$$\frac{dx}{dt} = \frac{15 \cdot D_{so}\, exp\left(-\frac{E_a}{R \cdot T}\right)}{R_p^2}(x^* - x) \qquad (III.2)$$

The mean pore radius, R_p, was considered equal to 50 nm, while the pre-exponential coefficient D_{so} was considered as one of the values to be calibrated based on the experimental results [312]. For each component of the adsorption chiller (evaporator, adsorber, desorber and condenser) an overall energy balance was applied. The detailed solved system is presented below in section III.1. Regarding the performance parameters of the adsorption chiller, the COP and the exergy efficiency, η_{ex}, were calculated based on the definitions of eq. (2.28)-(2.31).

With respect to the adsorption isotherm model the considered correlation and the involved constants, has been validated against experimental data for the water uptake provided by S. Kayal et al. [306]. As shown in Fig. III.2, the predictions of the considered equation (4) are within a 5% error compared to the experimental data. The slight under-prediction is mainly justified by the difference in the considered activation energy, which on the other hand allowed for more reasonable cycle times.

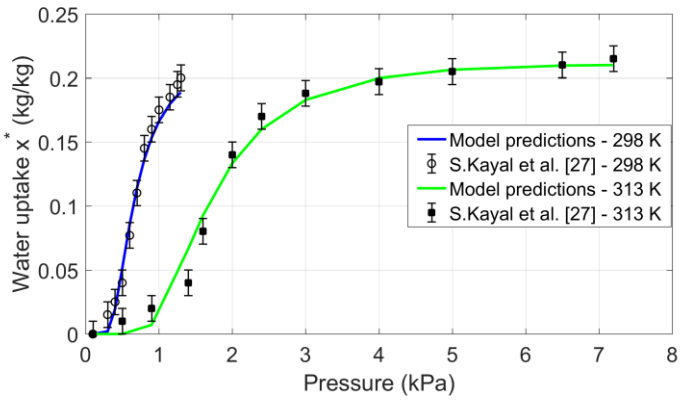

Fig. III.2. Model validation against experimental data for the water uptake published by S. Kayal et al. [306]

Fig. III.3 gives an overview of the model's predictions in terms of the secondary stream's temperatures during on-design operation of the adsorption chiller. Note that considering a constant temperature of the cooling fluid of the secondary stream of the adsorption chiller ($T_{MT,i}$) is not a fully realistic assumption, since this temperature exhibits a daily and seasonal variability. However, as stated in the assumption of a variable re-cooling temperature would necessitate carrying out off-design and transient simulations of the system which is beyond the scope of the present study. For this reason, the authors considered a fixed re-cooling temperature which is nonetheless representative of the climate conditions in Greece and thus ensures that there are no critical deviations between the calculated values and the actual behavior of the examined systems under the specified conditions.

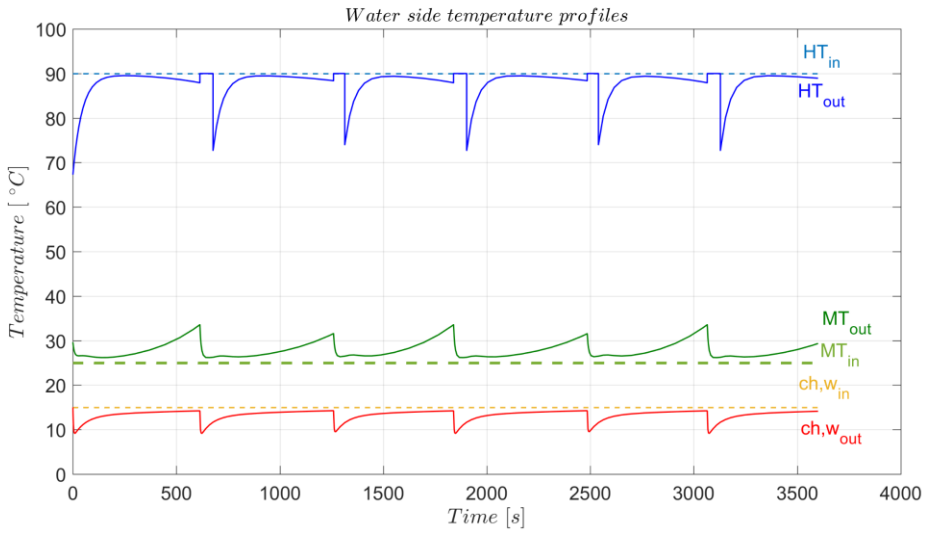

Fig. III.3. Overview of the secondary streams temperatures of the adsorption chiller based on the predictions of the developed model

III.1 Adsorption chiller components modelling

III.1.1 Evaporator

The overall energy balance on the evaporator is defined as follows:

$$\frac{dT_{evap}}{dt}\left(M_{cu,e}c_{p,cu} + M_{refr}c_{p,refr}\right) = -\left[h_{fg} + h_{refr}\left(p_{evap}, T_{ads}\right) - h_{refr}\left(T_{evap}\right)\right]M_{ze}\frac{dx_{ads}}{dt} + \dot{Q}_{ch,w} \quad (III.3)$$

Where $\dot{Q}_{ch,w}$ refers to the heat flux towards the chilled water circuit, which is equal to:

$$\dot{Q}_{ch,w} = \dot{m}_{ch,w}c_{p,ch,w}\left(T_{ch,w,i} - T_{ch,w,o}\right) \quad (III.4)$$

Regarding the chiller water temperature at the outlet, it is calculated using the logarithmic mean temperature difference (LMTD) method, as shown in below [114, 313]:

$$T_{ch,w,o} = T_{evap} + \left(T_{ch,w,i} - T_{evap}\right) exp\left[-\frac{(UA)_{evap}}{\dot{m}_{ch,w}c_{p,ch,w}}\right] \quad (III.5)$$

III.1.2 Adsorber

Under the assumption of same temperature for the refrigerant, the walls of the bed and the adsorbent, the energy balance in the adsorber is the following expression [314-317]:

$$\frac{dT_{ads}}{dt}\left(M_{cu,ads}c_{p,cu} + M_{ze}c_{p,ze} + M_{ze}c_{p,refr}\frac{dx_{ads}}{dt}\right) = \left[Q_{st} + h_{refr}\left(p_{evap}, T_{ads}\right) - h_{refr}\left(T_{evap}\right)\right]M_{ze}\frac{dx_{ads}}{dt} + \dot{m}_{MT1,w}c_{p,MT1,w}\left(T_{MT1,w,i} - T_{MT1,w,o}\right) \quad (III.6)$$

The isosteric heat of adsorption, Q_{st}, it is considered equal to $4.5 \cdot 10^5$ J/kg . Regarding the MT1 water temperature at the outlet, it is calculated using the logarithmic mean temperature difference (LMTD) method, as shown in below [114, 313]:

$$T_{MT1,w,o} = T_{ads} + \left(T_{MT1,w,i} - T_{ads}\right) exp\left[-\frac{(UA)_{ads}}{\dot{m}_{MT1,w} c_{p,MT1,w}}\right] \quad (III.7)$$

III.1.3 Desorber

The equations for the desorption are equivalent with those of the adsorption, with the difference that the balance in the desorber is determined by the condenser [314-317]:

$$\frac{dT_{des}}{dt}\left(M_{cu,des} c_{p,cu} + M_{ze} C_{p,ze} + M_{ze} c_{p,refr} \frac{dx_{des}}{dt}\right) = \left[Q_{st} + h_{refr}(p_{cond}, T_{des}) - h_{refr}(T_{cond})\right] M_{ze} \frac{dx_{des}}{dt} + \dot{m}_{HT,w} c_{p,HT,w}\left(T_{HT,w,i} - T_{HT,w,o}\right) \quad (III.8)$$

Regarding the HT water temperature at the outlet, it is calculated using the logarithmic mean temperature difference (LMTD) method, as shown in below [114, 313]:

$$T_{HT,w,o} = T_{des} + \left(T_{HT,w,i} - T_{des}\right) exp\left[-\frac{(UA)_{des}}{\dot{m}_{HT,w} c_{p,HT,w}}\right] \quad (III.9)$$

III.1.4 Condenser

The energy balance in the condenser shows that the balance is dominated mainly by the heat interaction between the desorber and the condenser and the heat interaction inside the condenser between the medium temperature (MT2) water, the heat exchanger walls and the refrigerant. The overall energy balance equation is expressed by the following differential equation [311, 314, 318]:

$$\frac{dT_{cond}}{dt}\left(M_{cu,c} c_{p,cu} + M_{refr} c_{p,refr}\right) = -\left[h_{fg} + h_{refr}(p_{cond}, T_{des}) - h_{refr}(T_{cond})\right] M_{ze} \frac{dx_{des}}{dt} + \dot{Q}_{MT2,w} \quad (III.10)$$

Where $\dot{Q}_{MT2,w}$ refers to the heat flux towards the MT2 water circuit, which is equal to:

$$\dot{Q}_{MT2,w} = \dot{m}_{MT2,w} c_{p,MT2,w}\left(T_{MT2,w,i} - T_{MT2,w,o}\right) \quad (III.11)$$

Regarding the MT2 water temperature at the outlet, it is calculated using the logarithmic mean temperature difference (LMTD) method, as shown in below [114, 313]:

$$T_{MT2,w,out} = T_{cond} + \left(T_{MT2,w,i} - T_{cond}\right) exp\left[-\frac{(UA)_c}{\dot{m}_{MT2,w} c_{p,MT2,w}}\right] \quad (III.12)$$

Concerning the heat capacities of the wall material, $c_{p,cu}$, and the zeolite, $c_{p,ze}$, these are taken equal to 510 J/kgK and 880 J/kgK, respectively.

Appendix IV. Complementary data of LCA studies

IV.1 Use phase consumption data for residential LCA

Below is presented an overview of the annual use phase consumptions calculated per system and implemented in the Simapro software for the analysis of section 6.3.

Table IV.1. Results for the thermal loads of the reference building per zone in Greece

Climatic zone	Zone A	Zone B	Zone C	Zone D
Annual heating demand (kWh/year)	3944.5	5864.7	8036.2	9481.9
Annual electricity demand for heating (kWhel/year)	39.0	57.9	65.5	77.3
Annual natural gas consumption (Nm^3/year)	383.1	569.5	780.4	920.8
Annual cooling demand (kWh/year)	2084.1	2216.2	1587.2	1181.8
Annual electricity demand for cooling (kWhel/year)	833.7	886.5	634.9	472.7

Table IV.2. Results for the air-water heat pump use phase consumption per zone in Greece

Climatic zone	Zone A	Zone B	Zone C	Zone D
Annual electricity demand for heating (kWhel/year)	1057.5	1629.7	2434.7	3080.5
Annual electricity demand for cooling (kWhel/year)	484.8	615.8	428.7	296.2
Total annual electricity demand (kWhel/year)	1542.3	2245.5	2863.4	3376.7

Table IV.3. Results for the ZEOSOL use phase consumption per zone in Greece

Climatic zone	Zone A	Zone B	Zone C	Zone D
Annual electricity demand for heating (kWhel/year)	673.2	1044.55	1636.72	2349.1
Annual electricity demand for cooling (kWhel/year)	298.7	359.88	251.64	177.9
Total annual electricity demand (kWhel/year)	971.9	1404.43	1888.36	2527

Table IV.4. Results for the solar absorption unit use phase consumption per zone in Greece

Climatic zone	Zone A	Zone B	Zone C	Zone D
Annual electricity demand for heating (kWhel/year)	787.58	1238.67	1926.7	2589.3
Annual electricity demand for cooling (kWhel/year)	292.2	325.72	228.7	167.2
Total annual electricity demand (kWhel/year)	1079.78	1564.39	2155.4	2756.5

Table IV.5. Results for the solar absorption unit use phase consumption per zone in Greece

Climatic zone	Zone A	Zone B	Zone C	Zone D
Total annual electricity demand (kWhel/year)	1079.78	1564.39	2155.4	2756.5

IV.2 Complementary data of residential LCA

Below are listed the comparative impact assessment results of the residential cooling/heating systems, presented in section 6.3, for climatic zones A, C and D.

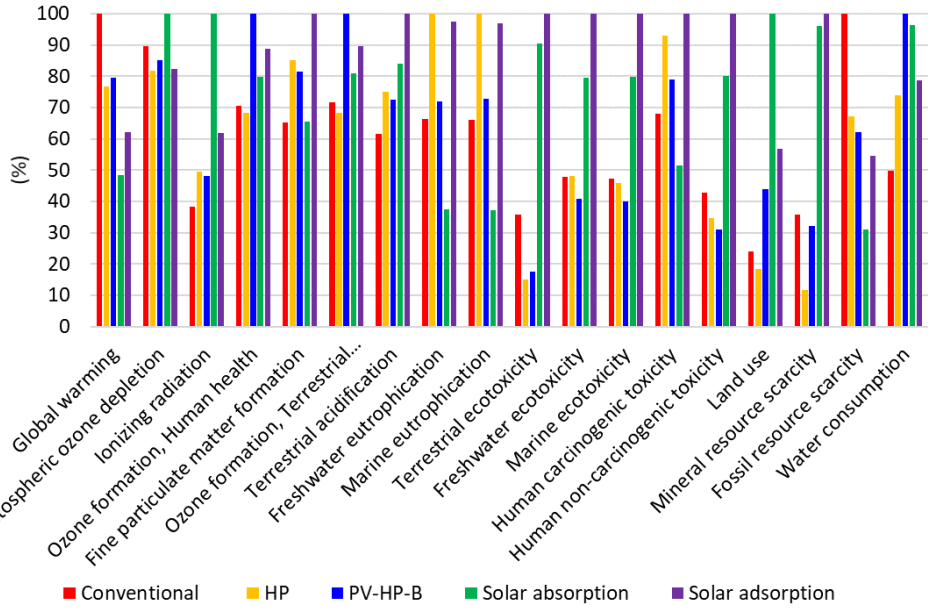

(a)

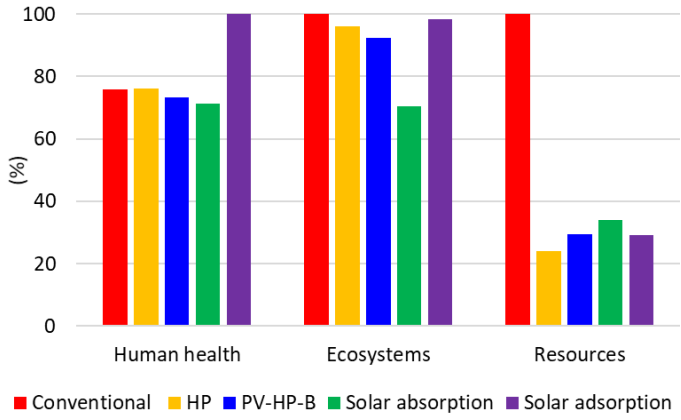

(b)

Fig. IV.1. Comparative Impact Assessment results of residential cooling/heating systems at (a) Midpoint Level and (b) Endpoint Level for the case of Chania (Zone A), Greece.

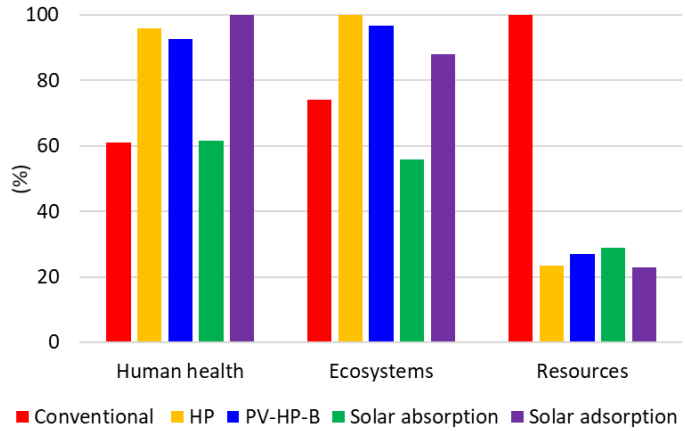

(a)

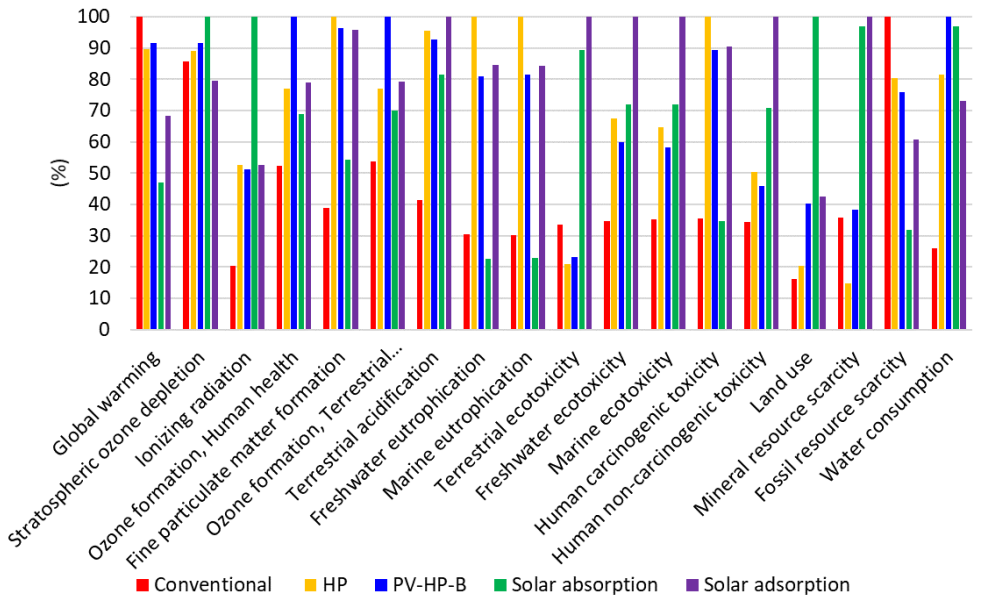

(b)

Fig. IV.2. Comparative Impact Assessment results of residential cooling/heating systems at (a) Endpoint Level and (b) Midpoint Level for the case of Thessaloniki (Zone C), Greece.

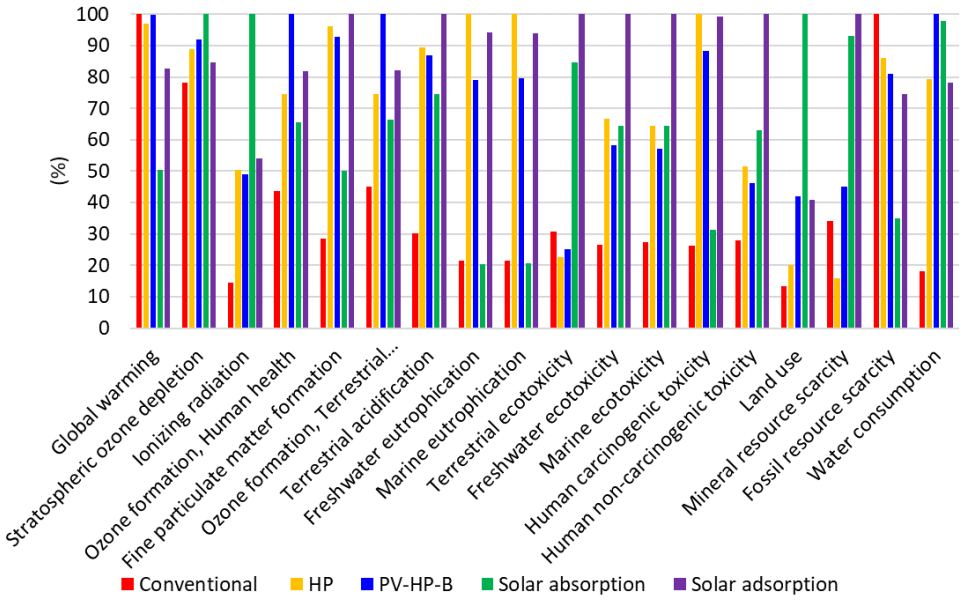

(a)

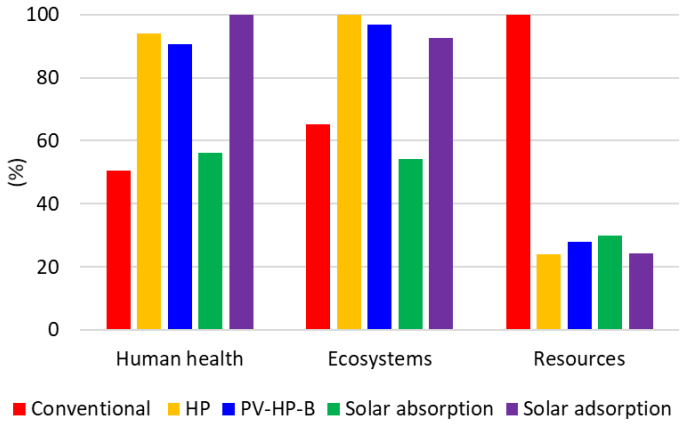

(b)

Fig. IV.3. Comparative Impact Assessment results of residential cooling/heating systems at (a) Midpoint Level and (b) Endpoint Level for the case of Kozani (Zone D), Greece.

IV.3 Complementary data of LCA on solar ORCs

Hereby are listed the comparative impact assessment results at Midpoint and Endpoint level of the solar driven ORC systems, presented in section 6.4, for climatic zones A, C and D.

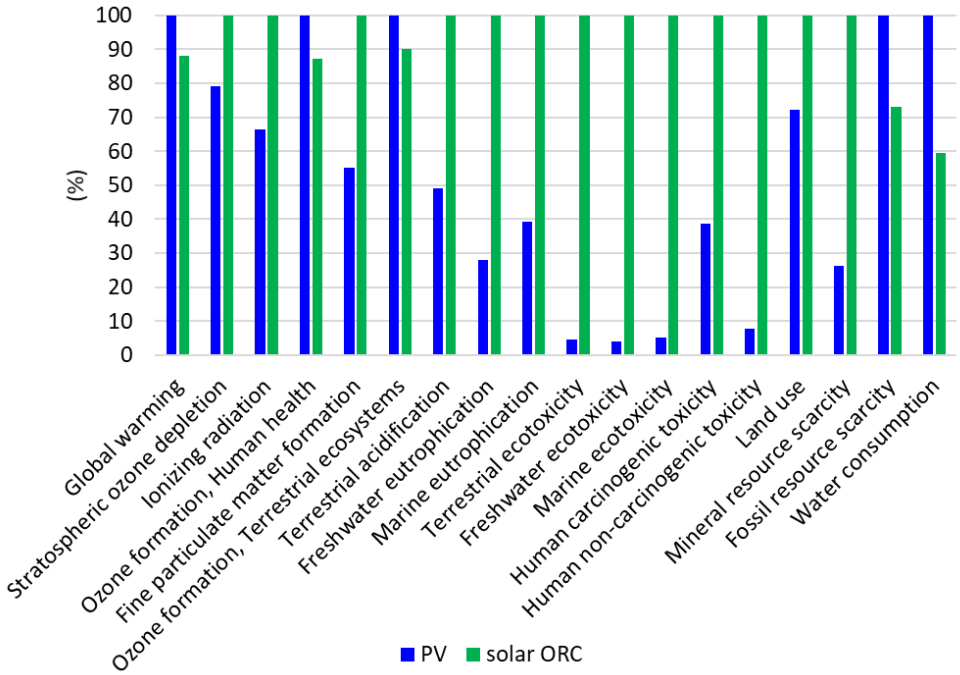

(a)

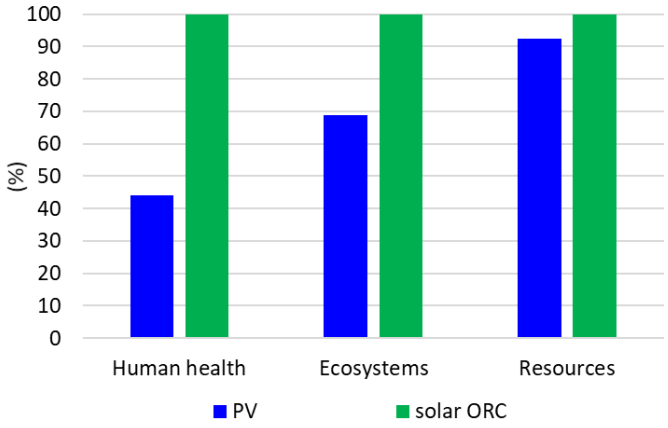

(b)

Fig. IV.4. Comparative Impact Assessment results of FPC driven ORC system operating with R152a in respect with a PV panel at (a) Midpoint Level and (b) Endpoint Level for the case of Chania (Zone A), Greece.

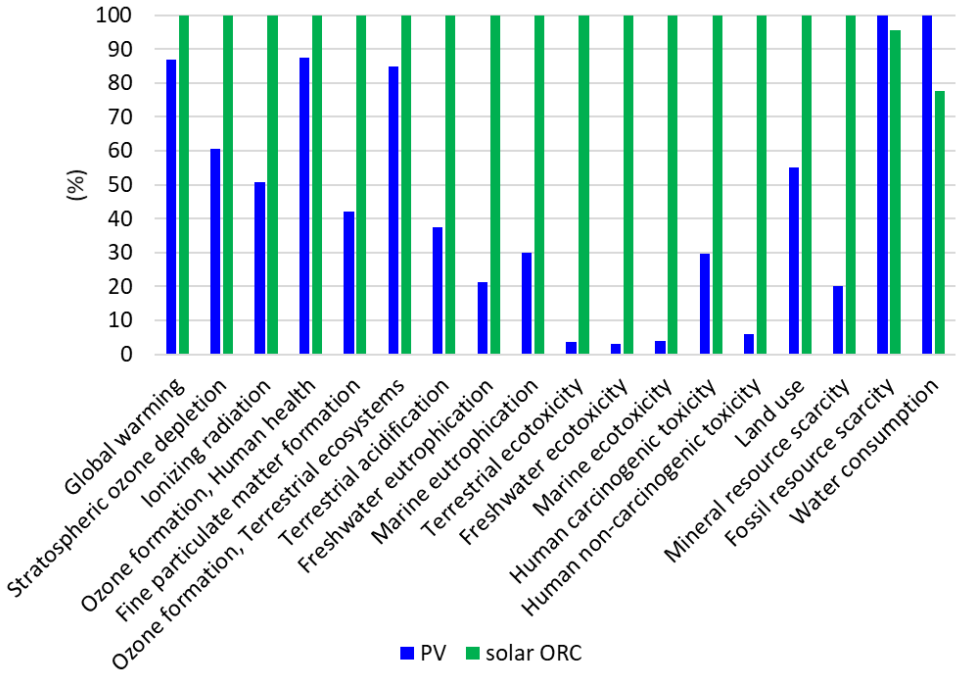

(a)

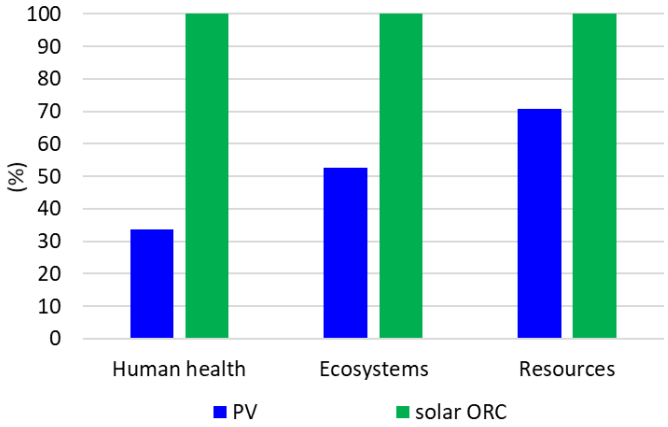

(b)

Fig. IV.5. Comparative Impact Assessment results of FPC driven ORC system operating with R152a in respect with a PV panel at (a) Midpoint Level and (b) Endpoint Level for the case of Thessaloniki (Zone C), Greece.

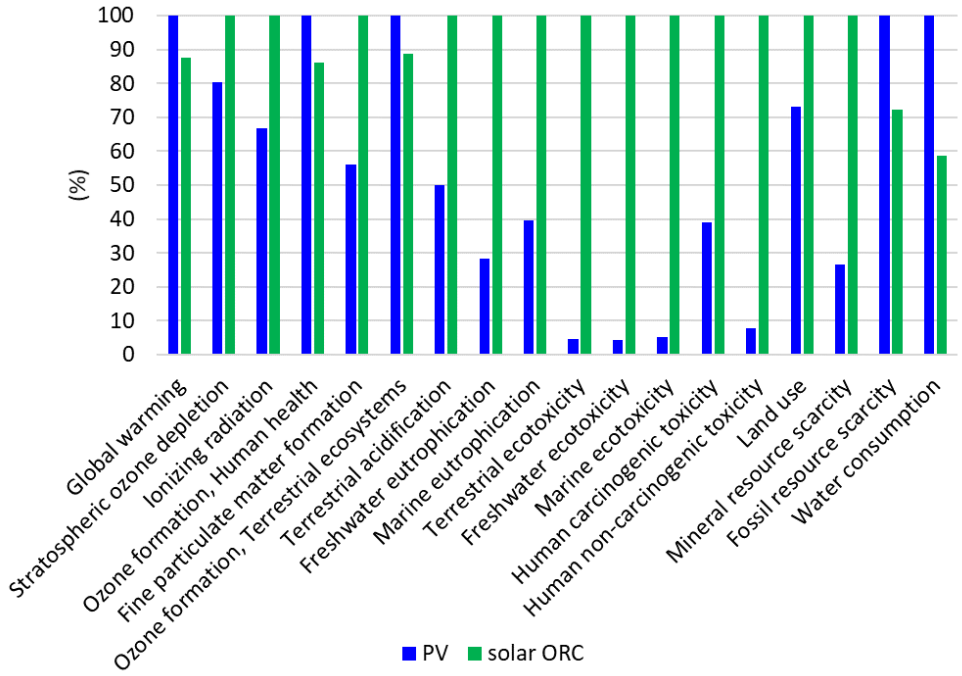

(a)

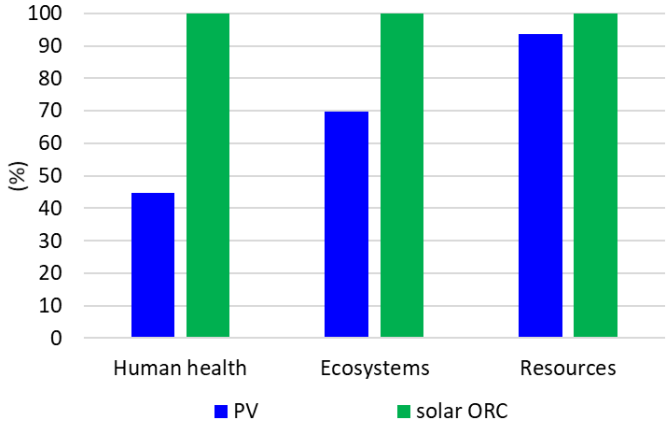

(b)

Fig. IV.6. Comparative Impact Assessment results of FPC driven ORC system operating with R152a in respect with a PV panel at (a) Midpoint Level and (b) Endpoint Level for the case of Kozani (Zone D), Greece